Dynamics of the Meiotic Division in *Drosophila* Males

Dissertation

zur

Erlangung der naturwissenschaftlichen Doktorwürde
(Dr. sc. nat.)

vorgelegt der

Mathematisch-naturwissenschaftlichen Fakultät

der

Universität Zürich

von

Soumya Chaurasia

aus

Indien

Promotionskommission

Prof. Dr. Christian F. Lehner (Vorsitz)

Prof. Dr. Stefan Luschnig

Prof. Dr. Clemens Cabernard

Prof. Dr. Alex Hajnal

Zürich, 2017

Contents

Acknowledgements

I would sincerely like to thank...

...Prof. Dr. Christian Lehner for giving me the opportunity to do my PhD thesis on such an exciting topic in his lab, for his valuable guidance and perpetual support especially during tough times. I have learned a lot during all these years and still have a long way to go.

...Ariane Blattner for her generous help with fly genetics and fly husbandry.

…Martina Trost and Sina Moser for their technical help.

...members of the Lehner lab for general assistance and maintaining a cordial lab atmosphere.

…my friends and colleagues, especially Stefano Leo, Kathrin Gerhard, Orlando Schwery, Martina Trost, Jade Glashauser and Nevena Zivanovic for always motivating me and standing by my side.

…members of Damian Brunner and Konrad Basler labs for their comments and suggestions during joint lab meetings.

…Susanna Bachmann and the MLS graduate program for an enriched scientific exposure in the heart of Zürich.

मैं धन्यवाद देना चाहूँगी अप्ने पूरे परिवार को जिन्होंने सदा मुझे प्रोत्साहित किया और हर समय आगे बढ़ने की प्रेरणा दी। इस्के साथ मैं उन सभी लोगों को भी कुछ श्रेय देना चाहूँगी जिन्होंने हमेशा जीवन की चुनौतियों को मेरे लिए केवल कठिन बनाया। इन्हीं अनुभवों से मुझे अत्यधिकआत्मिक शक्ति मिली। आज मैं एक समझदार इंसान हूँ। अंत में, अप्ने प्रिय मित्रों की, संयुक्ता, प्रियन्का, सुमित, कोमल, शिवम, निखिल, अर्पन, राजलक्ष्मी, श्रुति, शानू और नितिका की मैं सदा के लिए आभारी रहूंगी। आपके सहयोग के बिना मैं शायद इतने आगे नहीं आ पाती। आशा यही है कि आगे भी आपका प्यार और आशीर्वाद जीवन को खुशहाल बनाए रखेगा।

Zusammenfassung

Zur Produktion von Gameten für die sexuelle Fortpflanzung wird die Ploidität des eukaryotischen Genoms durch meiotische Teilungen von diploid auf haploid reduziert. Normalerweise trennt eine erste meiotische Teilung (Meiose I) die gepaarten homologen Chromosomen und verteilt diese auf entgegengesetzte Spindelpole. Während der Meiose I organisieren die beiden Schwesterzentromeren eines homologen Chromosoms zusammen nur ein einziges Kinetochor. Dies erklärt, warum die beiden Schwesterchromatiden während der ersten meiotischen Teilung zum selben Spindelpol hin gezogen werden. In der zweiten meiotischen Teilung wird aber, wie auch während der Mitose, von jedem der beiden Schwesterzentromeren ein funktionell eigenständiges Kinetochor organisiert. Daher werden in Mitose und Meiose II die beiden Schwesterchromatiden auf entgegengesetzte Spindelpole verteilt. Die molekularen Mechanismen, die für die funktionelle Vereinigung der Schwesterzentromeren in Meiose I und deren Individualisierung in Meiose II sorgen, werden erst ansatzweise verstanden. Zur besseren Charakterisierung wurde ein effizientes Verfahren für die lichtmikroskopische Beobachtung von meiotischen Teilungen mit hoher zeitlicher und räumlicher Auflösung entwickelt. Das Untersuchungsmaterial, intakte Zysten mit Spermatozyten, wurde aus transgenen Taufliegen der Spezies *Drosophila melanogaster* isoliert. Dank den Transgenen konnten diverse fluoreszierende Fusionsproteine exprimiert und beobachtet werden. Damit konnte die Dynamik von Komponenten des Zentromers (Cid/Cenp-A, Cenp-C), des Kinetochors (Mis12, Spc105, Nuf2), der Spindel (Tubulin) und des „Spindle assembly checkpoints (SAC)“ (Bub3, Rod) mit demjenigen der Chromosomen (His2Av) verglichen werden. Über die Analyse der ungestörten Meiose hinaus wurden auch Untersuchungen nach gezielter Interferenz mit Mutationen (*mnm*, *mad2*, X/0 Genotyp), RNAi (*Spc105*) oder Chemikalien (Colcemid) durchgeführt. Damit wurde untersucht, wie sich der Verlust von Homologenpaarung, SAC-, Kinetochor- und Spindelfunktion auf den Ablauf der meiotischen Teilungen auswirkt. Die Ergebnisse zeigen, dass die bipolare Integration von Chromosomen in die meiotischen Spindelapparate innerhalb eines erstaunlich kurzen Abschnittes der Prometaphase gelingt. Diese hohe Effizienz macht SAC-Funktion überflüssig, wenn ansonsten keine weiteren Störungen vorliegen. Inhibition der Spindelbildung bewirkt jedoch eine SAC-abhängige Verzögerung. Im Gegensatz dazu führt der verfrühte Verlust von

Homologenpaarung nur zu einer sehr kurzen Verzögerung in der Meiose I. Die sprunghaften Bewegungen von Kinetochoren der univalenten Chromosomen, die in der *mnm*-Mutante anstelle von normalen bivalenten Chromosomenpaaren in der Meiose I vorliegen, erfolgen aber über einen verlängerten Zeitraum bevor die meisten Chromosomen dann trotzdem in einer Metaphasenplatte immobilisiert werden. Diese Beobachtungen zeigen, dass die mechanischen Zugkräfte, die ein Kinetochorenpaar nach bipolarer Chromosomen-Orientierung partiell auseinanderziehen, die Anheftung von Kinetochoren an Spindelmikrotubuli sehr effizient stabilisieren. Ausserdem führt eine progressive globale Stabilisierung von solchen Kontakten schliesslich dazu, dass auch Chromosomen, die noch nicht mit der korrekten bipolaren Orientierung in die Spindel integriert worden sind und somit nicht den normalen Zugkräften ausgesetzt sind, eine stabile Spindelanheftung gewinnen können. Die zeitaufgelöste Messung des Abstandes zwischen Schwesterkinetochoren in bipolar integrierten univalenten Chromosomen in der Meiose I in der *mnm*-Mutante ergab Hinweise, dass die Individualisierung der Schwesterzentromeren beim Übergang von der Meta- in die Anaphase erfolgt und dass die Schwesterzentromeren danach weiterhin durch eine sehr elastische Verbindung zusammen gehalten werden. Daher kann die Schwesterzentromeren-Individualisierung während der normalen Meiose auch mit hochauflösender STED-Mikroskopie erst nach der bipolaren Chromosomen-Integration in der Meiose II-Spindel eindeutig nachgewiesen werden. Beim Beginn der zweiten meiotischen Teilung sind die Schwesterkinetochoren immer noch unmittelbar benachbart. Trotzdem erfolgt bipolare Chromosomen-Integration, die zu einer partiellen klar sichtbaren Trennung der Schwesterkinetochoren führt, in der Meiose II schnell und fast immer auf Anhieb richtig. Somit ergeben sich ausgesprochen deutliche Unterschiede zwischen den zellulären Strategien der Chromosomenverteilung während der männlichen Meiose in *D. melanogaster* und der bereits früher ebenfalls sorgfältig untersuchten Meiose I in Säugern (Maus und Mensch). Im Übrigen werden in der Arbeit noch Fortschritte zur Klärung der meiotischen Rolle von paralogen *D. melanogaster*-Genen für α-Kleisin-Proteine, sowie der Separase-vermittelten Spaltung dieser und anderer potentieller Separase-Substrate zusammengefasst.

Summary

Meiotic divisions achieve genome ploidy reduction from diploid to haploid for gamete production in the context of sexual reproduction in eukaryotes. The first division (meiosis I) usually separates paired homologous chromosomes onto opposite spindle poles. The two sister centromeres of a given homolog organize only one functional kinetochore during this first division. Therefore, both sister centromeres of a homolog are segregated to the same spindle pole during meiosis I. In contrast, during the following second division (meiosis II), each sister centromere organizes a separate functional kinetochore unit, as also during mitotic divisions. Therefore, sister centromeres are segregated to opposite spindle poles during meiosis II. The mechanisms controlling division-specific sister centromere behavior during meiosis are largely unknown. To explore these, efficient time lapse imaging of progression through both meiotic divisions with high temporal and spatial resolution was established using cysts of spermatocytes from transgenic Drosophila testis expressing various fluorescent fusion proteins. The temporal schedule of meiosis I and II was determined based on analyses with chromatin and microtubule markers. Within the obtained temporal framework, the localization dynamics of centromere proteins (Cid/Cenp-A and Cenp-C), kinetochore proteins (Mis12, Spc105, Nuf2) and spindle assembly checkpoint components (Bub3, Rod) was delineated. In combination with genetic and pharmacological perturbations (X/0 genotype, mutations in *mnm* and *mad2*, Spc105 depletion, colcemid addition), the responses to loss of physical linkage between homologs, as well as the responses to failure of kinetochore, spindle and SAC were analyzed. The results demonstrate that meiotic chromosome bi-orientation is normally achieved within a surprisingly brief part of prometaphase. This high efficacy of meiotic chromosome bi-orientation renders SAC function completely dispensable in otherwise unperturbed conditions. While loss of spindle function provoked a SAC-mediated arrest that is more robust than previously reported, premature homolog separation in *mnm* mutant meiosis I caused only a very limited overall delay. However, the kinetochores of univalents that are present in *mnm* mutant meiosis I instead of normal bivalents displayed rapid jumps for a prolonged period, but eventually also congressed into the metaphase I plate, apparently as a result of either sister kinetochore bi-orientation or merotelic attachments of one or both sister kinetochores. These results indicate that mechanical tension exerted on a kinetochore pair in response to successful bi-orientation stabilizes kinetochore attachment to meiotic spindle microtubules effectively. Moreover, progressive global stabilization appears to preserve irregular kinetochore attachments eventually even when they do not generate normal tension between paired kinetochores. Measurements of inter sister kinetochore distance in bi-oriented univalents in *mnm* mutant meiosis I over time suggested that sister centromere individualization occurs after the metaphase to anaphase I transition and that the separated sister centromeres are kept together by highly elastic tethers. As a result of these tethers, sister centromere individualization in normal meiosis cannot be detected before bi-orientation in meiosis II, not even by stimulated emission depletion (STED) microscopy. Sister kinetochores were still closely associated in a side-by-side configuration on the same chromosome face when interactions with microtubules started during normal prometaphase II. Nevertheless, bi-orientation accompanied by stretching apart of sister kinetochores was successfully completed in a few minutes without multiple attempts usually. In comparison with mammalian oocytes that have been analyzed previously with comparable resolution, major strategies of kinetochore orientation are strikingly different during Drosophila male meiosis. The thesis also summarizes progress towards understanding the functional contribution of α-kleisin paralogs (vtd/Rad21 and c(2)M) and separase-mediated cleavage of these and other potential substrates during male meiosis.

Preface

Meiosis is required in eukaryotes for sexual reproduction and occurs exclusively in the germline. It reduces ploidy in the prospective germ cells from diploid to haploid. Moreover, it includes usually meiotic recombination whereby maternal and paternal alleles are re-assorted into novel combinations. Therefore, meiosis acts to increase genetic diversity. In contrast, mitosis simply propagates the given genotype. Mechanistically, however, the meiotic divisions share extensive similarity with mitosis, except for some characteristic differences that are crucial for the success of meiosis.

Meiosis starts when chromosomes are replicated during the pre-meiotic S phase. Thereafter, homologous chromosomes are paired into bivalents. These are integrated into the spindle of the ensuing first meiotic division which segregates homologous centromeres away from each other to opposite spindle poles. Without an intervening S phase, cells enter into the second meiotic division where sister centromeres are segregated to opposite spindle poles. Thereby the end result of meiosis is achieved: four haploid daughter cells.

During the first meiotic division, sister centromeres behave in a special manner that is not observed during progression through mitotic division cycles. At the start of mitosis the two replicated sister centromeres present in each of the unpaired univalent chromosomes organize two functionally independent kinetochores. These two sister kinetochores become linked via kinetochore microtubules to opposite spindle poles. In striking contrast, at the start of meiosis I (MI), the two replicated sister centromeres of each chromosome behave as one functional unit and organize only one kinetochore (Figure 1). Bivalents that are generated by meiotic homolog pairing before entry into MI are therefore equipped with only two functional kinetochores, allowing their bi-orientation within the MI spindle and consequential segregation of homologous centromeres to opposite spindle poles. Importantly, for the success of the subsequent meiosis II (MII) it is essential that sister centromeres regain their functional independence (Figure 1). Each sister centromere needs to organize a fully functional kinetochore for bi-orientation of chromosomes within the MII spindle and segregation of sister chromatids to opposite spindle poles.

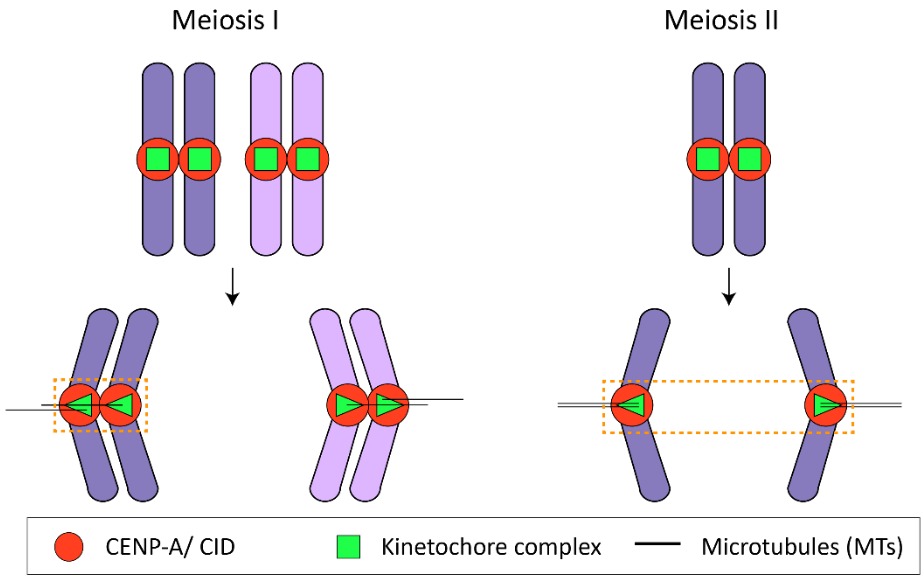

Figure 1. Characteristic behavior of sister kinetochores during meiosis: mono-oriented in meiosis I and bi-oriented in meiosis II (orange dotted lines). Pair of replicated homologous chromosomes are shown in light and dark purple. Arrows indicate onset of anaphase and chromosome distribution after segregation. For details, see text.

Apart from the special behavior of centromeres, which is the major focus of chapter 1 of this thesis, meiosis also relies on special processes that pair up homologous chromosomes before the first meiotic division and release the association between homologs just before the onset of anaphase I (Figure 2). Thereby sister centromeres remain paired, allowing their bi-orientation in the MII spindle. However, just before the onset of anaphase II, this residual association between sister chromatids needs to be resolved so that sister centromeres and the linked chromatids can be segregated onto opposite spindle poles during exit from MII. Chapter 2 in this thesis describes work on meiosis-specific sister chromatid cohesion. The corresponding results are more preliminary than those of the main chapter 1.

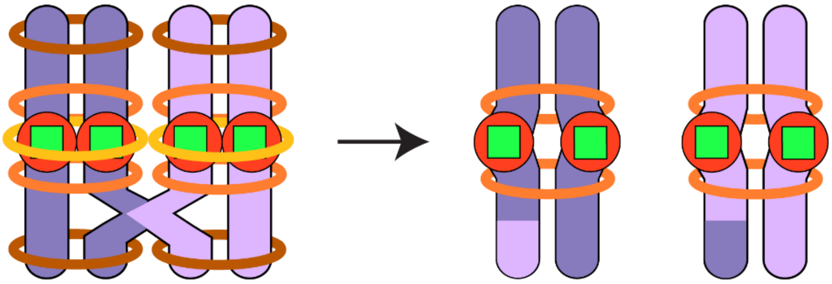

Figure 2. Characteristic behavior of sister kinetochores during meiosis: Resolution of centromeric associations (yellow rings) allows sister centromeres gain functional independence despite continued pairing of chromatids (orange rings). Pairing of sister chromatids is also mediated by arm cohesins (brown rings). Homologous recombination occurs via crossing over resulting in shuffling of genes. For details, see text.

The following two thesis chapters both have individual introduction sections. The relatively short introduction within chapter 2 is specific for experimental approaches and findings of this second chapter. In contrast, the introduction within the first chapter is more general, displaying background that is also relevant for the second chapter. This general introduction starts with an overview on our current understanding of mitosis. This process is considerably more accessible experimentally and hence better understood than meiosis. The initial part of the introduction is focused primarily on mitotic chromosome segregation and its control, presenting findings that are either known or believed to apply to meiosis as well. Thereafter, meiosis-specific process modifications and the state of the corresponding understanding will be summarized. The focus of this work is on meiotic chromosome segregation; meiotic recombination will not be considered.

Chapter 1:

Dynamics of the meiotic division in Drosophila males

Introduction

1.1 Molecular mechanisms controlling entry into and progression through M phase

The onset of M phase in case of mitosis, MI and MII, is thought to result from the switch-like maximal activation of M-Cyclin/Cdk1 complexes. The DNA damage and replication checkpoint prevents a premature M-Cyclin/Cdk1 activation. DNA replication during S phase converts each chromosome in a pair of sister chromatids. Sister chromatid cohesion keeps sister chromatids paired, allowing their bi-orientation in mitotic spindles. Cohesion is primarily mediated by cohesin, a ring like protein complex around sister chromatids that enforces their proximity in a topological manner (Haering et al., 2008; Lee and Amon, 2001; Nasmyth and Haering, 2005; Uhlmann, 2003). The cohesin complex is composed of four subunits SMC1, SMC3, SCC1/Rad21 and SCC3. The cohesive assembly around sister chromatids occurs already during S phase.

The switch-like activation of the master regulator M-Cyclin/Cdk1 at the G2/M transition activates condensin which is a protein complex similar to cohesin. Condensin activity in combination with topoisomerase II is thought to be largely responsible for chromosome condensation and the accompanying individualization of sister chromatids during pro- and prometaphase (Hirano et al., 1997; Uhlmann, 2016). M-Cyclin/Cdk1 activity phosphorylates hundreds of substrate proteins and thereby induces not just chromosome condensation but also spindle assembly and nuclear envelope breakdown, which marks the onset of prometaphase (Fisher et al., 2012). M-Cyclin/Cdk1 activity also triggers the assembly of kinetochores within the centromere regions of chromosomes. In mitosis, one individual kinetochore is assembled on both sister centromeres. The kinetochore, a complex network of proteins as further explained below, allows load-bearing attachment of sister chromatids to spindle microtubules during cell division. Bipolar orientation of sister chromatids is achieved when pulling forces of microtubule attachments from opposite poles are working against the resistive activity of cohesin rings. The resulting mechanical tension on kinetochores stabilizes the attachments of the kinetochore fibers of the spindle, and force balance positions the chromosomes into the metaphase plate until the onset of metaphase/anaphase transition (M/A transition).

Tension-regulated control of kinetochore attachments is thought to favor correct amphitelic over erroneous attachments (like syntelic) and contribute to correction of these attachment errors (see below). This error correction requires time. Premature anaphase onset needs to be prevented. For this, the spindle assembly checkpoint (SAC) comes into play (see also below). The SAC is activated by kinetochores that are not yet stably attached to the spindle. It delays onset of the metaphase/anaphase transition by inhibiting the activity of the anaphase promoting complex (APC/C). APC/C-Cdc20 activation results in M cyclin degradation and thereafter inactivation of Cdk1. Once Cdk1 is off, APC/C-Cdh1 can become active. The APC/C is a ubiquitin ligase that poly-ubiquitinylates M-Cyclins, securin and other proteins. The poly-ubiquitinylated proteins are degraded by the proteasome. Degradation of securin which functions as an inhibitor of the protease separase results in separase activity. This in turn results in proteolytic cleavage of the α-kleisin subunit (Rad21) of the cohesin complex and thereby eliminates sister chromatid cohesion. Anaphase, characterized by segregation of sister chromatids to opposite spindle poles, can start. Degradation of the M-Cyclins results in Cdk1 inactivation. Therefore, the processes triggered by Cdk1 activation during entry into M phase (chromosome condensation, spindle assembly, nuclear envelope breakdown) are reverted during telophase. Exit from mitosis is completed by cytokinesis.

1.2 Centromere and kinetochore

The centromere is a specialized chromosome region that acts as the recruitment site for proteins of the kinetochore complex (Rieder, 1982). Many eukaryotic species have regional centromeres typically made from several kilo- to megabases of repetitive DNA (about 170 bp α-satellite repeats in humans, shorter repeats in *Drosophila melanogaster*). However, point centromeres spanning just 125 bp as in *Saccharomyces cerevisiae* or holocentric centromeres covering the entire chromosomal length as in *Caenorhabditis elegans* also occur (McKinley and Cheeseman, 2016).

The centromere region is usually not specified by specific DNA sequences (except for the point centromeres of *S. cerevisiae*). Rather it is the presence of a specific chromatin type that specifies centromere identity epigenetically (McKinley and Cheeseman, 2016). Within centromeric chromatin, special nucleosomes are found that have a composition distinct from canonical nucleosomes. These centromeric nucleosomes are characterized by the presence of a centromere-specific histone H3 variant (Cse4 in budding yeast, CENP-A in mammals, CID in Drosophila) replacing canonical histone H3.

The kinetochore is the microtubule-binding interface at the centromere, and is thought to be comprised of 80-100 proteins (Musacchio and Desai, 2017). In most eukaryotes, the kinetochore core consists of an inner and outer layer. The inner, centromere-proximal layer is comprised of the so-called constitutive centromere-associated network (CCAN), which binds to CENP-A and contains up to 16 subunits in mammals.

The outer, centromere-distal layer of the kinetochore is made up of the KMN network of protein complexes (**K**nl1 complex, **M**is12 complex, **N**dc80 complex). In vertebrates, the Knl1 complex includes KNL1 (CASC5/Blinkin/Spc105/Spc105R) and ZWINT. The Mis12 complex is made up of four subunits namely Mis12 (or MIND), Nsl1 (or Mis14), Nnf1 and Dsn1 (or Mis13). Lastly, the Ndc80 complex is also comprised of four subunits (Ndc80 or Hec1, Nuf2, Spc24 and Spc25). The N-terminal tail and the following globular CH domain of Ndc80 binds microtubules efficiently. As detailed below, this activity is crucial for “end-on” attachment of the kinetochore to kinetochore microtubules. Moreover, as also summarized below, the KMN network also recruits the SAC proteins. Finally, the KMN network assembles a fibrous corona that forms an extended outer most region of the kinetochore. The outer corona contains motor proteins (dynein, Cenp-E) that are crucial for the initial interactions between microtubules and kinetochores. The expanded outer corona present early in mitosis maximizes the likelihood of microtubule capture (Hoffman et al., 2001; Magidson et al., 2015; Mosalaganti et al., 2017; Wynne and Funabiki, 2015). These initial interactions occur after nuclear envelope breakdown, when spindle microtubules invade the nucleoplasm. The initial interactions are usually between microtubules that interact “laterally” with kinetochore bound dynein. In these lateral interactions, microtubules graze tangentially across and beyond the kinetochore. Dynein, the major minus-end directed motor in cells, is recruited to the kinetochore via Spindly and the ROD–Zwilch–ZW10 (RZZ) complex that in turn appears to be recruited by the KMN network. Dynein moves laterally interacting kinetochores rapidly towards microtubule minus ends, i.e. towards the spindle pole. At the pole, microtubule density is maximal. Also the density of kinetochore microtubules (KT-MTs) that have already established end-on attachment with a stably congressed chromosome are maximal at the spindle pole. Therefore, the plus-end directed kinesin CENP-E within the outer corona comes into play. It can transport chromosomes on existing KT-MTs into the equatorial region where sister kinetochore bi-orientation is more likely to happen. Therefore, kinetochore dynein and CENP-E laterally transport chromosomes along microtubules towards and away from the poles, respectively, finally culminating in chromosome congression. The outer corona also hosts additional microtubule binding proteins like CLASP and CENP-F.

Lateral attachments of kinetochores must be converted into end-on attachments in order to achieve bi-orientation. This process is highly dynamic and is under complex regulatory control so that erroneous KT-MT attachments are corrected (see below error correction). The establishment of end-on attachment mediated via Ndc80 is thought to be accompanied by the removal of the outer corona. This corona shedding takes place along KT-MTs by dynein mediated transport of corona proteins. Large particles containing Dynein-Dynactin-Spindly-RZZ complexes along with other corona components and SAC proteins move away from kinetochores towards the spindle poles (Maiato et al., 2017; Musacchio and Desai, 2017). This contributes to SAC silencing (Mosalaganti et al., 2017). Moreover, it converts the shape of kinetochores from an extended crescent to a smaller, plate-like appearance. This change in kinetochore organization (large crescent at the start of prometaphase, small plate in metaphase) appears to increase the efficiency of the bi-orientation process (Magidson et al., 2015; Wynne and Funabiki, 2015). The end on attachment of the KT to the plus ends of KT-MTs via Ndc80 does not block microtubule dynamics at the plus ends. High resolution analysis has revealed that the binding of the Ndc80 complex to microtubules is sensitive to the protofilament conformation and suggested explanations for maintenance of binding to depolymerizing KT-MTs as required during anaphase (Alushin and Nogales, 2011). Moreover, the SKA complex identified in vertebrates has been shown to retain Ndc80 complex at depolymerizing microtubule tip ends (Schmidt et al., 2012).

While many features of kinetochore organization are rather well conserved in eukaryotes, there is also evidence for an unexpected evolutionary plasticity. Surprisingly, the CCAN is much simpler in some organisms like *C. elegans* and *D. melanogaster* where only one CCAN protein, CENP-C, seems to be present. Similarly, an equivalent to the SKA complex and Cenp-

F has not been found in *D. melanogaster* so far. Moreover, in *D. melanogaster*, also the KMN network has some special features (Figure 3).

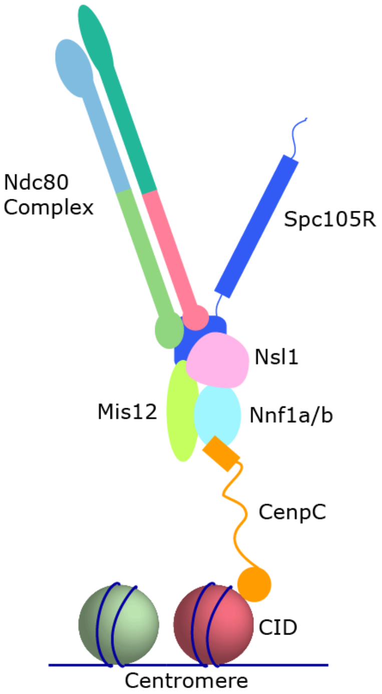

Figure 3. Major components of a Drosophila kinetochore complex (adapted from Singleton, 2016).

The Drosophila KMN network has several unusual features. For example, Dsn1 appears to be absent from the Mis12 complex. Moreover, two paralogues encoding the Mis12 complex subunit Nnf1 are present, *Nnf1a* and *Nnf1b*. *Nnf1a* and *Nnf1b* are functionally overlapping even though the protein products appear to behave differently during kinetochore recruitment of the Mis12 complex (Blattner et al., 2017). Finally, Drosophila Spc105, the KNL-1 homolog (designated as Spc105R in FlyBase) underwent considerable sequence divergence in comparison with orthologs in other species (Liu et al., 2016; Richter et al., 2016; Schittenhelm et al., 2009). The C terminal domain of Drosophila Spc105 appears to have taken over the functions of the missing Dsn1 protein (Przewloka and Glover, 2009). However, the mode of binding of Spc105 and the Ndc80 complex to the Mis12 complex is still not clearly understood (Singleton, 2016).

In *D. melanogaster*, the KMN network is recruited only by Cenp-C (Przewloka et al., 2011; Przewloka et al., 2007; Schittenhelm et al., 2007) while in other eukaryotes the CCAN components CENP-T/W also contribute to KMN recruitment (Musacchio and Desai, 2017).

The order of recruitment of KMN network proteins in Drosophila differs from that in humans. Mis12 and Spc105 are co-dependent in their recruitment to Cenp-C. The Ndc80 complex is recruited downstream of Spc105 and thus depends on prior recruitment of Spc105. Particularly, in Drosophila S2 cells, the assembly of Mis12 complex with Ndc80 requires Spc105 (Przewloka et al., 2007; Schittenhelm et al., 2009). In addition, Mis12 is constitutively present at the centromere (Venkei et al., 2011).

1.3 Error correction

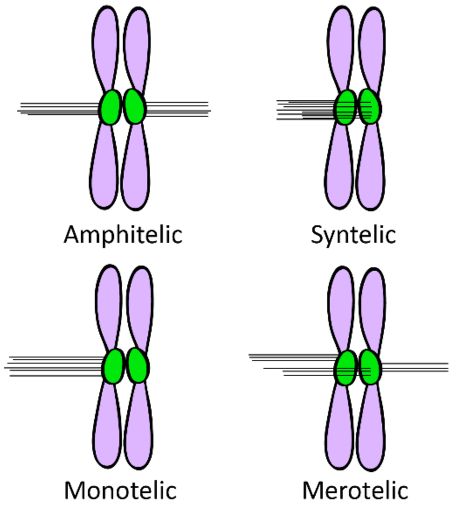

Figure 4. Modes of kinetochore microtubule end-on interactions (for details, see text).

During the progression from prometaphase to metaphase, some chromosomes may be delayed in connecting to the spindle, whereas others may be inappropriately attached (Cheeseman and Desai, 2008). The kinetochore microtubule end-on attachments are classified into four major types (Figure 4): *amphitelic*, when the two sister KTs are attached to microtubules with one KT being connected to only one spindle pole and the other KT to only the opposite spindle pole; *syntelic*, when both KTs are attached to microtubules from the same spindle pole; *monotelic*, when only one KT is attached to microtubules from one spindle pole and; *merotelic*, when at least one KT is attached to microtubules from both spindle poles. As kinetochore capture by spindle microtubules is a largely stochastic process, all four types of attachments can occur early in mitosis.

Anaphase onset before all chromosomes have reached bi-orientation (i.e. exclusively amphitelic attachments) results in chromosome segregation errors which can have deleterious consequences. Aneuploidies (like loss or gain of chromosome segments or complete chromosomes) and polyploidies (additional complete chromosome sets) predispose towards cancer and can by themselves cause pathology (for example trisomy 21) or lethality (for example the majority of spontaneous abortions). Therefore cellular mechanisms for correction of faulty attachments before anaphase onset have evolved.

The mechanisms that bring about error correction are only partially understood (Lampson and Grishchuk, 2017). Error correction presumably involves tension sensing. As a consequence of bi-orientation, sister kinetochores are spatially stretched away from the inner centromere region which hosts the Aurora B kinase. Aurora B kinase activity destabilizes kinetochore-microtubule attachments. However, bi-orientation stretches the attached kinetochores beyond the range of Aurora B kinase activity which is spatially graded with highest activity in the inner centromere region. The mechanical tension resulting from bi-orientation therefore stabilizes the attachment of kinetochores to spindle microtubules. In contrast, incorrect attachments (like mono- or syntelic) which do not generate comparable tension result in detachment of microtubules from kinetochores. This allows for additional attempts at attaching kinetochores which will be stabilized only when correct, i.e. amphitelic. The correction of merotelic attachments appears to be most difficult as considerable tension can be generated in this case.

Elegant experiments have provided evidence for the role of Aurora B kinase in error correction as described above. Graded Aurora B kinase activity has been demonstrated (Liu et al., 2009) and several kinetochore proteins are known to be phosphorylated by Aurora B. Moreover, the microtubule-binding affinity of several KMN network proteins is reduced by Aurora B kinase phosphorylation (Musacchio and Desai, 2017). Additional evidence suggests that error correction depends on players beyond Aurora B (Lampson and Grishchuk, 2017). Phosphatases are involved as well and the KMN network by itself seems to have an inherent ability in converting mechanical tension into increased binding affinity (catch bond like) (Akiyoshi et al., 2010).

Modeling has demonstrated that error correction is not necessarily dependent on tension sensing (Lampson and Grishchuk, 2017). Kinetochore geometry is crucial for this tension-sensing independent error correction. A back-to-back arrangement of sister kinetochores has been proposed to reduce the number of initial wrong attachments. A cup of chromatin underlying the kinetochore is proposed to have a shielding effect, allowing microtubules to contact the kinetochore only when they approach from the front direction. The resulting geometric bias favoring amphitelic over erroneous attachments (syntelic, merotelic) in combination with dynamic turn-over of attachments (not regulated by mechanical tension) is sufficient to correct occasional initial errors into correct attachments. Moreover, by reducing the dynamics of attachment turn-over globally over time (again independent of mechanical tension) correct attachments can nevertheless acquire strong KT fibers (Lampson and Grishchuk, 2017). In vertebrate cell mitosis, KT-MT stability increases and hence attachment turn-over decreases as Cyclin A levels decrease during prometaphase, thereby resulting eventually in stable attachments in metaphase. The presence of cyclin A during early prometaphase therefore stimulates the efficiency of error correction (Di Fiore and Pines, 2010; Kabeche and Compton, 2013). For faithful chromosome segregation, therefore, the stability of KT–MT attachments must fall within a narrow permissible and changing range compatible with error correction as well as with eventual SAC silencing (Musacchio and Salmon, 2007).

1.4 Spindle assembly checkpoint

The spindle assembly checkpoint (SAC) is a surveillance mechanism that ensures the fidelity of chromosome segregation (Foley and Kapoor, 2013; Musacchio, 2015; Musacchio and Salmon, 2007). The SAC is activated by unattached kinetochores. SAC activity inhibits the APC/C and thereby inhibits a premature metaphase to anaphase transition. However, once all kinetochores are attached to microtubules, the SAC is silenced, permitting entry into anaphase. SAC components include kinases like Mps1 and Bub1 as well as proteins without enzymatic functions like Mad1, Mad2, Mad3/BubR1 and Bub3. After activation, the SAC generates the mitotic checkpoint complex (MCC). Via binding to Cdc20 this MCC inhibits the APC/C. Mps1, a master regulator of SAC, appears to bind to Ndc80 in competition with KT-MTs. Therefore, Mps1 binds efficiently to unattached KTs but no longer to attached KTs. When bound to the KT, Mps1 phosphorylates Spc105 (within its MELT repeats) which allows the subsequent recruitment of the other SAC components. An additional pathway for recruitment of the SAC components Mad1 and Mad2 involves the RZZ complex (Foley and

Kapoor, 2013). There is increasing evidence that stable KT-MT attachments are sufficient to silence the SAC even in the absence of bi-orientation and tension (Etemad et al., 2015; Tauchman et al., 2015). However, it remains a possibility that tension sensing via or independent of AurB also regulates SAC activation directly. If indeed tension regulates the attachment of KTs to microtubules, absence of tension clearly activates the SAC indirectly by generating unattached KTs.

Interestingly, the SAC machinery has also been implicated in temporal control of the M/A transition in a manner that is independent of kinetochore function (Meraldi et al., 2004b). Observations made in frog embryos, where the SAC is not yet functional during the first cleavage divisions, have revealed that Cdk1 inactivation and hence exit from mitosis occurs automatically as a late consequence of Cdk1 activation at the start of M phase. In cells like HeLa, which have a functional SAC, a cytoplasmic pool of some SAC proteins appears to prolong the delay between Cdk1 activation and the consequential eventual Cdk1 inactivation. In HeLa cells, Mad2, BubR1 and Mps1 delay the exit from M phase in a kinetochore independent manner (Maciejowski et al., 2010; Meraldi et al., 2004a). During the syncytial divisions in Drosophila embryos, Mad2 and BubR1 have also been proposed to have this kinetochore independent timing function (Buffin et al., 2007; Rahmani et al., 2009). Most likely this timer function contributed by some of the SAC proteins also involves APC/C inhibition.

Importance of the SAC varies in different organisms and developmental stages (Foley and Kapoor, 2013; Sacristan and Kops, 2015). The SAC genes are essential in the mouse. Similarly, SAC function is required for successful proliferation of human cells in culture. In contrast, in otherwise unperturbed conditions, most of the SAC genes are not essential in yeast. In *D. melanogaster*, *mad2* is dispensable (Buffin et al., 2007). It has been proposed that the lower number of chromosomes present in the *D. melanogaster* karyotype might explain the relaxed SAC requirement compared to humans and mice.

The robustness of the SAC varies as well. Treatment of cells with high doses of microtubule poisons results in full SAC activation and causes a delay in mitosis that is about 4 times longer in cultured human cells compared to Drosophila S2R+ cells. However, even in humans cells, full SAC activation seems to be incapable of inhibiting the APC/C completely. Residual APC/C activity therefore permits cells to “slip” out of mitosis eventually despite continued SAC signaling, a process called mitotic checkpoint slippage (Rieder and Maiato, 2004). In early *C. elegans* embryos, slippage occurs rapidly, while a significantly longer delay is observed in late embryos. The ratio between cell size and the number of kinetochores appears to explain the developmental changes in SAC robustness at least in part (Galli and Morgan, 2016).

1.5 Spindle assembly and SAC in meiosis

Changes in cell size and kinetochore number, as well as some additional factors, are of considerable relevance when comparing division control during mitosis and meiosis. Moreover, in sexually reproducing animals, meiosis is coordinated with the production of two strikingly different and highly specialized types of gametes, sperm and egg. Usually, eggs are very large cells containing abundant stores of mRNA, proteins and nutrients produced during oogenesis. These maternally provided stockpiles support embryogenesis. In contrast, sperm consist primarily of a maximally compacted cell nucleus and a flagellum for motility. The research described in this thesis, was performed with testes from *D. melanogaster* and the process of spermatogenesis will be described in further detail below. The distinct specialization of egg and sperm has profound effects on many aspects of the meiotic divisions.

One of the adaptations enabling the production of large eggs is the asymmetric nature of the two meiotic divisions. In mammals, MI segregates one chromosome complement into a large egg cell and another complement into a small polar body, a terminal cell. In an analogous asymmetric manner, MII preserves egg size largely and generates a second small polar body. In *D. melanogaster* oocytes, an absence of cytokinesis during the meiotic divisions prevents egg size reduction even more effectively. Of the four haploid products generated by female meiosis in *D. melanogaster* only one is combined with the male pronucleus eventually, while the other three haploid products aggregate at the egg periphery where they enter into an arrest in M phase during the first mitosis of embryogenesis. In contrast to the female meiotic divisions, the divisions during male meiosis are symmetric. All four haploid products differentiate into sperm.

Another pronounced difference between female and male meiotic divisions is caused by the behavior of the centrosome. As centrosomes have a major effect on spindle formation, their number is under control. After centrosome duplication during interphase of the mitotic cell cycle, two centrosomes are present at the start of mitosis and they organize the poles of the bipolar spindle. Extra centrosomes are to be avoided as they can result in multipolar spindles and hence in the production of aneuploid cells. Centrosome number needs to be controlled not just during progression through mitotic division cycles but also during sexual reproduction. In many mammals, as also in *D. melanogaster* (Pimenta-Marques et al., 2016), centrioles and the associated centrosomes are therefore eliminated during oogenesis, but not during spermatogenesis. After fertilization with a sperm providing a centrosome, the zygote starts into the first mitotic cycle with one centrosome just like a normal mitotically proliferating cell. But centrosome elimination during oogenesis necessitates formation of acentrosomal spindles during the female meiotic divisions (Bennabi et al., 2016; Radford et al., 2017). In contrast, male meiotic divisions rely on centrosomal spindles. The mechanisms forming meiotic spindles in two sexes are therefore strikingly different.

Spindle assembly in *D. melanogaster* oocytes relies on chromatin driven microtubule nucleation. Microtubules grow out from the chromosomes that are strongly compacted into a karyosome. The chromosomal passenger complex (CPC) is critical for assembling this acentrosomal spindle (Colombie et al., 2008; Radford et al., 2012). Moreover, motor proteins focus the nucleated microtubules eventually into a bipolar structure. Some kinesin family members like Subito are important for female meiosis I spindles but not for mitotic spindles (Das et al., 2016). Similarly, while γ-tubulin is present in low amounts, it is not required for anastral spindle formation (Endow and Hallen, 2011).

In Drosophila spermatocytes, on the other hand, centrosomes act as major microtubule organizing centers (MTOCs), at least during MI which has been analyzed extensively (Inoue et al., 2004; Rebollo et al., 2004; Savoian and Glover, 2014), while MII has not been analyzed systematically. Mutations in *orbit/mast*, which encodes a MAP, confirmed that two distinct microtubule populations form the male meiosis I spindle. Centrosomal asters form an outer bipolar array where most microtubules remain on the cytoplasmic side of the membranes (ER and nuclear envelope). These membranes remain around the nucleus throughout meiosis. Only few astral microtubules enter into the nucleus through polar openings in the surrounding membranes. The second population of microtubules is intranuclear. These microtubules appear to be formed largely by an acentrosomal pathway relatively late when the chromosomes achieve full condensation. Interestingly, the majority of these microtubules appear to be nucleated at the remnants of the nuclear envelope rather than in the vicinity of chromosomes. The intranuclear microtubules are then bundled, associate with the chromosomes, and eventually end up organized into a bipolar anastral array that is co-oriented with the outer bipolar astral arrays. This outer array has been shown to position the cleavage furrow, while the inner array is required to propagate furrow ingression during exit from MI.

Yet another pronounced difference between the sexes concerns the temporal control of progression through meiosis. In humans, female meiosis is initiated in embryogenesis but it is not completed until much later. Immature oocytes arrest during diakinesis and remain arrested until puberty. During each menstrual cycle, a few re-start the meiotic process but only one oocyte is usually ovulated after arresting during metaphase of the second meiotic division. Completion of the second meiotic division requires fertilization. In particular this protracted arrest during diakinesis, lasting between 12 and 40 years, appears to be linked to the surprisingly high rate of meiotic chromosome segregation errors and its exponential increase with age in human oocytes (Webster and Schuh, 2017). While female meiosis is subject to pronounced developmental arrests, progression through male meiosis is a continuous process in humans and mice. In contrast to adult females, germline stem cells continue to proliferate in adult males, generating a continuous supply of cells that eventually progress through meiosis and differentiate into sperm. *In D. melanogaster*, proliferation of germline stem cells occurs in both male and female adults. However, female meiosis is still characterized by developmental arrests. The mature oocyte is arrested in metaphase of meiosis I. Completion of meiosis is triggered by egg activation that accompanies egg deposition.

Analyses of male meiotic divisions were started early in the history of experimental biology and these studies have provided seminal insights into the interactions between spindles, chromosomes and the temporal control of progression through M phase. Already the experiments by Dietz (Dietz, 1958) in spermatocytes of ostracod crustaceans suggested that mechanical tension might stabilize the binding of kinetochores to spindle fibers. Later, groundbreaking work was done in grasshopper spermatocytes (Nicklas and Koch, 1969). There, the role of mechanical tension was studied by micro-manipulation of chromosomes within living cells with the help of fine glass needles. These elegant experiments clearly demonstrated that mechanical tension leads to stabilization of kinetochore attachments to spindle microtubules and thereby controls progression through meiosis (Li and Nicklas, 1995; Li and Nicklas, 1997). Thus, the initial concepts for error correction and SAC were largely based on such studies with grasshopper spermatocytes.

Interestingly, studies with *D. melanogaster* oocytes have revealed that mechanical tension can have an effect on temporal control of progression through meiosis which is opposite of the effect discovered in grasshopper spermatocytes. In grasshopper male MI, tension stabilizes kinetochore attachments and thereby promotes SAC silencing and exit from MI. In contrast, in *D. melanogaster* oocytes tension promotes the developmental arrest in metaphase of MI (McKim et al., 1993).

In Xenopus, progression through MI in oocytes is not regulated by the SAC (Shao et al., 2013). In contrast, in mouse oocytes, the SAC is clearly functional during MI (Gorbsky, 2015; Touati and Wassmann, 2016). The metaphase to anaphase I transition is delayed in response to microtubule drugs and in the presence of unaligned chromosomes. The delay depends on the canonical SAC proteins. The SAC has also been implicated in the control of the metaphase to anaphase transition during MII in mouse oocytes, although the evidence is far more limited in this case (Tsurumi et al., 2004). While the SAC is clearly functional in mouse oocytes, it is considerably less effective than in male meiosis. In mouse spermatocytes, one or a few misaligned chromosomes are sufficient to block the onset of anaphase I and eventually result in apoptosis, similarly as in spermatocytes of praying mantids (Li and Nicklas, 1997). In contrast, a far more mild delay appears to result from the same problem during MI in mouse oocytes. Moreover, in mouse oocytes, the SAC during MI appears to respond far more strongly to the presence of unpaired chromosomes (univalents), as in *mlh1*$^{-/-}$ mutants where meiotic recombination does not occur, than to the presence of unpaired sister chromatids, as after premature inactivation of cohesin function (Tachibana-Konwalski et al., 2013).

1.6 Meiotic kinetochore architecture

A difference between mitosis and meiosis that is of chief importance, concerns the behavior of sister centromeres (Gorbsky, 2015; Hauf and Watanabe, 2004; Nasmyth, 2015). As emphasized earlier, while sister centromeres are linked to opposite spindle poles during mitosis and MII, they form a single functional kinetochore unit during MI so that they are linked together to the same spindle pole. It is clear therefore that sister centromere behavior is regulated during meiosis. The mechanisms that unite sister centromeres before MI and individualize them again before MII are poorly understood.

Ultrastructural studies of kinetochore organization during MI by serial sectioning were pioneered with *D. melanogaster* spermatocytes (Goldstein, 1981). Spermatocytes at different MI stages (early prometaphase, late prometaphase, metaphase/early anaphase, late anaphase) were analyzed. For each MI stage, between 9 and 16 kinetochores were studied by electron microscopy (EM). These observations revealed that the single MI kinetochore organized by the two sister centromeres of a half bivalent has the appearance of a bilaminar hemisphere (HS) before microtubule attachment in early prometaphase I. Subsequent EM analyses with *D. melanogaster* spermatocytes have largely confirmed this HS organization in prometaphase I (Church and Lin, 1982). Interestingly, the HS is converted into a double disc structure during progression through MI (Goldstein, 1981). In this double disc structure, the two closely associated bilaminar disks are arranged side-by-side (SS) on a common face of chromatin. It is assumed and of course very likely but not proven that each of the two disks represents the kinetochore structure assembled by one of the two sister centromeres. The transition from HS to SS organization appears to be completed already before the onset of anaphase I, at least in some chromosomes (Goldstein, 1981). Therefore, the HS->SS transition might occur already before full APC/C activation and consequential separase activation. However, the limited data is also compatible with a rapid HS->SS transition downstream of full APC/C activation in late metaphase. While sensors for monitoring separase activity by time lapse imaging have been described (Shindo et al., 2012; Yaakov et al., 2012), they have not yet been applied to meiosis.

An EM study with pig oocytes reported that the majority of kinetochores observed during MI had an SS organization (Lee et al., 2000). In addition, immunofluorescent staining with anti-Cenp-E as well as immuno-EM indicated that by MII sister kinetochores were no longer side-by-side (SS) but rather on opposite sides of the chromatin in a back-to-back configuration (BB) (Lee et al., 2000). Therefore, sister kinetochore organization during meiosis also progresses through an SS->BB transition. The analysis of Lee et al. (2000) did not reveal when the SS->BB transition had occurred. According to unpublished EM data mentioned in Church and Lin (1988), the SS arrangement of sister kinetochores in *D. melanogaster* male meiosis "is converted to a back-to-back arrangement as dyads enter the second meiotic division." Once cells are in metaphase II, the BB configuration is necessarily present, as bi-orientation is accompanied by stretching sister kinetochores away from each other towards the spindle poles. However, if the BB organization was indeed already present at entry into the second meiotic division, as suggested by Church and Lin (1988), this particular arrangement of sister kientochore would contribute considerably to the efficiency of bi-orientation, as it favors the amphitelic over syntelic attachments for geometrical reasons (see above, 1.3 Error correction). However, light microscopic studies with grasshopper spermatocytes (Paliulis and Nicklas, 2005) have suggested that sister kinetochores are still in an SS configuration at NEBD II, and that the BB configuration is reached only as a consequence of bi-orientation.

The analysis of kinetochore organization during meiosis in additional mammalian species beyond the initial EM study with pig oocytes, suggested that in mice and humans, the dynamic organization of sister centromeres and associated kinetochores during meiosis varies considerably. Immunofluorescent and EM analyses of mouse spermatocytes revealed a prometaphase I organization where the two sister kinetochores were fused into one structure where the two putative sister centromeres were joined along a conspicuous interface protruding into the chromatin mass (Parra et al., 2004; Suja et al., 1999; Suja et al., 1992). While this special SS organization was still present during early prometaphase II, a BB configuration was obvious at metaphase II.

In contrast to the apparent tight association of sister centromeres during mouse meiosis, the connections between these entities is strikingly relaxed in human meiosis. Recent light microscopic analyses with human oocytes (Holubcova et al., 2015; Patel et al., 2015; Zielinska et al., 2015), have clearly demonstrated that sister kinetochores are separated to a surprising degree at the start of the first meiotic division. In contrast to mouse oocytes where sister kinetochores can be resolved only occasionally by immunofluorescence, they are clearly apart in the large majority of chromosomes. Moreover, the separation between sister kinetochores at MI onset, increases with increasing age in humans. The separation reaches widths that readily allow independent attachment of sister kinetochore to opposite poles of the MI spindle. Therefore, the unusual separation of sister kinetochores at the start of MI in human oocytes contributes significantly to the high error rate of female meiosis and likely explains the documented occurrence of reverse segregation in humans (Ottolini et al., 2015; Webster and Schuh, 2017).

Progress in elucidating the molecular mechanisms that enforce sister centromere mono-orientation during MI has been achieved primarily in budding and fission yeast. In budding yeast, the monopolin complex is required for mono-orientation during MI. The monopolin complex is composed of four subunits (Csm1, Lrs4, Hrr25/caseine kinase 1delta and Mam1). Mam1 is expressed exclusively during meiosis, while the other subunits are also expressed during progression through mitotic cell cycles where they provide additional functions. Biochemical and structural analyses of the monopolin complex suggest that it acts as a clamp that physically crosslinks the two sister kinetochores (Corbett et al., 2010; Ye et al., 2016). In vitro, the monopolin complex was shown to be sufficient to convert kinetochores isolated from mitotic cells into kinetochores that have the physical properties of meiosis I kinetochores (Sarangapani et al., 2014). Compared to mitotic and MII kinetochores, the MI structure forms stronger attachments to microtubules, indicating that it represents a fusion of the two sister kinetochores into one structure with twice as many microtubule binding sites. Note that the MI kinetochore in budding yeast appears to bind a single microtubule, as also during MII and mitosis (Winey et al., 2005). Hence merotelic attachments are impossible in budding yeast.

Mam1 appears to be present exclusively in budding yeast and closely related species. It is not recognizable in fission yeast. Homologs of the additional monopolin subunits Csm1, Lrs4 and Hrr25 exist in fission yeast. But they are not required for sister kinetochore mono-orientation during meiosis I. While budding yeast has point centromeres, which bind a single centromere-specific nucleosome and organize a kinetochore that binds only one KT-MT, the centromeres of fission yeast are more regional, hosting several centromere-specific nucleosomes and directing the assembly of a kinetochore that binds about three KT-MTs. In fission yeast, Csm1 and Lrs4 appear to clamp together the multiple KT-MT binding sites within a sister kinetochore rather than bringing together sister kinetochores, as indicated by the strong increase of merotelic attachments in the absence of these proteins (Gregan et al., 2007).

An elegant genetic approach in fission yeast has identified the *Moa1* gene as being required for sister kinetochore mono-orientation during MI (Yokobayashi and Watanabe, 2005). Subsequent work has revealed the presence of homologous proteins in budding yeast (Spo13) and mammals (Meikin) (Kim et al., 2015). In the mouse, Meikin is expressed exclusively in ovaries and testis. It binds directly to Cenp-C. Meikin is not only required for sister kinetochore mono-orientation during MI, but also for protection of centromeric cohesion during MI. Strikingly, the sequence conservation between Moa1, Spo13 and Meikin is minimal. In essence, it is restricted to a Ser-Thr-Pro motif that functions as a polo-box domain (PBD)-binding site. In Moa1, this motif has been shown to be required for the recruitment of Polo kinase. An obvious Meikin homolog cannot be identified in the genome sequences of animals outside the vertebrates. However, given the minimal sequence conservation between Meikin and the yeast homologs (Moa1, Spo13), the presence of Meikin homologs in other animals, including *D. melanogaster* is certainly not excluded.

Interestingly, recent results obtained from analyses in *D. melanogaster* oocytes have implicated the kinetochore component Spc105/Knl1 in sister centromere mono-orientation. (Radford et al., 2015). Whether Spc105/Knl1 provides a similar function during male meiosis has not yet been analyzed.

1.7 Meiosis-specific features of cohesion

The details of how Meikin functions during meiosis are far from being clear. The fission yeast homolog Moa1 appears to function upstream of Rec8 which is a meiosis-specific α-kleisin subunit of the cohesin complex. Apart from the α-kleisin subunit, the highly conserved core of the cohesin complex contains a heterodimer of Smc1 and Smc3. These Smc proteins have globular head regions that associate into ATPase domains. In addition, the SMCs have extended coiled coil regions (Gruber, 2017). The cohesin core binds additional subunits (Scc3, Pds5, Wapl, Soronin) (Gruber, 2017; Haarhuis et al., 2014). The core complex is ring shaped and can topologically trap either one or two chromatids within the ring in an ATP dependent manner. Thereby it can provide sister chromatid cohesion or also create chromatid loops that bring enhancers into vicinity with partner promoters or create larger chromosomal domains within a chromatid, perhaps by loop extrusion (Fudenberg et al., 2016; Sanborn et al., 2015). The details of how chromatids are entrapped and released by the cohesin ring are studied intensely. In part it is still controversial, whether and if so which protein-protein interaction faces within the cohesin ring are opened during loading around chromatids or during release of chromatids, i.e., entry and exit gates are debated. Loaders like Scc2/Scc4 as well as several factors inhibiting (Eco1 acetylase, Soronin) or stimulating release (Wapl, Separase) have been identified. Separase is used for the removal of the residual sister chromatid cohesin, so that sister chromatids can be segregated to opposite spindle poles during mitosis. Separase is activated late in metaphase. Its site-specific endoprotease activity results in proteolytic cleavage of the α-kleisin subunit, which opens the cohesin ring.

During meiosis, cohesin is of crucial importance for several meiosis-specific processes (Biswas et al., 2016; Rankin, 2015; Severson and Meyer, 2014). Meiosis-specific functions depend at least in part on the expression of meiosis-specific subunits. The number and type of meiosis-specific cohesin subunits vary between different organisms. During canonical meiosis, cohesin complexes are required early in prophase for the formation of the axial elements in chromosomes which are then transformed into the lateral elements of the synaptonemal complex (SC) during synapsis of homologous chromosomes whereby lateral elements are crosslinked by transverse filaments anchored within the central element of the SC (Gyuricza et al., 2016).

Beyond SC formation, cohesin has also been implicated in sister centromere mono-orientation during MI. Analyses in fission yeast meiosis have provided the most extensive and compelling evidence. The meiosis-specific α-kleisin Rec8 was first identified and shown to be required for centromere mono-orientation in fission yeast. Rec8 is expressed exclusively during meiosis while the “mitotic” Rad21 α-kleisin is present during mitosis and meiosis. Rec8 cohesin can establish sister chromatid cohesion within the centromeric region, while Rad21 cohesin can only provide cohesion within the chromosome arm regions (Sakuno et al., 2009). Accordingly, it was proposed that the meiosis-specific Rec8 cohesin complexes keep the sister centromere regions in close apposition. As a result of this close association of sister centromeres at the start of MI, they might organize a single kinetochore unit and thereby cause sister centromere mono-orientation (Sakuno et al., 2009). Evidence from plants and mice support the notion that Rec8 cohesin is required for sister kinetochore mono-orientation during MI (Chelysheva et al., 2005; Golubovskaya et al., 2006; Tachibana-Konwalski et al., 2013). In contrast, sister kinetochore mono-orientation in budding yeast does not depend on the Rec8 homolog, presumably because in this species the monopolin complex functions as a meiosis-specific sister kinetochore clamp. Apart from the exception of budding yeast, meiosis-specific cohesin are therefore very likely to be generally important for sister kinetochore mono-orientation during MI in eukaryotes. However, it is not known whether the sister centromere cohesion imposed by meiosis-specific cohesin is already sufficient to enforce sister kinetochore mono-orientation. Moreover, the properties explaining why Rec8 cohesin but not Rad21 cohesin can be recruited within the centromeric region are also not known. Moa1/Meikin and the recruited polo kinase are probably required to maintain centromeric cohesion until the onset of MI but they do not appear to be responsible for initial establishment. Importantly, it also remains to be clarified how centromeric cohesion is removed between MI and MII so that sister kinetochores are again bi-oriented in MII. Cleavage of centromeric Rec8 after separase activation in late metaphase I might appear as an obvious mechanism for sister centromere individualization. However, analyses in *D. melanogaster* spermatocytes have suggested that sister centromere individualization between MI and MII might not involve separase activity (Blattner et al., 2016). Moreover, as Rec8 cohesin within the pericentromeric region is known to be protected from separase-mediated inactivation during MI, centromeric Rec8 cohesin would have to be devoid of this protection, if indeed separase were to bring about sister centromere individualization during meiosis.

The protection of Rec8 cohesin within the pericentromeric region during MI is actually absolutely essential for the overall success of meiosis (Kitajima et al., 2006; Marston, 2015; Watanabe, 2005). It is this persistence of pericentromeric sister chromatid cohesion during MI in combination with sister centromere individualization that allows the bi-orientation of sister kinetochores during MII. In contrast to pericentromeric sister chromatid cohesion, sister chromatid cohesion within the chromosome arm regions needs to be completely abolished during in late metaphase I in canonical meiosis. Sister chromatid cohesion within the chromosome arm region in combination with cross overs resulting from meiotic recombination keep homologous chromosomes paired in bivalents. Homolog segregation to opposite spindle poles during MI therefore requires separase-mediated cleavage of cohesin within the chromosome arm regions which allows chiasmata terminalization (Buonomo et al., 2000; Kitajima et al., 2006; Marston, 2015; Watanabe, 2005). Presumably, therefore, the “prophase pathway” that removes cohesin from the arm regions already during pro- and prometaphase of mitosis in a Wapl-dependent reaction (Haarhuis et al., 2014) has to be at least partially inhibited during MI, so that bivalents are not separated prematurely.

The molecular basis of Rec8 cohesin protection specifically within the pericentromeric region during MI is understood to a considerable extent. The shugoshin family proteins play a crucial role (Kitajima et al., 2004; Marston, 2015; Watanabe and Kitajima, 2005). The *D. melanogaster Mei-S332* gene was found early on to be required for protection of pericentromeric cohesin during MI. A genetic screen in fission yeast revealed the fission yeast homolog Shugoshin. Subsequent analyses revealed homologs to be present generally within eukaryotes. Shugoshins are recruited to the pericentromeric region as a result of histone H2A phosphorylation by Bub1 kinase. Shugoshins in turn recruit a phosphatase PP2A complex. This phosphatase activity maintains Rec8 in an non-phosphorylated state within the pericentric region. In contrast, within the chromosome arm regions, Rec8 is successfully phosphorylated by Hrr25/casein kinase 1delta or Dbf4-dependent Cdc7 kinase (Ishiguro et al., 2010; Katis et al., 2010). Only Phosphorylated Rec8 is a substrate of separase. Pericentromeric Rec8 cohesin is therefore protected from cleavage by separase during MI, while Rec8 cohesin in the chromosome arm regions is removed, allowing homolog segregation.

In budding yeast, Hrr25/casein kinase 1delta has also been shown to be involved in the elimination of Shugoshin and PP2A from the pericentromeric region during MII (Arguello-Miranda et al., 2017). As a result, also the pericentromeric Rec8 is phosphorylated during MII, in contrast to MI, and hence cleaved by separase. The cleavage of pericentromeric Rec8 cohesin late in metaphase II allows the segregation of sister kinetochores to opposite spindle poles during anaphase II.

Given the crucial importance of Rec8 for the success of meiosis, it comes as a surprise that *D. melanogaster* appears to use distinct proteins to cover the meiotic Rec8 functions. Based on sequence comparisons, the *c(2)M* gene encodes an α-kleisin that is most similar to the meiotic Rec8 branch (Heidmann et al., 2004). In addition, the *D. melanogaster* genome contains the *verthandi (vtd)*/*Rad21* gene which codes for the mitotic α-kleisin (Hallson et al., 2008; Warren et al., 2000). While *D. melanogaster* Rad21 has clearly been shown to function as expected (Pauli et al., 2008), the C(2)M protein provides only some of the meiotic Rec8 functions (Heidmann et al., 2004; Manheim and McKim, 2003). It is involved in SC formation (Anderson et al., 2005; Gyuricza et al., 2016; Heidmann et al., 2004; Manheim and McKim, 2003; Mehrotra and McKim, 2006; Tanneti et al., 2011; Urban et al., 2014). In *D. melanogaster*, the protection of pericentromeric cohesion during MI depends on the genes *orientation disrupter (ord)*, *sisters on the loose (solo)*, and *sisters unbound (Sunn)* (Bickel et al., 1996; Goldstein, 1980; Krishnan et al., 2014; Mason, 1976; Yan and McKee, 2013; Yan et al., 2010). None of these genes codes for a protein with obvious similarity to the α-kleisins. However, at least some appear to associate physically with Smc1/3. Therefore it has been suggested that an alternative cohesin complex provides some of the functions that are normally fulfilled by Rec8 cohesin in other species (Gyuricza et al., 2016).

In conclusion, the spatially controlled establishment and resolution of cohesin along the chromosome is of paramount importance for the success of meiosis. Three functionally distinct pools of cohesin (centromeric, pericentromeric and along arm regions) that are differentially regulated during progression through meiosis have been postulated. The molecular mechanisms responsible for this differential control are only partially understood. Control of cleavage by separase is clearly important. Moreover, these mechanisms are evolutionary plastic, as illustrated clearly by *D. melanogaster* where the issues are particularly puzzling. Chapter 2 of this thesis describes my approaches for the characterization of separase activity and potential substrates during meiosis.

1.8 Drosophila spermatogenesis

The characteristics of spermatogenesis in *D. melanogaster* provide some invaluable advantages for the characterization of the meiotic divisions. The testis in this species is a blind ended tube with layers of muscle and epithelial cells on the outside and germline cells inside (Fuller, 1993). These germline cells are associated with somatic support cells that are also present within the testis tube. The undifferentiated germ line stem cells are at the closed apical tip of the testis tube. Spermatogenesis is accompanied by transport towards the other open distal end, where mature sperm is delivered into the seminal vesicle. As a result, cells in progressive stages of spermatogenesis are spatially ordered along the tube, facilitating cytological analysis. The stem cells are maintained at the apical tip by a niche formed by the somatic "hub" cells. Associated with the hub are not only the germline stem cells (GSCs) but also the somatic cyst stem cells (CyScs). The GSCs give rise to sperm; the CySCs generate the support cells. Asymmetric division of a GSC and associated CySCs produce daughter cells maintaining stemness as well as daughters committed to differentiation (Figure 5). The differentiating germline daughter cell, the spermatogonial cell, is encapsulated by two CySC derivatives, the cyst cells. Four mitotic spermatogonial divisions with incomplete cytokinesis (IC) yield a cyst containing 16 interconnected spermatocytes, encapsulated by the two cyst cells (Figure 5). After an extended G2 phase characterized by extensive cell growth and gene expression, the 16 mature primary spermatocytes proceed through the two meiotic divisions, giving rise to a cyst of 64 round spermatids. The spermatids undergo dramatic morphological change, i.e., sperm head formation and tail elongation. Thereby they are transformed into slender highly extended cells up to 2 mm in length. Finally, sperm individualization occurs when the 64 sister cells are separated from each other. Mature sperm coils and passes into the seminal vesicle where they are stored until mating.

Cyst formation by incomplete cytokinesis is not unique to *D. melanogaster* spermatogenesis. Cysts with 16 germline cells are also formed during *D. melanogaster* oogenesis where they become enveloped by somatic follicle cells and where only one germline cell completes meiosis and 15 differentiate as nurse cells. During incomplete cytokinesis (IC) the contractile ring closes only partially and forms a stable intercellular bridge called a ring canal (Fuller, 1993; Mathe et al., 2003; Ong and Tan, 2010). In this manner, all newly generated cells remain interconnected, thus facilitating the exchange of proteins, mRNAs, and organelles between interconnected cells as shown through analysis in Drosophila oocytes (Braun et al., 1989; Ventela et al., 2003). Incomplete cytokinesis and connection via intercellular bridges is also observed widely during animal gametogenesis including mammalian spermatogenesis and oogenesis (Greenbaum et al., 2011; Lei and Spradling, 2016).

One aspect of male meiosis in *D. melanogaster*, however, is very special at least in comparison with other popular model organisms. In this organism, meiosis in the male involves neither SC formation nor meiotic recombination (Fuller, 1993; McKee et al., 2012). Instead of SC and meiotic recombination an alternative system for keeping homologs paired in a bivalent is used in *D. melanogaster*. Three genes, *modifier of Mdg4 in Meiosis* (*mnm*), *stromalin in Meiosis* (*snm*)/*SA-2*, and *teflon* (*tef*) have been identified as specifically required for this alternative homolog conjunction (Arya et al., 2006; McKee et al., 2012; Thomas et al., 2005; Tomkiel et al., 2001). The expression of these genes is restricted to spermatocytes. The TEF protein contains Zn fingers, MNM a Zn finger and BTB/POZ domain. These domains most likely allow for protein-protein interactions. SNM is similar to the SCC3/Stromalin family of proteins that function as accessory cohesin subunits. However, the localization of SNM is distinct from that of Smc1/3, suggesting that it is not functioning as a cohesin subunit. It is therefore still unclear how these proteins function biochemically to achieve homolog conjunction during MI. In case of the XY bivalent, TEF is actually not required and MNM/SNM were shown to localize very prominently to the paring centers of the sex chromosomes, i.e., to intergenic repeats within the rDNA loci on the X and Y chromosome (Arya et al., 2006; McKee et al., 2012; Thomas et al., 2005; Tomkiel et al., 2001). Recently, separase has been shown to be required for the elimination of homolog conjunction during late metaphase I (Blattner et al., 2016). In the absence of separase function, the MNM and SNM proteins do not disappear from the XY pairing center during anaphase I and all bivalents fail to separate.

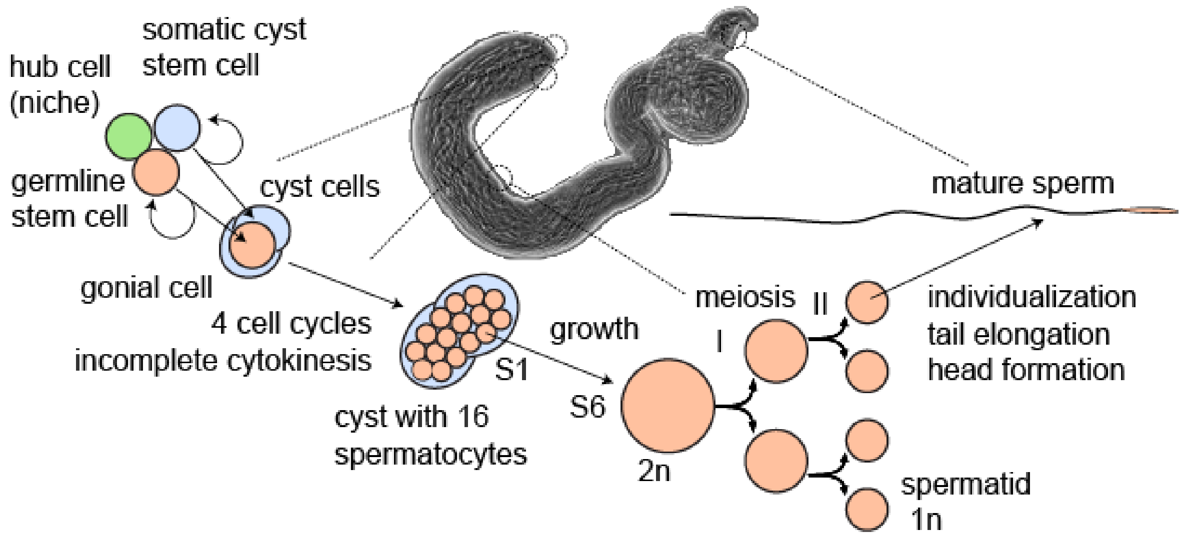

Figure 5. Drosophila spermatogenesis- Spatio-temporal array of spermatogenetic stages in an adult Drosophila testis (Raychaudhuri et al., 2012).

1.9 Time lapse analysis of the meiotic divisions

Our understanding of the mitotic division process is far better than that of the meiotic divisions. This primarily reflects a difference in experimental accessibility. Culture of eukaryotic cells has been established more than half a century ago. Moreover, methods for synchronization of progression through mitotic cell cycles are at hand. Mitotic divisions can therefore be studied readily, not only microscopically but also biochemically. In contrast, there are no methods for an efficient production of animal cells that will progress through the meiotic divisions with or without previous cell cycle synchronization. In general, therefore, meiotic divisions are studied with material isolated directly from the organism. In some invertebrate and vertebrate species (like clam, starfish, Xenopus), the isolation of relatively large numbers of oocytes is feasible. Moreover, fertilization or artificial activation of these oocytes usually induces resumption and completion of meiosis. While these experimental systems have been and will continue to be of some help, they also have various limitations, including an absence of efficient and precise genetic methodology. In contrast, in animal model organisms that are readily amenable to genetic manipulations, the isolation of cells for the analyses of the meiotic divisions is rather difficult. As experimental accessibility in comparison to animals is far better in budding and fission yeast, our understanding of the meiotic processes is most advanced in these species. However, as a result of evolutionary plasticity, the meiotic processes are to some extent distinct in yeast and animals. Analyses of meiosis in animal systems are therefore important as well. Moreover, as long as the limitations concerning biochemical approaches persist (limited numbers of cells progressing synchronously through the meiotic divisions), alternative approaches exploiting genetics in combination with microscopic analyses with high spatial and temporal resolution are of particular importance. Therefore, the development of efficient time lapse imaging approaches for the analysis of *D. melanogaster* spermatocytes progressing through the meiotic division has been a major focus of this thesis.

Beyond analyses in yeast (Arguello-Miranda et al., 2017; Hayashi et al., 2006; Hirose et al., 2011; Tsuchiya et al., 2011), time lapse imaging of meiotic divisions with high spatial and temporal resolution is now fairly routinely applied with oocytes from humans, mice, *Caenorhabditis elegans* and *Drosophila* (Endow and Komma, 1997; Gilliland et al., 2007; Gluszek et al., 2015; Holubcova et al., 2015; Kitajima et al., 2011; Patel et al., 2015; Pfender et al., 2015; Skold et al., 2005; Wolff et al., 2016; Yoshida et al., 2015; Yoshida et al., 2016; Zielinska et al., 2015). Among these species, *D. melanogaster* has the simplest karyotype. The number of haploid chromosomes is only four. Moreover, some chromosome can be readily identified because of their characteristic morphology. The X chromosome (also sometimes designated as chromosome I) is telocentric, while the two large autosomes (chromosome 2 and 3) are metacentric. Chromosome 4 is like a very small dot. Finally, the Y chromosome is submetacentric. The comparatively low number of chromosomes in *D. melanogaster* simplifies the tracking of kinetochores through the meiotic divisions. As pointed out earlier, in comparison to spermatocytes, oocytes usually contain large amounts of stored material including yolk which increases autofluorescent background. Moreover, female meiosis is relatively slow and characterized by developmental arrests. It is therefore difficult to analyse and compare both meiotic divisions. Therefore, the current study was completed with spermatocytes.

Analyses of progression through the meiotic divisions with live spermatocytes was started more than 70 years ago, primarily using insects like grasshoppers and praying mantids (Nicklas, 1997). These analyses usually employed phase contrast and differential interference contrast (DIC) microscopy but not yet fluorescence imaging of cellular components marked by the expression of fluorescent fusion proteins (Salmon and Tran, 2007). In these pioneering studies, kinetochores and their interactions with spindle microtubules were typically not directly visible but inferred from position and movements of the chromosomes. In combination with micromanipulation of chromosomes and spindles with fine glass needles these analyses have provided extremely important conceptual insights into how error correction and surveillance of attachments proceed, as well as into the control of spindle and kinetochore properties (Nicklas, 1997; Zhang and Nicklas, 1999).

To exploit the powerful genetic methodology available in *D. melanogaster*, time lapse imaging was eventually also applied with spermatocytes from this species. The most popular protocol used for time lapse imaging with *D. melanogaster* spermatocytes involves dissection of testis in halocarbon oil. This allows short term imaging for up to 1 hr (Church and Lin, 1985; Gao et al., 2008; Inoue et al., 2004; Rebollo et al., 2004; Savoian et al., 2000). An alternative protocol involves culture of isolated primary spermatocytes in cell culture medium which supports viability over longer time periods (Blattner et al., 2016; Cross and Shellenbarger, 1979; Dunleavy et al., 2012; Gartner et al., 2014). However, analyses of complete spermatocyte cysts progressing through both divisions at a temporal and spatial resolution that is sufficiently high to track kinetochores directly have not yet been reported so far. Most publications have focussed on MI, while MII has been almost completely ignored. Kinetochore tracking with fluorescent kinetochore proteins has not yet been attempted. By now a series of transgenic *D. melanogaster* strains expressing functional fluorescent variants of the centromere and kinetochore proteins has been generated (Heeger et al., 2005; Schittenhelm et al., 2010; Schittenhelm et al., 2009; Schittenhelm et al., 2007; Schuh et al., 2007). In addition, many other transgenic strains expressing fluorescent markers allowing the visualization of chromosomes and spindles are available as well. As shown below, these tools indeed permit efficient analyses of progression through the male meiotic divisions in wild-type, as well as in mutants or after knockdown of genes by RNAi.

Specific objectives

An efficient and comprehensive description of the behavior of centromeres and kinetochores during progression through both meiotic divisions is important for an understanding of the mechanisms that control chromosome segregation during animal meiosis. In my PhD thesis, I have therefore addressed the following objectives:

1. Development of a protocol that allows time lapse imaging of progression through both meiotic divisions at high temporal and spatial resolution with D. melanogaster spermatocytes

2. Detailed characterization of the spatial and temporal program of progression through both meiotic divisions in minimally perturbed intact spermatocyte cysts, including the behavior of centromere and kinetochore proteins and the efficiency of the chromosome bi-orientation process.

3. Analysis of significance and robustness of the SAC during both meiotic divisions

4. Analysis the role of mechanical tension between kinetochore pairs for bi-orientation of bivalents during MI, as revealed by the chromosome behavior in *mnm* mutants where homolog conjunction is defective.

5. Characterization of the role of the kinetochore protein Spc105 for sister centromere association at the start of MI in spermatocytes

6. Analysis of sister centromere individualization between MI and MII. When does the SS->BB transition occur? Is it achieved already before spindle microtubules start to interact with the kinetochores in MII, or is it a consequence of these interactions?

Materials and methods

Fly strains

Genotype	_Abbreviated name_	Reference/Source/ Comment
w*; P{w^+, gHis2AvD-mRFP} II.2	_His-mRFP II.2_	(Schuh et al., 2007)/Lehner stock #1144
w*; P{w^+, gCid-EGFP-Cid} II.1	_Cid-EGFP (CGC)_	(Schuh et al., 2007)/Lehner stock #684
w*; P{w^+, gSpc105-EGFP} II.1	_Spc105-EGFP II.1_	(Schittenhelm et al., 2007)/Lehner stock #440
w*; P{w^+, gMis12-EGFP} II.2	_Mis12-EGFP II.2_	(Schittenhelm et al., 2007)/Lehner stock #966
w*; P{w^+,gi2xtdTomato-CenpC II.3}/ (CyO floating)	_gi2xtdTomato-CenpC II.3_	(Althoff et al., 2012)/Lehner stock # NT88
w*; UbiP{GFP(S65T)-ßTub56D}17-1	_GFP-ßTub56D (II)_	(Inoue et al., 2004)/DGRC Kyoto # 109603
w*; UbiP{ w^+, RFP-Spd-2} (#31)	_mRFP-Spd2 (II)_	(Novak et al., 2014) Jordan Raff Lab/this work
w*; P{w^+, gEGFP-Nuf2} II.1	_Nuf2- EGFP_	(Schittenhelm et al., 2007)/Lehner stock #254
w*; P{w^+, gEGFP-Bub3} II.1	_Bub3-EGFP_	(Pandey et al., 2005)/ Lehner stock #60
w*; P{w^+, gEGFP-Rod} II	_Rod-EGFP_	(Buffin et al., 2005)/ Lehner stock #RP26
y^1 w*; P{w^+, Sep2-GFP.SG}3	_Sep2-GFP_	(Silverman-Gavrila et al., 2008)/ this work
w*; Ubq11P{w^+, EGFP- αtubulin 84B}	_EGFP-αTub84B_	(Dobbelaere et al., 2008)/Lehner stock #AB68
$M(3)76A^1$, kar^2, ry^1, Sb^1	_MKRS_	Lehner lab common stock
TM6B, Tb, $Antp^{Hu}$	_TM6B_	Lehner lab common stock

w*; ; mnm[Z3-5578] /TM6B, Tb, $Antp^{Hu}$	_w*; ; mnm^{5578}/TM6B_	(Thomas et al., 2005)/Lehner stock # 1416
w*; ; mnm[Z3-3298]/TM3 Ser	_w*; ; mnm^{3298}/TM3, Ser_	(Thomas et al., 2005)/Lehner stock # 1415
w*; ; snm[Z3-0317]/TM3 Ser	_w*; ; snm^{0317}/TM3, Ser_	(Thomas et al., 2005)/Lehner stock # 1417
w*; ; snm[Z3-2138]/TM6B	_w*; ; snm^{2138}/TM6B_	(Thomas et al., 2005)/Lehner stock # 1418
w*; ; mad2[GE22825]	_w*; ; $Mad2^{p1}$_	(Buffin et al., 2007)/ Lehner stock #744
y^1 w^{67c23}; P{EPgy2}mad2[EY21687]/TM3, Sb^1 Ser^1 floating	_w*; ; $Mad2^{p2}$_	Bloomington #22495
w*; ; $Spc105^1$/TM3, Sb, P{w^+, Ubx-lacZ}	_w*; $Spc105^1$_	(Schittenhelm et al., 2009)/Lehner stock #523
_C(1; Y)1, y^1 v^1 f^1 B^1: y+/C(1)RM, y^2 $su(w^a)^1$ w^a_	_XO_	Bloomington #700
w*; P{lacO.256x, hsp26-SIP1, hsp70-mini-w+}55B	_lacO-55B (LW79D)_	(Danzer and Wallrath, 2004)/Lehner stock #JB175
w*; P{Hsp83-GFP.lacI}2, P{His2AvD-mRFP1}II.1	_GFP-LacI, His-mRFP_	Bloomington #25377/ Lehner stock #JB172
y^1 sc* v^1;; P{y[+t7.7] v[+t1.8]=TRiP.HMS01752}attP2	_Spc105R V20 RNAi_	TRiP/ Bloomington #38534
y^1 sc* v^1;; P{y[+t7.7] v[+t1.8]=TRiP.GL00392}attP2	_Spc105R V22 RNAi_	TRiP/ Bloomington #35466
_w^{1118}; P{GD7306}v44594_	_Spc105R RNAi GD 44594 (II)_	VDRC #44594
_w^{1118}; P{GD7306}38512_	_Spc105R RNAi GD 38512 (III)_	VDRC #38512
w^{1118}; P{attP,y^+,w^3}106153	_Spc105R RNAi KK 109322_	VDRC 109322
w*;; P{w^+,bamP-GAL4-VP16 III}	_bam-GVP III_	(Chen and McKearin, 2003)
w*; Ubq11P{w^+, EGFP- αtubulin 84B}, P{w^+, gHis2AvD-mRFP} II.2 / CyO, P{ry^+, ftz-lacZ} ; P{w^+,bamP-GAL4-VP16 III}	_EGFP-αTub II, His-mRFP II.2; bam-GVP III_	Lehner stock #AB68

w*; P{w^+, gCid-EGFP-Cid} II.1 (cgc), P{w^+, gHis2AvD-mRFP} II.2 / CyO, P{ry^+, ftz-lacZ} ; P{w^+,bamP-GAL4-VP16 III}	_CGC II.1, His-mRFP II.2; bam-GVP III_	(Blattner et al., 2016)
w*; P{w^+, gCid-EGFP-Cid} II.1 (cgc), P{w^+, gHis2AvD-mRFP} II.2 / CyO, P{ry^+, ftz-lacZ}	_CGC II.1, His-mRFP II.2_	Lehner Stock #706
w*; P{w^+, gMis12-EGFP} II.2, P{w^+, gHis2AvD-mRFP} II.2 / CyO, P{ry^+, ftz-lacZ}	_Mis12-EGFP II.2, His-mRFP II.2_	This work
w*; P{w^+, gMis12-EGFP} II.2, P{w^+, gHis2AvD-mRFP} II.2 / CyO, P{ry^+, ftz-lacZ}; P{w^+,bamP-GAL4-VP16 III}	_Mis12-EGFP II.2, His-mRFP II.2; bam-GVP III_	This work
w*; P{w^+,gi2xtdTomato-CenpC II.3}/ CyO; MKRS/TM6B, Tb, Antp^{Hu}	_2xtdTomato-CenpC II.3/CyO; MKRS/TM6B_	This work
w*; P{w^+, gCid-EGFP-Cid} II.1 (cgc), UbqP{w^+,RFP-Spd-2} (#31)/ CyO	_mRFP-Spd2 (II), CGC II.1_	This work
w*; UbiP{GFP(S65T)-ßTub56D}17-1, P{w^+, gHis2AvD-mRFP II.2}/CyO	_GFP-ßTub56D II, His-mRFP II.2/ CyO_	This work
w*; UbiP{GFP(S65T)-ßTub56D}17-1 , P{w^+,gi2xtdTomato-CenpC II.3}/ CyO, P{Dfd-GMR-nvYFP}2	_GFP-ßTub56D II, 2xtd-tomato-CenpC II.3/ CyO dfd-YFP_	This work
w*; UbiP{GFP(S65T)-ßTub56D}17-1 , P{w^+,gi2xtdTomato-CenpC II.3}/ CyO, MKRS/TM6B, Tb, Antp^{Hu}	_GFP-ßTub56D II, 2xtd-tomato-CenpC II.3/-''-CyO ; MKRS/TM6B_	This work
w*; UbiP{GFP(S65T)-ßTub56D}17-1 , P{w^+,gi2xtdTomato-CenpC II.3}/ CyO, P{Dfd-GMR-nvYFP}2; P{w^+,bamP-GAL4-VP16 III}	_GFP-ßTub56D II, 2xtd-tomato-CenpC II.3/ CyO dfd-YFP; bam-GVP III_	This work
w*; P{w^+, gEGFP-Nuf2} II.1/CyO ; MKRS/TM6B, Tb, Antp^{Hu}	_w*; EGFP-Nuf2 II.1/CyO; MKRS/TM6B_	This work, rebalanced/ Lehner stock _#254_
w*; P[w^+, gEGFP-Bub3] II.1, P{w^+, gHis2avD-mRFP} II.2 ; MKRS/TM6B, Tb, Antp^{Hu}	_EGFP-Bub3 II.1, His-mRFP II.2; MKRS/TM6B_	This work
w*;; P{y[+t7.7] v[+t1.8]=TRiP.HMS01752}attP2/ TM6B, Tb, Antp^{Hu}	_Spc105 V20 RNAi/TM6B_	This work
w* ; gSpc105-EGFP II.1/CyO,P{ry^+,ftz-lacZ}; Spc105^1/TM6B, Tb, Antp^{Hu}	_Spc105-EGFP II.1/CyO; Spc105^1/ TM6B_	Lehner stock #JB25
w*; If/CyO,P{ry^+,ftz-lacZ} ; y^1 sc* v^1; P{y[+t7.7] v[+t1.8]=TRiP.HMS01752}attP2/TM6B, Sb, Antp^{Hu}	_If/CyO; Spc105 V20 RNAi/TM6B_	This work
w*; P{w^+, gCid-EGFP-Cid}II.1, P{w^+, gHis2avD-mRFP}II.2 (# 706)/CyO P{Dfd-GMR-nvYFP}2; P{w^+,bamP-GAL4-VP16 III}, mnm[Z3-3298] / TM6B, Tb, Antp^{Hu}	_CGC II.1, His-mRFP II.2/CyO dfd GMR; bam-GVP III, mnm^{3298}/TM6B_	(Blattner et al., 2016)

w*; P{w$^+$, gCid-EGFP-Cid}II.1, P{w$^+$, gHis2avD-mRFP}II.2 (# 706)/CyO P{Dfd-GMR-nvYFP}2; P {w$^+$, bamP-GAL4VP16 III}, snm[Z3-0317] / TM6B, Tb, Antp^{Hu}	_CGC II.1, His-mRFP II.2/CyO dfd GMR; bam-GVP III, snm^{0317}/TM6B_	(Blattner et al., 2016)
w*;; Spc105 v20 RNAi, snm[Z3-2138] (1) /TM6B, Tb, Antp^{Hu}	_Spc105 V20 RNAi, snm^{2138} (1)/ TM6B_	This work
w*;; Spc105 v20 RNAi, mnm[Z3-5578] (18)/TM6B, Tb, Antp^{Hu}	_Spc105 V20 RNAi, mnm^{5578} (18)/ TM6B_	This work
w*; P{w$^+$, gEGFP-Bub3 II.1}, P{w$^+$, gHis2avD-mRFP} II.2	_RP14_	(Pandey et al., 2005)/Lehner stock #RP14
w*; P{w$^+$, GFP-Rod II}, P{w$^+$, gHis2avD-mRFP} II.2/CyO	_RP16_	(Pandey et al., 2005)/Lehner stock #RP16
w*; P{w$^+$, gCid-EGFP-Cid} II.1 (cgc), P{w$^+$, gHis2avD-mRFP} II.2, P{ w$^+$, matα4-GAL4-VP16}V2H/ (CyO floating)	_FA 157_	(Althoff et al., 2012)/ Lehner stock #FA157
w*; P{w$^+$, gCid-EGFP-Cid} II.1 (cgc), P{w$^+$, gHis2avD-mRFP} II.2, P{ w$^+$, matα4-GAL4-VP16}V2H / (CyO floating); mad2^{p1}[GE22825]	_FA 159_	(Althoff et al., 2012)/ Lehner stock #FA159
w*; Sp/ CyO; P{EPgy2}mad2^{p2}[EY21687]/ TM6B, Tb, Antp^{Hu}	_Sp/CyO; mad2^{p2}/-''- TM6B, Hu_	This work, rebalanced Bloomington #22495
y^1 w^{67c23};; P{EPgy2}mad2[EY21687]/TM3, Sb^1 Ser^1 floating	_mad2^{p2}/-''- or TM3, Ser_	Bloomington #22495

Efficiency of Spc105 RNAi lines

To rule out possible off-target effects, several RNAi transgenes targeting various subregions within the *Spc105R* transcript were tested. Two lines were from the TRiP consortium, V20 HMS01752 and V22 GL00392 lines targeting the same subregion showed strongest reduction in male fertility (upto >98%) when expressed using *bam-GAL4VP16* driver. Three additional lines targeting two other subregions were from the VDRC library. While two (GD 44594, KK 109322) showed a substantial reduction in fertility (upto >75%), one seemed to be completely non-functional (GD 38512) (Chaurasia, 2012). The RNAi line based on VALIUM 20 (V20 HMS01752) was used for all experiments in this thesis.

High resolution live imaging of progression through male meiosis

As described in the introduction, two different types of media have been used for live imaging with *D. melanogaster* spermatocytes in previously published studies. Several authors have dissected testis in halocarbon oil, followed by disruption of the testis for the release of spermatocytes and imaging these with preparations mounted in halocarbon oil. My attempts with this approach revealed that spermatocyte cysts tended to disintegrate during the release from testis. Moreover, cyst disruption appeared to preclude reliable long term imaging. The resulting low viability usually allowed analysis of progression through a most one meiotic division. The alternative to embedding in halocarbon oil was the use of tissue culture media. As these media result in relatively high levels of auto-fluorescent background, several potentially less-autofluorescent substitutes (testis buffer (Cenci et al., 1994), phosphate buffered saline (PBS) (Sambrook et al., 1989), Ringer’s solution (Koh and Hille, 1997), Robb’s saline (Robb, 1969), insulin-supplemented Schneider’s medium (Handke et al., 2014) were evaluated. However, none of these substitutes allowed meiotic divisions to proceed after mounting for time lapse imaging. It is conceivable that photodamage contributed considerably to the failure of these initial imaging trials since they were performed with a wide-field fluorescence microscopy setup (Zeiss Cellobserver HS). Photodamage might have incurred even though frame rates (3-5 min intervals) and exposure times (30 – 50 msec) were kept low. Eventually, a successful protocol could be established using complete Schneider’s medium for dissection and mounting in combination with a spinning disk confocal microscope

(VisiScope Spinning Disk Confocal System from Visitron including an inverted Olympus IX83 microscope, a CSU X1 Yokagawa Spinning Disk and a Photometrics "evolve" EM 512 digital EMCCD camera equipped for red/green dual channel fluorescence observation). Complete Schneider's medium was Schneider's medium (ThermoFisher Scientific, #21720) supplemented with 10% fetal bovine serum (FBS) (Invitrogen) and 1% penicillin/streptomycin (Invitrogen, #15140). In the final preparations, even after imaging for 5-6 hours (with a stack acquisition interval of 45 sec), cysts were still able to enter into the meiotic divisions. However, the results described here were obtained with cysts that progressed through meiosis soon after the onset of imaging (within 0-2 hours).

Testes were dissected from male pupae at the stage where their color was still white or light brown. At this developmental stage, spermatogenesis is already underway in a number of cysts. However, almost none of these cysts have already progressed far beyond the meiotic divisions into the late stages of spermatogenesis (sperm tail elongation, individualization, coiling). As a result, the fraction of cysts progressing through the meiotic divisions is relatively high during these stages. Medium brown pupae, which already contain the characteristic gas bubbles, were avoided; they have a very hard pupal case and are difficult to dissect. Pupae of the male sex were identified with a stereomicroscope for fluorescence detection when fluorescent markers were used for genotype identification. The spherical gonads in male pupae are larger and more transparent than that of female pupae. Alternatively, males were already selected during the wandering stage 3rd instar larval stage based on gonad morphology, followed by ageing in a fresh vial with standard Drosophila food until the early pupal stages.

Preparations were imaged using 35 mm dishes with glass bottom (MatTek Corporation, #P35G-1.5-14-C). For setting up the preparations, a Whatman filter paper (#No.1) was cut into a ring that covered the entire peripheral region of the dish except the central round opening over the glass bottom coverslip. 300 µL autoclaved water was added to wet the filter paper, preventing evaporation of the sample medium during imaging. Before testis dissection, complete Schneider's medium was pipetted into each of the three cavities of a glass depression slide. The posterior 2/3rd of the pupal case was held by gently clenching with a pair of forceps and the remaining 1/3rd part of the pupal case was torn away with another pair of forceps such that contents are released. All interior material was then slowly pushed from the anterior towards the posterior end ensuring that testes were displaced into the medium. Using extra fine tungsten needles, the two testes that were still attached to the fat body were isolated and washed in new medium in the second cavity of the depression slide. Excess fat body was removed carefully. Some remaining bits of fat body did not interfere because they floated up eventually in the final preparation. 10-12 testes were dissected for each preparation. 45 µL of medium was pipetted into the center of the 35 mm dish such that the drop did not touch the peripheral wetted filter paper. The isolated testes were gently transferred into this drop using tungsten needles. Testes were disrupted by placing the two tungsten needles at opposite poles of the globular testis. By dragging the needles apart in opposite directions, testes were opened and intact cysts dispersed in the center of the dish. To dampen cyst mobility during subsequent imaging, 15 µL of 1% w/v methylcellulose (Sigma #M0387) in Schneider's medium was pipetted on top of the drop with dispersed cysts. The added methylcellulose, after settling down, flattened out the cysts above the glass bottom cover slip without disturbing the ability of the cells to divide. The dish was gently swirled a few times so that all cysts settled down at the center of the dish. Before mounting on the microscope stage, the dish was sealed with a strip of parafilm. Time-lapse imaging was performed in a room with temperature control at 25°C. Spinning disc confocal microscope with an Olympus IX83 and a Yokogawa CSU-X1 unit (Visitron systems) was used for all experiments. Acquisition of time lapse data of complete cysts for scoring entry into meiosis was done with 40x/1.3 oil objective (dz=800 nm, 30-40 sections, dt= 45sec). Acquisition of time lapse data of intact cysts for scoring meiosis duration in wildtype and other genotypes was done with 60×/1.42 oil objective (dz=500 nm, 25-35 z-sections, dt= 45 sec). Finally, high resolution movies for tracking chromosomes, kinetochores and microtubules were done with 100×/1.4 oil immersion objective (dz=300 nm, 40-45 z-sections, dt= 10 sec). Images were acquired using a EMCCD camera.

Administration of drugs was done directly in the imaging dish by pipetting small volumes (ca. 1 µL). For all microtubule depolymerization experiments, Demicolcine/Colcemid (Sigma #D6165, Stock solution 10 mM in DMSO) was used to obtain a final dilution of 10 µM.

STED nanoscopy

For preparation and staining of testes, a published protocol (Wurm et al., 2010) was used with the following modifications. Late larval and pupal testes (about 25) were dissected in testis buffer (183mM KCl, 47mM NaCl, 10 mM TrisHCl pH 6.8). Fat body was removed gently without disrupting the testes. Testes were then transferred to a drop (15 µl) of testis buffer on a poly-L-lysine-treated slide and cut open with a Tungsten needle to spill the contents. Squashing was done gently by placing a 22 mm x 22 mm cover slip on the drop. After two minutes of incubation, the slide was frozen in liquid nitrogen. The cover slip was flipped off with a razor blade in the frozen state. The slide was quickly placed into 100% ethanol (at -20°C) for 10 min. The slide was placed flat in a dish and the region with the squashed testes was overlaid with 0.4 ml of 4% PFA in PBS for 7 min. Permeabilization was done twice in PBST-DOC (PBS + 0.3% Triton-X (20% stock) + 0.3% Sodium deoxycholate (10% stock))for 15 min each. Slides were stored in PBS containing 0.1% Triton X-100 (PBST) until the next step. To retain reagents over the region of the slide with the squashed testis during the subsequent labeling steps, ImmEdge (Hydrophobic Barrier PAP Pen, Vector laboratories) was applied around this region. Blocking was done for 30 min in the blocking solution (PBST containing 5% FBS). The primary antibody (Rabbit α-EGFP, #IS28, 1:3000; Schittenhelm et al., 2007) was centrifuged at 4°C for 20 min at 10,000g and diluted in blocking solution (5% FBS in PBST). Incubation was done overnight at 4°C, or for 2 hours at room temperature, in a humid chamber. Slides were rinsed with PBST. Four washing steps in PBST, each for 15 minutes, were done. Additional blocking before incubation with the secondary antibody was done for 30 min. The stock solution with the secondary antibody (GαRab STAR 635P, Abberior) was also centrifuged before dilution, as described above for the primary antibody. GαRab STAR 635P was used at a dilution of 1:200. Incubation was again done overnight at 4°C, or for 2 hours at room temperature, in a humid chamber. Thereafter, washing was done as after the primary antibody. For DNA staining, Hoechst 33258 (1 µg/µl in PBS) was applied for 5 minutes followed by three washes with PBS. Finally, a drop of Prolong diamond (ThermoFisher Scientific, P36965) was added and a cover slip no 1.5 (Zeiss, 18x18 mm, thickness 0.170 mm ± 0.005 mm). Before imaging, samples were left flat for curing at room temperature for at least 24 hours before imaging.

Imaging was performed with a Leica SP8 inverse STED 3X at the Center for Microscopy and Image Analysis of the University of Zurich. Spermatocytes during the meiotic stages were identified based on the DNA staining. Single sections were acquired with an optimized three channel image sequence. First, the DNA channel was acquired using a confocal mode. Second, Cid-EGFP staining was acquired also using the confocal mode. Third, Cid-EGFP staining was imaged using a STED mode. STED using continuous wave depletion with a 592 nm laser line as well as using a time gated mode with a pulsed 775 nm laser line for depletion were evaluated initially. The time gated mode was found to result in less photo-damage and better resolution.

Deconvolution

In many analyses (Fig 9, 10, 11, 13, 15, 17-30) image data was deconvolved for presentation and further analysis. Deconvolution was done using Huygens Professional Deconvolution Software (SVI, Netherlands). Microscopic parameters were adjusted based on metadata. For all images, a theoretical point spread function calculated by the software in combination with the classic maximal likelihood estimation algorithm was used. Default settings were adequate for most images. For some analyses (Fig 9, 26, 30), optimal signal to noise ratio and maximum number of iterations were estimated for each channel.

Image analysis

The time points of transitions from a particular phase of meiosis into the next were assigned after visual inspection of the time lapse sequences. In the large majority of the analyses, scoring of the transitions relied primarily on the His2Av-mRFP signals. Moreover, in addition Cid-EGFP signals or those from kinetochore proteins fused to EGFP were considered as well. Importantly, in case of these localized EGFP signals at the centromere or kinetochore, an additional autofluorescent background signal reflecting mitochondria could readily be observed in the green channel after digital signal enhancement. These background signals were also considered for scoring transition time points. The scoring criteria are illustrated in Figure 6 and briefly explained in the following.

1. prophase -> prometaphase transition

During prophase of meiosis I and II, a relatively weak diffuse His2Av-mRFP signal was observed throughout the nucleus in addition to somewhat stronger signals on the chromosomes. Eventually the diffuse signals were observed to drop precipitously, presumably as a result of nuclear envelope breakdown (NEBD). The first frame, in which this rapid drop of the diffuse signal was already clearly apparent, (Figure 6A for meiosis I, Figure 6B for meiosis II) was set as onset of prometaphase.

2. prometaphase -> metaphase transition

During prometaphase of meiosis I and II, the pairs of centromeres/kinetochores associated with each bivalent and dyad, respectively, were highly mobile. In contrast, during metaphase all pairs were far more stable and arranged within a metaphase plate. The frame, where the last pair of centromeres/kinetochores had lost its mobility after having congressed into the metaphase plate with its axis between the two centromere/kinetochore signals in parallel to the spindle axis, was scored as onset of metaphase I (Figure 6A for meiosis I, Figure 6B for meiosis II). The scoring of metaphase onset was more reliable than suggested by FigureA,B, since centromere/kinetochore movements over many time frames before and after the transition were inspected, rather than just the two bordering the transition as shown in the figure. The direction of the spindle axis was inferred from mitochondrial autofluorescence, and/or retrospectively from the chromosome movements during anaphase. In metaphase, mitochondria are arranged in a cylinder around the spindle axis. In case of the analysis of the termporal dynamics of meiosis II (Fig. 4), the metaphase onset was primarily scored based on the chromosome movements because sister centromere/kinetochore separation remains very limited and hence the determination of the inter sister kinetochore axis more demanding.

3. metaphase -> anaphase transition

During both meiosis I and II, the first anaphase frame could be readily scored based on the centromere/kinetochore movements (Figure 6A for meiosis I, Figure 6B for meiosis II). While the distance between a pair of centromeres/kinetochores increases barely during metaphase, it increases abruptly and far more rapidly during anaphase. The first frame, where this rapid separation of centromere pairs was already clearly apparent, was scored as anaphase onset. The His2Av-mRFP signals of the chromosomes were far less informative concerning anaphase onset. At early anaphase when centromeres/kinetochores had already started to move apart, chromosomes still displayed comparatively little change. In meiosis I, the separation of the X-

Y bivalent and occasionally also other bivalents lagged somewhat behind. In these cases, anaphase onset was scored when the majority had started to move apart.

4. anaphase -> telophase transition

Scoring the transition from anaphase to telophase was not trivial. Anaphase comprises anaphase A and B. At the time point where the centromeres/kinetochores reached the spindle poles (end of anaphase A), spindle pole separation (anaphase B) was still continuing. The end of anaphase B was difficult to score as pole separation slowed down very gradually. Therefore the onset of contractile furrow activity, which occurred more abruptly, was scored as telophase onset. Onset of contractile furrow activity was revealed by autofluorescence of the mitochondrial aggregate. The first frame, where a dark zone in the middle of the mitochondrial aggregate within the central plane started to become apparent and where at the outer periphery of the mitochondrial aggregate an inward curvature was detectable, was scored as telophase onset (Figure 6A for meiosis I, Figure 6B for meiosis II).

5. telophase -> interphase

After completion of meiosis I, secondary spermatocytes enter into an interphase that is desiganted as interkinesis. After completion of meiosis II, interphase of early spermatids is observed. The first frame of interphase after meiosis I and II was taken as the one where the mass of chromatin has reached a perfectly round shape and where the autofluorescence of the mitochondrial aggregate indicated completion of cytokinesis. In this case there were crescent shaped mitochondrial aggregates in opposite daughter cells with an obvious gap in the autofluorescent signals (Figure 6A for meiosis I, Figure 6B for meiosis II). Clustering of centromere signals was not useful for scoring the onset of interkinesis, as its extent was variable.

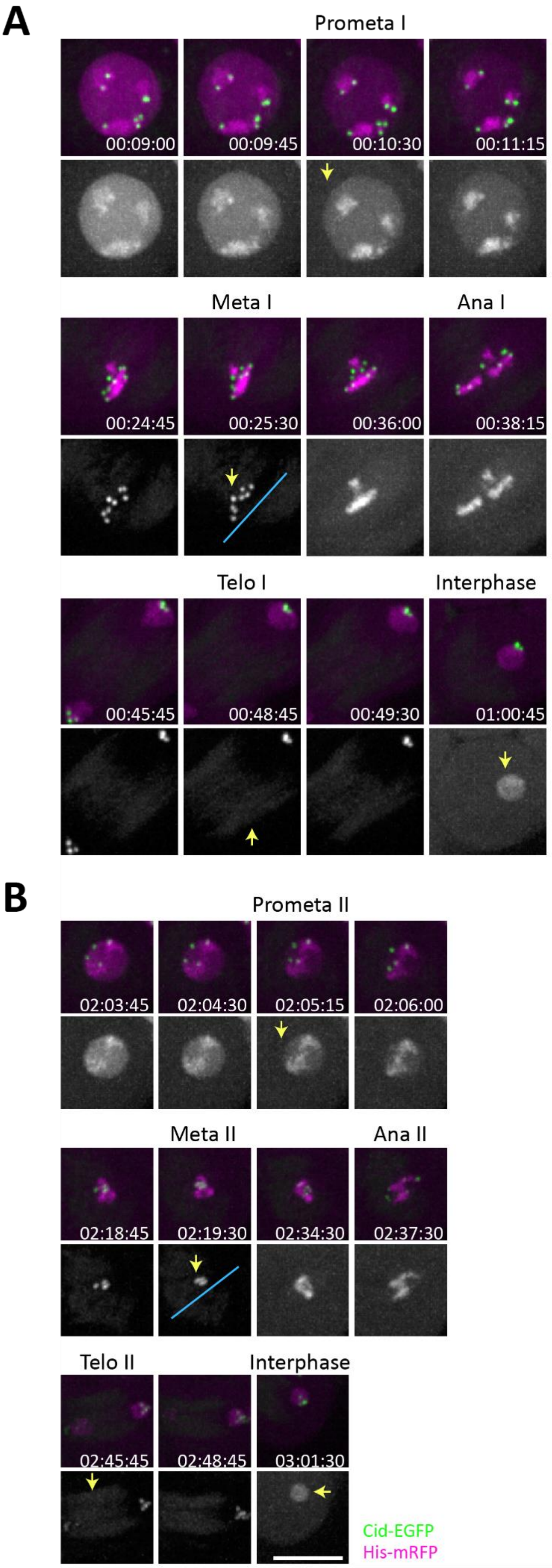

Figure 6: Criteria for scoring meiotic phase transitions

The criteria used for the scoring of phase transitions during meiosis I (A) and meiosis II (B) are illustrated with image sequences acquired with spermatocytes expressing *His2Av-mRFP* and *Cid-EGFP*. The signals in the green channel were enhanced so that the autofluorescence of the mitochondrial derivative is readily visible. Time (hh:min:sec) is indicated in the lower left corner. The onset of a particular phase is indicated by yellow arrows and the name of the phase is given above the panel. A blue line indicates the orientation of the spindle axis. See text for additional explanations. Scale bar = 10 µm.

Centromere/kinetochores were tracked during progression through meiosis in part automatically using the corresponding features of Imaris 7.7.2 and 8.3.0 software (Bitplane). With the most dense image data covering progression though meiosis I (10 sec spacing between time points and 500 nm spacing between z sections) the software identified the great majority of the centromere/kinetochores signals correctly when choosing detection of “sphere” with a diameter of 500 nm followed by autoregressive tracking. Inadvertently identified background artefacts were deleted manually. Missing centromere/kinetochore signals were identified also manually. The connections between centromere/kinetochore signals between two consecutive time points were usually also made correctly by the software. However, in particular during the phase of rapid movements during prometaphase I, considerable manual correction which was also taking the associated His2Av-mRFP signals into account was required. Eventually, the tracks were assigned to distinct chromosomes (see result section for a description of the chromosome-specific features).

During meiosis II, the two sister centromere/kinetochore signals were so extensively superimposed in the large majority of dyads, in particular until metaphase, that they could not be resolved individually and hence also not be tracked automatically. For some analyses, therefore, the two sister centromere/kinetochores were tracked as a pair rather than individually. In this case, automatic tracking followed by manual correction was applied. In some of the analyses, however, the position of each sister centromere/kinetochore was estimated after visual inspection and defined manually with Imaris software, as described in the results section.

After tracking, the xyz coordinates of centromeres/kinetochores were exported for each time point from Imaris into an Excel table and inter centromere/kinetochore distances, as well as the angle between inter centromere/kinetochore axes and the spindle axis were carried out using Excel (Microsoft Office). In most analyses, the vector of the spindle axis was determined as follows. Each centromere/kinetochore pair associated with either a bivalent during meiosis I or a dyad during meiosis II defines a vector in space. The centromere/kinetochores that migrated together to the same spindle pole during anaphase were either all at the origin or all at the end of these vectors. The direction of the spindle axis was then calculated by averaging the direction of all these vectors over a period of 30-40 frames during metaphase. In some cases, the spindle vector was also determined manually based on the directions of the centromere/kinetochore movements during anaphase. The values for centromere/kinetochore speeds calculated by the Imaris software, were also exported into an Excel table for the calculation of average speeds.

To determine the separation between sister centromeres/kinetochores at defined time points during meiosis II (Fig. 15 and Fig 17), the feature ‘Measurement points’ of the Imaris software was used. For these analyses, a given signal representing a pair of sister centromeres/kinetochores was visually inspected while rotating a three dimensional image reconstruction with Imaris in space. Thereby the longest axis of no-spherical signals was assessed, followed by manual selection of the center of two equal sized spheres positioned so that they fill the signal optimally.

For the quantification of the signal intensities at centromeres/kinetochores over time (Fig. 6, 7, 9, 11), the feature ‘Isosurfaces’ of the Imaris software was used. Parameters were selected so that the large majority of the centromeric signals was isolated by automatic segmentation. The integrated signal intensities of all the recognized isosurfaces in a cell were summed at each time point.

Imaris and Image J were used for the generation of maximum intensity projections which were used in the figures unless stated otherwise. Graphs were generated with Excel or GraphPad prism. P values were calculated using a two tailed student t test in GraphPad prism (* = $p < 0.05$; ** = $p < 0.01$; *** = $p < 0.001$). Adobe Photoshop and Illustrator were used for the assembly of the figures.

Results

1 Dynamics of unperturbed male meiosis in Drosophila

1.1 Entry into the meiotic divisions spreads wave-like across the cyst

During the mitotic cell cycle, the G2/M transition involves bi-stable, switch-like regulation of Cdk1 and counteracting phosphatases with various positive feedback loops (Mochida et al., 2016). As the sixteen spermatocytes within a cyst are interconnected by ring canals, entry into the meiotic divisions of a first spermatocyte might therefore start a wave of M phase onset that spreads rapidly from cell to cell throughout the cyst. While previous reports are consistent with this notion, cyst fragmentation of earlier in vivo imaging protocols has precluded a precise analysis. Moreover, fixed testis squash preparations do not provide accurate temporal resolution. To monitor the temporal and spatial sequence of entry into the first meiotic division, time lapse imaging was performed with intact cysts isolated from males expressing histone H2A-mRFP (His2Av-mRFP). Scoring nuclear envelope breakdown (NEBD), as indicated by a rapid loss of diffuse nucleoplasmic His2Av-mRFP signals, indeed revealed a wave-like propagation of entry into meiotic M phase (Fig. 1A). The second spermatocyte entering M phase was always observed to be a neighbor of the first. Subsequent entries into M phase did also obey such a neighbor rule in case of the predominant majority of spermatocytes. In addition, the temporal program of entry into M phase was found to be similar in different cysts (Fig. 1B). On average, every 87 +/- 45 sec (n = 6 cysts) one of the 16 spermatocytes within a cyst entered MI, and the interval between NEBD in the first and last spermatocyte was around 18 min. However, meiotic entry waves did not propagate without some variability. Occasional delays were considerable (Fig. 1B, cyst 5). In conclusion, the observed spatial and temporal program of entry into the first meiotic division in cysts suggests that a wave of Cdk1 activation spreads from cell to cell.

The four mitotic division cycles at the start of spermatogenesis, which convert a spermatogonial cell into a cluster of 16 spermatocytes, result in a characteristic pattern of connectivity where the two daughter cells of the first division have the maximum number of four ring canal connections to neighboring cells, while the remainder has three, two or one such connection. In the female germline, where 16-cell clusters with ring canal connections are formed as well, a cytoskeletal network extending throughout the cluster is known to concentrate specific factors in the two cells with four ring canals, thereby informing cell fate decisions (Cox et al., 2001; Roth and Lynch, 2009). It appeared conceivable, therefore, that analogous transport processes might make spermatocytes with four ring canal connections most likely to enter the meiotic divisions first. To evaluate this notion, time lapse imaging was performed with cysts isolated from males expressing Septin2-GFP and His2Av-mRFP. Septin marks the ring canals (Hime et al., 1996; O'Neill and Clark, 2016). The movies (n = 3) demonstrated that the first spermatocyte undergoing NEBD is not necessarily one of the two cells with four ring canals (Fig. 2). Statistically more extensive analyses would be required to assess whether and how ring canal connectivity might affect the temporal and spatial program of entry into meiosis I within a cyst in alternative ways.

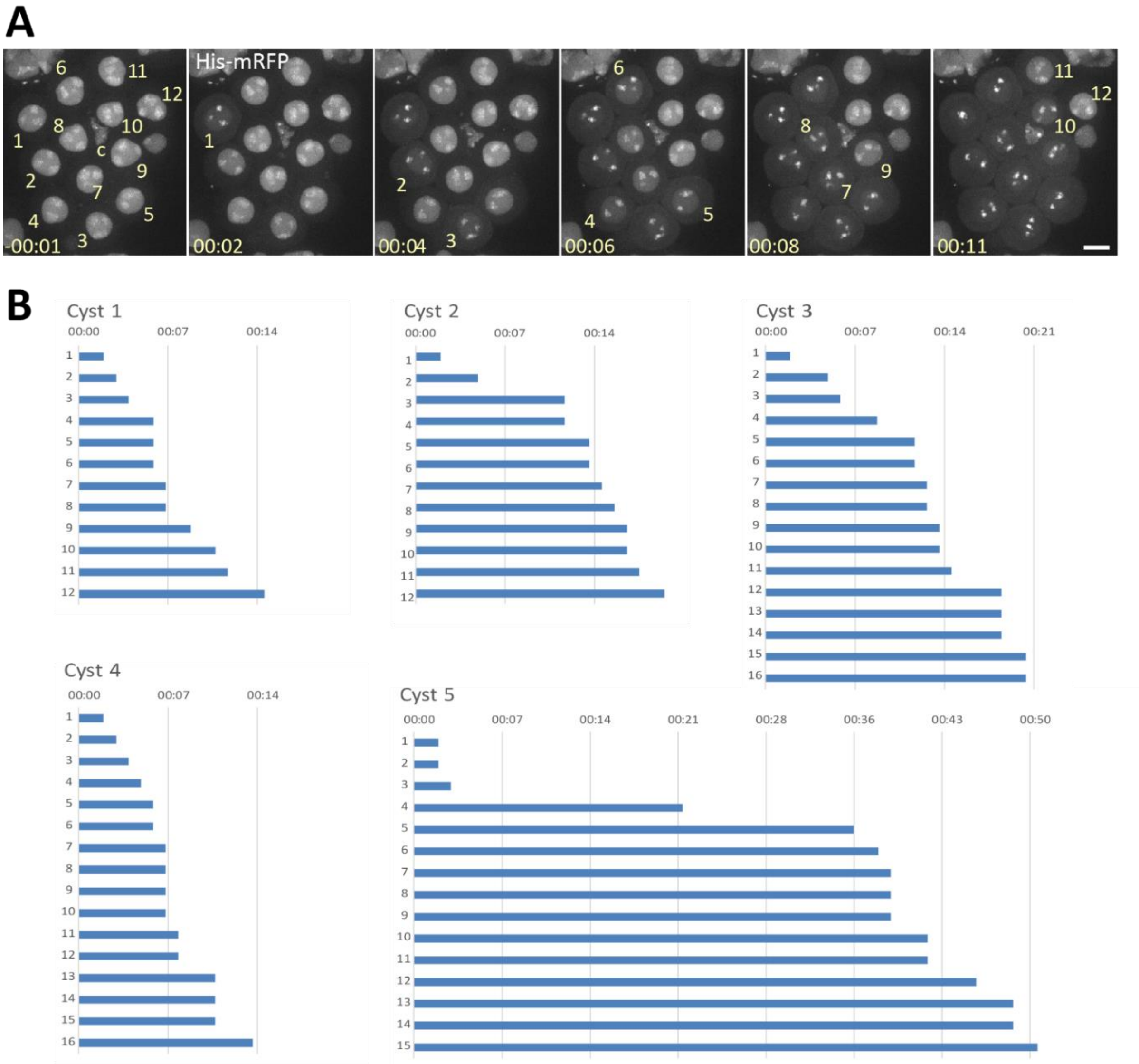

Fig 1: Entry into the meiotic divisions spreads wave-like across the cyst

A. Selected still frames after time lapse imaging of a spermatocyte cyst from a fly expressing *His2Av-mRFP.* Numbers indicate the temporal sequence of NEBD I in the spermatocytes visible within the image stack. The somatic cyst cell (c) within this stack is indicated. Time (hours:minutes) is given in the lower left corner. Time point 0 was chosen to be 2 min before the first NEBD I within the image stack. Scale bar = 10 µm. **B.** Time lines indicating the temporal sequence of NEBD I in 5 different cysts. Cyst 1 is shown in A. Time point 0 was always chosen to be 2 min before the first NEBD I within the image stack. Right ends of the blue lines indicate NEBD I.

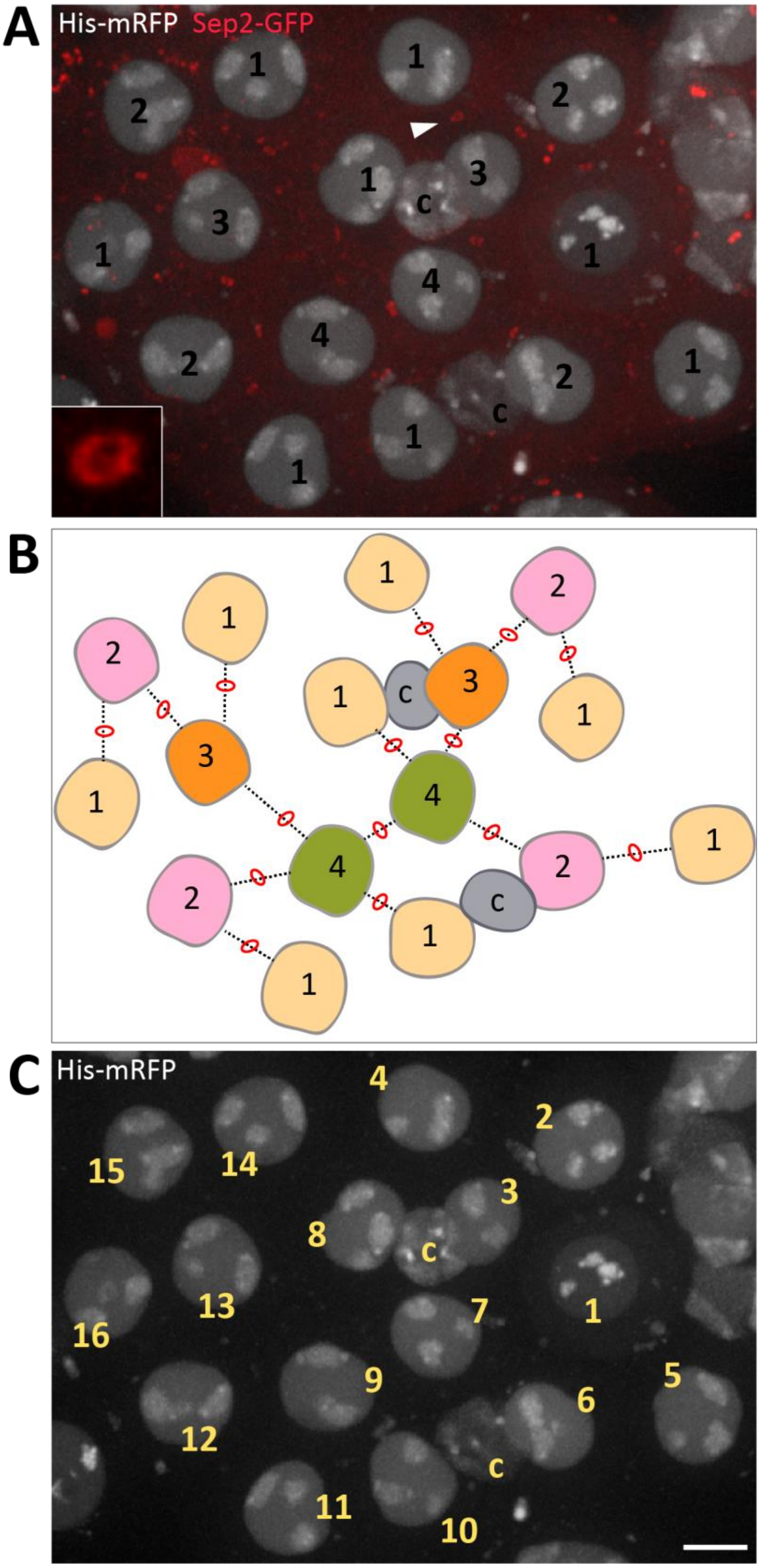

Fig 2: The spermatocytes with 4 ring canals are not the first to enter meiosis I within a cyst

Time lapse imaging of progression into MI with an intact cyst isolated from a fly expressing His2Av-mRFP (grey) and Sep2-GFP (red) was performed. The time point where the first spermatocytes has undergone NEBD I is displayed. **A, B.** Numbers indicate the number of ring canal connections for each spermatocyte within the cyst. The inset in (A) provides a tilted high magnification view of the ring canal indicated with the white arrowhead. Cyst cells (c). **C.** Numbers indicate temporal sequence of NEBD I within the cyst. The first cell entering MI does not have four ring canals. Scale bar = 10 µm.

1.2 The order of entry into meiosis I within a cyst predicts the order of anaphase I onset

In the mitotic cell cycle, the metaphase-to-anaphase transition is a crucial control point. This transition is delayed by the spindle assembly checkpoint (SAC) until all chromosomes are aligned correctly within the spindle. As chromosome alignment involves a random search and capture of kinetochores by dynamic spindle microtubules, the duration from NEBD to anaphase onset exhibits extensive stochastic variation in cultured vertebrate cells (Dick and Gerlich, 2013; Held et al., 2010; Rieder et al., 1994). (Rieder et al. 2014: "... mean values are of little use in predicting when a particular PtK2 cell will enter anaphase."). Accordingly, the temporal order of NEBD at the start of the first meiotic division is not expected to predict the order of anaphase I onset within a given cyst. However, time lapse analysis of His2Av-mRFP expressing cysts revealed the opposite trend. The spatial and temporal program of anaphase I onset was largely a repetition of that observed before for NEBD I (Fig. 3A,B). Within a cyst, the variation of the duration from NEBD I to anaphase onset was limited (Fig. 3C). These observations indicated that the M/A transition during the first meiotic division is primarily governed by a timer that is started at entry into MI. Completion of MI was also not subject to substantial temporal variation. The duration of anaphase I and telophase I in different cells of a cyst was very similar.

1.3 The order of entry into meiosis I predicts the dynamics of progression through interkinesis and meiosis II within a cyst

The gentle isolation of intact cysts, their cultivation and appropriate imaging conditions readily allowed time lapse imaging beyond the first meiotic divisions. Although image stack depth was often not chosen to be wide enough for imaging all cells of a cyst throughout the whole of meiosis I and II, it allowed tracking of a majority of cells. This tracking indicated that the two daughter cells of the spermatocyte which had entered first into meiosis I were usually the first to enter and exit interkinesis, as well as the first to complete meiosis II (Fig. 3A,B). The duration from NEBD to the metaphase to anaphase transition was somewhat more variable in meiosis II compared to meiosis I (Fig. 3C). Nevertheless, apart from minor exceptions, the temporal order observed at entry into MI was maintained throughout progression through meiosis I, interkinesis and meiosis II. This result suggest that a timer started at the onset of meiosis presumably controls the temporal dynamics of progression through the meiotic divisions.

Fig 3: Order of entry into meiosis I predicts the order of all subsequent meiotic stages
A. Stills after time lapse imaging of a spermatocyte cyst from a fly expressing *His2Av-mRFP*. The cyst chosen in Fig. 1 for illustration of the temporal order of NEBD I is also shown here. The selected time points illustrate NEBD I, Anaphase I, NEBD II and anaphase II in the spermatocytes that were the first (cell 1, left) and second (cell 2, right), respectively, to enter meiosis I. Time (hours:minutes:seconds) indicated in the lower left corner; cell 1 and cell 2 circled in yellow and orange, respectively. Scale bar = 10 µm. **B.** Lines indicating the time of onset of NEBD I, anaphase I, NEBD II and anaphase II for all cells within the image stack shown in A. Daughter cells generated in meiosis I were designated with "a" and "b". Some daughter cells are missing in the diagram, because meiosis I displaced them out of the image stack. **C.** Histogram illustrating the variability in the duration of the period from NEBD to the metaphase/anaphase transition during MI (left) and MII (right) within the cyst shown in A and B.

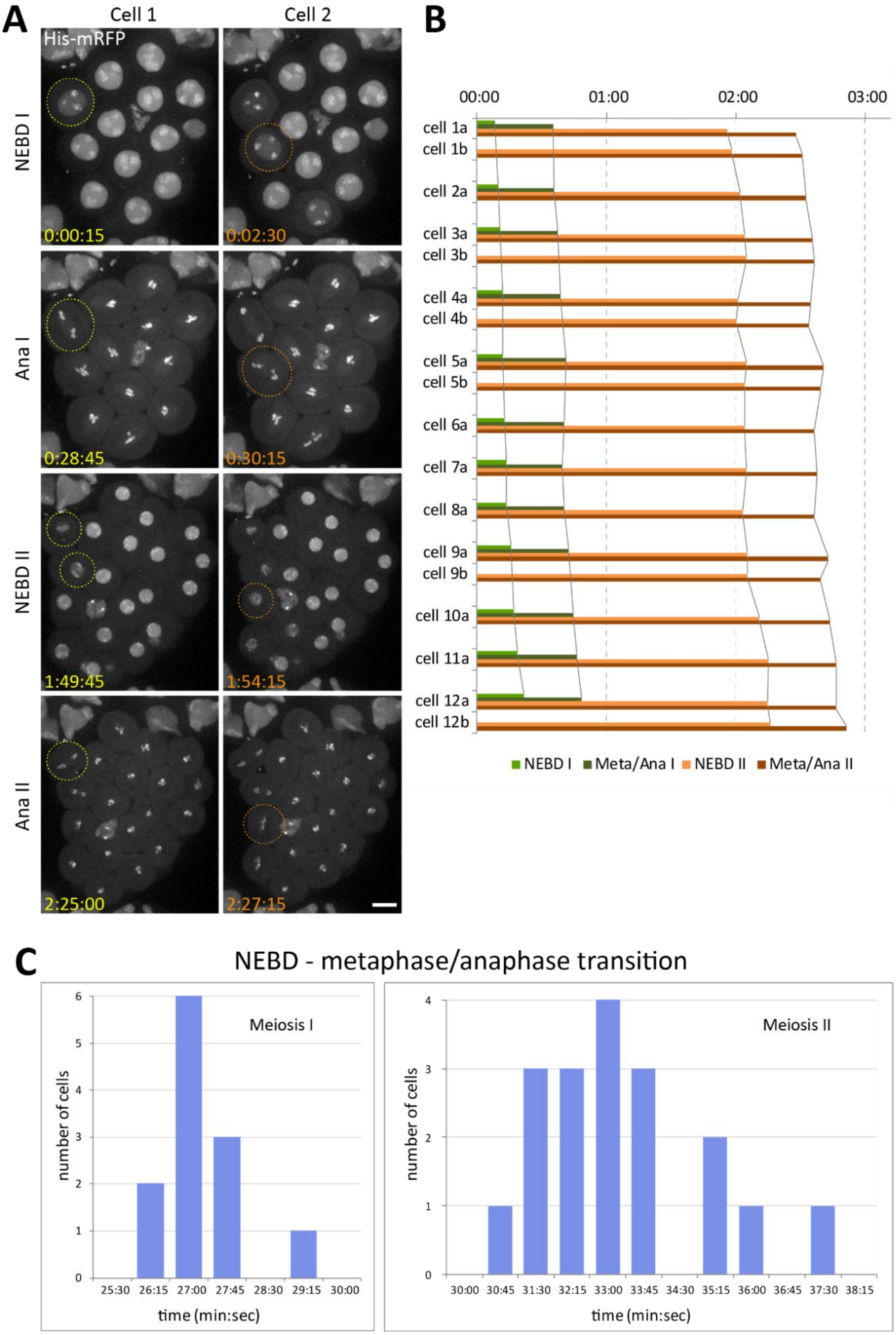
A
Cell 1
Cell 2
His-mRFP
NEBD I
Ana I
NEBD II
Ana II
0:00:15
0:02:30
0:28:45
0:30:15
1:49:45
1:54:15
2:25:00
2:27:15
B
00:00
01:00
02:00
03:00
cell 1a
cell 1b
cell 2a
cell 3a
cell 3b
cell 4a
cell 4b
cell 5a
cell 5b
cell 6a
cell 7a
cell 8a
cell 9a
cell 9b
cell 10a
cell 11a
cell 12a
cell 12b
NEBD I
Meta/Ana I
NEBD II
Meta/Ana II
C
NEBD - metaphase/anaphase transition
Meiosis I
number of cells
0
1
2
3
4
5
6
25:30
26:15
27:00
27:45
28:30
29:15
30:00
time (min:sec)
Meiosis II
number of cells
0
1
2
3
4
30:00
30:45
31:30
32:15
33:00
33:45
34:30
35:15
36:00
36:45
37:30
38:15
time (min:sec)

1.4 Cyst-to-cyst variation of the temporal dynamics of progression through the meiotic divisions

Progression through meiosis occurs with little temporal cell-to-cell variation within a cyst, likely also as a result of ring canal-mediated interconnectivity. Independent cysts, however, might progress through meiosis at different speed. To explore temporal variation among cysts, a total of eight cysts were analyzed from start of meiosis I to end of meiosis II. Moreover, seven additional cysts, with which progression through a substantial part but not the entire meiotic division process had been imaged, were included in the analysis as well. Each of the analyzed cysts was from a distinct testis. In each cyst, three non-neighboring cells were analyzed and the average durations of the distinct meiotic steps (Fig. 4A) in these three cells were taken as representative for the corresponding cyst. The comparison indicated that distinct cysts do not progress through meiosis with substantial temporal variation (Fig. 4B). The average time required for completion of both meiotic division (from NEBD I until end of MII) was less than three hours (166 +/- 11 min s.d., n = 8). Meiosis I, interkinesis and meiosis II each lasted for almost an hour (Fig. 4C) (MI: 58 +/- 6 min., s.d., n = 14; IK: 56 +/- 11 min., s.d., n = 12; MII: 56 +/- 8 min., s.d., n = 8). Meiosis I and II were also similar with regard to the duration of the different phases (Fig. 4C) with anaphase being the shortest and the least variable. Interestingly, neither in meiosis I nor in meiosis II, prometaphase displayed a pronounced variability. Prometaphase variability was comparable (meiosis I) or even less (meiosis II) than that of metaphase. If the period required for chromosome bi-orientation was highly variable as a result of stochastic kinetochore search and capture during prometaphase, followed by metaphase of constant length determined by SAC silencing with invariant kinetics after bi-orientation of the last chromosome, the variability of prometaphase would be expected to be more extensive than that of metaphase. The observed results indicate that the dynamics of progression through both meiotic divisions is dominated by timer-like control. Stochasticity of bi-orientation does not contribute significantly to temporal control, at least during unperturbed meiosis.

Fig 4: Cyst-to cyst variation of temporal dynamics of progression of meiosis

Cysts isolated from flies expressing *His2Av-mRFP* and *Cid-EGFP* were used for time lapse imaging. The duration of the distinct phases (prometa-, meta-, ana- and telophase) during MI and MII as well as that of interkinesis was determined. **A.** The distinct phases of the meiotic divisions are illustrated with representative still frames. Only one daughter cell is shown in telophase. Time (hours:minutes:seconds) indicated in the lower left corner. Scale bar = 5 µm. **B.** Dot plot representing the duration of meiotic stages illustrated in A, as well as average +/- s.d. (n ≥ 12 cysts). **C.** Timeline representing average duration of the distinct meiotic stages.

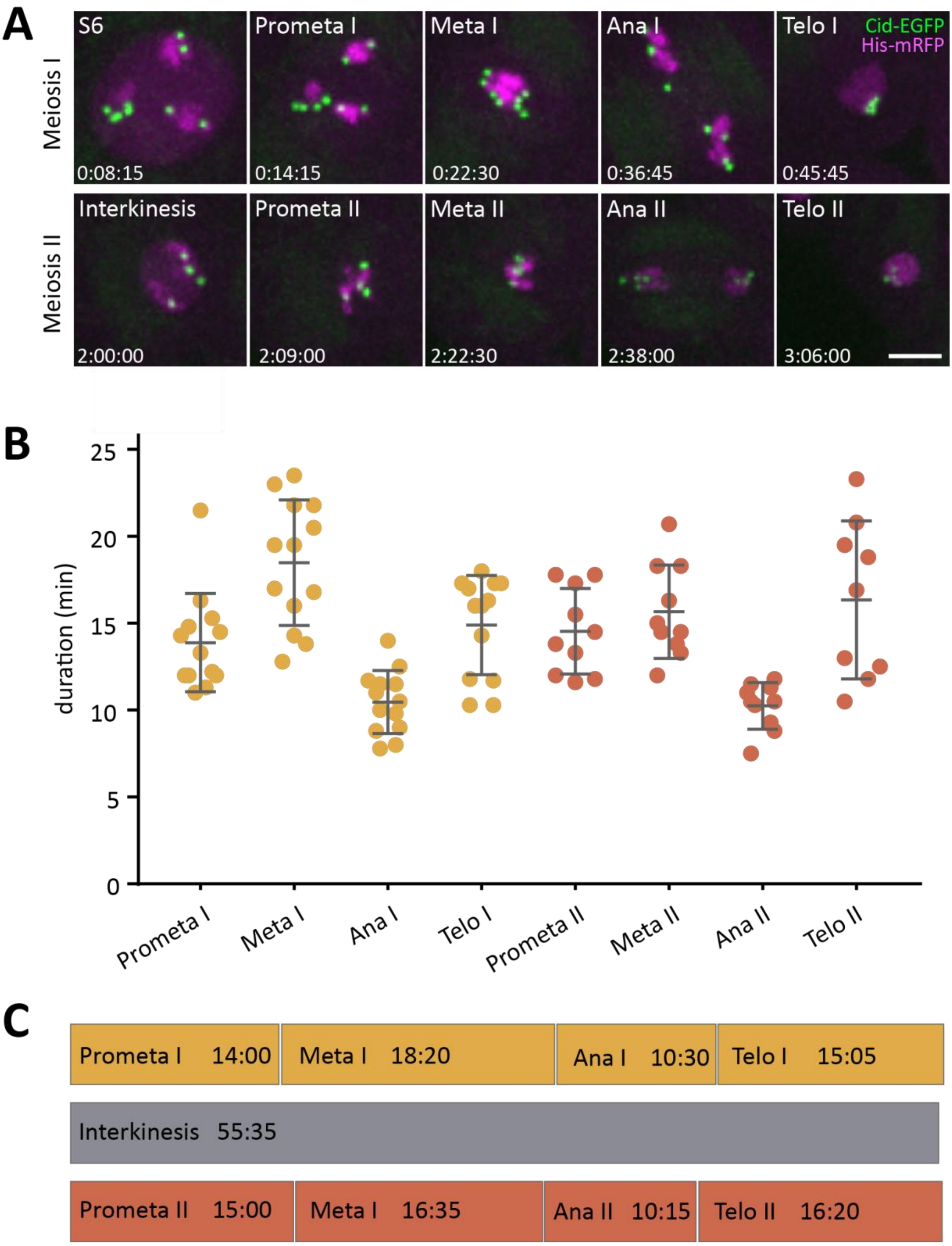
A
Meiosis I
S6
0:08:15
Prometa I
0:14:15
Meta I
0:22:30
Ana I
0:36:45
Telo I
0:45:45
Cid-EGFP
His-mRFP
Meiosis II
Interkinesis
2:00:00
Prometa II
2:09:00
Meta II
2:22:30
Ana II
2:38:00
Telo II
3:06:00
B
duration (min)
0
5
10
15
20
25
Prometa I
Meta I
Ana I
Telo I
Prometa II
Meta II
Ana II
Telo II
C
Prometa I 14:00
Meta I 18:20
Ana I 10:30
Telo I 15:05
Interkinesis 55:35
Prometa II 15:00
Meta I 16:35
Ana II 10:15
Telo II 16:20

2. The delay of anaphase I onset caused by loss of tension between homologous centromeres is limited

Checkpoints activated in case of certain process failures might dominate over the timer mechanism that controls unperturbed progression through the meiotic divisions. Mitosis in various cell types including Drosophila embryonic cells (Pauli et al., 2008) involves control by mechanical tension between sister kinetochores resulting from bi-orientation of chromosomes within the spindle. Absence of tension promotes detachment of kinetochore from kinetochore microtubules (Foley and Kapoor, 2013; Sacristan and Kops, 2015). To assess the maximal response to a loss of mechanical tension, the dynamics of progression through meiosis was analyzed with males transheterozygous for *mnm* null alleles. *mnm* is specifically required for homolog conjunction during Drosophila male meiosis. In *mnm* mutants, therefore, univalents instead of bivalents are segregated during meiosis I (Blattner et al., 2016; Thomas and McKee, 2007).

Time lapse imaging with *mnm* null mutant spermatocytes expressing Cid-EGFP and His2Av-mRFP revealed that chromosome territories were often abnormal already in spermatocytes (in two thirds of the S6 spermatocytes, n = 23; 2 cysts), as expected (Thomas and McKee, 2007). In these abnormal spermatocytes, territories were partially or completely separated into two sub-regions. During chromosome condensation at the start of the meiotic division, the two sub-regions of a territory were sometimes condensing into an apparently normal looking bivalent, suggesting that homologs can retain some associations in *mnm* mutants. Early in prometaphase I, therefore, around 45% of the spermatocytes still had a normal appearance with four regular bivalents (Fig. 5A). However, when kinetochores started to interact with microtubules, as suggested by their saltatory movements, all remaining bivalents were separated rapidly into independent univalents (Fig. 5A). In mid prometaphase I, therefore, univalents instead of bivalents were present in *mnm* mutants (96%, n = 23 spermatocytes from 2 cysts).

Since the univalents did not form a normal metaphase I plate, a M/A transition could not be scored reliably during meiosis I in *mnm* mutants. Therefore the duration of complete meiotic divisions was determined to assess whether a loss of tension between homologs delays progression though meiosis I. The duration of meiosis I was found to be significantly extended in *mnm* mutants compared to controls (Fig. 5C) (by 10 min, $p < 0.0001$, t test; for *mnm* n = 35 spermatocytes from 7 cysts; for control the data shown in Fig. 4B was used). In contrast, meiosis II was not extended in *mnm* mutants (for *mnm* n= 22 spermatocytes from 5 cysts; for control the data shown in Fig. 4B was used). A largely normal timing of MII in *mnm* mutants is actually expected since chromosome organization during meiosis II in *mnm* mutants should be equivalent to that during normal meiosis II (Blattner et al., 2016; Thomas and McKee, 2007). As in wild-type, dyads are present at the start of MII in *mnm* mutants although in variable numbers as a result of random segregation of univalents during MI.

The analysis of *mnm* mutants confirmed that the presence of univalents is indeed detected and delays meiosis I completion. However, the delay of 10 minutes observed during meiosis I in *mnm* mutants, where exclusively univalents (i.e., eight) instead of the normal four bivalents are segregated, was considerably shorter than that reported for the case of four univalents with a more limited data set (16 minutes; (Rebollo and Gonzalez, 2000). Obviously, the response to a loss of tension between homologs during male meiosis I is far less dramatic in Drosophila compared to praying mantids. While a single univalent is not sufficient to extend male meiosis I in Drosophila (Rebollo and Gonzalez, 2000), a univalent X chromosome arising spontaneously in about 10% of mantid spermatocytes causes a metaphase I arrest lasting for more than five hours (Callan and Jacobs, 1957; Nicklas et al., 1995).

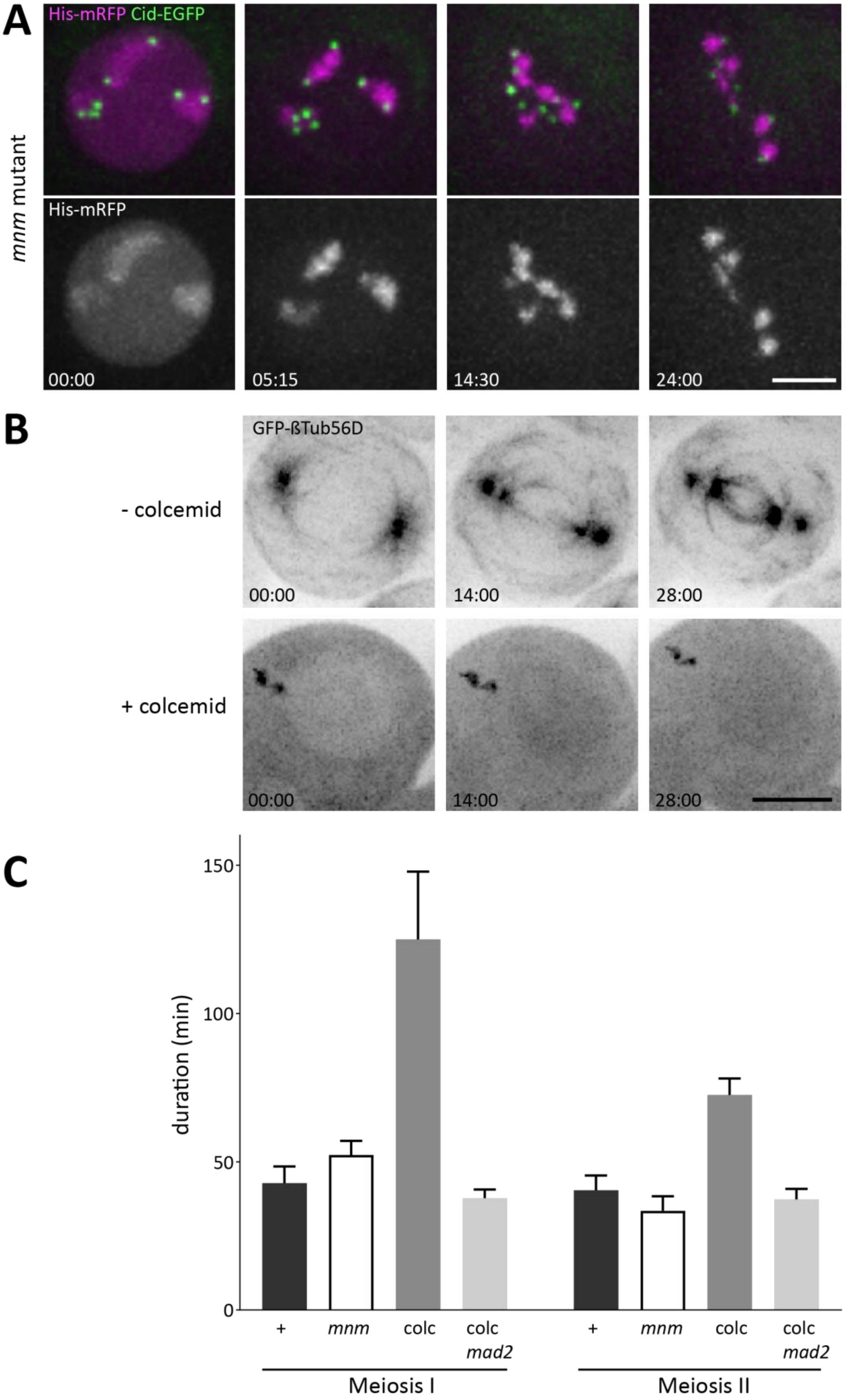
A
His-mRFP Cid-EGFP
mnm mutant
His-mRFP
00:00
05:15
14:30
24:00
B
GFP-ßTub56D
- colcemid
00:00
14:00
28:00
+ colcemid
00:00
14:00
28:00
C
duration (min)
150
100
50
0
+
mnm
colc
colc *mad2*
+
mnm
colc
colc *mad2*
Meiosis I
Meiosis II

Fig 5: Comparison of the effects on temporal dynamics of progression through meiosis caused by loss of homolog conjunction or spindle function

A. Stills were selected after time lapse imaging of progression through MI with cysts from _mnm_ mutant flies expressing _Cid-EGFP_ and _His2Av-mRFP_ (_w*; Cid-EGFP, His2Av-mRFP/+;_ mnm^{3298}/mnm^{5578}). Time (min:sec) is indicated in the lower left corner. Time point 0 corresponds to the onset of NEBD I. The selected spermatocyte still has a normal appearance with three chromosome territories at NEBD I, but 24 min later univalents are present instead of bivalents. Scale bar = 5 µm. **B.** Time lapse imaging with spermatocytes expressing _GFP-ßTub56D_ and _His2Av-mRFP_ (not shown) demonstrates that colcemid (10 µM) prevents spindle formation effectively. Time information as in (A). Scale bar = 10 µm. **C.** Bar diagram representing average duration (+/- s.d.) of the period from onset of NEBD until onset of contractile furrow activity in cysts from the indicated genotypes and treatments: + (_w*; Cid-EGFP, His2Av-mRFP; bamP-GAL4VP16_) (n = 14 spermatocytes in MI and 8 in MII), _mnm (w*; Cid-EGFP, His2Av-mRFP/+;_ mnm^{3298}/mnm^{5578}_)_ (n = 35 in MI and 22 in MII), colc (colcemid treated _w*; Cid-EGFP, His2Av-mRFP; bamP-GAL4VP16_) (n = 10 in MI and 6 in MII), colc _mad2_ (colcemid treated _w*; Cid-EGFP, His2Av-mRFP, matα-GAL4/CyO_ or _sp;_ $mad2^{p1}/ mad2^{p2}$) (n = 9 in MI and 27 in MII). For each bar the analyzed spermatocytes were from >7 distinct testes. The difference in MI between control and _mnm_ mutants is highly significant ($p < 0.0001$, t test).

3. Loss of spindle assembly checkpoint function causes a mild acceleration of meiotic anaphase onset

In principle, loss of tension between homologs might cause only a very limited delay during Drosophila male meiosis I because the SAC might not be functional in spermatocytes. However, previous time lapse imaging with spermatocytes isolated from colchicine-fed males suggested that the SAC is functional (Rebollo and Gonzalez, 2000). Analyses after taxol addition have led to the same conclusion (Savoian et al., 2000). For confirmation, cultured cysts were administered with colcemid at the start of in vivo imaging. Experiments with GFP-ßTub56D cysts demonstrated that this treatment resulted in rapid depolymerization of MTs except for some remnants restricted to the centrosomes (Fig. 5B). By quantifying the dynamics of progression through meiosis I, colcemid was observed to cause a delay of about 80 min (Fig. 5C). This meiosis I delay was five times longer than that observed in previous analyses with colchicine-fed males (Rebollo and Gonzalez, 2000), because colcemid addition to cultured spermatocytes just before imaging might result in more extensive microtubule depolymerization than feeding. Similarly, the delay observed here was fourfold longer than that observed after taxol addition (Savoian et al., 2000).

To assess SAC robustness during meiosis II, colcemid was applied to cysts during interkinesis. Also in case of meiosis II, this caused a significant delay of about 32 min (Fig. 5C). Compared to meiosis I, this delay was considerably shorter. SAC strength therefore seems greater in meiosis I than meiosis II. Interestingly, analyses in mouse oocytes have also indicated that single chromatids are more effective in SAC activation than univalents during meiosis I (Tachibana-Konwalski et al., 2013).

To confirm that SAC activation causes the colcemid-induced delays observed during the meiotic divisions, *mad2* null mutant spermatocytes were analyzed analogously after exposure to colcemid. In *mad2* mutants, colcemid was unable to prolong the meiotic M phases beyond the duration observed in unperturbed wild-type meiosis (Fig. 5C), demonstrating that the meiotic delays induced by colcemid in wild type were indeed SAC-dependent, as expected.

Time lapse analyses with spermatocytes expressing Bub3-EGFP (Pandey et al., 2007) further confirmed that the SAC is functional during the meiotic divisions (Fig. 6). Before entry into meiosis I, Bub3-EGFP was not detectable in spermatocytes. About 5 minutes after NEBD, it started to accumulate on kinetochores (Fig. 6A). During metaphase I, kinetochore signal intensities decreased but they were still detectable at the onset on anaphase I (Fig. 6A). Kinetochore signal intensities dropped further during anaphase I and by late telophase I they were no longer above background (Fig. 6A). During interkinesis, Bub3-EGFP was also undetectable (Fig. 6B). During the second meiotic division, Bub3-EGFP behavior was essentially identical as in meiosis I (Fig. 6B). Addition of colcemid before the onset of the first meiotic division resulted in maintenance of high Bub3-EGFP levels on kinetochores during the delay in M phase (Fig. 6B). Beyond Bub3-EGFP, analyses with GFP-Rod confirmed that this SAC component is also expressed during Drosophila male meiosis (Fig. 7; see also below Fig. 18). The subcellular localization of GFP-Rod during the meiotic divisions appeared very similar to that observed during early embryonic mitoses (Basto et al., 2004) and it was also in agreement with immunofluorescent analyses in spermatocytes (Scaerou et al., 1999). The presence of Rod during Drosophila female meiosis has been described before (Gluszek et al., 2015; Radford et al., 2015). Compared to female meiosis, the intensity of GFP-Rod on KT microtubules during the streaming phase appeared to be rather low.

Fig 6: Bub3-EGFP localization during progression through meiosis in the presence and absence of microtubules

Time lapse imaging was performed with cysts from flies expressing Bub3-EGFP and His2Av-mRFP (*w*; gEGFP-Bub3 II.1, His2Av-mRFP II.2*). Colcemid was added in some of the experiments either before MI or before MII (not shown). Representative spermatocytes during meiosis I (**A**) and meiosis II (**B**) are shown. Analogous behavior was observed in all other spermatocytes analyzed (12 spermatocytes from 2 different cysts without colcemid treatment and 8 spermatocytes from 2 different cysts with colcemid treatment). The curves represent the EGFP intensity of the kinetochore signals observed in the displayed spermatocytes. Scale bar = 3 µm (A) and 2 µm (B).

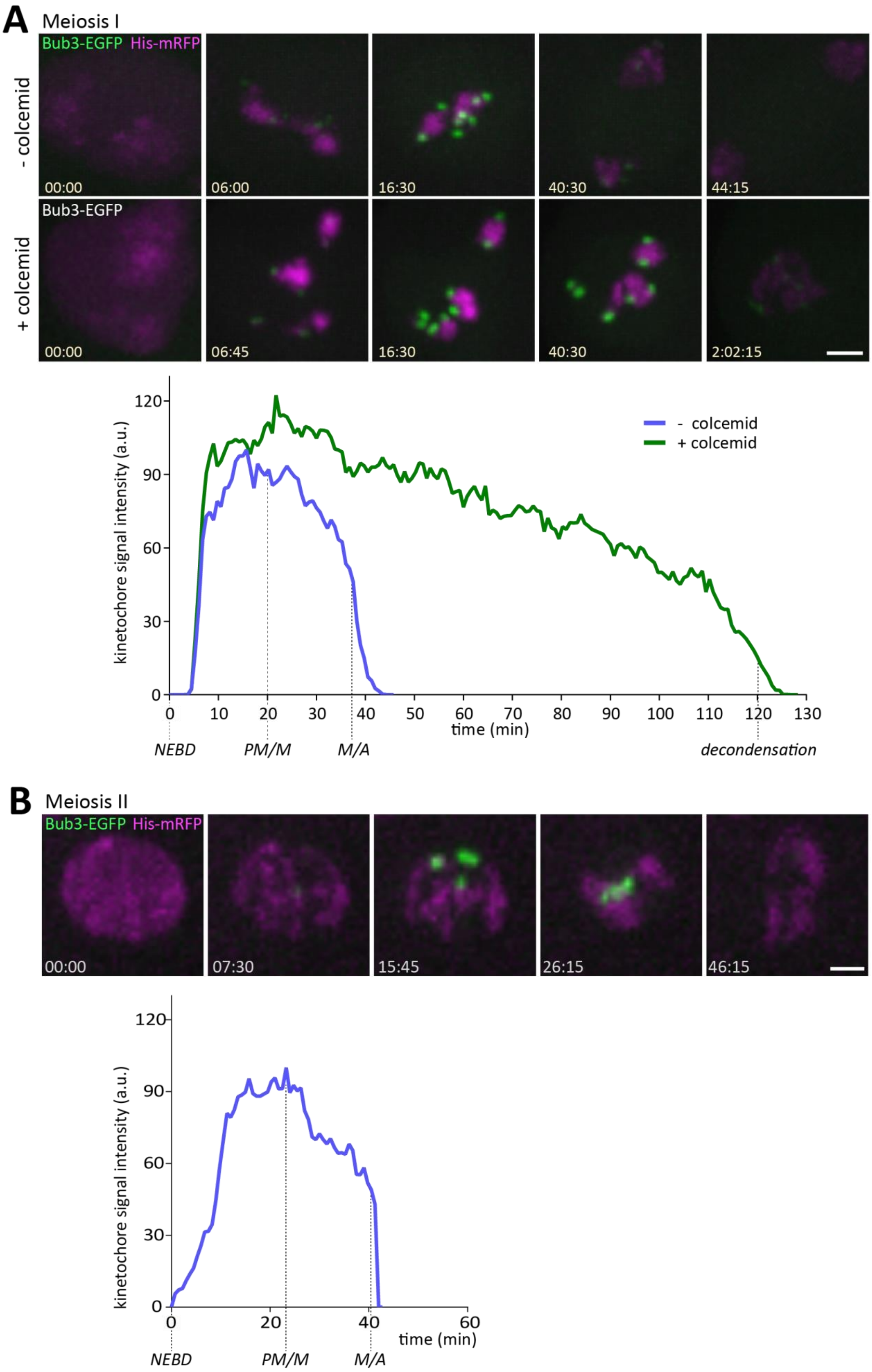
A
Meiosis I
Bub3-EGFP His-mRFP
- colcemid
00:00
06:00
16:30
40:30
44:15
Bub3-EGFP
+ colcemid
00:00
06:45
16:30
40:30
2:02:15
kinetochore signal intensity (a.u.)
0
30
60
90
120
- colcemid
+ colcemid
0
10
20
30
40
50
60
70
80
90
100
110
120
130
time (min)
NEBD
PM/M
M/A
decondensation
B
Meiosis II
Bub3-EGFP His-mRFP
00:00
07:30
15:45
26:15
46:15
kinetochore signal intensity (a.u.)
0
30
60
90
120
0
20
40
60
time (min)
NEBD
PM/M
M/A

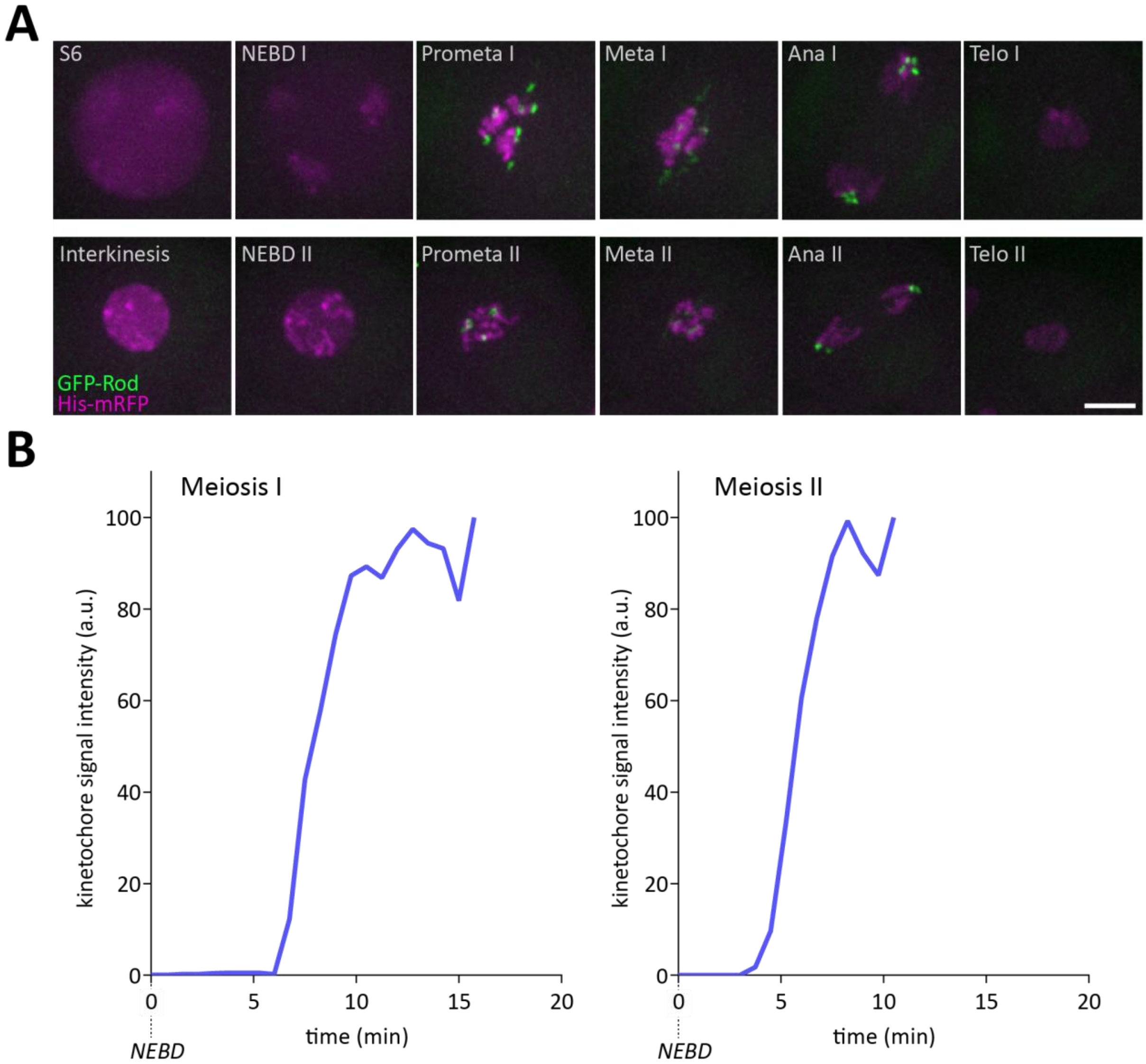

Fig 7: Localization of GFP-Rod during meiosis

Time lapse imaging was performed with cysts from flies expressing GFP-Rod and His2Av-mRFP (*w*; GFP-Rod, His2Av-mRFP II.2/CyO).* Representative stills illustrate GFP-Rod localization during meiosis I and II (**A**). Scale bar = 5 µm. Quantification of GFP signals on kinetochores resulted in intensity profiles (**B**) documenting the accumulation on the kinetochores until the maximal values were reached. The subsequent poleward streaming of GFP-Rod on KT-MTs precludes meaningful quantification with the applied procedure (see Materials and Methods). Analogous behavior was observed in all the analyzed cells (7 spermatocytes from 2 different testes in meiosis I and also in meiosis II).

As the SAC is clearly functional during Drosophila male meiosis, the consequences of its absence on the temporal dynamics of progression through meiosis were carefully studied. Null mutations in Drosophila *mad2* are known to abolish SAC function completely with only minor effects on viability and fertility (Buffin et al., 2007). To assess the role of SAC in the control of meiotic division dynamics, time lapse imaging was performed with *mad2* mutant spermatocytes expressing Cid-EGFP and His2Av-mRFP. The duration of the period from NEBD to the metaphase-to-anaphase transition, as well as that of the subsequent period from the metaphase-to-anaphase transition until onset of cytokinesis was determined. The *mad2* mutants were either transheterozygous for two distinct null alleles ($mad2^{P1}/mad2^{P2}$) or homozygous for one of those ($mad2^{P1}/mad2^{P1}$). Compared to controls, which have two functional $mad2^{+}$ gene copies, the onset of anaphase occurred prematurely in the *mad2* null mutants during both meiotic divisions (Fig. 8, Blue scatter plot). In contrast, the dynamics of completion of meiosis I and II was not significantly altered in the *mad2* null mutants (Fig. 8, grey scatter plot). Spermatocytes from *mad2* heterozygotes ($mad2^{P1/+}$ and $mad2^{P2/+}$) were analyzed as well. Somewhat unexpectedly, the M/A transition in these was observed to be advanced as well, either only in meiosis II ($mad2^{P1/+}$) or in both divisions ($mad2^{P2/+}$) (Fig. 8). In principle, the effects observed in the *mad2* heterozygotes might reflect partial *mad2* haploinsufficiency and genetic background effects, although both explanations do not appear to be very likely. Clearly, however, the acceleration of anaphase onset in the heterozygotes was not as pronounced as in the *mad2* null mutants. Overall these findings indicate that the SAC causes some delay of anaphase onset during progression through unperturbed meiotic divisions. Abolition of this delay by *mad2* null mutations did not cause severe chromosome missegregation. Although metaphase I was substantially shortened in the *mad2* null mutants, bivalents were aligned in a metaphase plate of normal appearance at the time when anaphase started. In 22 *mad2* mutant cells, where chromosome segregation during meiosis I was tracked, only one bivalent (of 88 in total) failed to disjoin. Moreover, in 30 *mad2* mutant cells analyzed during meiosis II, all chromosomes (i.e., 120) segregated regularly. The absence of severe meiotic abnormalities is consistent with the fact that male fertility of *mad2* null mutants was reported to be near normal (60% of control in case of $mad2^{P1}/mad2^{P1}$; (Buffin et al., 2007).

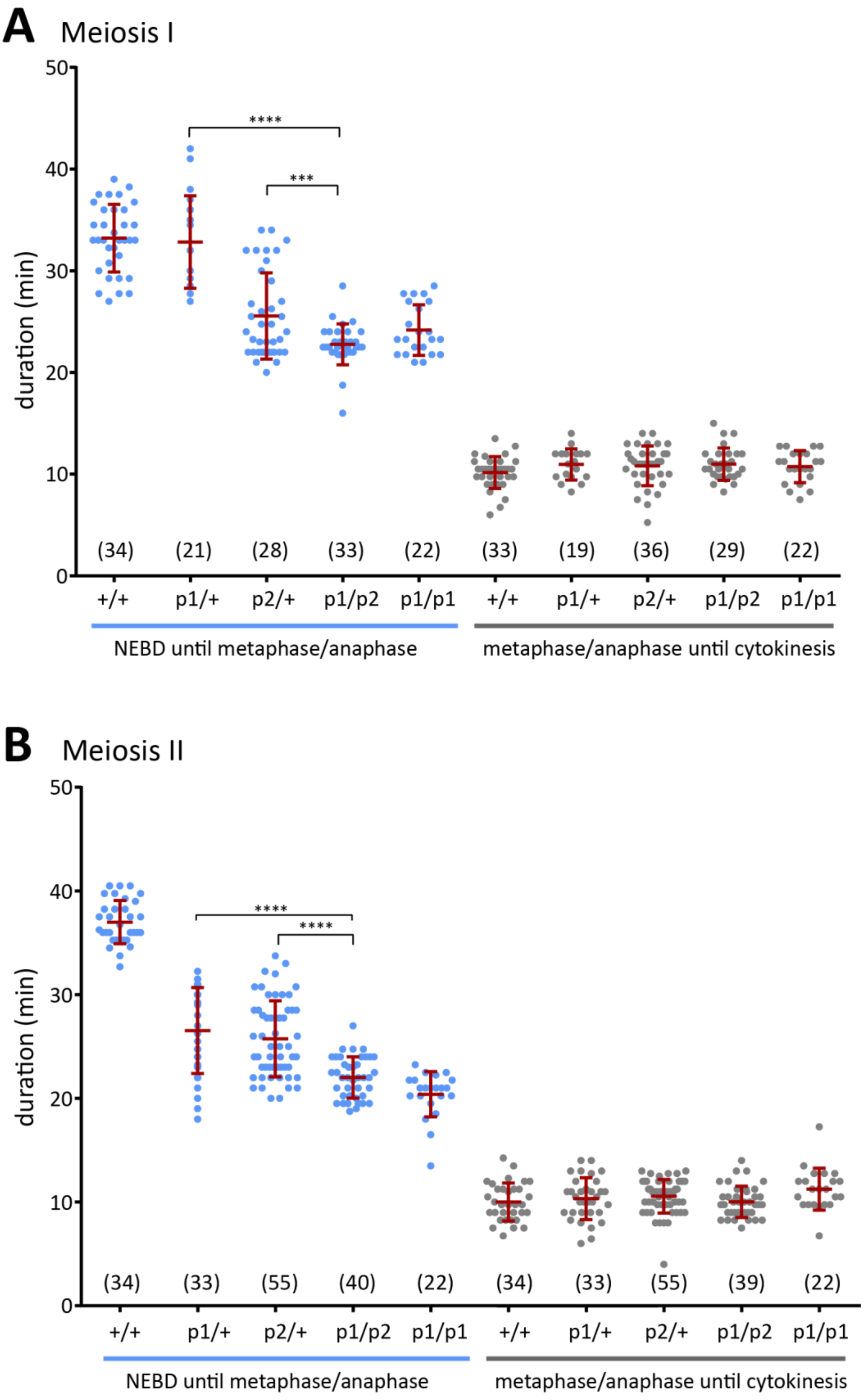
A
Meiosis I
duration (min)
0
10
20
30
40
50
****
***
(34)
(21)
(28)
(33)
(22)
(33)
(19)
(36)
(29)
(22)
+/+
p1/+
p2/+
p1/p2
p1/p1
+/+
p1/+
p2/+
p1/p2
p1/p1
NEBD until metaphase/anaphase
metaphase/anaphase until cytokinesis
B
Meiosis II
duration (min)
0
10
20
30
40
50
****
****
(34)
(33)
(55)
(40)
(22)
(34)
(33)
(55)
(39)
(22)
+/+
p1/+
p2/+
p1/p2
p1/p1
+/+
p1/+
p2/+
p1/p2
p1/p1
NEBD until metaphase/anaphase
metaphase/anaphase until cytokinesis

In conclusion, my findings confirm that the SAC is functional during male meiosis. In fact, it is considerably more robust than suggested previously (Rebollo and Gonzalez, 2000; Savoian et al., 2000). When all kinetochores are unattached (as in the presence of colcemid), the delay imposed by the SAC is close to 1.5 hours, at least during meiosis I. This delay by exclusively unattached bivalents was found to be eightfold longer than the delay observed in *mnm* mutants, where exclusively univalents instead of bivalents interact with the spindle during meiosis I. Therefore, loss of spindle attachments appears to be recognized far more effectively than loss of stable linkage between homologous centromeres during male meiosis.

Even during unperturbed meiosis, the SAC delays anaphase onset significantly, although not to a degree essential for the overall success of meiosis. This observation further emphasizes that progression through the meiotic divisions in Drosophila males appears to be governed predominantly by a timer. Apparently, this timer provides ample time for meiotic chromosome bi-orientation, making the SAC dispensable in unperturbed conditions.

Fig 8: Temporal dynamics of progression through meiosis in *mad2* mutants
Time lapse imaging was performed using cysts isolated from flies expressing Cid-EGFP and His2Av-mRFP. Moreover, as indicated, the flies carried different *mad2* alleles: +/+ (*w*; Cid-EGFP, His2Av-mRFP, matα-GAL4/CyO; mad2*$^{+}$*/mad2*$^{+}$), p1/+ (*w*; Cid-EGFP, His2Av-mRFP, matα-GAL4/CyO; mad2*^{p1}*/mad2*$^{+}$*);* p2/+ (*w*; Cid-EGFP, His2Av-mRFP, matα-GAL4/CyO* or *Sp; mad2*^{p2}*/mad2*$^{+}$), p1/p2 (*w*; Cid-EGFP, His2Av-mRFP, matα-GAL4/CyO* or *Sp; mad2*^{p1}*/mad2*^{p2}), p1/p1 (*w*; Cid-EGFP, His2Av-mRFP, matα-GAL4/CyO; mad2*^{p1}*/mad2*^{p1}). Dot plots represent the durations, as well as the average (+/- s.d.) of the indicated periods during meiosis I (**A**) and meiosis II (**B**). Numbers in brackets indicate number of analyzed spermatocytes. For each average, these cells were from at least 7-8 different testes.

4. Kinetochore behavior during male meiosis

The Drosophila male meiotic divisions are dramatically shorter than those that have been previously characterized by careful time-resolved analyses. Twenty minutes appear to be sufficient for chromosome bi-orientation during meiosis I, as indicated by the analysis of the *mad2* mutants. In contrast, the corresponding process takes many hours in Drosophila oocytes (Gilliland et al., 2007; Theurkauf and Hawley, 1992) respectively, mammalian oocytes (Holubcova et al., 2015; Kitajima et al., 2011), and five hours in grasshopper spermatocytes (Nicklas, 1961; Nicklas and Ward, 1994). To elucidate the impressive efficiency of chromosome bi-orientation during the meiotic divisions in Drosophila males, the process was analyzed in detail.

4.1 Recruitment of kinetochore proteins during Drosophila male meiosis

Chromosome bi-orientation within spindles depends on a functional kinetochore. During mitosis the kinetochore is assembled at the start of M phase. To analyze kinetochore assembly during Drosophila male meiosis, time lapse imaging was performed with spermatocytes obtained from males with transgenes driving the expression of fully functional EGFP or tdTomato fusions to Cenp-A/Cid, Cenp-C, Knl1/Spc105, Mis12 or Nuf2 under control of the respective *cis* regulatory regions (Heeger et al., 2005; Schittenhelm et al., 2009; Schittenhelm et al., 2007; Schuh et al., 2007). Simultaneous imaging of His2Av-mRFP (Schuh et al., 2007) or GFP-ßTubulin56D (Inoue et al., 2004).was used as well. Thereby the dynamics of chromosome condensation, kinetochore assembly and spindle assembly could be compared.

4.1.1 Kinetochore foundation proteins and chromosomes

Cenp-A/Cid, a centromere-specific histone H3 variant, marks the centromere epigenetically. By time lapse imaging, centromeric Cenp-A/Cid-EGFP signals were detected continuously before, during and after the male meiotic divisions (Fig. 4A) confirming findings previously obtained with fixed preparations (Dunleavy et al., 2012; Raychaudhuri et al., 2012). As reported earlier, S5 spermatocytes usually displayed seven and occasionally eight Cid-EGFP dots. Based on shape and intensity of the associated His2Av-mRFP signals, the Cid-EGFP dots could be assigned to different chromosomes.

The large autosomes (chromosome 2 and chromosome 3) were associated with the most extended His2Av-mRFP territories. Each territory contained two Cid-EGFP dots. Each of these dots represents a pair of sister centromeres. These sister centromeres were so closely associated that they could not be resolved usually (see below).

The homologs of chromosome 4, which is far smaller than all other chromosomes, were usually next to the XY chromosome territory before NEBD I. Moreover, often only a single Cid-EGFP dot was present before NEBD I, indicating a tight association of all four sister centromeres of the two chromosome 4 homologs. The single Cid-EGFP dot was eventually converted into two Cid-EGFP dots, each representing the closely associated sister centromeres of one chromosome 4 homolog. The last conversions from single to two Cid-EGFP dots that were observed occurred at NEBD (as indicated by a rapid loss of diffuse nucleoplasmic His2Av-mRFP signals) in parallel with an accelerated condensation of territories into compact chromosomes. In case of chromosome 4, however, there was almost no associated His2Av-mRFP signal detectable even in the fully condensed state. During prometaphase and metaphase of meiosis I, therefore, the chromosome 4 bivalent was characterized by a pair of Cid-EGFP dots lacking associated His2Av-mRFP masses (Fig. 9A).

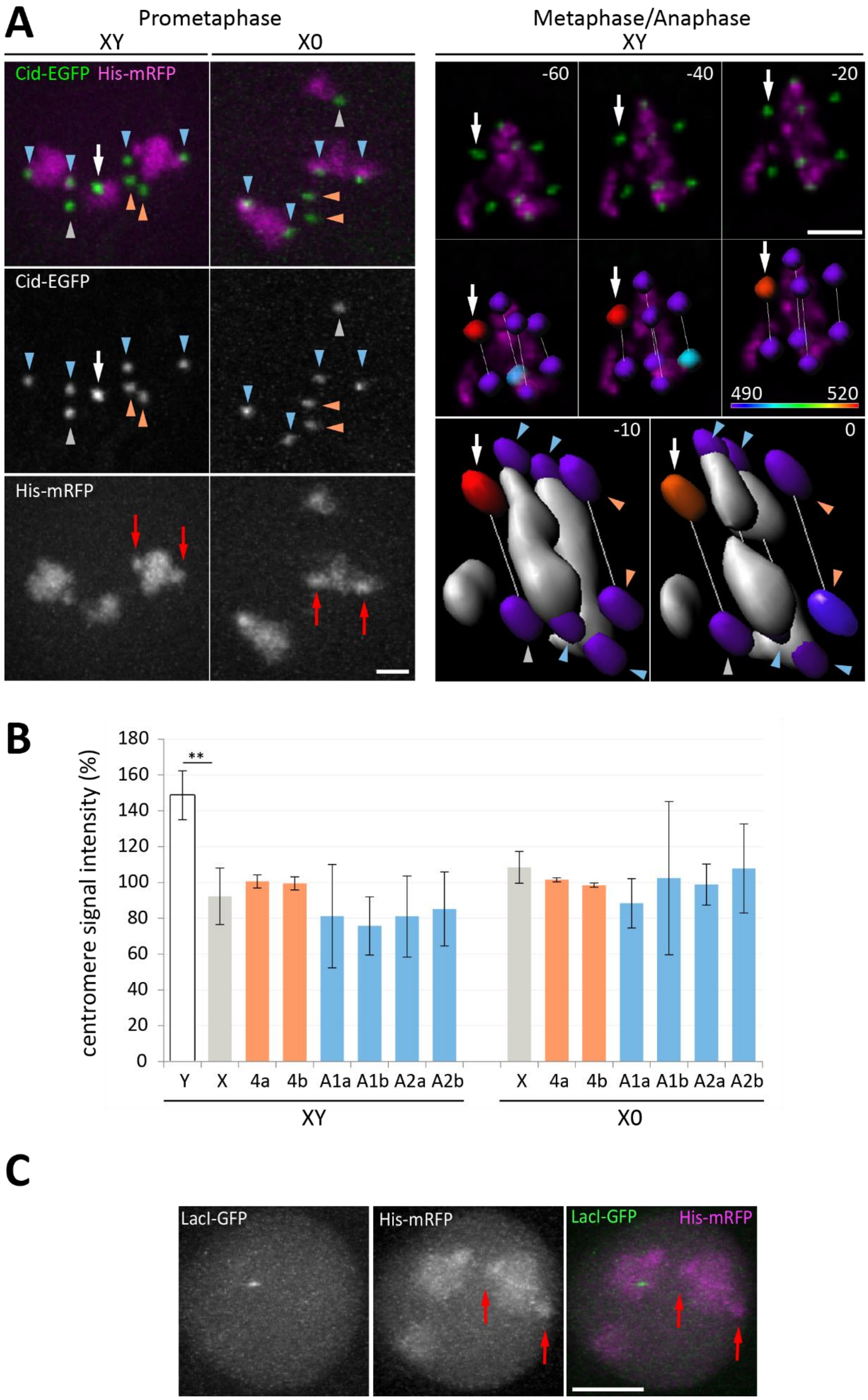
A
Prometaphase
XY
X0
Metaphase/Anaphase
XY
Cid-EGFP His-mRFP
Cid-EGFP
His-mRFP
-60
-40
-20
490
520
-10
0
B
centromere signal intensity (%)
180
160
140
120
100
80
60
40
20
0
**
Y
X
4a
4b
A1a
A1b
A2a
A2b
X
4a
4b
A1a
A1b
A2a
A2b
XY
X0
C
LacI-GFP
His-mRFP
LacI-GFP His-mRFP

Fig 9: Chromosome-specific patterns of His2Av-mRFP and Cid-EGFP fluorescence
To corroborate that the Cid-EGFP dot associated with the Y centromere is more intense than those at all the other centromeres, a comparison of XY with X0 spermatocytes by time lapse imaging was preformed with cells also expressing *Cid-EGFP* and *His2Av-mRFP*. (**A**) Selected still frames from prometaphase and during the metaphase-to-anaphase transition of meiosis I are shown, as indicated. The Y centromere is indicated by white arrows. Arrowheads indicate the centromeres of chromosome 2 and 3 (blue), chromosome 4 (orange) and chromosome X (grey). Red arrows indicate the centromere-proximal His2Av-mRNA-positive blobs characteristic of chromosome 2. The right panel illustrating the metaphase to anaphase transition in XY spermatocytes indicates that the Y centromere, which is characterized by the most intense Cid-EGFP dot, is associated with chromatin that has only very low levels of His2Av-mRFP. Time (sec) is indicated in the upper right corner; time point 0 is the first anaphase frame. Cid-EGFP intensities quantified after spot segmentation are color-coded in the middle and bottom rows. The amount of His2Av-mRFP associated with the different centromeres is visualized by the white isosurfaces in the bottom row. Scale bars = 2 µm. **B.** Bar diagram representing average intensity (+/- s.d.) of centromeric Cid-EGFP signals observed in XY spermatocytes (n = 4) and X0 spermatocytes (n = 3). While the centromeres associated with X, Y and 4th chromosomes were identified as described in the text, the more difficult identification of the two large autosomes (A1 and A2) as either chromosome 2 or 3 was not attempted in these analyses. In each cell, the average intensity of the chromosome 4 centromeres was set to 100%. The difference of Cid-EGFP intensity associated with the Y and X centromere, respectively, was highly significant ($p < 0.0017$, t test). **C.** Time lapse imaging with spermatocytes having a *lacO* repeat array on one of the two chromosome 2 homologs and expressing *GFP-lacI-nls* as well as *His2Av-mRFP* allowed the identification of the large autosome characterized by prominent centromere-proximal His2Av-mRFP blobs (red arrows) as chromosome 3. A still frame from early prometaphase is shown. Scale bar = 5 µm.

One of the two Cid-EGFP dots associated with the His2Av-mRFP mass of the XY bivalent was clearly more intense than the other (Fig. 9A). This brightest Cid-EGFP dot was previously identified as the Y centromere (Raychaudhuri et al., 2012), an interpretation challenged recently (Kwenda et al., 2016). Therefore, the chromosomal assignment of the brightest Cid-EGFP dot was re-evaluated. Tracking the brightest Cid-EGFP dot beyond the M/A I clearly confirmed its association with the XY bivalent, because this particular bivalent was characteristically resolved during anaphase I into two dramatically unequal His2Av-mRFP masses, in contrast to all the other autosomal bivalents which were separated symmetrically into two equivalent masses (Fig. 9A). One of the two distinct chromatin masses arising from the XY bivalent during anaphase I had only very little associated His2Av-mRFP but the brightest Cid-EGFP dot, whereas the other had a weaker Cid-EGFP dot followed by a centromere-proximal region with low levels of His2Av-mRFP and a distal region with high levels of His2Av-mRFP (Fig. 9A). Assuming the regions with low His2Av-mRFP levels to be heterochromatic, these observations are fully consistent with the interpretation that the Y centromere contains higher levels of Cenp-A/Cid than all the other chromosomes (Fig. 10A), as originally proposed (Raychaudhuri et al., 2012).

To corroborate this interpretation further, XO spermatocytes expressing Cid-EGFP and His2Av-mRFP were generated and analyzed by time lapse imaging. Consistent with earlier reports(Hardy et al., 1981; Lifschytz and Meyer, 1977) (Church, 1988; Hardy et al., 1981; Lifschytz and Meyer, 1977), XO spermatocytes frequently progressed through meiosis with severe abnormalities, precluding a reliable assignment of centromeres to chromosomes. It is well established that XO spermatocytes cannot generate pi-RNAs from the Y chromosomal *Su(Ste)* repeat locus and therefore express the X-chromosomal *Ste* repeats, resulting in protein aggregation and in defects during chromosome segregation and fertility (Malone et al., 2015). However, some XO spermatocytes were observed to progress quite normally through meiosis I, allowing an unequivocal identification of chromosomes and quantification of the associated centromeric Cid-EGFP signals (Fig. 9A). In these XO spermatocytes, the His2Av-mRFP mass associated with the X univalent had the characteristics predicted by the chromosome assignments proposed above (Fig. 9A and Fig. 10A). Moreover, Cid-EGFP signal intensity within the centromeric dot associated with this univalent X was comparable to those of the autosomal Cid-EGFP dots (Fig. 9B). Comparable intensity of centromeric Cid-EGFP signals in chromosome X and autosomes was also observed in XY spermatocytes (Fig. 9B). In contrast, the Y centromere in XY spermatocytes had significantly higher levels of Cid-EGFP (Fig. 9A, B). The recent discrepant conclusions presumably reflect experimental limitations of the chosen immuno-FISH approach (Kwenda et al., 2016) which might lead to some inappropriate centromere assignments. Quantification of immunofluorescent signals can suffer from accessibility and fixation problems in particular when combined with DNA FISH. Moreover, the AATAC probe hybridizes to a location that is not closely linked to the Y centromere, which however is often close to those of the X and fourth chromosome in spermatocytes. Tracking centromeres and chromosomes in live spermatocytes during meiosis I allows a far more reliable chromosome identification. Of note, as a consequence of the separation between the rDNA loci and centromeres on the X and Y chromosomes, the Y centromere is actually most of the time closer to the His2Av-mRFP mass of the centromere-proximal euchromatin of the X chromosome than the X centromere. Moreover, Cid-EGFP dot intensities strongly depend on position along the z-axis. At times where the Y centromere is far more distant from the coverslip than other centromere signals, its higher Cid-EGFP level is not necessarily apparent.

The His2Av-mRFP labelled chromatin masses representing the two major autosome bivalents formed by chromosome 2 and 3 were quite similar in appearance during prometaphase I. However, tracking these His2Av-mRFP masses over time revealed some characteristic differences, although not evident at each and every time point because of rapid morphological changes during meiotic chromosome movements. One of the large autosomal bivalents was characterized by prominent centromere-proximal blobs of high His2Av-mRFP intensity which were not seen in the other large autosomal bivalent, in particular in early prometaphase (Fig. 9A). Exploiting the lacO/lacI-GFP system (Vazquez et al., 2001) the large autosomal bivalent with these pericentromeric His2Av-mRFP blobs was identified as the one formed by chromosome 3 (Fig. 9C).

In conclusion, by time lapse imaging during meiosis I, an identification of the different bivalents (XY, 2, 3 and 4) based on the associated His2Av-mRFP signals is feasible. In case of XY and chromosome 4, this is straightforward, but distinction of the two large autosomes requires very careful tracking. As described further below, the identification of the different bivalents revealed some bivalent-specific aspects of bi-orientation.

Identification of individual chromosomes during meiosis II was more difficult compared to meiosis I. In meiosis II, His2Av-mRFP signals were spatially more convoluted and clustered, often precluding a simple reliable isolation of these signals into distinct chromosomes. However, analyses during prometaphase II before maximal spindle-mediated chromosome clustering revealed two classes of secondary spermatocytes (Fig. 10B). Half of these spermatocytes were in a first class, where three Cid-EGFP dots were associated with substantial His2Av-mRFP masses and a fourth Cid-EGFP dot was essentially free of associated His2Av-mRFP. The other half of the spermatocytes were in the second class, where only two Cid-EGFP dots had substantial His2Av-mRFP associated and the two other were essentially free. Moreover, one of these latter Cid-EGFP dots was usually more intense than all the others. These observations confirm that the Y chromosome and the fourth chromosome have only very low levels of His2Av-mRFP associated. Accordingly, the first and second class of secondary spermatocytes are those with X and Y chromosome, respectively.

Low levels of His2Av in the chromosomes 4 and Y, as well as in the centromere-proximal heterochromatin of the X have also been observed before in larval brain neurobasts (Rong, 2008). This pattern of His2Av depletion is not evident in analyses of polytene chromosomes of larval salivary glands (van Daal and Elgin, 1992) where these chromosomal regions are strongly underreplicated. Moreover, the apparent dramatic enrichment of His2Av in the heterochromatin of the X chromosome observed in ChIP-Seq analyses with embryos (Zhang and Pugh, 2011) presumably reflects the fact that this analysis was restricted to the mapped 1% of X chromosomal peripheral heterochromatin and hence ignoring the unmapped 99%.

Analysis of the His2Av-mRFP signals also revealed that chromosome appearance was evidently different in prometaphase I and II. The alternative homolog conjunction system of Drosophila male meiosis was suspected to contribute to the differential chromosome morphology during prometaphase I and II. The alternative homolog conjunction system keeps homologs associated until onset of anaphase I (McKee et al., 2012; Thomas et al., 2005; Tsai and McKee, 2011). It might also confer sister chromatid associations. Accordingly, the Separase-dependent inactivation of the alternative homolog conjunction system in late metaphase I (Blattner et al., 2016) might not only allow the separation of homologs during anaphase I, but might also release associations between sister chromatids within the arm regions (while the Ord/Sunn/Solo-mediated sister chromatid cohesion in the pericentromeric regions persists until late metaphase II; (Goldstein, 1980; Krishnan et al., 2014; Mason, 1976; Miyazaki and Orr-Weaver, 1992; Yan et al., 2010). To evaluate the possibility that the alternative homolog conjunction system contributes to associations between sister chromatids during early meiosis I, chromosome appearance during prometaphase I was compared between control and *mnm* mutant spermatocytes. As the alternative homolog conjunction system is inactive in *mnm* mutants, the resulting univalents might also lack associations between sister chromatid arms and hence display a more prometaphase II-like appearance already during prometaphase I. This was indeed the case. While the His2Av-mRFP domains during prometaphase I typically formed a rather uniform mass in case of bivalents in wild-type spermatocytes (Fig. 9A), they were clearly more differentiated in the univalents present in *mnm* mutant spermatocytes. This was most clearly apparent in case of the X chromosome. Since His2Av-mRFP levels are high in the centromere-distal euchromatic portions of the X chromosome and very low in its centromere-proximal heterochromatin as well as very low throughout the Y chromosome (Fig. 10A), the His2Av-mRFP labeling of the XY bivalent is more confined than in the large autosomal bivalents and hence more often clearly traceable. This made it plainly apparent that the X sister chromatids were closely associated along their entire length during prometaphase I in wild-type. In contrast, they were clearly resolved in *mnm* mutant spermatocytes (Fig. 10A). During prometaphase II, they were also resolved in wild-type (Fig. 10B), consistent with the results from analyses of testis squash preparations (Goldstein, 1980).

In conclusion, chromosome appearance is far more compact during normal prometaphase I than during prometaphase II, because the alternative homolog conjunction systems not only keeps homologs but apparently also sister chromatids in close association.

During interkinesis and prometaphase II, four Cid-EGFP dots were usually detectable in secondary spermatocytes (Fig. 4A). Until metaphase II, each Cid-EGFP dot was observed to split into a pair of dots, as analyzed in further detail below. During anaphase II, the pairs were separated apart to opposite spindle poles (Fig. 4A). After completion of meiosis II, each secondary spermatid usually had four Cid-EGFP dots with an intensity that was reduced to half of that observed during prometaphase I where the two sister centromeres were still united (Dunleavy et al., 2012; Raychaudhuri et al., 2012).

Beyond Cenp-A/Cid, Cenp-C is the only known additional constitutive centromere protein in *Drosophila melanogaster* which does not have genes coding for any of the other components of the constitutive centromere-associated network (CCAN) identified in species from yeast to humans (Heeger et al., 2005; Musacchio and Desai, 2017; Schittenhelm et al., 2007). To characterize expression and localization during Drosophila male meiosis, time lapse imaging was performed with testis isolated from males carrying a *tdTomato-CenpC* transgene (Althoff et al., 2012). These analyses indicated that expression and localization of Cenp-C during male meiosis is apparently identical to that of Cenp-A/Cid (data not shown; see below).

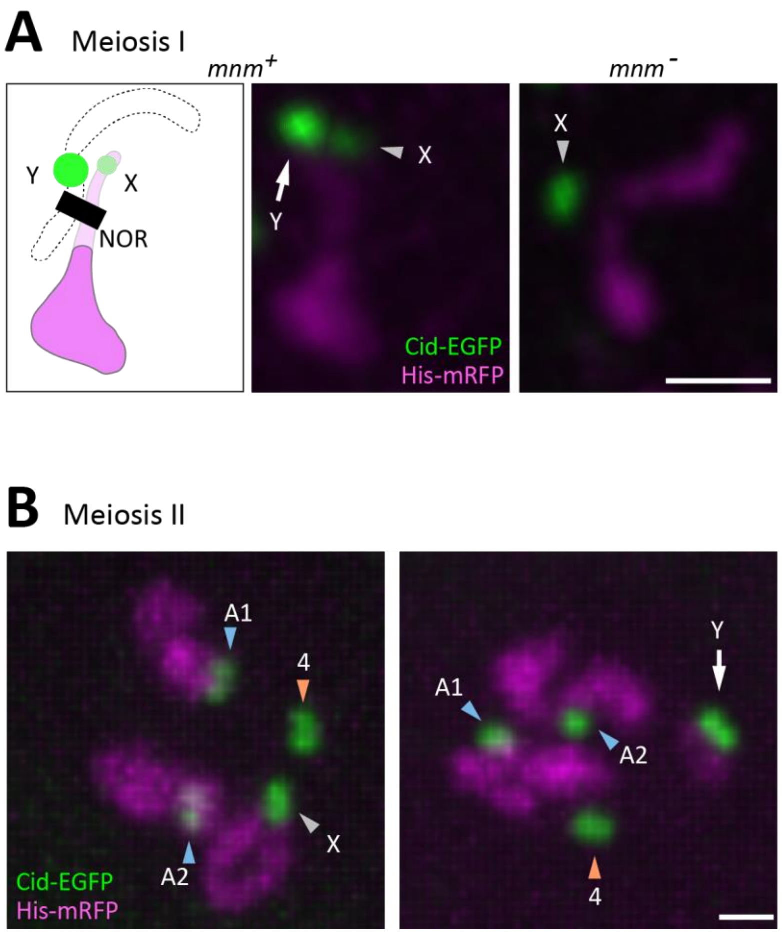

Fig 10: The alternative homolog conjunction system is responsible for sister chromatid association during meiosis I

Time lapse imaging with spermatocytes expressing *His2Av-mRFP* and *Cid-EGFP* was used for chromosome identification. **A.** Progression through meiosis I was analyzed in the presence (*mnm*$^{+}$) and absence (*mnm*$^{-}$) of the system responsible for homolog conjunction during male meiosis I. Conjunction of the X and Y chromosome is confined to the pairing sites located in their rDNA loci (black bar in cartoon). High magnification views from prometaphase illustrate the appearance of the XY bivalent (*mnm*$^{+}$) and the univalent X (*mnm*$^{-}$), respectively. As emphasized (cartoon), the Y chromosome contains only very low levels of His2Av-mRFP, and in the X chromosome His2Av-mRFP is primarily present in the centromere-distal arm region. While the two sister chromatids of the X chromosome are tightly associated when the alternative homolog conjunction is functional (*mnm*$^{+}$), they are completely separated in the arm region in the absence of homolog conjunction (*mnm*$^{-}$). **B.** During normal prometaphase II, the two sister chromatids of the X chromosome are also separated. Only 50% of the prometaphase II cells contain the X chromosome (left panel). The other 50% contain the Y chromosome (right panel). The centromeres are indicated as in Fig. 9: white arrow for Y, arrowheads for X (grey), chromosome 4 (orange) and large autosomes (blue). Scale bars = 1 µm.

4.1.2 The KMN network of kinetochore proteins

To assess the temporal dynamics of KMN recruitment to the centromere during the male meiotic divisions in Drosophila, time lapse analyses were performed with spermatocytes expressing Nuf2-EGFP, Spc105-EGFP or Mis12-EGFP in combination with His2Av-mRFP.

The Ndc80 complex component Nuf2-EGFP could not be detected in spermatocytes during G2 (Fig. 11A). Accumulation on kinetochores became detectable about 20 min before NEBD I (indicated by a rapid loss of diffuse nucleoplasmic His2Av-mRFP signals) (Fig. 11A,D). After a slow initial phase, Nuf2-EGFP accumulation occurred a few minutes after NEBD I rapidly reaching maximal levels about 10 min after NEBD I (Fig. 11D). In late telophase I, Nuf2-EGFP disappeared from kinetochores (Fig. 11A) and remained undetectable during interkinesis (Fig. 11F). The behavior during meiosis II was analogous to that in meiosis I (Fig. 11F).

The dynamics of Spc105-EGFP observed during meiosis I and II was highly similar to that of Nuf2-EGFP. Being undetectable in spermatocytes during G2 (Fig. 11B), kinetochore accumulation of Spc105-EGFP started about 10-12 min before NEBD I (Fig. 11D). The slow initial accumulation was also followed by rapid accumulation after NEBD I. After disappearance from kinetochores during MI exit, Spc105-EGFP was again detectable on kinetochores during MII (Fig. 11G).

The behavior of Mis12-EGFP was clearly distinct from that of Spc105-EGFP and Nuf2-EGFP. In contrast to these latter KMN components, Mis12-EGFP was clearly detectable on centromeres of spermatocytes throughout the long growth phase in G2 (Fig. 11C, and data not shown). The centromeric Mis12-EGFP levels observed during this phase were around 50% of the maximal levels detected later during MI. Towards the end of the G2 phase, however, centromeric Mis12-EGFP signals first decreased to a minimum observed about 30 min before NEBD I (Fig. 11C). Thereafter centromeric signals increased again, more rapidly after NEBD I, until they reached maximum levels early in prometaphase I (Fig. 11C,D). In contrast to the abrupt disappearance of Spc105-EGFP and Nuf2-EGFP from kinetochores during exit from meiosis I, Mis12-EGFP decreased only very slowly to a minimum where it was no longer detectable about 15 min before NEBD II (Fig. 11E, H). Thereafter, centromeric Mis12-EGFP signals again increased during the second meiotic division (Fig. 11H), disappeared in telophase II and were absent in spermatids.

Earlier analysis of early embryonic mitoses (Venkei et al., 2012) had revealed that Mis12 localization to the centromere during interphase and mitosis is mechanistically distinct. Similarly, in meiosis the requirements for centromeric Mis12 localization before and after NEBD I were found to be distinct, as revealed by RNAi experiments (Fig. 12). Spc105 depletion was achieved by *bamP-GAL4VP16* driven expression of *UASt-V20-Spc105*^{RNAi} in early spermatocytes. This resulted in almost complete male sterility. Comparable effects on fertility were obtained with several Spc105-RNAi transgenes targeting different regions. Moreover, cytological analyses with fixed samples, as well as time lapse imaging, revealed the specific defects expected from an inactivation of kinetochore function (see below). Spermatocyte-specific Spc105 depletion also abolished centromeric Mis12-EGFP localization during but not before the first meiotic division (Fig. 12). Finally, Spc105 knock down also abolished the recruitment of the SAC protein Bub3-EGFP to kinetochores (Fig. 12) and resulted in an accelerated completion of the meiotic divisions (Fig. 12), similar as in *mad2* mutants (Fig. 8), indicating that SAC function during the meiotic divisions depends on Spc105.

In summary, the dynamics of KMN network assembly on kinetochores during entry into meiosis I appear to be somewhat different from that described in early embryos. While accumulation of the Ndc80 complex was reported to occur only after NEBD in early embryos (Venkei et al., 2012), it started already before NEBD in case of meiosis I and II. Moreover, centromeric Mis12, which was detected throughout interphase during the early embryonic cycles (Venkei et al., 2012), was found to decrease strongly before meiosis I and even more dramatically before meiosis II. In both cases, however, the rate of KMN protein accumulation on kinetochores increased strongly after NEBD. While it is not excluded that the subtle differences in the dynamics of KMN components on centromeres during mitosis in early embryos and male meiosis might reflect distinct regulation, the relatively subtle differences could also be more apparent than real. It is conceivable that a relatively high background fluorescence in early embryos might result in a somewhat lower detection sensitivity compared to analyses with spermatocytes. Therefore, Ndc80 complex assembly might possibly start slightly ahead of NEBD also in early embryos. Moreover, as the meiotic divisions occur on a roughly tenfold slower time scale compared to early embryonic mitoses, the transition from the interphase to the M phase mode of Mis12 centromere localization might be less compressed and hence more evident in case of the meiotic divisions.

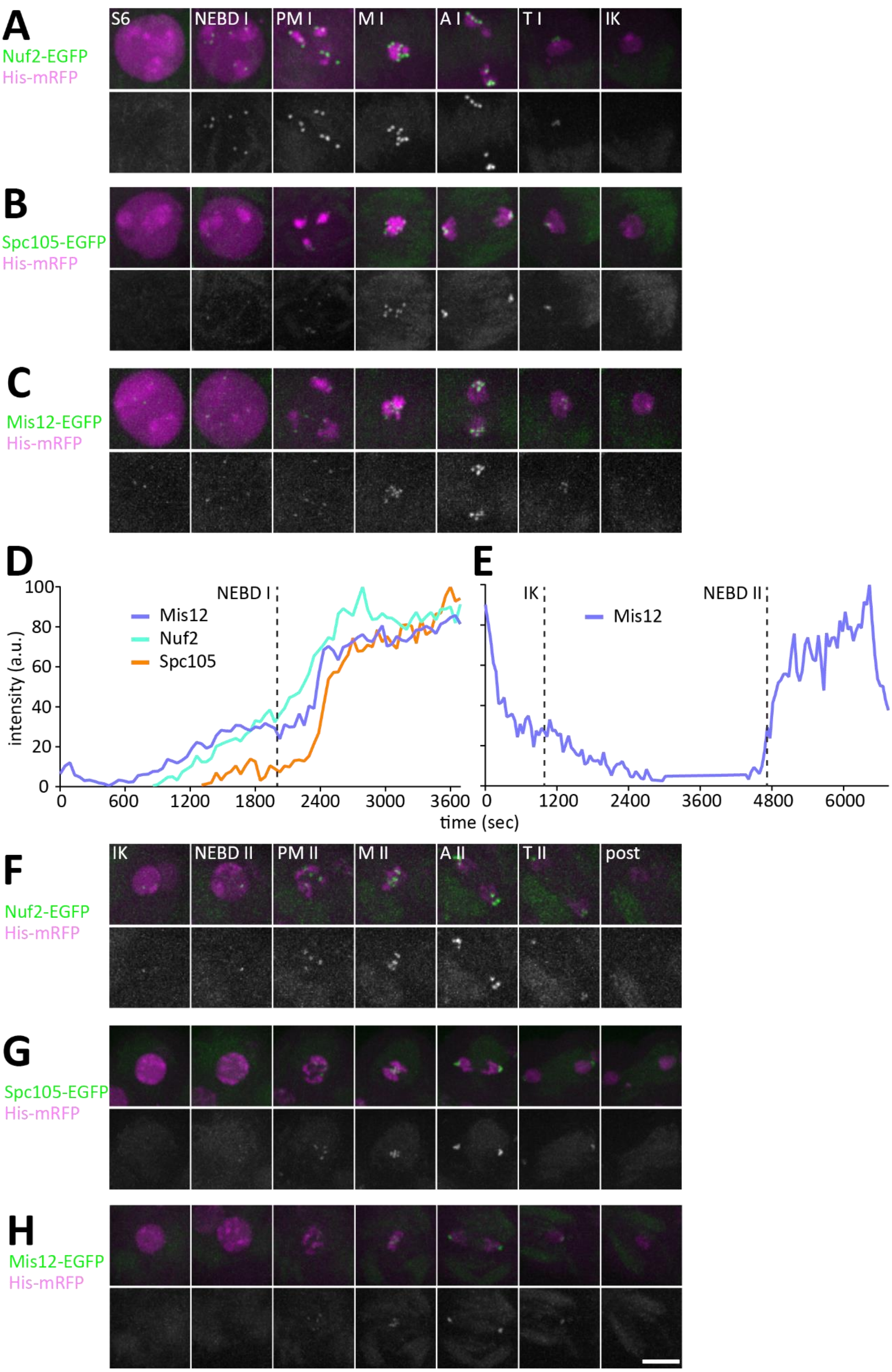
A
Nuf2-EGFP
His-mRFP
S6
NEBD I
PM I
M I
A I
T I
IK
B
Spc105-EGFP
His-mRFP
C
Mis12-EGFP
His-mRFP
D
intensity (a.u.)
100
80
60
40
20
0
NEBD I
Mis12
Nuf2
Spc105
0
600
1200
1800
2400
3000
3600
E
IK
NEBD II
Mis12
0
1200
2400
3600
4800
6000
time (sec)
F
Nuf2-EGFP
His-mRFP
IK
NEBD II
PM II
M II
A II
T II
post
G
Spc105-EGFP
His-mRFP
H
Mis12-EGFP
His-mRFP

Fig 11: Localization of KMN network components during meiosis

Time lapse imaging with spermatocytes was used to analyse the localization of KMN network proteins (Nuf2, Spc105 and Mis12) fused to EGFP. Spermatocytes also expressed *His2Av-mRFP* allowing the monitoring of progression through the meiotic divisions. Representative spermatocytes at the indicated stages during meiosis I and II are shown (S6, NEBD, PM: prometaphase, M: metaphase, A: anaphase, T: telophase, IK: early interkinesis, post: early post-meiosis II). **A,F.** Nuf2-EGFP (*w*; His2Av-mRFP; EGFP-Nuf2 III.1*). **B,G.** Spc105-EGFP (*w*; His2Av-mRFP/ Spc105-EGFP II.1*). **C,H.** Mis12-EGFP (*w*; His2Av-mRFP/ Mis12-EGFP II.2*). **D.** EGFP signal intensities at kinetochores from representative cells during entry into MI. Maximal intensity was set to 100 arbitrary units (a.u.). NEBD was used for curve alignment. **E.** While EGFP-Nuf2 and Spc105-EGFP disappeared abruptly from kinetochores during telophase I and remained undetectable during interkinesis, Mis12-EGFP disappearance progressed slowly through much of interkinesis as illustrated by the curve representing EGFP intensities at the kinetochore. Scale bar = 5 µm

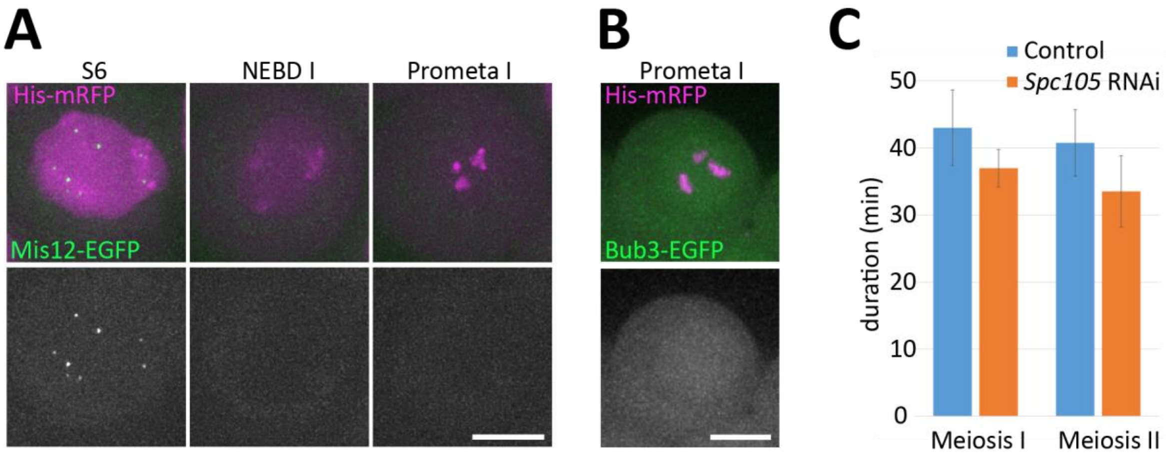

Fig 12: Effects of Spc105 depletion on Mis12 and Bub3 kinetochore localization, as well as on temporal dynamics of progression through meiosis.

Spc105 was depleted in spermatocytes (*bamP-GAL4VP16/ UASt-Spc105*^{RNAi}) and the consequences were analyzed by time lapse imaging using spermatocytes expressing *His2Av-mRFP* as well as *Mis12-EGFP* (**A**) or *Bub3-EGFP* (**B**). Scale bars = 10 µm. **C.** Quantification of the duration of MI and MII revealed that both divisions were accelerated after Spc105 knockdown. Bar diagram indicates average duration (+/- s.d., n = 36 spermatocytes from 12 different cysts for control during MI and 27 spermatocytes from 9 cysts during M II, n = 17 spermatocytes from 7 cysts for Spc105 depletion during MI and 10 spermatocytes from 6 cysts during MII. The acceleration resulting from Spc105 depletion during MI and MII was found to be highly significant (p = 0.004 in case of MI and 0.007 in case of MII, t test).

4.1.3 Spindle formation

Beyond kinetochore assembly, spindle formation is also required for chromosome segregation during the meiotic divisions. Spermatocytes expressing GFP-ßTub56D or GFP-αTub84B under control of the ubiquitin promoter have been used in several studies describing meiosis I spindle dynamics by time lapse imaging (Gao et al., 2008; Inoue et al., 2004; Rebollo et al., 2004; Savoian, 2015; Savoian and Glover, 2014). However, comparable analyses during meiosis II have not yet been published. Therefore, to compare spindle formation during meiosis I and II, GFP-ßTub56D was used for live imaging. Moreover, simultaneous imaging of His2Av-mRFP was performed to obtain a reference for comparison of assembly dynamics of spindle and kinetochore.

As reported earlier (Rebollo et al., 2004; Savoian and Glover, 2014), centrosomes were observed to migrate from the cell periphery to the nuclear envelope during S6 (Fig. 13A). At NEBD I, as indicated by a rapid loss of diffuse nucleoplasmic His2Av-mRFP signals, the two centrosomes were on opposite sides of the nuclear envelope associated with pronounced microtubule asters (Fig. 13A). NEBD I in spermatocytes is known to be incomplete. During prometaphase I, the nuclear envelope becomes fenestrated in the polar region, while it remains intact in the lateral regions fortified with several layers of closely associated endoplasmic reticulum (Tates, 1971). Interestingly, for several minutes after the onset of rapid decrease of diffuse nucleoplasmic His2Av-mRFP signals, microtubules remained excluded from the nuclear region. Thereafter, microtubule polymerisation was detected within the nucleus (7.5 min. after NEBD) most prominently from two foci close to the cytoplasmic centrosomes which resulted in the formation of an inner nuclear spindle (Fig. 13A). In agreement with earlier reports (Rebollo et al., 2004; Savoian and Glover, 2014), this initial microtubule formation within the spermatocyte nuclear region did not occur in close association with chromatin in stark contrast to female meiosis (Bennabi et al., 2016; Radford et al., 2017). Concomitant with intranuclear MT formation, astral MTs started to penetrate into the nuclear region. Subsequent concerted bundling of the outer centrosomal spindle MTs and the inner nuclear spindle MTs resulted in a more precise co-orientation of the two spindles (Fig. 13A). During metaphase, bundles of KT-MTs as well as interpolar MTs became increasingly stronger (Fig. 13A). Completion of meiosis I was accompanied by the changes in spindle organization (Fig. 13A) described earlier (Gao et al., 2008; Inoue et al., 2004).

The single centrosome delivered into each daughter cell generated during meiosis I needs to split so that a regular bipolar spindle is assembled during meiosis II. Centrosome splitting was observed already during late telophase I (Fig. 13A). Time lapse movies made with spermatocytes expressing the centriole marker mRFP-Spd2 (Novak et al., 2014) in combination with Cid-EGFP also disclosed the accompanying centriole separation (Fig 13B). After splitting, the resulting pair of centrosomes remained in close proximity during the first few minutes of interkinesis. Thereafter, centrosome separation started. Using the axis connecting two daughter nuclei as a reference indicated that both centrosomes migrated apart from each other along the nuclear envelope reaching positions on opposite sides in mid interkinesis (Fig. 13A). Therefore, the axis of the meiosis II spindle was preferentially perpendicular to that of meiosis I.

At the start of the second meiotic divisions, prominent cytoplasmic MT asters were again formed. Overall, subsequent dynamics of spindle formation during meiosis II was very similar to that of meiosis I (Fig. 13A). NEBD, as indicated by a rapid loss of diffuse nucleoplasmic His2Av-mRFP signals, was again followed by a period of several minutes, during which MTs were still excluded from the nucleus. However, in comparison with meiosis I, the appearance of MTs within the nuclear region was not accompanied by an immediate formation of inner spindle poles, suggesting that MT bundling activities might be weaker at the start of meiosis II. Inner spindle poles slowly became more prominent and were obvious by metaphase.

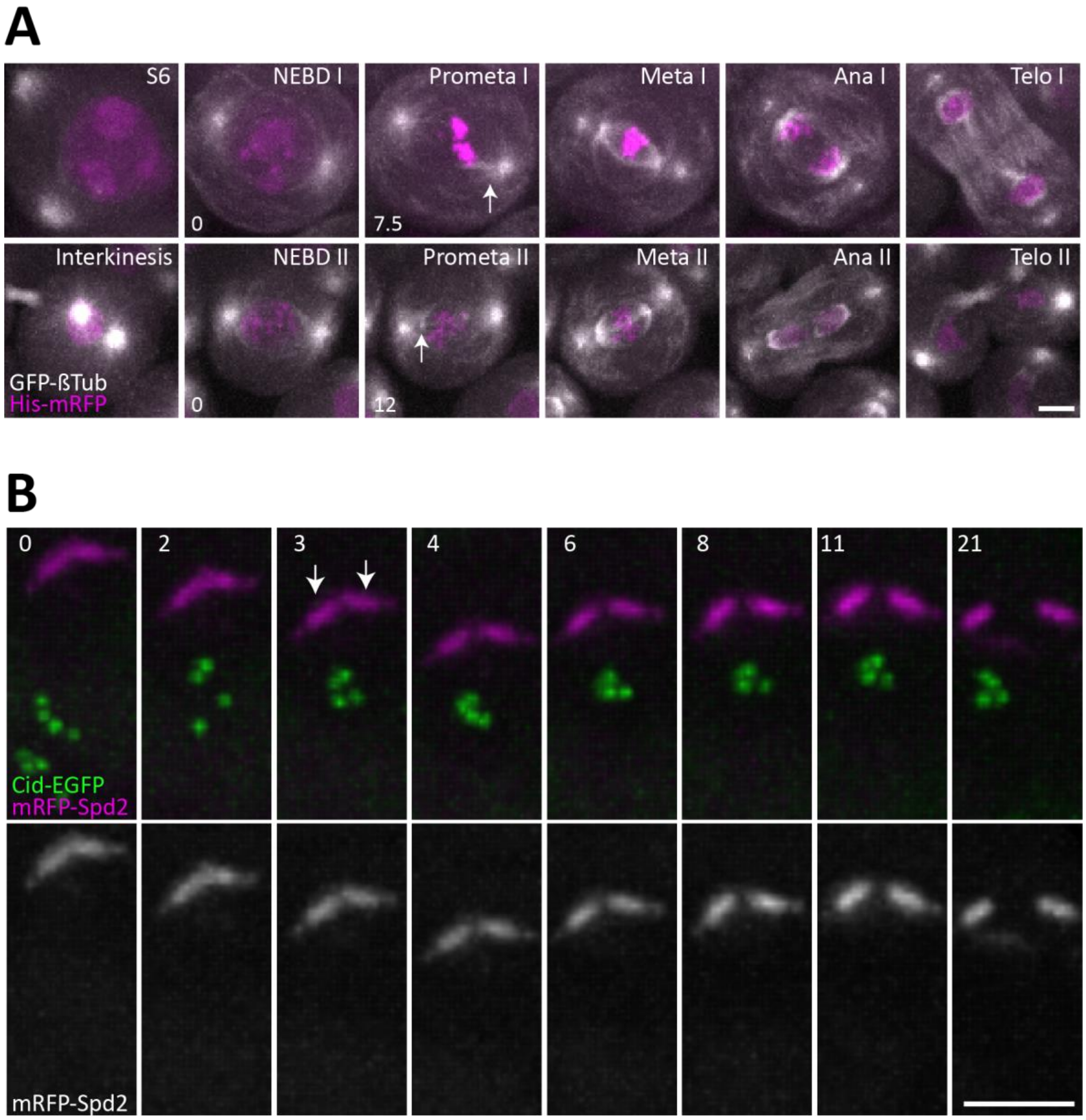

Fig 13: Spindle assembly and centrosome separation during meiosis

A. To monitor spindle assembly during meiosis I and II, time lapse imaging was done with spermatocytes expressing *His2Av-mRFP* and *GFP-ßTub56D* (*w*; UbiP-GFP-ßTub56D, His2Av-mRFP/CyO*). Stills from a representative spermatocyte at the indicated stages are shown. At the onset of both divisions, an astral cytoplasmic outer spindle is first formed. Appearance of microtubules in the nuclear region and formation of an inner spindle (white arrows) is delayed. The time of inner spindle pole formation (min) after NEBD onset is indicated in the lower left corner of the prometaphase panels. **B.** Separation of centrioles after meiosis I was analyzed by time lapse imaging using spermatocytes expressing mRFP-Spd2 and Cid-EGFP *(w*; Cid-EGFP II.1, UbiP-mRFP-Spd2 II)*. Time (min) is indicated in the lower left corner; time point 0 was set at onset of anaphase I. Centriole splitting becomes detectable in late anaphase I. Centrioles start to migrate apart and reach their final position (not shown) about 30 minutes before entry into meiosis II. Scale bars = 5 µm.

4.2. Meiosis-specific regulation of kinetochore behavior

The success of meiosis is critically dependent on differential regulation of sister kinetochore behavior during the first and the second meiotic division. Sister kinetochores are mono-oriented during meiosis I and bi-oriented during meiosis II. EM analyses have revealed that the two sister kinetochores cannot be resolved in Drosophila spermatocytes at the start of the first meiotic division (Church and Lin, 1982; Goldstein, 1981) (Fig. 14A). At this stage, a single kinetochore in form of a hemispherical structure (HS) is present on each chromosome (Fig. 14A). Later during meiosis I, chromosomes with two spatially separate kinetochores were observed. These two kinetochores, presumably sister kinetochores, have the shape of a flat disc and are arranged side-by-side (SS) on one face of the chromosome (Fig 14A). Although this SS configuration was seen in cells classified to be in metaphase I (Church and Lin, 1982; Goldstein, 1981), it is conceivable that these SS cases were from very late metaphase cells. Hence it remains a possibility that the HS->SS transformation might actually occur downstream of APC/C activation. According to unpublished EM data mentioned in Church and Lin (1988), the side-by-side arrangement “is converted to a back-to-back arrangement as dyads enter the second meiotic division.” Publications clearly documenting such a transition and when it occurs do not exist apparently. A back-to-back (BB) configuration (Fig. 14A), however, can be expected to be present at the latest when metaphase II has been reached. If BB kinetochore configuration was indeed already present at entry into the second meiotic division, as stated by Church and Lin (1988), it would likely contribute considerably to the efficiency of bi-orientation, as it favors the correct amphitelic over syntelic attachments for geometric reasons. However, analysis with grasshopper spermatocytes (Paliulis and Nicklas, 2005) have suggested that sister kinetochores are still in a SS configuration at NEBD II, and that the BB configuration is reached only as a consequence of bi-orientation. By performing time lapse imaging using various fluorescent centromere and kinetochore marker proteins as well as STED, it was assessed whether light microscopy allows scoring of the HS, SS and BB sister kinetochore configurations and the corresponding transitions in Drosophila male meiosis.

4.2.1 Coupling of sister kinetochores before and during entry into meiosis I

To evaluate whether Spc105 is also required for the coupling of sister centromeres during male meiosis, it was depleted in spermatocytes expressing Cid-EGFP and His2Av-mRFP. Entry into and progression through the male meiotic divisions was analyzed by time lapse imaging. No abnormalities were detected in Spc105 depleted spermatocytes before NEBD I. However, after NEBD I severe defects were readily apparent. In control spermatocytes, as described in detail below, many bivalents displayed phases of rapid and poleward directed movements that were led by a kinetochore, indicating interactions between spindle microtubules and kinetochores. Moreover, all bivalents in control spermatocytes reached bi-orientation within the spindle later in prometaphase I with end-on attached kinetochores and maintained stable bi-orientation throughout metaphase I, followed by homolog segregation during anaphase I. In contrast, after Spc105 depletion, bivalent movements were strongly reduced and never led by kinetochores (see below), indicating that Spc105 depletion results in complete inactivation of kinetochore function.

After Spc105 depletion, spermatocytes displayed the normal number of seven to maximally eight Cid-EGFP dots before the onset of the meiotic divisions. Moreover, in striking contrast to the observations in oocytes (Radford et al., 2015), Spc105 depletion did also not result in an increase in the number of Cid-EGFP dots in prometaphase (Fig. 14B; n= 18 spermatocytes).

The apparent differential Spc105 requirement for sister centromere linkage during female and male meiosis I, respectively, might be explained by the alternative homolog conjunction system that is specifically active in males. This system might provide additional linkage between sister centromeres, making the contribution of Spc105 functionally redundant. To evaluate this notion, Spc105 was depleted in *mnm* mutant spermatocytes expressing Cid-EGFP and His2Av-mRFP. However, even in these spermatocytes there was no increase in the number of Cid-EGFP dots before and during meiosis I (Fig. 14B; n = 18 spermatocytes). These observations indicate that Spc105 is not required for linkage of sister kinetochores during meiosis I in Drosophila males.

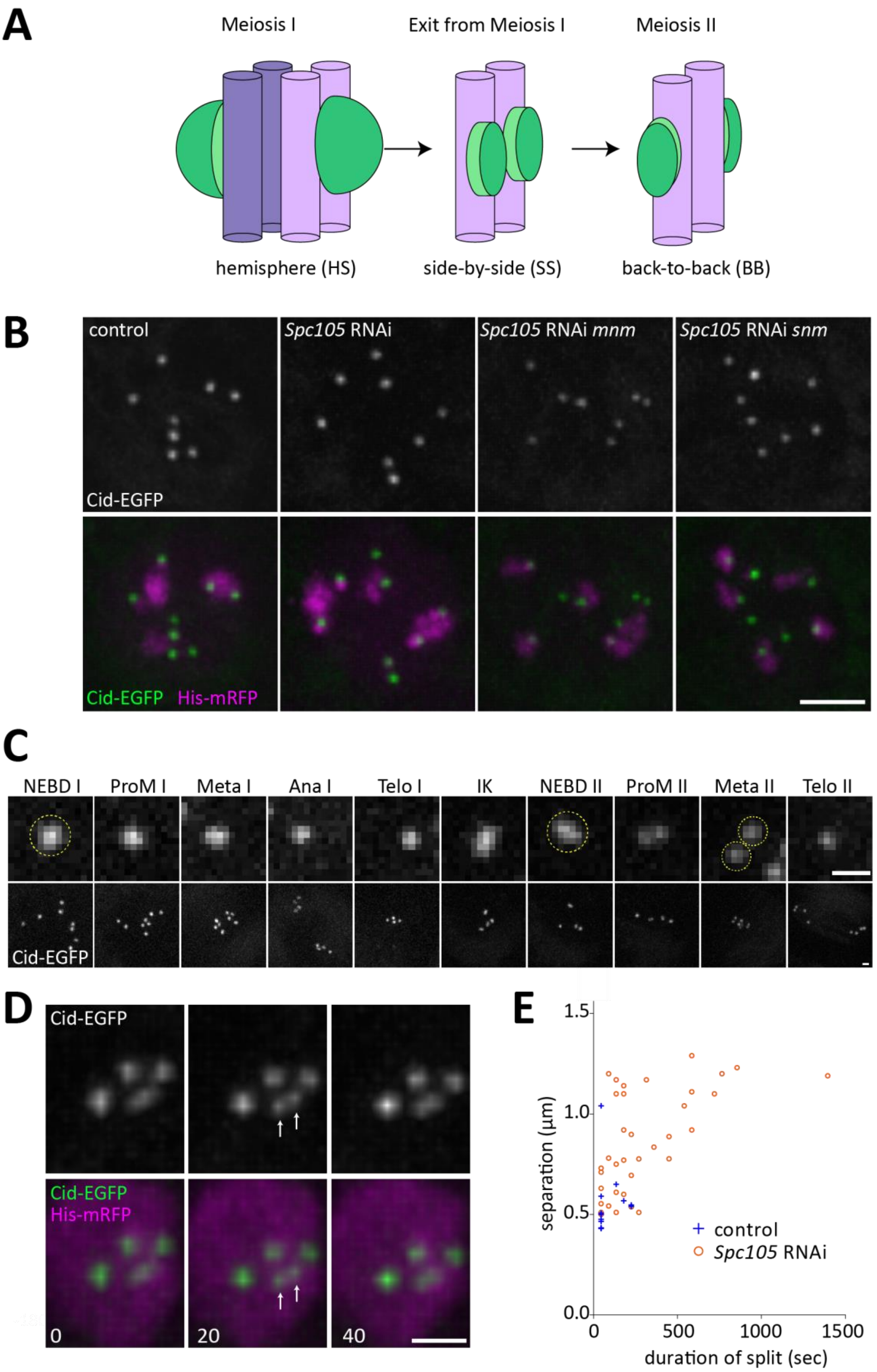
A
Meiosis I
Exit from Meiosis I
Meiosis II
hemisphere (HS)
side-by-side (SS)
back-to-back (BB)
B
control
Spc105 RNAi
Spc105 RNAi *mnm*
Spc105 RNAi *snm*
Cid-EGFP
Cid-EGFP His-mRFP
C
NEBD I
ProM I
Meta I
Ana I
Telo I
IK
NEBD II
ProM II
Meta II
Telo II
Cid-EGFP
D
Cid-EGFP
Cid-EGFP
His-mRFP
0
20
40
E
1.5
1.0
0.5
0.0
separation (µm)
0
500
1000
1500
duration of split (sec)
+ control
○ *Spc105* RNAi

Fig 14: Coupling and release of sister centromeres before MI and MII, respectively.
A. Schematic illustration of sister kinetochore organization during male meiosis. By EM (Goldstein, 1981) a single hemispherical structure (HS), in which the two sister kinetochores could not be differentiated, was observed at the start of MI. Progression through MI was shown to be accompanied by a transition from an HS to an SS organization, where two closely associated disc-like sister kinetochores were distinguishable. Eventually, the SS organization is converted into a BB organization where the two sister kinetochores are arranged back to back with the inner centromere regions in between. The molecular basis and exact time point of the HS->SS and the SS->BB transitions are not known. **B.** Time lapse analyses after Spc105 depletion and in mutants revealed that sister centromere coupling at the start of MI does not depend on the function of Spc105 and the alternative homolog conjunction system. Spermatocytes expressing *His2Av-mRFP* and *Cid-EGFP* were isolated from flies with the indicated genotypes: control (*w*; Cid-EGFP, His2Av-mRFP; bamP-GAL4VP16*), Spc105 RNAi (*w*; Cid-EGFP, His2Av-mRFP; UASt-V20-Spc105^{RNAi}/bamP-GAL4VP16*), Spc105 RNAi *mnm* (*w*; Cid-EGFP, His2Av-mRFP; UASt-V20-Spc105^{RNAi} mnm^{5578}/mnm^{3298}, bamP-GAL4VP16*), Spc105 RNAi *snm* (*w*; Cid-EGFP, His2Av-mRFP; UASt-V20-Spc105^{RNAi} snm^{2138}/snm^{0317}, bamP-GAL4VP16*). Still frame from representative spermatocytes early in prometaphase I reveal the normal number of eight Cid-EGFP dots in all three genotypes. Scale bar = 5 µm. **C.** Time lapse imaging with spermatocytes expressing His2Av-mRFP (not shown) and Cid-EGFP was performed to monitor sister centromere organization during progression though meiosis. Large yellow circles indicate that sister centromere appearance is not significantly different at NEBD I and NEBD II. Even at NEBD II, the two sister centromeres are not clearly resolved. However, at metaphase II the two sister centromeres are clearly resolved (small yellow circles). Scale bars = 1 µm. **D.** Although sister centromeres remain closely associated until metaphase II, occasional transient breathing was detected by time lapse imaging. Selected stills illustrate a transient splitting event (indicated by white arrows) during interkinesis. Scale bar = 2 µm. **E.** Scatter plot representing the separation width and duration of the transient splitting events observed during interkinesis in the indicated genotypes. All events observed after tracking 92 Cid-EGFP dots in controls and 150 after Spc105 knockdown.

4.2.2 Individualization of sister kinetochores before meiosis II

While the molecular mechanisms that couple sister centromeres during meiosis I remain unclear, it is crucial that this coupling is eliminated in a timely manner so that sister centromeres can be bi-oriented during the second meiotic division. Based on analyses by electron microscopy (Goldstein, 1981), the individualization of sister centromeres starts already during meiosis I. While the two sister kinetochore initially form a hemispherical structure (HS) during prometaphase I, in which they cannot be resolved, they become re-arranged during meiosis I into a double disc structure, where the two sister kinetochores are located side-by-side (SS) on chromatin spaced by a gap of a few nanometers only (Goldstein, 1981) (Fig. 14A).

To analyze the re-organization of sister kinetochores during progression through the meiotic divisions in Drosophila males, the Cid-EGFP signals acquired by time lapse imaging with spermatocytes were analyzed carefully. As predicted by the EM studies (Church and Lin, 1982; Goldstein, 1981), the sister KTs could not be resolved before NEBD I (Fig. 14C) except for transient splitting events (see below). Apart from such transient splitting events, single Cid-EGFP dots representing tightly paired sister centromeres were also present throughout meiosis I (Fig. 14C). The conversion from HS -> SS organization revealed by electron microscopy (Church and Lin, 1982; Goldstein, 1981) was therefore not detectable with spinning disk confocal fluorescence microscopy of Cid-EGFP. As the separation between sister kinetochores revealed by electron microscopy during exit from meiosis I is in the range of a few nanometers only (Church and Lin, 1982; Goldstein, 1981), light microscopic resolution of sister kinetochores in the SS configuration is actually not expected.

By analyzing also the subsequent progression through interkinesis and meiosis II, we evaluated carefully whether fluorescence microscopy might reveal an SS -> BB transition. However, no persistent change in sister centromere organization was apparent during interkinesis (Fig. 14C). Intriguingly, though, the time lapse analyses clearly revealed occasional transient splitting of a Cid-EGFP dot into two (Fig. 14D). Careful inspection of other meiotic phases demonstrated that such splitting events were not unique to interkinesis. Analogous occasional splitting events were detected throughout meiosis I, interkinesis and prometaphase II. These splitting events did not appear to involve exclusively the sister centromere pair of a particular chromosome within a cell. There was no obvious difference in the frequency of splitting events between various stages of meiosis and thus their occurrence appeared to be stochastic. Frequency, duration and maximal separation distance of these splitting events could be analyzed most readily during interkinesis (Fig. 14E). Twenty three secondary spermatocytes each having four sister kinetochore pairs were tracked throughout interkinesis which lasts close to an hour (Fig. 4C). A total of 13 splitting events were observed, i.e. about 0.17 events per sister centromere pair per hour. While a clear separation into two distinct maxima was only apparent during a few frames usually (i.e., for about 20-40 sec), a minority lasted longer (up to 3 min) (Fig. 14E). The maximal spatial separation between the two fluorescence maxima was around 550 nm (Fig. 14E). As the microscopic resolution along the z axis is clearly below this distance, the actual frequency of sister centromere breathing is presumably somewhat higher.

Interestingly, analyses of sister centromere breathing during interkinesis after Spc105 depletion, revealed an increased frequency of splitting events (0.3 per sister centromere pair and hour, n = 150 pairs tracked throughout interkinesis), as well as increased durations and maximal separation distances (Fig. 14E). Since Spc105 is not detectable at the centromere during interkinesis (Fig. 11G), the observed increase in sister centromere breathing during interkinesis after Spc105 depletion is presumably an indirect consequence from its absence during the preceding meiosis I. By an analysis of splitting events during exit from meiosis I (anaphase I and telophase I), we addressed whether Spc105 depletion might have even more obvious effects on sister centromere coupling during the stages where it is normally present. However, the difference in the frequency of splitting events between spermatocytes with and without Spc105 depletion was not greater than during interkinesis. In controls, 28% of a total of 112 sister centromere pairs displayed a splitting event during exit from meiosis I. After Spc105 depletion, 58% of the sister centromere pairs revealed a split (n = 128). Moreover, the fraction of transiently splitting sister centromere pairs was not increased when Spc105 was depleted in *mnm* mutant spermatocytes (50%, n = 224).

In conclusion, progression through meiosis I and interkinesis as well as entry into meiosis II was not accompanied by persistent separation of sister centromeres to an extent detectable by analysis of Cid-EGFP by spinning disk confocal microscopy. However, time lapse imaging clearly revealed occasional transient splitting events throughout this period. Therefore, even at the start of meiosis I, sister centromere linkage appears to be dynamic rather than totally rigid and stable. Moreover, although Spc105 depletion before female meiosis has far more drastic effects on sister centromere linkage (Radford et al., 2015), our observation in spermatocytes support the notion that Spc105 somehow contributes to this dynamic coupling. It might assist in the recruitment or protection of hypothetical dynamic sister centromere linkers. In Spc105 depleted spermatocytes, fewer linkers might be present, permitting more extensive sister centromere breathing.

To evaluate whether a transformation of sister centromeres from an SS into a BB configuration might be detectable early during meiosis II, we analyzed the shape and appearance of the Cid-EGFP signals in more detail. At NEBD II sister centromere pairs were still represented by a single Cid-EGFP dot in the great majority of cases and time points. However, the Cid EGFP dots were often elliptic rather than perfectly circular within the microscopic x-y plane. Assuming that such elliptic signals might represent a superimposition of two circular sister centromere signals, the extent of the spatial sister centromere separation was estimated by measuring the distance between the two assumed circle centers. The resulting distance should be an approximate estimate of the upper bound of sister centromere separation. It is certainly not an accurate estimate of this upper bound, as discussed in more detail in materials and methods (orientation of the interkinetochore axis is probably random at NEBD II. When it is along the optical z axis, the distance measurement is performed as if it was within the x-y plane, causing an underestimation). Nevertheless, a statistical comparison of analogous measurements at different time points during meiosis II should reveal even relatively small changes in the average sister centromere separation. The measurements were done at selected time points during entry into meiosis II (Fig. 15). A first time point was selected at NEBD. The next time point was chosen to be 5 min after NEBD II, i.e., just before interactions between kinetochores on spindle microtubules set in (see below). Additional time points were chosen 12 and 18 min after NEBD II, respectively. At 12 min after NEBD II, about 50% of the chromosomes have usually reached bi-orientation, and the last chromosome has normally reached bi-orientation before 18 min after NEBD II (see below). While the estimated maximal separation between sister centromeres did not increase within the first 5 min after NEBD II, it was significantly increased at 12 min and even more at 18 min after NEBD II (Fig. 15). At these later time points, the separation was often so extensive that two distinct Cid-EGFP maxima were clearly resolved. Therefore, the inter sister centromere separation measured at 18 min (720 nm) represents more accurately the actual distance between the sister centromere centers of bi-oriented chromosomes in meiosis II than the estimates at the earlier time points.

The increase in sister centromere separation that was observed during entry into meiosis II appeared to be concomitant with chromosome bi-orientation, suggesting that it might be dependent on pulling forces mediated by kinetochore microtubules. To address the role of microtubules, time lapse analyses were repeated after addition of colcemid (Fig. 15). These analyses confirmed that normal separation of sister centromeres depends on microtubules. In the presence of colcemid, separation barely increased within 18 min after NEBD II (Fig. 15).

To address the role of kinetochores, sister centromere separation was also analyzed after Spc105 depletion in spermatocytes (Fig. 15). Similar as in the presence of colcemid, separation was no longer detected after kinetochore inactivation within 12 min after NEBD II. As Spc105 depletion also eliminates the SAC, a premature exit from meiosis II occurred in some of the secondary spermatocytes already before 18 min after NEBD II, causing extensive sister centromere separation (Fig. 15) by chromosome decondensation in combination with squeezing forces exerted by the cytokinetic contractile furrow.

Fig 15: Sister centromere separation in meiosis II
After time lapse imaging with spermatocytes expressing *His2Av-mRFP* and *Cid-EGFP*, the inter sister centromere distance was determined at the indicated time points (min after onset of NEBD II). The dot plot represents individual measurements as well as average (+/- s.d.) obtained for the indicated conditions: control (*w*; Cid-EGFP, His2Av-mRFP; bamP-GAL4VP16*), n = 24 sister centromere pairs from more than three different cysts; colcemid (same genotype as control in the presence of colcemid), n = 16 from > 3; Spc105 RNAi (*w*; Cid-EGFP, His2Av-mRFP; UASt-V20-Spc105*^{RNAi}*/bamP-GAL4VP16*), n = 46 from > 6. As indicated (**), the average sister centromere separation observed after 18 min the presence of colcemid was highly significant (p = 0.0026, t test).

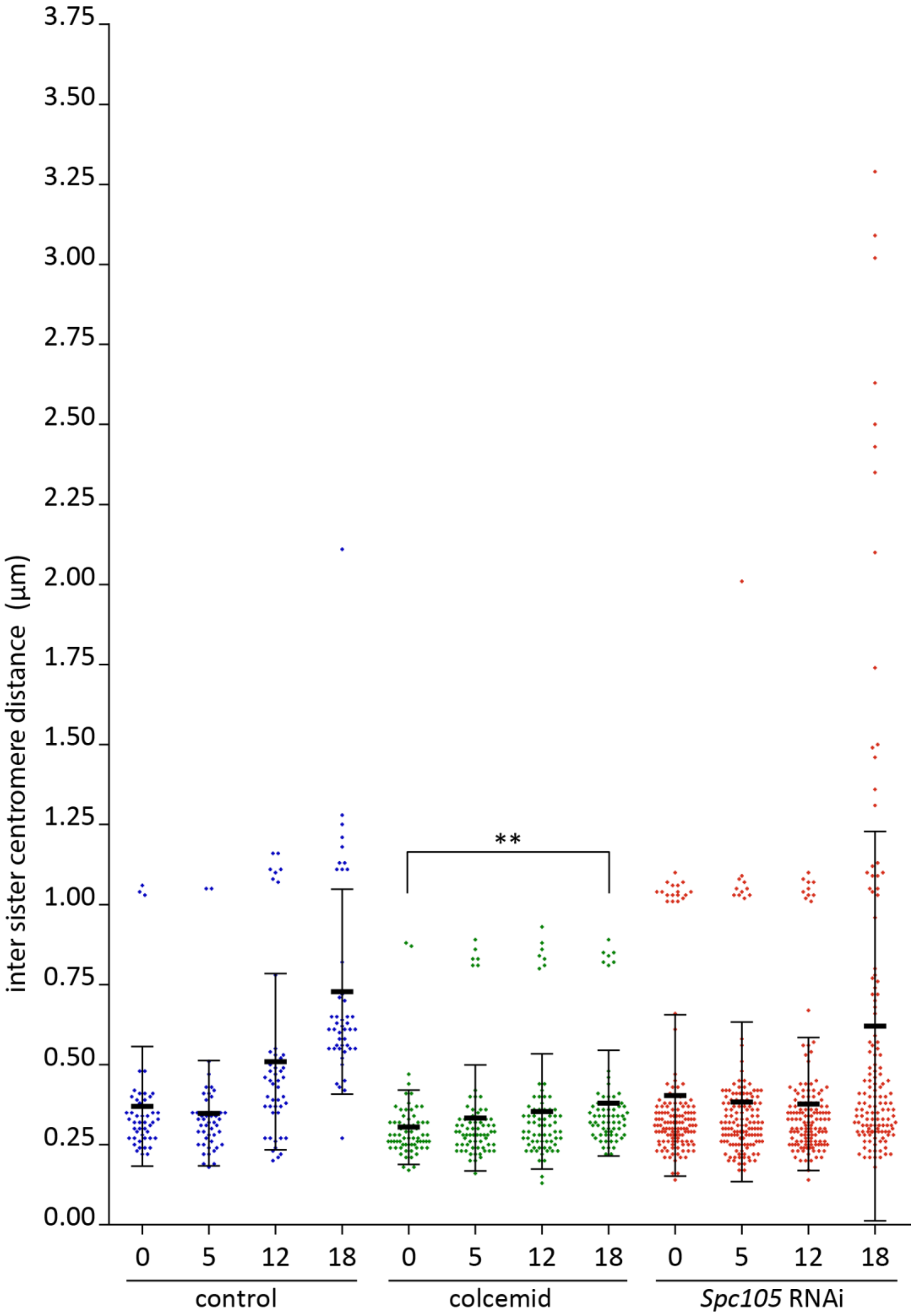
3.75
3.50
3.25
3.00
2.75
2.50
2.25
2.00
1.75
1.50
1.25
1.00
0.75
0.50
0.25
0.00
inter sister centromere distance (µm)
**
0
5
12
18
0
5
12
18
0
5
12
18
control
colcemid
Spc105 RNAi

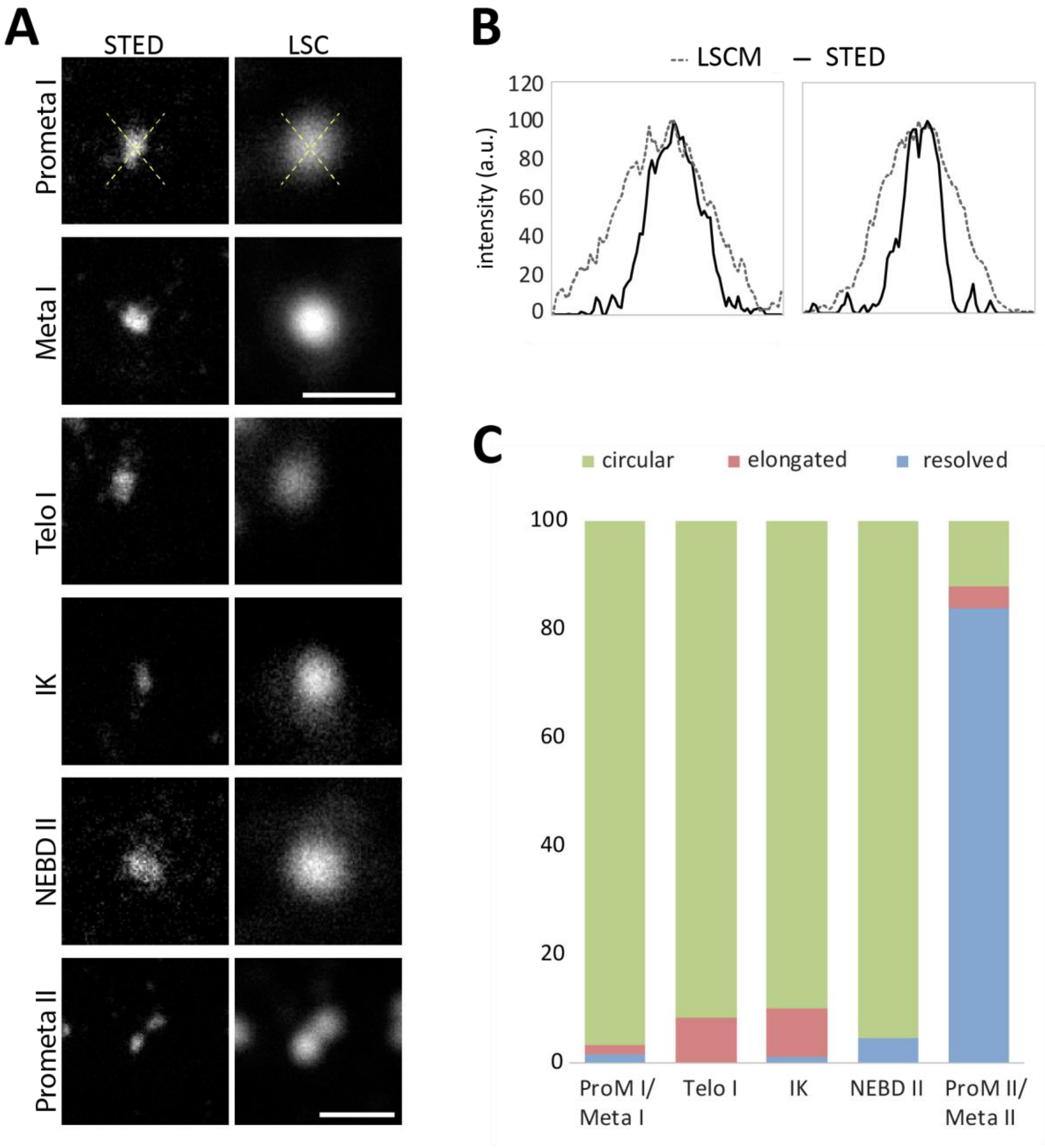

Fig 16: Analysis of sister centromere organization during meiosis by STED nanoscopy

Testis squash preparations with spermatocytes expressing *Cid-EGFP* were fixed and labeled with anti-GFP and a DNA stain (not shown) allowing their staging. **A.** Representative single optical sections through a given Cid-EGFP dot acquired by STED and confocal laser scanning (LSC) microscopy, respectively, from the indicated stages are displayed. Scale bars = 1 µm, all panels displayed at the same magnification except for prometa II. **B.** Line intensity curves along the yellow dotted lines in (A) confirm increased resolution of image acquisition by STED . **C.** Quantification of the fraction of Cid-EGFP dots with a circular (see for example (A) meta I), elongated (see for example (A) interkinesis) and resolved (see for example (A) prometa II) organization at the indicated stages.

To improve spatial resolution for the detection of possible HS -> SS -> BB transitions, STED microscopy was employed. As Cid-EGFP signal intensities were not sufficiently strong for time lapse image with STED microscopy, fixed samples were used for anti-EGFP immunofluorescent staining. Immunofluorescent detection of Cid-EGFP by STED resulted in increased spatial resolution, as expected (Fig. 16A,B). However, even with this approach, it was impossible to resolve the two sister centromeres reliably before the onset of bi-orientation during prometaphase II (Fig. 16A,C).

Within the mitotic kinetochore, Cid is localized within the inner plate, while Mis12 is more peripheral (Schittenhelm et al., 2007). In case of a BB configuration, the Mis12-EGFP signals originating in the two sister kinetochores are therefore expected to be spaced farther apart than the Cid-EGFP signals. Unfortunately, immunofluorescent Mis12-EGFP detection was less sensitive than that of Cid-EGFP, in particular during the meiotic divisions apparently at least in part because of antibody accessibility problems (data not shown). Instead of STED microscopy with fixed samples, Mis12-EGFP was therefore used for time lapse imaging with the spinning disk confocal microscope. As analogous analyses with Cid-EGFP had revealed some marginal sister centromere separation after NEBD II in the presence of colcemid, Mis12-EGFP and its potentially increased resolution was used to evaluate this apparent microtubule-independent change in the sister kinetochore configuration during entry into meiosis II (Fig. 17). Indeed, even in the absence of colcemid, a significant increase in sister kinetochore separation was already apparent 5 min after NEBD II (Fig. 17). Moreover, the inter-sister kinetochore distance observed after bi-orientation (18 min after NEBD II) was greater when determined with Mis12-EGFP compared to Cid-EGFP (950 +/- 100 nm, n = 44 KT pairs vs 720 +/- 320 nm, n = 24 KT pairs, respectively). Interestingly, in the presence of colcemid, statistically significant separation of sister kinetochores after NEBD II was observed as well (Fig. 17). In the absence of microtubules, the separation of sister kinetochores was far slower and less extensive than in the presence of microtubules. At the time when interactions between microtubule and kinetochores start during meiosis II (about 5 min after NEBD II), this slight microtubule-independent reconfiguration of sister kinetochores does not appear to have reached an extent of BB organization that should assist effectively in favoring amphitelic over syntelic attachments.

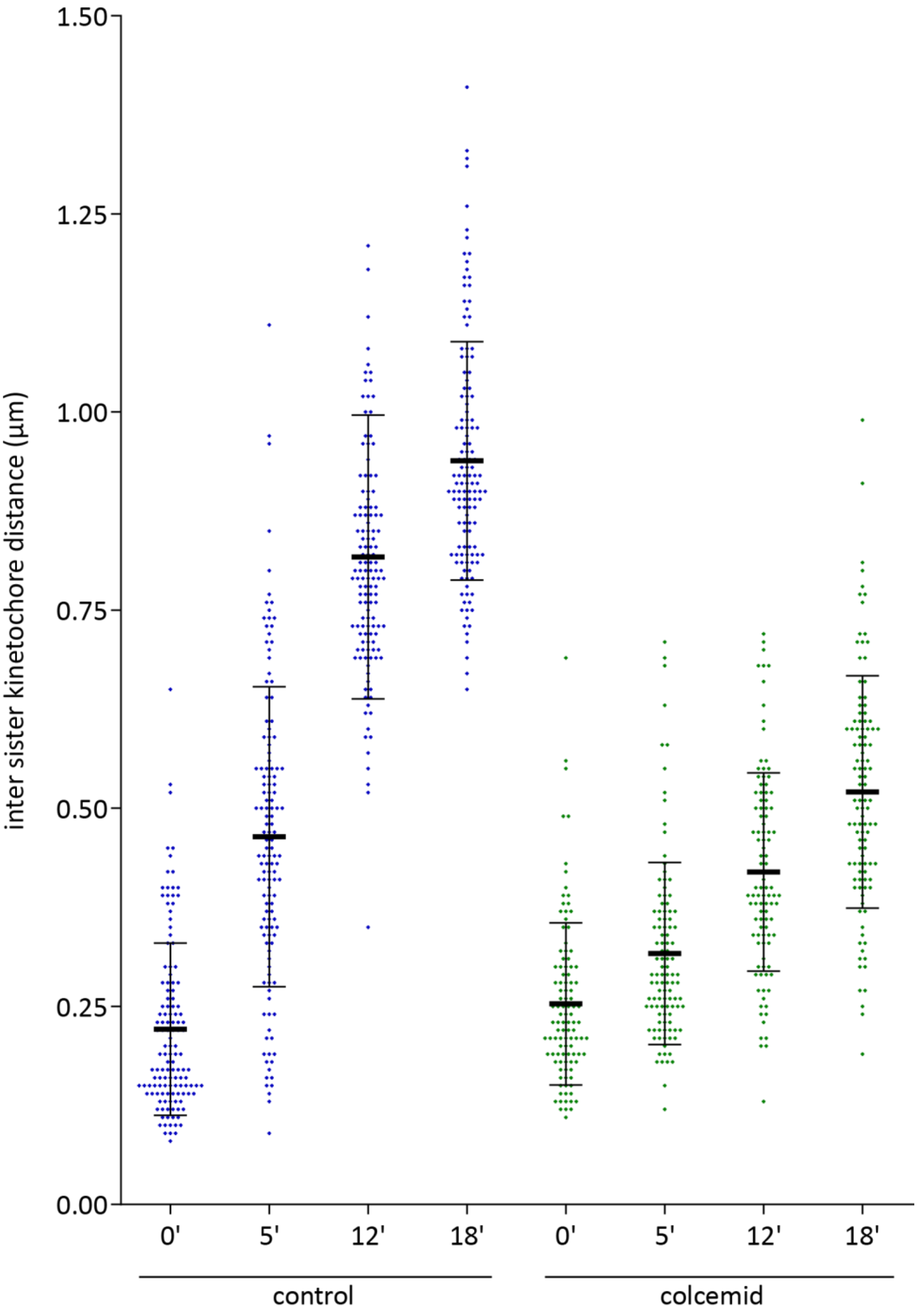

Fig 17: Sister kinetochore separation in meiosis II
After time lapse imaging with spermatocytes expressing *His2Av-mRFP* and *Mis12-EGFP* (*w*; Mis12-EGFP, His2Av-mRFP*) in the absence (control) or presence of colcemid (colcemid), the inter sister kinetochore distance was determined at the indicated time points (min after onset of NEBD II). Dot plot representing individual measurements as well as average (+/- s.d.) obtained with n = 44 sister kinetochore pairs from 11 spermatocytes from more than 2 cysts (control) and n = 36 sister kinetochore pairs from 9 spermatocytes from more than 2 cysts (colcemid). Average sister kinetochore separation was found to increase significantly between all time points ($p < 0.001$, t test).

Rod is a component of the outer kinetochore corona and therefore even further peripheral than Mis12-EGFP (Karess, 2005; Przewloka et al., 2007; Venkei et al., 2012). Time lapse imaging with GFP-Rod and His2Av-mRFP was used to study the configuration of the outer corona of sister kinetochores at the onset of meiosis II (Fig. 18). Interestingly, the initial GFP-Rod accumulation after NEBD II often occurred in two closely spaced crescent shaped structures on each chromosome. These structures, formed just before the onset of interactions between microtubule and kinetochores (see below), were spatially more extended than the Cid-EGFP and Mis12-EGFP signals detected at this stage. Importantly, the two GFP-Rod crescents were always on same side of chromosome (Fig. 18), i.e., in an SS rather than in a BB configuration.

In summary, the results of spinning disk confocal and STED microscopy indicate that progression beyond meiosis I is not accompanied by a striking rearrangement of sister centromeres until the onset of meiosis II. When the interactions between kinetochores and spindle microtubules start early in prometaphase II, sister centromeres are still in an SS rather than a BB organization. The BB arrangement, which is clearly evident in metaphase II eventually, is the result of bi-orientation. It is not already reached before the interactions between kinetochores and spindle microtubules start in prometaphase. At this early prometaphase stage, some limited subtle change in sister kinetochores arrangement seems to have occurred however. This microtubule-independent change (Fig 15 and 17) might reflect chromosome condensation.

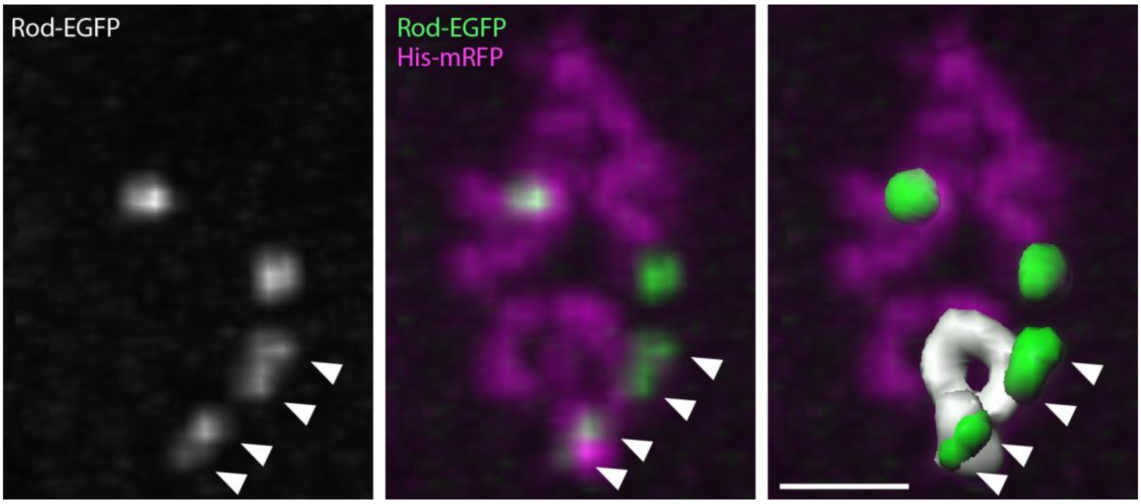

Fig 18: Rod localization in prometaphase II.
Time lapse imaging was performed with spermatocytes expressing *GFP-Rod* and *His2Av-mRFP*. High magnification views from a still frame with a representative early prometaphase II cell are shown. Isosurfaces obtained after segmentation of the GFP-Rod (green) and His2Av-mRFP (white) signals in the right most panel indicate that the two outer corona regions (highlighted by GFP-Rod) of a given sister kinetochore pair are in an SS configuration on top of the chromatids rather than in a BB configuration with the chromatids in between. Two overlapping objects obtained from the His2Av-mRFP signal segmentation are shown. Analogous observations were made in all three processed cells. Scale bar = 3 µm.

According to spinning disk confocal and STED microscopy, sister kinetochores are separated minimally at the start of meiosis II. To address whether sister kinetochore separation is more pronounced at the start of mitosis in comparison to meiosis II, time lapse imaging was done using spinning disk confocal microscopy and identical settings with syncytial Drosophila embryos collected from the same *Cid-EGFP*, *His2Av-mRFP* genotype used before for the analyses of male meiosis. The same procedure was used to estimate sister centromere separation at NEBD and metaphase during mitosis 11-13 of early embryogenesis. Separation between sister centromeres was observed to be marginally larger (about 18%) at NEBD of mitosis compared to meiosis II (Fig. 19). A comparably small difference in the separation of sister centromeres in mitosis and meiosis II was also detected during metaphase (Fig. 19). In conclusion, the sister centromere arrangement at the start of meiosis II is similar to that in mitosis. Also at the start of mitosis in Drosophila embryos, sister centromeres are not in an obvious BB configuration with wide inter sister centromere separation. In comparison with these *in vivo* studies, cytological analyses involving swelling of cultured cells or larval brains in hypotonic sodium citrate (Blower et al., 2002) followed by squashing or cytocentrifuging appear to exaggerate the extent of sister separation and BB configuration at the start of mitosis. While mitosis and meiosis II appear to be quite similar in that the spindle appears to be required for the separation of the kinetochores for eventual bi-orientation, meiosis I is strikingly different in this regard. The separation of homologous centromeres at NEBD I, is an order of magnitude larger compared to NEBD II (Fig. 19).

The spatial arrangement of kinetochores in Drosophila males is dramatically different at the start of meiosis I and II, respectively. Late in interkinesis before meiosis II, the two sister centromeres of a chromosome are at most 220 nm apart, apparently still in an SS arrangement. In contrast, in an S6 spermatocyte before meiosis I, the separation between the two pairs of united sister centromeres is usually several micrometers in case of a large bivalent (those of chromosome II, III and XY). This extensive separation at the start of male meiosis is actually also very different from the situation at the start of Drosophila female meiosis where most or all centromeres are tightly clustered within the chromocenter region of the karyosome (Gluszek et al., 2015). Moreover, synaptonemal complex (SC) components persist at centromeres during female meiosis whereas there is no SC in male meiosis (Hawley, 2002; Vazquez et al., 2002). Chromosome condensation and kinetochore assembly at the start of the male meiotic divisions does not change the spatial arrangements of the centromeres substantially. Therefore, the kinetochore arrangements at the start of both male meiotic divisions do not appear to be optimized towards prevention of attachment errors. The SS arrangement at the start of meiosis II could favor syntelic attachments over the correct amphitelic attachments which have to prevail at the end of prometaphase II. Similarly, the two widely separated HS kinetochores of a bivalent present at the start of meiosis I are far from the design proposed to be optimal for favoring amphitelic over syntelic attachments (Hauf and Watanabe, 2004) where kinetochores are (1) in a stiff BB configuration and (2) each within a cup of surrounding and shielding chromatin so that only MTs coming straight from in front can contact the kinetochore.

The apparent attachment error-prone centromere configuration geometry at the start of the male meiotic divisions in Drosophila in combination with the remarkable speed of these division and the limited power to delay them in response to loss of linkage between centromeres tension (see section 2.) and loss of attachment (see section 3.) raises questions how meiosis can actually succeed. A speed of error correction might be required that is far beyond what has been observed so far. To analyze and compare the processes of chromosome bi-orientation and segregation during MI and MII, kinetochores were carefully tracked over time.

Fig 19: Comparison of the distance between sister centromeres at the start of meiosis I, II and mitosis

After using identical settings for time lapse imaging with spermatocytes and embryos expressing Cid-EGFP and His2Av-mRFP, the distance between sister centromeres was measured at NEBD and in metaphase. **A.** Representative still frames are displayed. The two homologous centromere pairs are often very widely separated in bivalents during meiosis I, as indicated by the yellow dotted line, sister centromeres cannot be resolved initially at the start of meiosis II and mitosis, as indicated by the yellow dotted circles. Scale bar = 2 µm. **B.** Dot plot representing individual measurements as well as average (+/- s.d.), n = 16 centromere pairs (meiosis I), 51 sister centromere pairs (meiosis II) and 42 sister centromere pairs (mitosis) at NEBD; n = 48 centromere pairs (meiosis I), 42 sister centromere pairs (meiosis II) and 51 sister centromere pairs (mitosis) at metaphase. Differences between average distance were statistically significance (t test): (*) p = 0.024, (***) p = 0.0058.

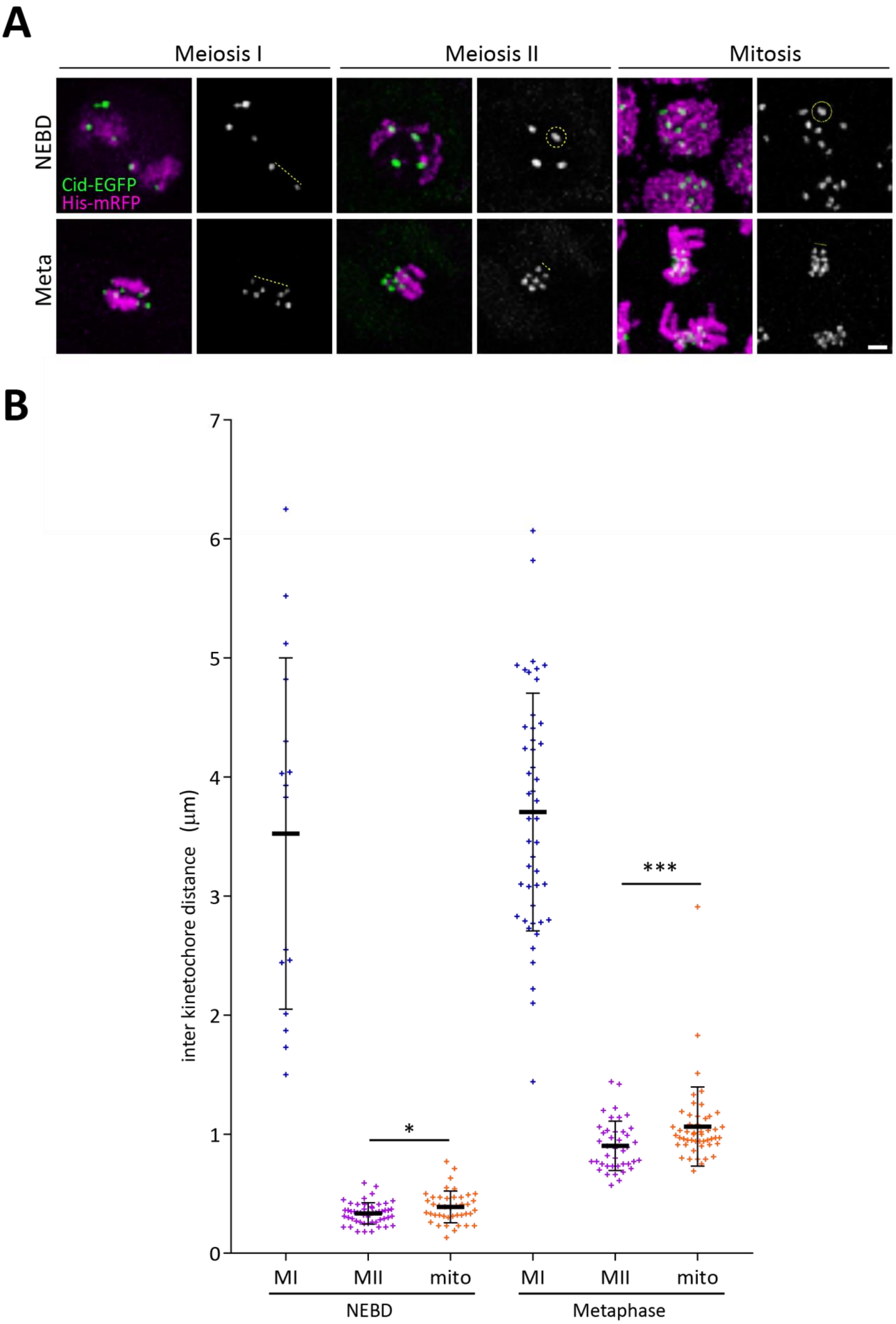
A
Meiosis I
Meiosis II
Mitosis
NEBD
Meta
Cid-EGFP
His-mRFP
B
inter kinetochore distance (µm)
0
1
2
3
4
5
6
7
*
***
MI
MII
mito
MI
MII
mito
NEBD
Metaphase

4.3 Kinetochore inspection at high resolution during male meiosis

4.3.1 Interactions of kinetochores and microtubules

To characterize interactions of kinetochores with microtubules during the male meiotic divisions, tdTomato-CenpC was imaged simultaneously with GFP-ßTubulin56D. The latter transgene was found to confer the best microtubule detection sensitivity for time lapse imaging compared to alternative tubulin transgenes (His2AvP-mCherry-αTub84B (II), P. Radermacher and C.F. Lehner, unpublished; (Dobbelaere et al., 2008). With these fluorescent marker proteins, NEBD was no longer precisely scorable, as after time lapse imaging with His2Av-mRFP. In the following analyses, the time point of NEBD was assigned based on the appearance of microtubule organization and its correlation with the appearance of the His2Av-mRFP signals established in the preceding analyses (see Fig. 13).

During meiosis I, the first distinct microtubules within the nuclear region, which became detectable on average about 7.5 min after NEBD (see 4.1.2), were not astral microtubule (as indicated by the orientation of most of the initial MTs) and not associated with kinetochores usually (Fig. 20, t = 2:00 and 3:10). These rapidly growing nuclear microtubules became efficiently bundled in polar regions, forming the poles of an intranuclear spindle (Fig. 20). The concomitant and progressive bundling at both the outer centrosomal astral poles and the inner nuclear spindle poles transformed the nuclear region from a spherical into a more lemon-like shape and caused microtubules to pivot inwards so that their orientation became increasingly parallel to the spindle axis (Fig. 20). Thereby microtubules were brought increasingly into closer proximity with kinetochores, which remained relatively steady during this initial phase. Moreover, the progressive bundling also appeared to sweep the bivalents from their widely separated peripheral positions successively into the central region. Tracking the kinetochores in 3D over time confirmed that initially kinetochores underwent limited and only concerted movements where all kinetochores were kept in the original spatial constellation (Fig. 21A). Subsequently, jumps which rapidly translocated a pair of kinetochores into a distinct direction started and broke up the original constellation (Fig. 21A,B). We assume that these jumps resulted from transport along microtubules that had come into contact with at least one of the jumping kinetochore pair. Unfortunately, such contacting microtubules were often not clearly detectable in the GFP-ßTubulin56D channel, particularly in case of the intial jumps (Fig. 21C). Our microtubule detection sensitivity therefore appeared to be insufficient for a reliable visualization of single microtubules, while sufficiently strong microtubule bundles were evident. In case of later jumps, strong microtubule bundles adjacent to the jumping kinetochore pair were often seen (Fig. 21C), but an unequivocal identification of the relevant microtubule track remained difficult because of the high microtubule density. Eventually, kinetochore pairs were observed to congress into the metaphase plate (Fig. 22). In favorable cases, the ßTubulin56D-GFP channel revealed a potential explanation for this final congression. For example (Fig. 22A), an apparent merotelic attachment was resolved concomitant with the onset of congression. In parallel with congression, kinetochore microtubule bundles became increasingly more robust. In metaphase, the end-on attachment of kinetochores to these bundles was very clearly apparent (Fig. 22B).

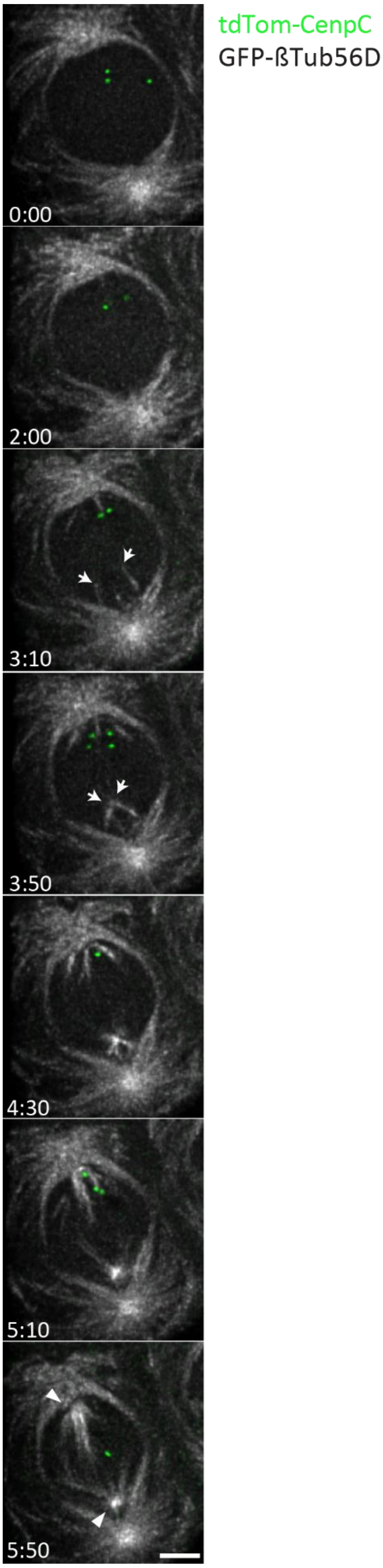

Fig 20: Simultaneous imaging of microtubules and centromeres during entry into meiosis I
Time lapse imaging was performed with spermatocyte cysts expressing *tdTomato-CenpC* and *GFP-ßTub56D* (*w*; g2xtdTomato-CenpC, UbiP-GFP-ßTub56D*). Still frames at selected time points as indicated (min:sec after NEBD I) illustrate the results observed in a representative spermatocyte. Each panel is a maximum intensity projection of 3-4 equatorial optical sections with 300 nm spacing. Arrows indicate initial formation of anastral intranuclear microtubules that are eventually bundled into the poles of the intranuclear spindle (arrowheads). See text for further explanations. Scale bar = 4 µm

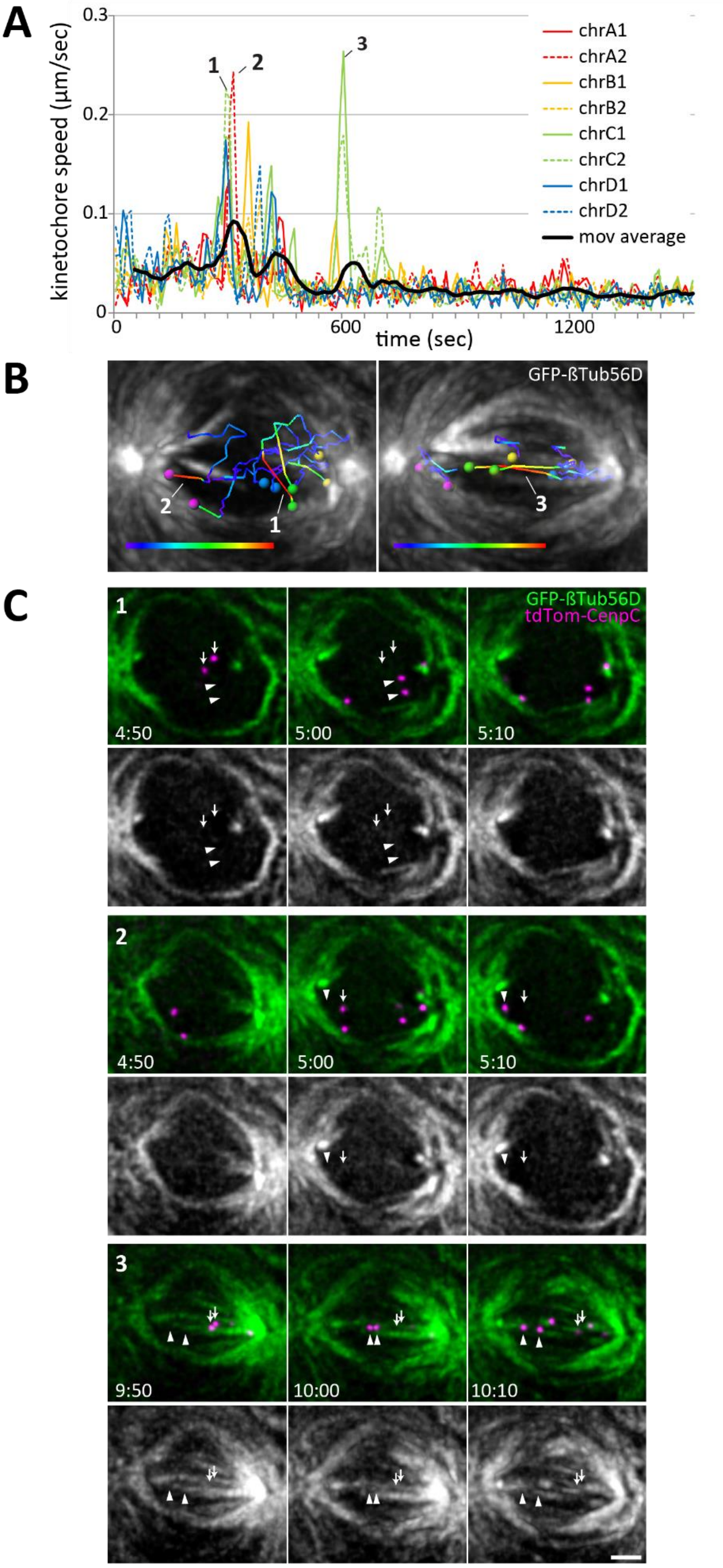

Fig 21: Initial contacts between kinetochores and microtubules during prometaphase I

Time lapse imaging was performed with spermatocyte cysts expressing *tdTomato-CenpC* and *GFP-ßTub56D* (*w*; g2xtdTomato-CenpC, UbiP-GFP-ßTub56D*). **A.** All eight centromeres present in a spermatocyte were tracked during entry into meiosis I until metaphase I, followed by determination of centromere speed. The resulting speed curves from a representative cell are displayed. The numbered centromere jumps events are documented in the additional panels (B,C). **B.** Centromere tracks illustrating pronounced centromere jump events are displayed with a color code reflecting centromere speed. Tracks covering the past 15 time points were overlaid on a still frame from the time point just after the jump. **C.** The spatial distribution of centromeres and microtubules during jump events is documented in three consecutive time frames (min:sec after start of imaging). Arrows indicate centromere positions prior to the jump, arrowheads those after the jump. See text for further explanations. Scale bar = 3 µm.

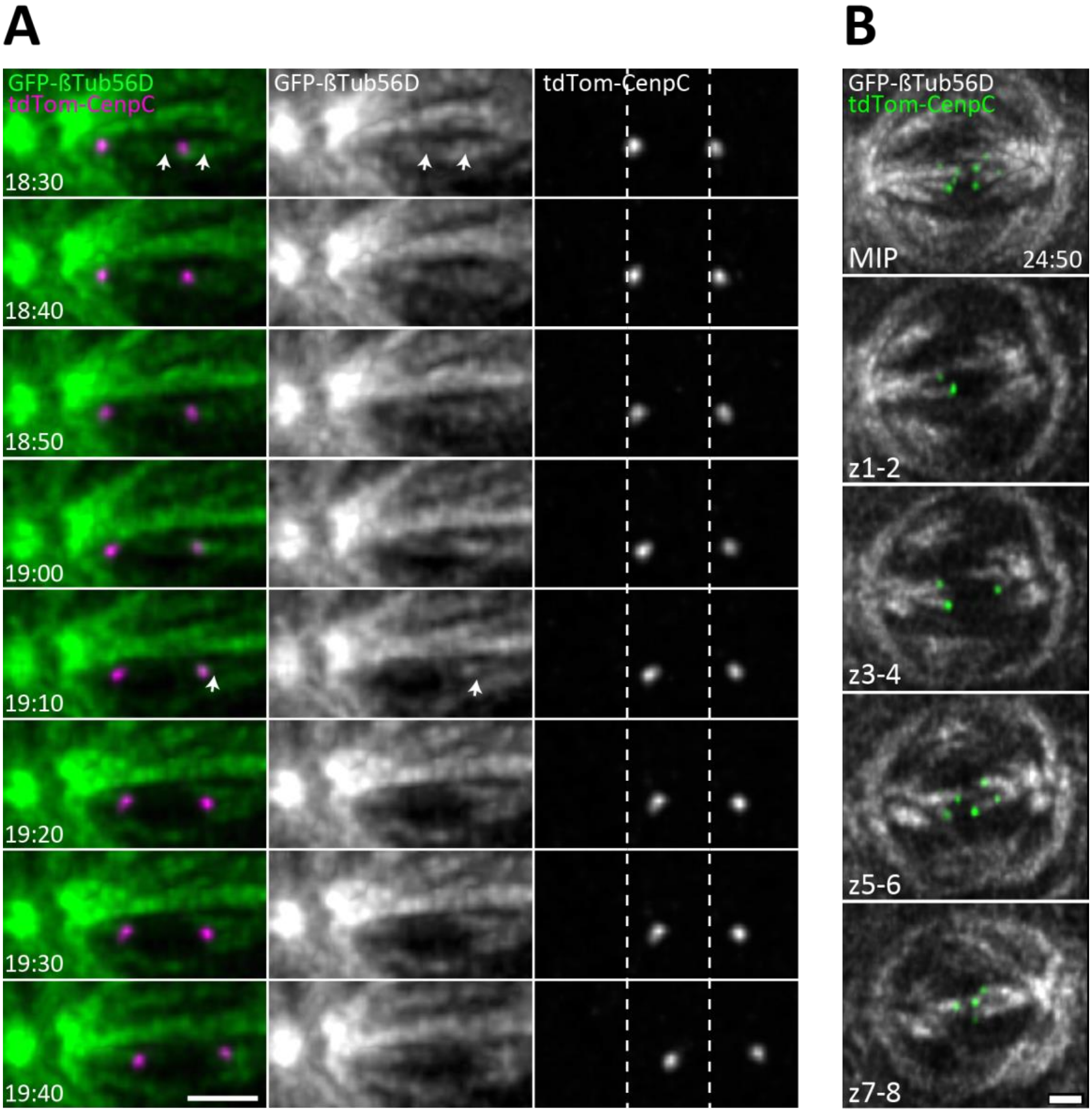

Fig 22: Congression of bivalents into the metaphase I plate

Time lapse imaging was performed with spermatocyte cysts expressing *tdTomato-CenpC* and *GFP-ßTub56D* (*w*; g2xtdTomato-CenpC, GFP-ßTub56D*). **A.** High magnification views documenting the onset of final congression of a bivalent into the metaphase I plate. Maximum intensity projections of only those optical sections containing the two centromeres of the chosen bivalent are shown at the indicated time points (min:sec after NEBD I). One centrosome and the associated inner spindle pole are visible on the left side. Spindle axis is horizontal. Dotted white lines mark the initial centromere positions for reference. The onset of final congression of this bivalent is accompanied by the apparent disappearance of merotelic connections (white arrow) of the centromere on the right with the spindle pole on the left. **B.** End-on attachments of kinetochores to strong KT-MT bundles in stably bi-oriented bivalents in metaphase I illustrated in a representative spermatocyte. A maximum intensity projection (MIP) of 8 optical sections with 300nm spacing is shown in the top panel, while MIPs of only two sections (section numbers as indicated) are displayed below. Scale bar = 3 µm.

A corresponding analysis was completed for meiosis II as well. As in meiosis I, the first microtubules detected within the nuclear region were not associated with kinetochores (Fig. 23A). Bundling of these intranuclear microtubules into spindle poles occurred more slowly than during MI. Prominent inner poles were only formed when the final congression of chromosomes into the metaphase plate was already underway (Fig. 23A). Tracking of kinetochores during meiosis II also revealed kinetochore jumps in prometaphase II (Fig. 23D). However, the two sister kinetochores were often so closely associated in particular in early prometaphase that they could not be resolved, as described above. Therefore, sister kinetochore pairs were tracked rather than individual kinetochores.

Although the large majority of sister kinetochores were so closely associated at the start of MII that they could not be resolved individually, occasional transient separation of sister kinetochores clearly occurred also during prometaphase II (Fig. 23B), as already described above. These transient separation events were not accompanied by association with detectable microtubules (Fig. 23B) and the orientation of the transient inter sister kinetochore axes were random rather than oriented towards a spindle pole (Fig. 23B). It is conceivable therefore that these transient sister kinetochore separation events are microtubule-independent.

The first kinetochore jumps during prometaphase II were also not always observed to occur in association with clearly detectable microtubules (Fig. 23E), as already noticed in case of meiosis I. As prometaphase II proceeded, kinetochores were often associated with detectable microtubules, although these were less obviously bundled into a pole compared to meiosis I (Fig. 23C). The frequent presence of detectable microtubules around kinetochore during mid and late prometaphase suggested that kinetochore might either efficiently stabilize microtubules or also nucleate their polymerization. Similar to meiosis I, strong kinetochore microtubule bundles were observed during metaphase II, when also the two sister kinetochores were maximally and permanently stretched apart (Fig. 23F).

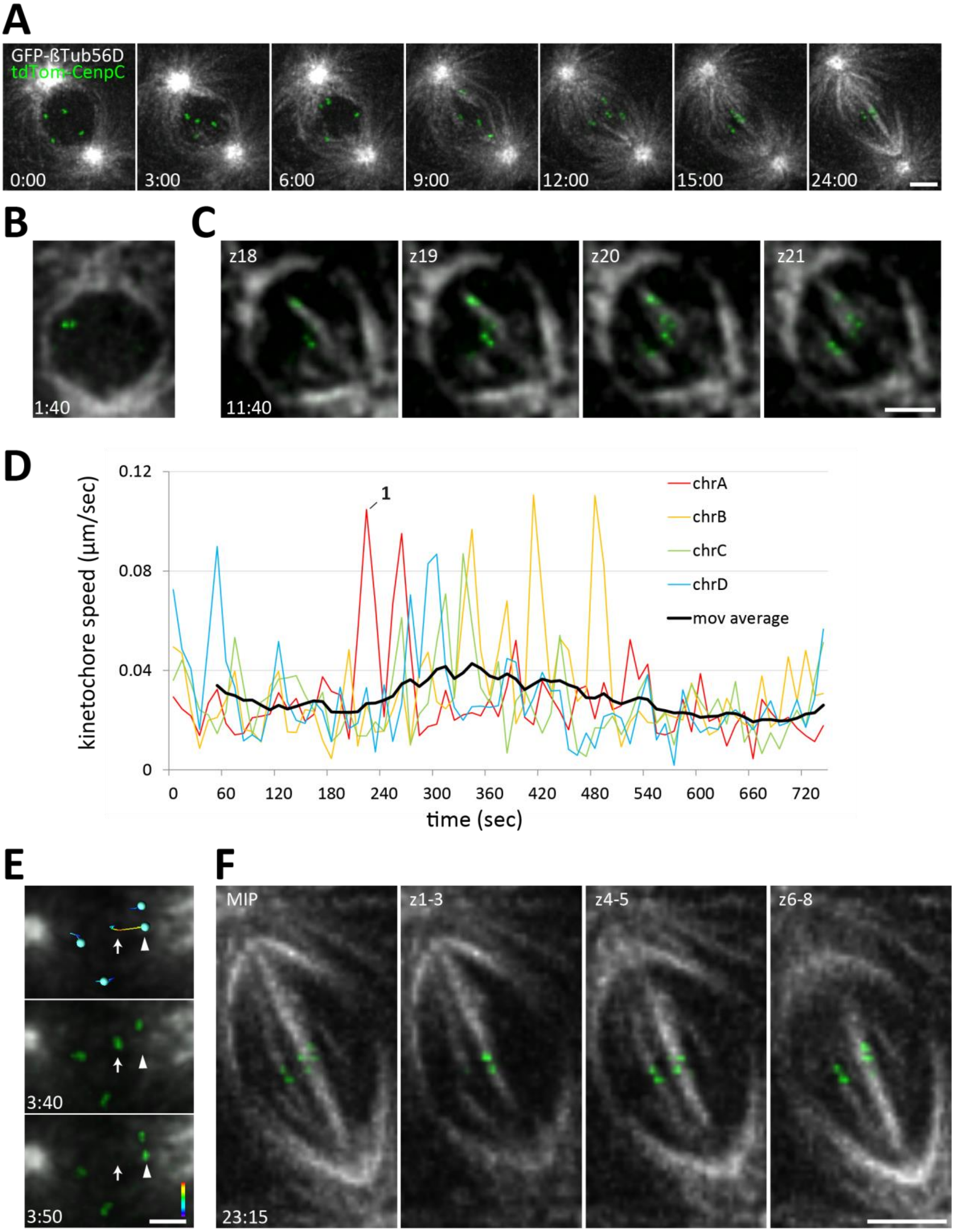
A
GFP-ßTub56D
tdTom-CenpC
0:00
3:00
6:00
9:00
12:00
15:00
24:00
B
1:40
C
z18
z19
z20
z21
11:40
D
kinetochore speed (µm/sec)
0.12
0.08
0.04
0
0
60
120
180
240
300
360
420
480
540
600
660
720
time (sec)
1
chrA
chrB
chrC
chrD
mov average
E
3:40
3:50
F
MIP
z1-3
z4-5
z6-8
23:15

Fig 23: Simultaneous imaging of microtubules and centromeres during meiosis II
Time lapse imaging was performed with spermatocyte cysts expressing *tdTomato-CenpC* and *GFP-ßTub56D* (*w*; g2xtdTomato-CenpC, UbiP-GFP-ßTub56D*). **A.** Still frames at selected time points as indicated (min:sec after NEBD II) illustrate progression until metaphase II in a representative spermatocyte. Each panel is a maximum intensity projection of 3-4 equatorial optical sections with 300 nm spacing. Scale bar = 2 µm. **B.** A single optical section documenting an example of a transient sister kinetochore separation event during early prometaphase with an inter kinetochore axis that is not oriented towards one of the spindle poles and without associated detectable microtubules. Scale bar = 3 µm. **C.** Later movements of centromere pairs during prometaphase II occur frequently in association with detectable microtubules that are not necessarily oriented towards a spindle pole. Four consecutive z-sections are shown. Scale bar = 3 µm. **D.** The four sister centromere pairs were tracked in a representative cell from entry into meiosis II until metaphase II, followed by determination of centromere speeds. The displayed speed curves also reveal a first centromere jump event (1) which is documented in panel (E). **E.** Arrows indicate the position of a selected centromere pair before the first jump, and arrowheads that after the jump. The top panel presents tracks of the centromere pairs during the past four time points in colors reflecting centromere speed as an overlay onto the still frame from the time point just after the jump. The middle and bottom panels document the localization of microtubules and centromere pairs before and after the jump, respectively. Scale bar = 2 µm. **F.** End-on attachments of centromeres to strong KT-MT bundles in metaphase II. Left most panel is a MIP comprising of 8 optical sections with 300 nm spacing. MIPs of only a few sections (as indicated) are shown in the additional panels. Scale bar = 3 µm.

4.3.2 Kinetochore tracking during meiosis I

Unfortunately, microtubule detection sensitivity was not sufficient for an unequivocal direct observation of the initial interactions between microtubules and kinetochores at the start of both meiotic divisions. During both divisions, some of the initial jumps of individual chromosomes led by a kinetochore occurred in the absence of clearly recognizable microtubule tracks along the jump trajectories. Therefore, for further analysis of the meiotic chromosome bi-orientation processes, we examined only kinetochore tracks. Since accurate kinetochore tracking was facilitated considerably by simultaneous observation of chromosomes, Mis12-EGFP was used in combination with His2Av-mRFP. Similar as in earlier studies (Church and Lin, 1985; Nicklas, 1961; Nicklas and Koch, 1969; Savoian and Glover, 2014), where DIC or phase microscopy had been used to monitor chromosome movements, we extracted information from the dynamic changes in direction of movements although this time looking directly at kinetochores.

The analysis of kinetochore speed over time confirmed the observations made with tdTomato-CenpC and GFP-ßTubulin56D. After NEBD (as indicated by a rapid loss of diffuse nucleoplasmic His2Av-mRFP signals) it took several minutes until a first kinetochore jump started breaking up the kinetochore constellation established in G2 before the start of the first meiotic division and quite stably maintained until this first jump (Fig. 24A,B). The initial period of prometaphase from NEBD until the first kinetochore jump will be designated as prometaphase A in the following, while the subsequent period from the first jump until bi-orientation and congression of the last chromosome will be called prometaphase B. On average, prometaphase A was found to last for about 5 +/- 1:30 min (n = 6 spermatocytes from 2 cysts). The onset of prometaphase B was well correlated with the appearance of the poles of the intranuclear spindle in meiosis I, andthe duration of prometaphase B was around 9:45 +/- 3 min (n = 9 spermatocytes from 3 cysts). This short temporal interval is sufficient for attachment of kinetochores to spindle microtubules, error correction and chromosome congression during meiosis I. At the onset of prometaphase B, the average kinetochore speed clearly increased to a maximum. Maximal kinetochore speeds observed during prometaphase B were up to 0.26 µm/sec (= 16 µm/min) (Fig 21). Chromosome bi-orientation during prometaphase B was accompanied by a decrease in kinetochore speed. Throughout metaphase, kinetochore speeds remained minimal, followed by an increase during anaphase

(Fig. 24A,B). Kinetochore speed during anaphase was around 0.04 µm/sec (= 2.4 µm/min) (similar as reported by (Savoian, 2015; Savoian and Glover, 2014; Savoian et al., 2000) and therefore clearly lower than that observed during the rapid kinetochore jumps of prometaphase B, which presumably reflect dynein-driven movements after lateral associations of kinetochores to microtubules (Asbury, 2017).

Beyond kinetochore movements, the angle between the spindle axis and the line connecting the two kinetochores of a bivalent was also highly informative (Fig. 24C). Bi-orientation reduces this angle to zero. Analysis of the angle over time accurately revealed the time of the final bi-orientation for the large majority of bivalents. Moreover, these curves also indicated that the final bi-orientation of bivalents was not preceded by transient bi-orientation events that lasted for several time frames (i.e., for ≥ 20 sec). The virtual absence of transient bi-orientation was fully confirmed by the analysis of kinetochore movements. By carefully monitoring the bi-orientation process of each bivalent within a total of five distinct spermatocytes, the frequency of kinetochore reorientation was determined. A kinetochore reorientation event was only scored, when a particular kinetochore was observed to jump suddenly towards one of the poles, followed by a jump towards the opposite pole at a later time point, as illustrated by the examples in Fig. 24E and F. In each of the five cells, only one such kinetochore reorientation event could be detected during meiosis I. Moreover, in only one of those events, the partner kinetochore was observed to become pulled slightly towards the opposite pole during the time in between the two jumps of the other partner kinetochore. Therefore, this particular event has the hallmarks suggesting an initial transient bi-orientation where the two kinetochores are connected and pulled to opposite spindle poles, followed by their release from the spindle and their reorientation within the spindle. All other reorientation events appear to involve bivalents where one of the two partner kinetochores is released after a transient interaction with one of the poles, while the other kinetochore is not engaged with the poles. While our analysis cannot reveal cases where a transient interaction of a kinetochore with a spindle pole is not accompanied by evident changes in its movement (direction, speed), our results nevertheless demonstrate that bivalents are essentially never released after they have established bi-orientation during the first meiotic division in Drosophila males. This finding is in striking contrast to those made in mouse oocytes where each bivalent reoriented more than three times on average during prometaphase I (Kitajima et al., 2011). Overall our observations suggest that kinetochore end-on attachments in Drosophila male meiosis I develop slowly and that their stability might be particularly dependent on mechanical tension. Accordingly, end-on attachments would develop rarely and all those that do not generate tension would be extremely short-lived, while those that do generate tension would be stabilized very rapidly. The striking increase in kinetochore bundle strength that was found to accompany the final congression into the metaphase I plate after bi-orientation is entirely consistent with this interpretation.

Determination of the distance between the two kinetochores of a bivalent (Fig. 24D) supported the expectation that bi-orientation results in mechanical tension. The distance between the two kinetochores of a bivalent observed before entry was highly variable (between 0 and 7.5 µm) from cell to cell and from bivalent to bivalent. However, chromosome condensation during entry into the first meiotic division reduced this variability and brought the separation to about 2 µm (Fig. 24D). Bi-orientation and congression into the metaphase plate was clearly accompanied by stretching of the inter kinetochore distance about twofold (Fig. 24D). Interestingly, the inter kinetochore distance during metaphase was characteristically different in distinct bivalent. In particular in case of the small chromosome 4 it was significantly smaller (Fig. 24G).

As the Y kinetochore has higher levels of centromere and kinetochore proteins (Raychaudhuri et al., 2012); Fig. 9 and 10) it might be expected to take up a metaphase position closer to the spindle pole than all the other kinetochores. However, this was not observed reproducibly. Similarly, the kinetochores of chromosome 4 might be expected to migrate faster to the pole during anaphase, since it contains 5-12 fold less DNA compared to the other chromosomes. However, there was at most a slight increase in anaphase speed of chromosome 4 relative to the others, consistent with the well-established notion that anaphase speed is largely independent on chromosome size (Asbury, 2017; Nicklas, 1965; Raj and Peskin, 2006).

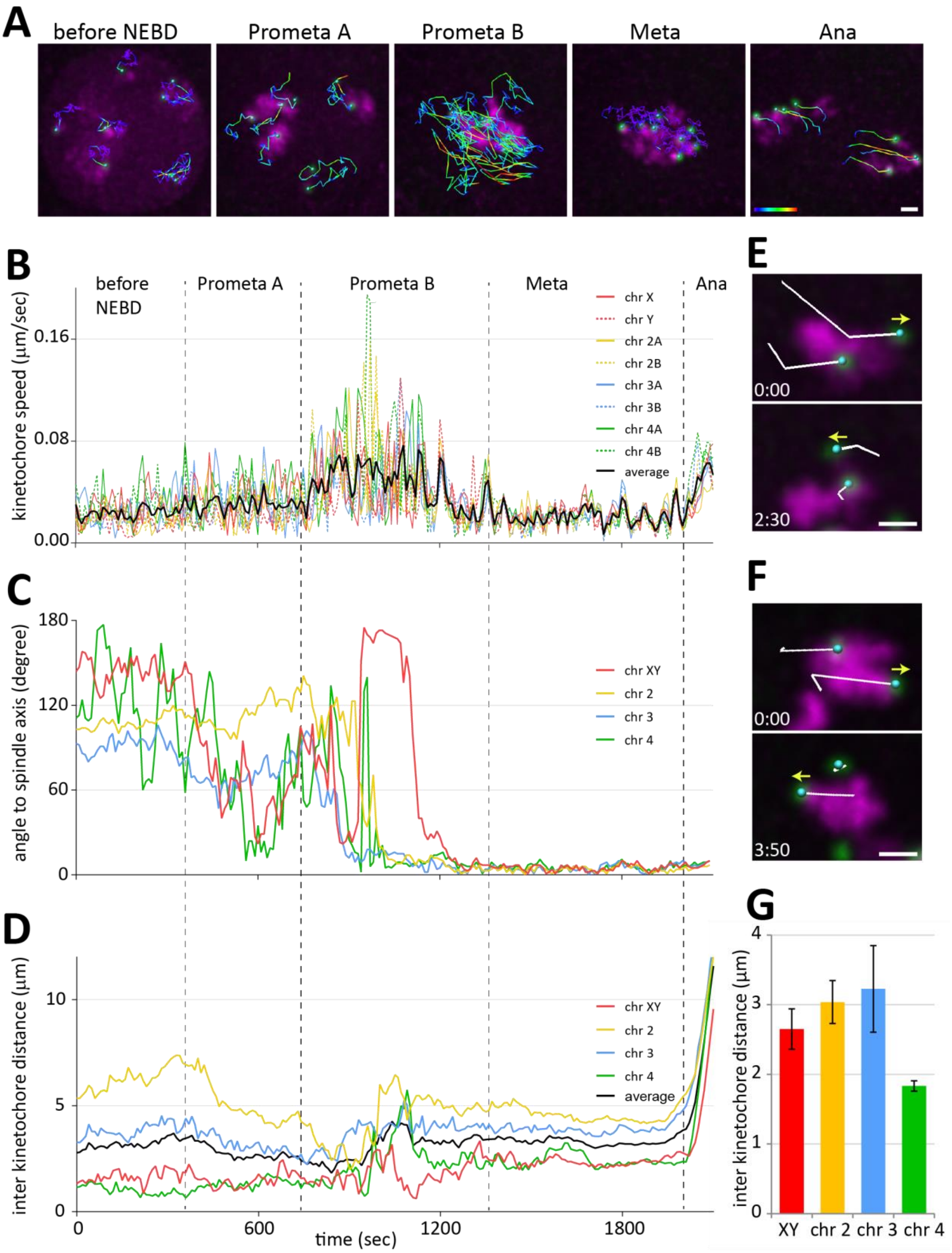
A
before NEBD
Prometa A
Prometa B
Meta
Ana
B
before NEBD
Prometa A
Prometa B
Meta
Ana
kinetochore speed (µm/sec)
0.16
0.08
0.00
chr X
chr Y
chr 2A
chr 2B
chr 3A
chr 3B
chr 4A
chr 4B
average
E
0:00
2:30
C
angle to spindle axis (degree)
180
120
60
0
chr XY
chr 2
chr 3
chr 4
F
0:00
3:50
D
inter kinetochore distance (µm)
10
5
0
chr XY
chr 2
chr 3
chr 4
average
0
600
1200
1800
time (sec)
G
4
3
2
1
0
inter kinetochore distance (µm)
XY
chr 2
chr 3
chr 4

Fig 24: Kinetochore movements during meiosis I
Time lapse imaging was performed with spermatocyte cysts expressing *Mis12-EGFP* and *His2Av-mRFP* (*w*; His2Av-mRFP/ Mis12-EGFP II.2*). All eight kinetochores present in a spermatocyte were tracked during meiosis I, followed by determination of kinetochore speed. **A.** The kinetochore tracks observed in a representative spermatocyte during the indicated phases are displayed as an overlay on the still frame at the end of the corresponding phase. Tracks are in colors representing kinetochore speed. Maximal speeds are observed during prometaphase B. **B.** Curves representing kinetochore speed over time. **C.** Curves representing the angle between the axis connecting the two kinetochores in a bivalent and the spindle axis over time. **D.** Curves representing the distance between the two kinetochores in a bivalent over time. Black dotted lines mark phase transitions. Chromosomes are color coded. **E**, **F**. Still frames documenting two distinct kinetochore re-orientation events. Images were oriented so that the spindle axis is horizontal. The images were overlaid with the tracks of the past two frames. Yellow arrows indicate the direction of movement of the re-orienting kinetochore which is to the right in the top panel and to the left after re-orientation in the bottom panel. The time interval separating the two still frames is indicated (min:sec) **G.** Bar diagram indicating average inter kinetochore distance (+/- s.d.) observed at late metaphase I in the different *D. melanogaster* chromosomes as indicated (n = 6 spermatocytes). Scale bars = 2 µm

To confirm that the kinetochore jumps observed during prometaphase B depend on interactions with microtubules, I performed centromere tracking after knock down of Spc105, a component of the KMN network which provides the major microtubule end-on binding activities at the kinetochore. Spermatocyte-specific Spc105 depletion was achieved by *bamP-GAL4VP16* driven expression of *UASt-V20-Spc105*^{RNAi} in a background with the *Cid-EGFP* and *His2Av-mRFP* transgenes. In the Spc105-depleted spermatocytes, Cid-EGFP tracking clearly revealed an absence of prometaphase B with its characteristic rapid kinetochore jumps (Fig. 25A,B). While Cid-EGFP mobility was found to increase slightly after NEBD I (Fig. 25B), it never reached the level observed in control during prometaphase B (Fig. 24B). Moreover, the eventual orientation of the inter-kinetochore axes along the spindle axis that occurred during control prometaphase B (Fig. 24C) was not observed after Spc105 depletion (Fig. 25C). Also the eventual stretching apart of the two kinetochores of a bivalent that was typically observed during control prometaphase B (Fig. 24D) was absent after Spc105 depletion (Fig. 25D). During the following premature exit from meiosis I in Spc105-depleted spermatocytes (see Fig. 12), contractile furrow activity squeezed the decondensing chromosomes apart towards spindle poles. During this “pseudo-anaphase”, mostly whole bivalents were segregated randomly into the two daughter secondary spermatocytes (Fig. 25A) rather than regularly disjoined homologs as in controls. Occasionally, even a bivalent was squeezed apart, resulting in the segregation of the corresponding homologs into distinct daughter cells. In contrast to homolog segregation during normal anaphase I, the movement of chromosomes was not lead by a kinetochore during exit from meiosis I after Spc105 depletion (Fig. 26B).

Meiotic chromosome missegregation after Spc105 depletion was also confirmed by counting the number of centromere signals per nucleus in telophase I and telophase II, respectively. In case of normal meiosis, this number was found to be invariably four, as expected (Fig. 26C). In contrast, in random samples of Spc105-depleted cells, this number was variable, ranging from 0 to 8 (Fig. 26C). 8:0 segregation could be observed occasionally during meiosis I after Spc105 depletion (although not within the limited sample analyzed for Fig. 26C). Importantly, the number of centromere signals per nucleus at the start of meiosis, was always the normal 8, confirming that Spc105 depletion does not interfere with the gonial mitotic divisions during cyst formation.

All observations indicated that Spc105 depletion inactivated kinetochore function in spermatocytes completely. Without a functional kinetochore, neither the rapid kinetochore jumps nor the eventual bi-orientation of bivalents occurred. Interestingly, however, the bivalents still underwent remarkable congression after Spc105 depletion (Fig. 25A, 26A). While the Cid-EGFP dots were widely distributed at NEBD, they always became increasingly concentrated within the spermatocyte center also after Spc105 depletion. We suggest that this residual congression results from the polar ejection forces generated by the spindle in combination with the microtubule bundling at the inner spindle poles (Fig. 20). During Drosophila male meiosis I, therefore, spindle formation appears to have consequences opposite from those observed during mitosis in cultured human cells (Cai et al., 2009) and during mouse meiosis I (Kitajima et al., 2011) where a prominent inner spindle displaces the far more numerous chromosomes into a surrounding prometaphase belt of chromosomes. However, also in Drosophila male meiosis I, the spindle-imposed kinetochore-independent chromosome positioning during prometaphase presumably increases the efficiency of bi-orientation.

To confirm that the eventual kinetochore-independent confinement of bivalents within the central region observed after Spc105 depletion results from forces exerted by the spindle, we analyzed colcemid treated spermatocytes (Fig 26A). While the congression of Cid-EGP signals within the central region was clearly apparent 15 min after NEBD in all Spc105 depleted spermatocytes (n = 21 spermatocytes from 3 cysts), we did not observe a comparable congression in colcemid treated spermatocytes within this period (n = 13 spermatocytes from 3 cysts) (Fig. 26A). Microtubules are therefore indeed required for the kinetochore-independent congression of bivalents observed after Spc105 depletion during meiosis I.

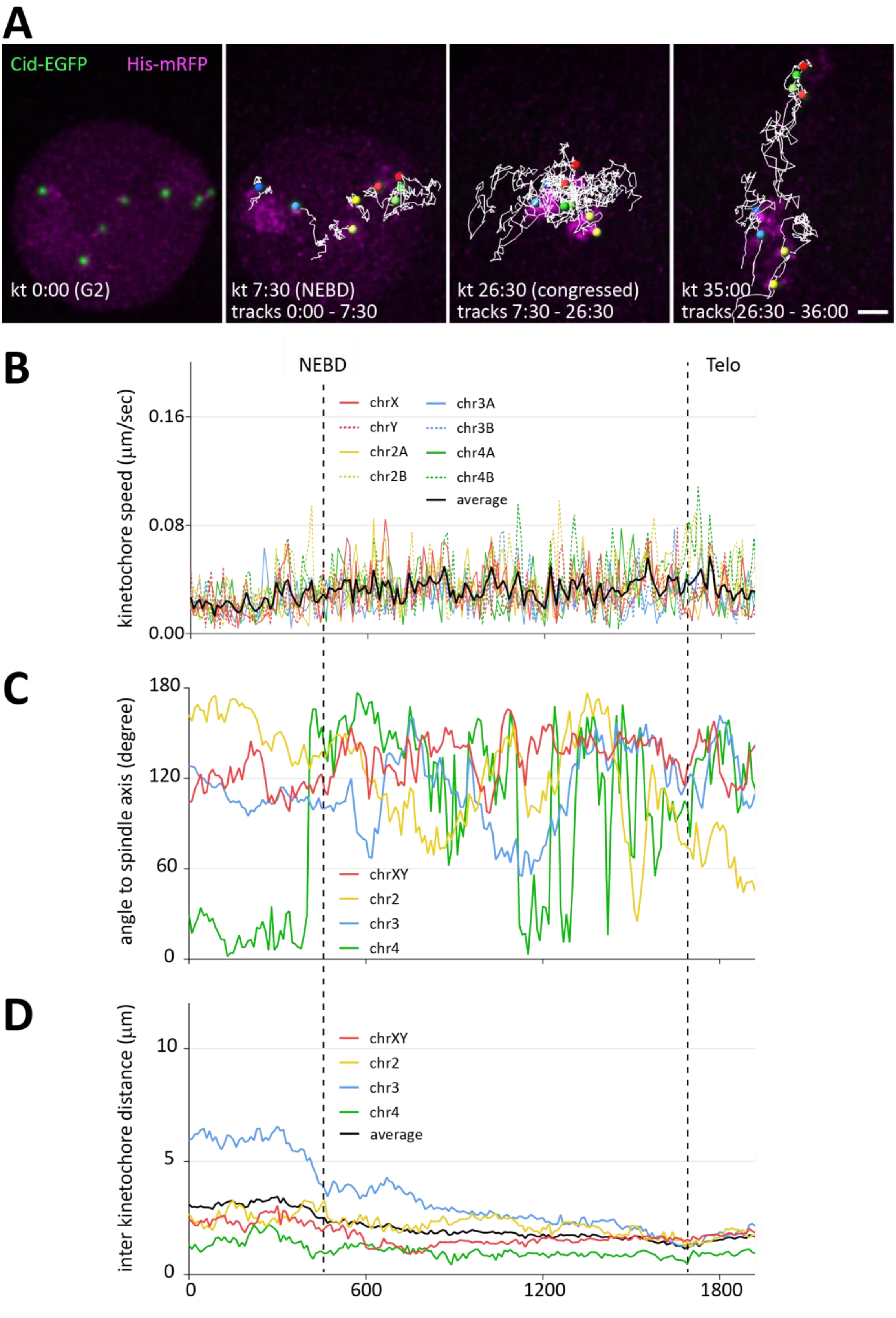
A
Cid-EGFP
His-mRFP
kt 0:00 (G2)
kt 7:30 (NEBD)
tracks 0:00 - 7:30
kt 26:30 (congressed)
tracks 7:30 - 26:30
kt 35:00
tracks 26:30 - 36:00
B
NEBD
Telo
kinetochore speed (µm/sec)
0.16
0.08
0.00
chrX
chrY
chr2A
chr2B
chr3A
chr3B
chr4A
chr4B
average
C
angle to spindle axis (degree)
180
120
60
0
chrXY
chr2
chr3
chr4
D
inter kinetochore distance (µm)
10
5
0
chrXY
chr2
chr3
chr4
average
0
600
1200
1800

Fig 25: Kinetochore movements during meiosis I after Spc105 depletion

Time lapse imaging was performed with spermatocyte cysts expressing *Cid-EGFP* and *His2Av-mRFP* as well as *bamP-GAL4VP16* and *UASt-V20-Spc105*^{RNAi} for Spc105 depletion. All eight centromeres present in a spermatocyte were tracked during meiosis I. **A.** The centromere tracks observed in a representative spermatocyte during the indicated phases are displayed as an overlay on the still frame at the end of the corresponding phase. Centromeres are widely distributed at NEBD (second panel from left) and effectively congressed (third panel from left) before exit from meiosis I. **B.** Curves representing centromere speed over time. **C.** Curves representing the angle between the axis connecting the two homologous centromeres in a bivalent and the spindle axis over time. **D.** Curves representing the distance between the two homologous centromeres in a bivalent over time. Black dotted lines mark phase transitions. Chromosomes are color coded. Scale bar = 3 µm.

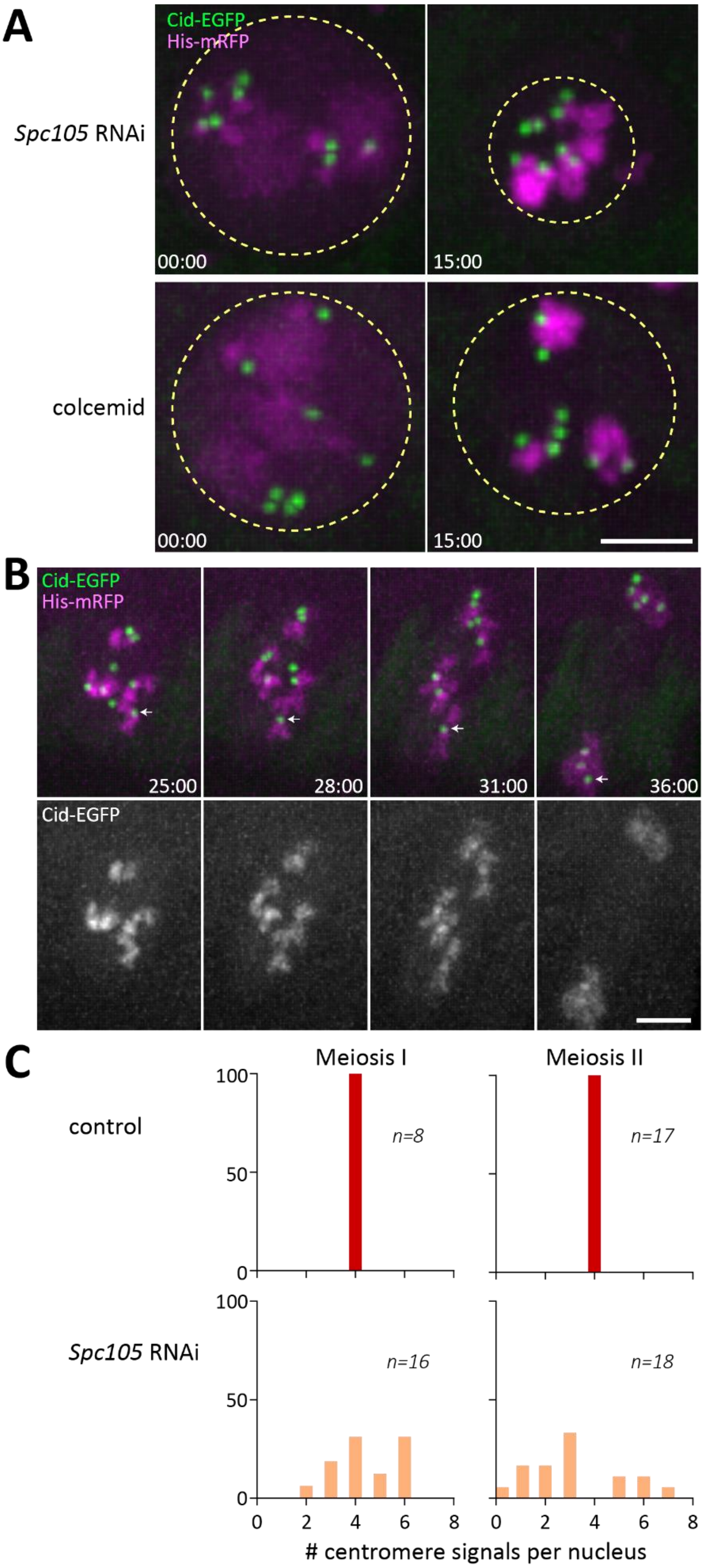
A
Cid-EGFP
His-mRFP
Spc105 RNAi
00:00
15:00
colcemid
00:00
15:00
B
Cid-EGFP
His-mRFP
25:00
28:00
31:00
36:00
Cid-EGFP
C
Meiosis I
Meiosis II
control
n=8
n=17
Spc105 RNAi
n=16
n=18
100
50
0
0
2
4
6
8
centromere signals per nucleus

Fig 26: Chromosome distribution after Spc105 depletion during male meiosis.
Chromosome distribution during meiosis was analyzed by time lapse imaging with spermatocyte cysts expressing *Cid-EGFP* and *His2Av-mRFP.* For kinetochore ablation by Spc105 depletion, the spermatocytes also expressed *bamP-GAL4VP16* and *UASt-V20-Spc105*^{RNAi}. For ablation of microtubules, spermatocytes were treated with colcemid. **A.** The comparison of still frames at the start (00:00) and later in prometaphase (15:00) indicates that congression of bivalents into the central region during meiosis I does not require kinetochore function (top row) but microtubules (bottom row). Yellow dotted circles indicate the regions occupied by chromosomes **B.** Still frames illustrate that the chromosome movements during telophase I that are observed after Spc105 depletion are not led by centromeres. One of the non-leading centromeres is indicated (arrows). Time (min:sec after NEBD) is indicated in the lower right corner. Scale bars = 5 µm. **C.** The counts of the Cid-EGFP dots per cell in daughters generated during MI and MII, respectively, indicate that chromosomes are segregated randomly after Spc105 depletion. While the expected number of four Cid-EGFP dots per cell was observed in all control cells (upper row of histograms), variable numbers were seen after Spc105 depletion (lower row).

To evaluate the role of mechanical tension for meiotic chromosome bi-orientation, we tracked Cid-EGFP dots during meiosis I in *mnm* mutant spermatocytes, in which homolog conjunction is defective. The univalents present during meiosis I in these mutant cells are not expected to attain stable end-on attachment. This expectation is based on the assumption that stable end-on attachment depends on the mechanical tension resulting from pulling forces exerted by the spindle on bi-oriented bivalents during normal meiosis I. Accordingly, the initial part of prometaphase B with the characteristic rapid poleward chromosome jumps (which are presumably mediated by transient lateral interactions of a kinetochore with spindle microtubules), is predicted to persist in *mnm* mutants, in contrast to normal meiosis where these jumps are rapidly followed by bi-orientation within about ten minutes. Indeed, in *mnm* mutants, the rapid kinetochore-led univalent jumps occurred over a greatly extended period (Fig. 27A). Characteristically, a given kinetochore was observed to make about 4.5 times more excursions (i.e., a trip from the polar to the equatorial region, or vice versa) in *mnm* mutants compared to normal meiosis I (see also Fig. 27B). This finding clearly confirms the notion that mechanical tension contributes effectively to stabilization of end-on attachments during normal meiosis I.

Interestingly, however, the rapid jumps and excursions of univalents in *mnm* mutants did not continue throughout meiosis I. Kinetochore speed decreased throughout prometaphase

B (Fig. 27A). After about 25 minutes, kinetochore positions were just as stable as during normal metaphase I (Fig. 27A). Moreover, the large majority of kinetochores were within the central region of the *mnm* mutant cells during this metaphase (Fig. 27B), as if they had achieved bi-orientation.

Since our analyses after Spc105 depletion had revealed kinetochore independent congression of bivalents, it appeared conceivable that in *mnm* mutants the univalent congression was equally independent of bi-orientation. However, in a first class comprising about 40% of all univalents, the Cid-EGFP dots (n = 24 from 3 cells) within the equatorial plane became noticeably elongated along the spindle axis during metaphase I in *mnm* mutants (Fig. 27C,D), suggesting that sister kinetochores were being stretched apart. An estimate of the maximal separation of the sister kinetochores within metaphase I indicated that the separation was on average 330 nm (n = 4 cells from 3 cysts). Therefore, the separation remained clearly below the distance between sister centromeres observed after bi-orientation during normal meiosis II (720 nm; Fig. 15, see also below). But during exit from meiosis I, their separation increased transiently even beyond that observed during metaphase II. Timing and extent of this stretching was variable among the class I univalents. While an unequivocal scoring of the metaphase to anaphase transition during during meiosis I in *mnm* mutant spermatocytes was surprisingly difficult based on the time lapse imaging, telophase I onset was clearly revealed by chromosome decondensation. Assuming that also in *mnm* mutants the metaphase to anaphase transition occurred roughly 10 minutes before telophase onset (Fig. 4), it appeared that this transition was followed rapidly by increased stretching apart of the putative sister kinetochores in case of the most extensively stretched class I univalents (Fig. 27C,D). Moreover, even further stretching occurred after telophase onset (Fig. 27C, D). Many class I univalents were primarily stretched during telophase (Fig. 27 C). All of the class I univalents characterized by stretched Cid-EGFP dots were severely lagging during exit from meiosis I, displaying minimal movements. These observations demonstrate that at least some univalents achieve bi-orientation within the spindle after an extended prometaphase B during meiosis I in *mnm* mutants. In all likelihood, sister kinetochores are linked to opposite poles in these class I chromosomes.

In a comparable number of congressed univalents in *mnm* mutants, however, stretching of the Cid-EGFP signals did not occur during metaphase and exit from meiosis I (Fig. 27C,D). In comparison to the class I univalents, these class II chromosomes were observed to move somewhat faster towards one of the poles when chromosome condensation started. However, kinetochore speed during the movements of chromosomes in this second class was far below that of anaphase in normal meiosis I. Moreover, the movements were not necessarily led by the kinetochore. Finally, in the class III of univalents, in which Cid-EGFP stretching was also absent, poleward chromosome movement was observed earlier, already before the onset of chromosome decondensation (Fig. 27C,D). Moreover, poleward movement in these cases was always led by the kinetochore, even though kinetochore speed was also below normal anaphase I velocities. Based on these observations, we suggest that the kinetochores of class II and III univalents also reached bi-orientation within the meiosis I spindles during the extended prometaphase B. However, rather than having sister kinetochores linked to opposite poles, we assume that either one or both of the closely paired sister kinetochores was merotellically attached to opposite spindle poles. While these merotelic attachments might result in approximate force balance in class II, an imbalance might drive slow poleward movement in class III. Alternative explanations cannot be ruled out. In principle, class III univalents might have monopolar attachments and congression of class II univalents might be kinetochore independent (as observed after Spc105 depletion). Hence these univalents might not have any kinetochore attachments. However, given the remarkable efficiency of bi-orientation during normal meiosis and assuming that loss of *mnm* function only eliminates homolog conjunction without additional effects on kinetochore structure, these alternative interpretations appear to be unlikely.

Within a given *mnm* mutant spermatocyte, the number of class I, II and III univalents was somewhat variable. About 50% did not contain class III univalents. Interestingly, a M/A transition was never plainly apparent in the *mnm* mutant spermatocytes. If the mechanism responsible for keeping sister kinetochores paired was completely inactivated immediately downstream of APC/C and separase activation, a concerted rapid increase in the separation of sister kinetochores comparable to that during normal metaphase II would be expected in all class I univalents, thereby also clearly indicating the M/A transition. However, only few class I univalents displayed a putative sister kinetochore separation already after the inferred time of the M/A transition. The majority of separation occurred later during telophase concomitant with chromosome decondensation. Presumably, it is the spindle that still pulls the sister kinetochores transiently apart in class I univalents during telophase I. Chromosome decondensation in the absence of pulling forces during exit from meiosis I, as after Spc105 depletion, is not accompanied by sister kinetochore separation. We conclude that the increasing separation of sister kinetochores in class I univalents in *mnm* mutant spermatocytes during exit from meiosis I reveals the process of sister kinetochore individualization and suggests that this process is dependent on the M/A transition. Most likely sister kinetochore individualization during exit from meiosis I occurs in steps. In part, sister kinetochore linkage appears to be eliminated already soon after APC/C and separase activation during anaphase I, followed by removal of additional linkage during telophase I perhaps downstream of Cdk1 inactivation.

The separation of sister kinetochores in class I univalents during exit from meiosis I was transient. We assume that the meiosis-specific pericentromeric sister chromatid cohesion, which survives meiosis I and which is provided by the Ord/Solo/Sunn proteins in Drosophila (Bickel et al., 1996; Khetani and Bickel, 2007; Webber et al., 2004; Yan et al., 2010), precludes complete separation and re-installs close apposition of sister kinetochores after spindle disassembly in late telophase I. At the start of interkinesis, sister kinetochores were again closely associated in *mnm* mutants and also at the time of NEBD II, the estimated separation of sister kinetochores in *mnm* mutants was indistinguishable from controls (n= 4 cells, 51 KT pairs, iKTD = 300 +/- 160 nm). These observations demonstrate that after the M/A transition of meiosis I the individualized sister centromeres are still kept in close association by highly elastic tethers. This surprisingly elastic behavior contrasts with the plasticity observed during meiosis II in grasshopper spermatocytes where detachment of bi-oriented chromosomes from metaphase II spindles was not followed by re-association of sister kinetochores (Paliulis and Nicklas, 2005).

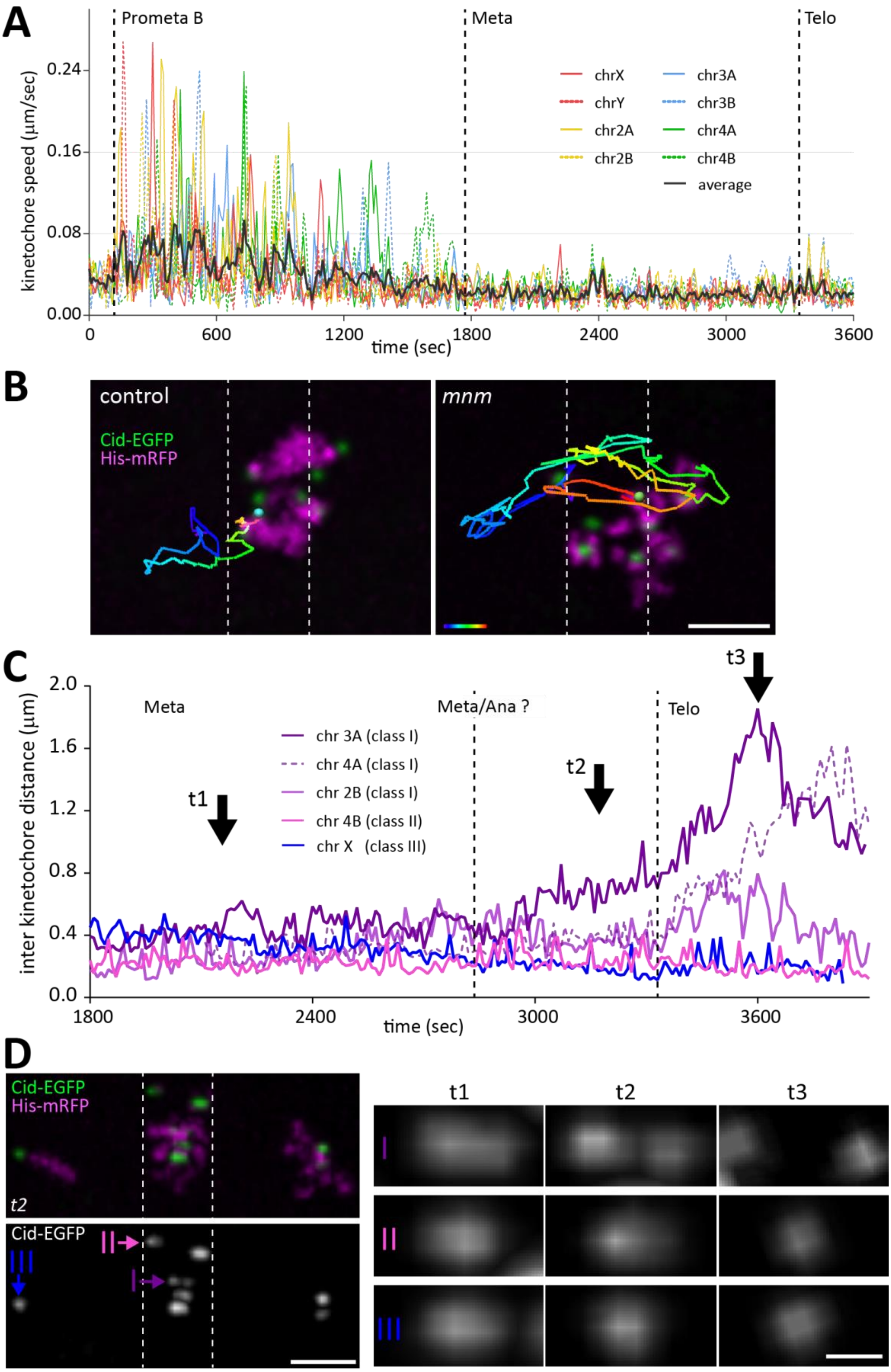
A
Prometa B
Meta
Telo
kinetochore speed (µm/sec)
0.00
0.08
0.16
0.24
0
600
1200
1800
2400
3000
3600
time (sec)
chrX
chrY
chr2A
chr2B
chr3A
chr3B
chr4A
chr4B
average
B
control
Cid-EGFP
His-mRFP
mnm
C
inter kinetochore distance (µm)
0.0
0.4
0.8
1.2
1.6
2.0
1800
2400
3000
3600
time (sec)
Meta
Meta/Ana ?
Telo
t1
t2
t3
chr 3A (class I)
chr 4A (class I)
chr 2B (class I)
chr 4B (class II)
chr X (class III)
D
Cid-EGFP
His-mRFP
t2
Cid-EGFP
III
II
I
t1
t2
t3
I
II
III

Fig 27: Kinetochore behavior in *mnm* mutants during meiosis I
Time lapse imaging was performed with spermatocyte cysts from *mnm* mutant flies expressing *Cid-EGFP* and *His2Av-mRFP* (*w*; Cid-EGFP, His2Av-mRFP/+; mnm*^{3298}/*mnm*^{5578}). All eight centromeres present in a spermatocyte were tracked during meiosis I. **A.** Curves representing centromere speed over time. Black dotted lines mark phase transitions. Note that onset of metaphase in *mnm* mutants was scored when centromere jumps ended rather than after bi-orientation of the last bivalent as in controls. Chromosomes are color coded. **B.** Comparison of centromere tracks in control and *mnm* mutants indicates that centromere migration and re-orientation extends over a longer time period in the absence of homolog conjunction. The track of one representative centromere from NEBD until metaphase is displayed as an overlay on the still frame at metaphase onset. The track color indicates time. The dotted lines demarcate the metaphase plate region (3 µm width corresponding to about ¼ of the pole-to-pole distance). Univalents in *mnm* mutants travel across this midzone far more frequently than the bivalents in controls. Scale bar = 3 µm. **C.** Curves representing the distance between the two sister centromere of a univalent over time. Black dotted lines mark phase transitions. While onset of telophase was detectable, the metaphase to anaphase transition was assumed to be 10 min before telophase onset, as in controls. The arrows (t1, t2, t3) indicate the time points, at which the appearance of the Cid-EGFP signals in representative univalents is illustrated in panel D. Based on centromere behavior, the univalents were assigned to one of three distinct classes (see text). **D.** The characteristic position of the centromere within the cell (left most column), as well as its characteristic appearance at high magnification (additional columns) is illustrated for one representative example from each of the three univalent classes (I, II, III). See (C) for explanation of time points (t1, t2, t3). Scale bar = 3 µm (left most column) and = 0.5 µm (additional columns).

4.3.3 kinetochore tracking during meiosis II

At the start of meiosis II, sister kinetochores are still closely associated side-by-side on one side of the chromosome. This spatial arrangement is predicted to favor mono-orientation. Eventual bi-orientation might therefore require frequent correction of erroneous attachments. To analyze how sister kinetochores arrive at bi-orientation, they were tracked after time lapse imaging of progression through meiosis II in cells expressing *Mis12-EGFP* and *His2Av-mRFP*.

The arrangement of kinetochores and chromosomes at the start of meiosis II was evidently different from that at meiosis I onset. In case of meiosis I, spacing of the large autosomal and XY bivalents and the corresponding kinetochores is maximized by chromosome territory formation in early spermatocytes. In contrast, at the start of meiosis II, dyads were in a Rabl configuration (Fig. 28). During interkinesis, kinetochores remained on the side of the nucleus close to which they were pulled during meiosis I, although the tight centromere clustering at the end of anaphase I was relaxed during telophase I. When chromosomes became visible as a result of re-condensation at the start of the second meiotic division around NEBD, it was evident that chromosome arms still extended away from the kinetochores towards the other end of the nucleus with telomeres being most distal. The fact that the meiosis II spindle axis is perpendicular to that of meiosis I (see Fig. 13B), which positions the sister kinetochores and chromosomes into a Rabl configuration before the onset of meiosis II, might therefore help in avoiding syntelic sister kinetochore attachments (Fig. 28).

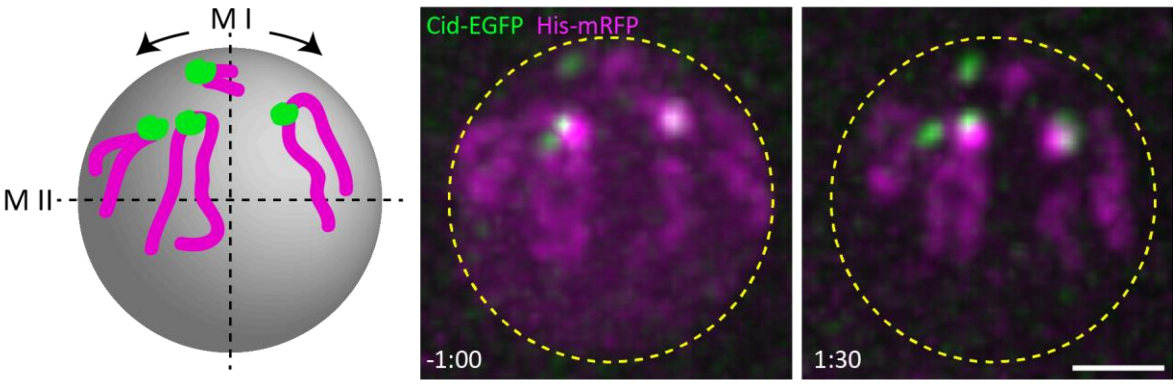

Fig 28: Dyads are in a Rabl orientation at the start of meiosis II
Time lapse imaging was performed with spermatocyte cysts expressing *Cid-EGFP* and *His2Av-mRFP.* A scheme and representative still frames document the distribution of chromosomes and centromeres at the start of meiosis II. Time is indicated in the lower left corner (min:sec), NEBD is at time = 0. All centromeres are together on one side. The chromosome arms with the telomeres at the end extend towards the opposite site. The scheme in the left panel also illustrates the orientation of the axes of the MI and MII spindles by dotted lines. The arrows indicate the direction of migration of the two centrosomes that set up the MII spindle. Scale bar = 2 µm.

Plotting kinetochore speed during progression through meiosis II (Fig. 29A) resulted in curves qualitatively similar to those obtained in case of meiosis I. The initial phase of prometaphase (prometaphase A) was free of individual kinetochore jumps that altered their original kinetochore constellation. In contrast during the following prometaphase B, such kinetochore jumps were clearly present although not quite as rapid as during meiosis I (compare Fig. 24B and 29A), probably reflecting the reduced cell size during meiosis II.

Kinetochore tracking during meiosis in the presence of colcemid (Fig. 30A) and after Spc105 depletion (Fig. 30B) demonstrated that the kinetochore jumps observed during normal prometaphase II were dependent on both functional kinetochores and microtubules. Spc105 depletion also revealed that spindle formation resulted in kinetochore-independent chromosome congression into the central region (Fig. 30D), as already observed in case of meiosis I (Fig. 26A). Moreover, analysis of kinetochore behavior during meiosis II further confirmed that Spc105 depletion resulted in a complete failure of dyad bi-orientation (Fig. 30C). Sister kinetochores were also observed to separate after Spc105 depletion, but compared to normal meiosis II kinetochore, splitting occurred with a considerable temporal delay (on average 14 min later) a few minutes before telophase onset and not strictly in the direction of the spindle axis (Fig. 30C). During telophase, kinetochores moved poleward but sister kinetochores co-segregated (Fig. 30C). Therefore, sister kinetochore separation after Spc105 depletion presumably reflects the elimination of pericentromeric cohesion after the M/A II transition, and kinetochore pair movements during telophase reflect the forces exerted by the contractile furrow.

Interestingly, prometaphase B was surprisingly short during meiosis II. In the example illustrated in Fig. 29, it took only five minutes between the first jumps and bi-orientation of the last dyad. Average duration was only 7 +/- 2 min (n = 20 KT pairs; 2 cysts). Bi-orientation was clearly also revealed by analysis of both the angle between inter sister kinetochore and spindle axis (Fig. 29C) and the distance between sister kinetochores (Fig. 29B). Tracking the inter sister kinetochore distance over time confirmed that pulling forces resulting from attachment to kinetochore microtubules is primarily responsible for the separation of sister kinetochores, as revealed by the earlier measurements at selected time points and in different conditions (Fig 15 and 17). As illustrated (Fig. 29D), it was usually a poleward kinetochore jump that initiated sister kinetochore separation. Before the first jump, sister kinetochores remained closely associated (except for rare occasional breathing events). The jump movement of the leading sister kinetochore led also to orientation of the inter sister kinetochore axis along the spindle axis. Rapidly thereafter sister kinetochores established bi-orientation, as suggested by their increasing spatial separation. This first stretching event was then followed by congression into the metaphase plate and stable maintenance of bi-orientation until anaphase (Fig. 29D). Only rarely, an initial bi-orientation was observed to be released before reaching stable bi-orientation in a second stretching event (Fig. 29E). Careful tracking of five cells, i.e. 20 dyad chromosomes, revealed only one such unequivocal release after bi-orientation and recapture (Fig. 29E) and two additional less prominent cases. We conclude that despite the initial side by side organization of sister kinetochores, their bi-orientation occurs with breathtaking speed usually at first attempt. As discussed, this remarkable bi-orientation efficacy presumably requires an exquisite tension sensitivity of kinetochore attachments to spindle microtubules.

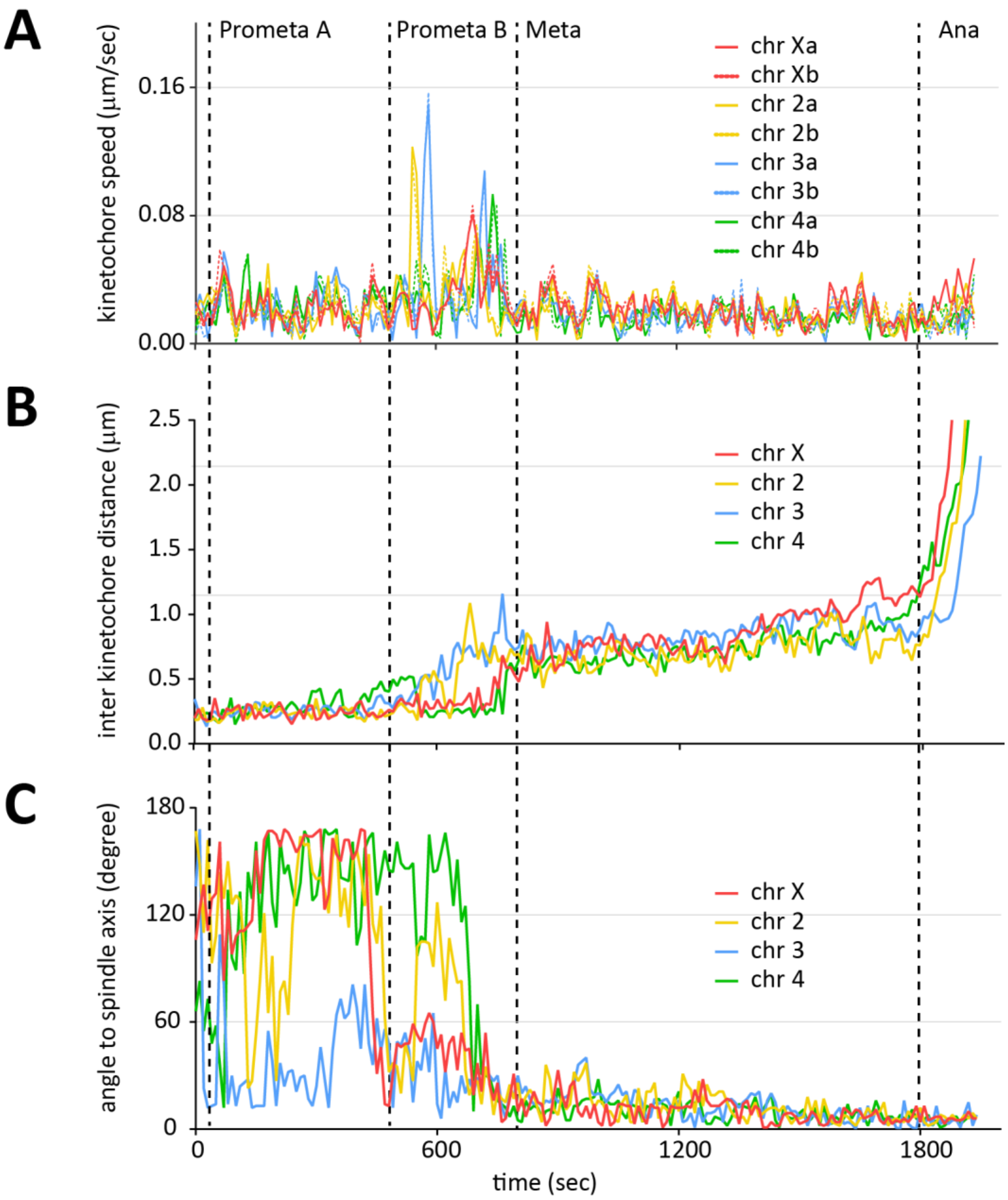

Fig 29: Kinetochore movements during meiosis II

Time lapse imaging was performed with spermatocyte cysts expressing *Mis12-EGFP* and *His2Av-mRFP* (*w*; His2Av-mRFP; Mis12-EGFP II.2*). All eight kinetochores present in a spermatocyte were tracked during meiosis II. Data from a representative cell is shown. **A.** Curves representing kinetochore speed over time. **B.** Curves representing the distance between the two sister kinetochores in a dyad over time. **C.** Curves representing the angle between the axis connecting the two sister kinetochores in a dyad and the spindle axis over time. Black dotted lines mark phase transitions. Chromosomes are color coded. (*Continued on next page*)

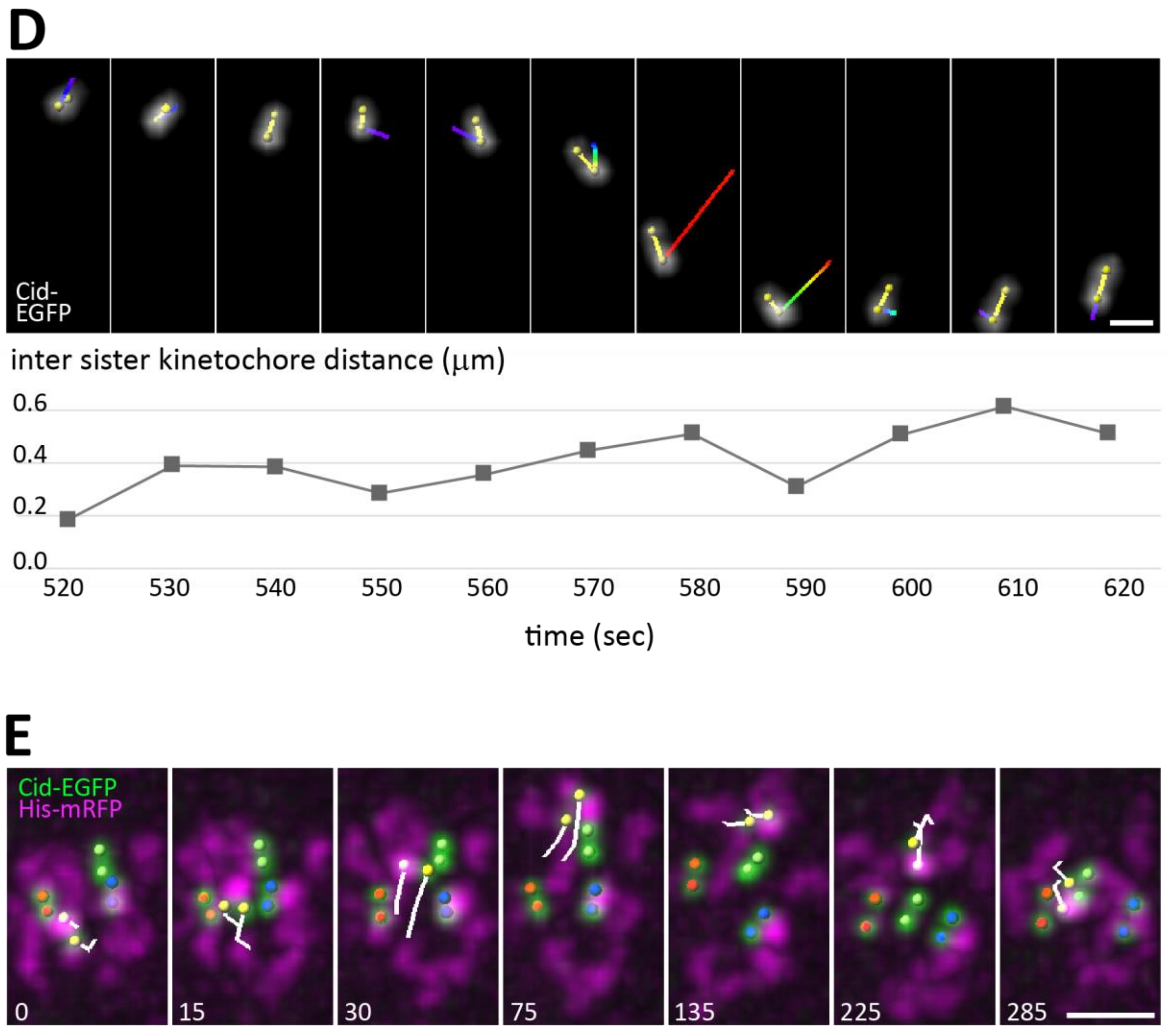

D. Still frames with high magnification views of a sister kinetochore pair and a graph of the distance between the two sister kinetochores (yellow line in stills) at the corresponding time points documenting a characteristic bi-orientation event. The track overlay describes the displacement of one sister kinetochore from the preceding to the displayed time point. Track color indicates speed. Spindle axis is vertical. At around 550 sec (after NEBD) the sister kinetochore with overlaid tracks takes the lead in a movement to the lower spindle pole that transiently stretches the kinetochores apart. At around 610 sec, the other sister kinetochore is stretched away towards the upper pole. Thereafter the sister kinetochore pair starts the final congression movement into the metaphase plate (not shown). Scale bar = 0.7 µm. **E.** Still frames documenting one of the rare re-orientation events. The dyad with the kinetochores marked in yellow moves out of the metaphase towards the upper spindle pole and returns back into the metaphase plate with the sister kinetochores in flipped orientation. Time is indicated in the lower left corner (sec). Spindle axis is vertical. Scale bar = 2 µm.

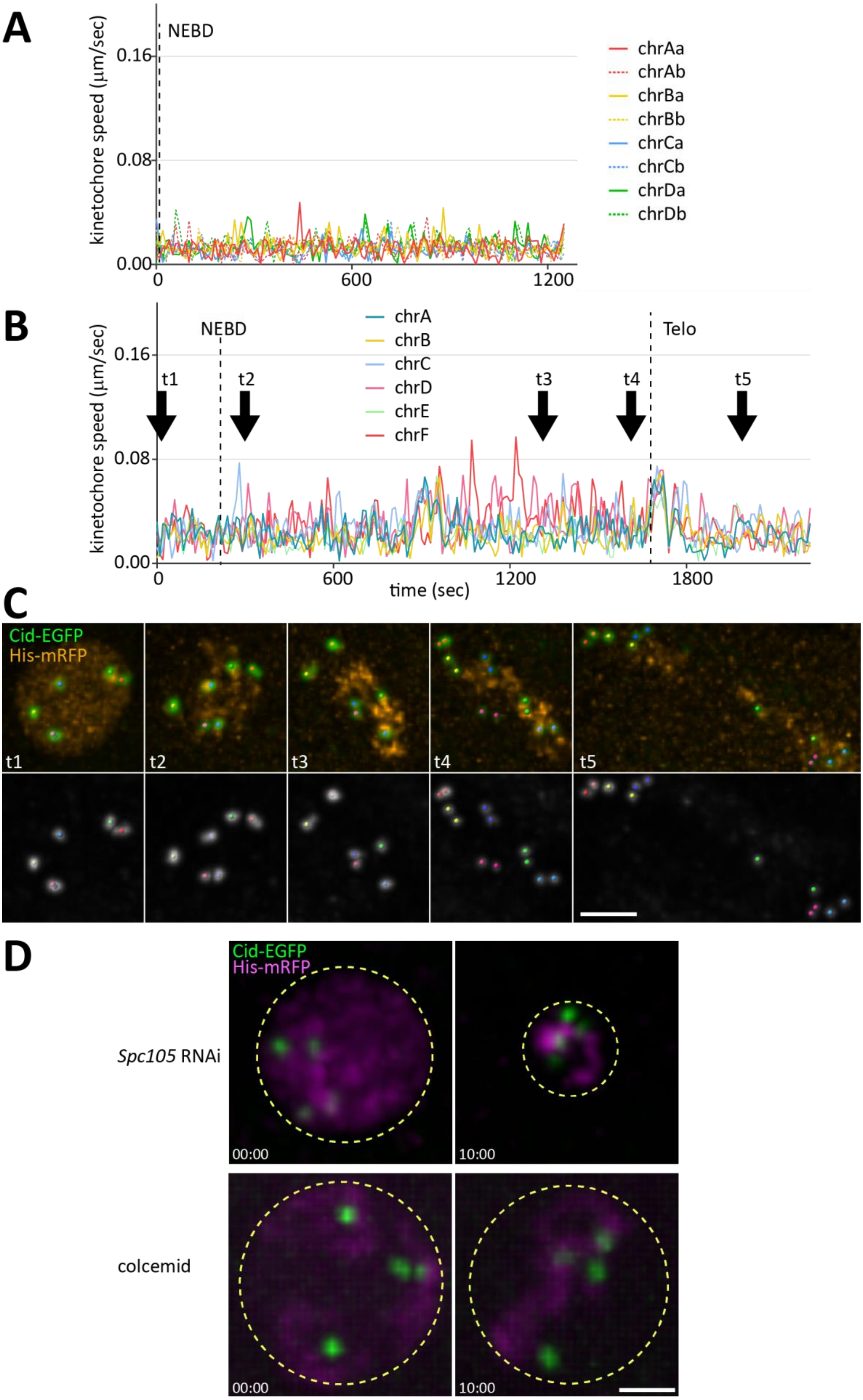
A
kinetochore speed (µm/sec)
NEBD
0.16
0.08
0.00
0
600
1200
chrAa
chrAb
chrBa
chrBb
chrCa
chrCb
chrDa
chrDb
B
kinetochore speed (µm/sec)
NEBD
Telo
t1
t2
t3
t4
t5
chrA
chrB
chrC
chrD
chrE
chrF
0.16
0.08
0.00
0
600
1200
1800
time (sec)
C
Cid-EGFP
His-mRFP
t1
t2
t3
t4
t5
D
Cid-EGFP
His-mRFP
Spc105 RNAi
colcemid
00:00
10:00
00:00
10:00

Fig 30: Centromere movements during meiosis II after ablation of kinetochores and microtubules
Centromere movements during meiosis II were analyzed by time lapse imaging with spermatocyte cysts expressing *Cid-EGFP* and *His2Av-mRFP.* For ablation of microtubules, spermatocytes were treated with colcemid. For kinetochore ablation by Spc105 depletion, the spermatocytes also expressed *bamP-GAL4VP16* and *UASt-V20-Spc105*^{RNAi}. **A.** Curves describing centromere speed after Colcemid administration. **B.** Curves describing centromere speed after Spc105 depletion. Black bars (t1-t5) indicate the time points at which chromosome and centromere distribution is illustrated with the still frames shown in (C). **C.** Still frames at selected time points (see B) illustrate delayed sister kinetochore separation and chromosome movements during exit from MII concomitant with chromosome decondensation in the absence of kinetochore function presumably by the forces exerted by the contractile furrow. Sister kinetochores are co-segregated during these movements, rather than segregated apart as in normal MII. Scale bar = 3 µm. **D.** The comparison of still frames at the start (00:00) and later in prometaphase (10:00) indicates that congression of dyads into the central region during meiosis II does not require kinetochore function (top row) but microtubules (bottom row). Yellow dotted circles indicate the regions occupied by chromosomes. Scale bar = 2 µm.

Discussion

The meiotic divisions are of paramount importance for sexual reproduction of eukaryotes. The two meiotic divisions achieve genome ploidy reduction from diploid to haploid. Moreover, these divisions contribute to increased genetic diversity by segregating novel combinations of parental alleles into the haploid cells. Therefore, chromosome segregation during the meiotic divisions is in part stochastic. But many aspects of the chromosome distribution process need to be regulated very accurately for the generation of functional euploid gametes. As meiotic divisions share many similarities with mitotic divisions, which are far more accessible experimentally, some of the regulatory mechanisms are already well understood at the molecular level. Yet the most interesting meiosis-specific aspects are still only very poorly understood.

My PhD thesis research was intended to promote future mechanistic understanding of how the meiotic divisions succeed in producing euploid products. In an initial step, an efficient protocol was established allowing time lapse imaging of progression through both meiotic divisions with high temporal and spatial resolution with intact cysts of spermatocytes from *D. melanogaster*. While comparable high resolution imaging of both meiotic divisions has already been achieved with yeast, previous studies in animals were focused primarily on meiosis I in oocytes where spindle assembly and temporal dynamics are strikingly different (Holubcova et al., 2015; Kitajima et al., 2011; Webster and Schuh, 2017).

Exploiting this protocol, the temporal schedule of progression through meiosis I and II in spermatocyte cysts was characterized. The 16 spermatocytes within a cyst are interconnected by ring canals in *D. melanogaster*, similar to gonial cells in other animals including mammals. My analyses established that a wave of entry into meiosis spreads primarily from cell to interconnected cell at a rate of about 1.5 min per cell. Moreover, the temporal order of entry into meiosis I was found to predict also the dynamics of all subsequent progress through meiosis rather well. Therefore, in contrast to cultured mammalian cells, where the timing of anaphase onset and hence the complete mitosis is highly variable as a result of the stochasticity of kinetochore capture (Dick and Gerlich, 2013; Held et al., 2010; Rieder et al., 1994), progression through male meiosis in *D. melanogaster* is largely governed by a timer rather than by the stochasticity of kinetochore capture. This timer provides sufficient time for complete bi-orientation of all chromosomes before anaphase onset even when the SAC component Mad2 is absent and therefore anaphase onset during both meiosis I and II modestly advanced.

In principle, a timer governed, SAC-independent control is predicted to result in a slow progression through meiosis. The timer needs to delay anaphase onset to the point where the probability of having reached the correct bi-orientation of all chromosomes is close to 100%, while SAC control enables anaphase onset soon after bi-orientation of the last chromosome. Yet male meiosis in *D. melanogaster* is rather fast. As shown here, this reflects a remarkable efficiency of chromosome bi-orientation. On average the time between the first kinetochore microtubule contact until bi-orientation of the last chromosome was below 10 minutes during both meiosis I and II (compared to about 12 hours in meiosis I in human oocytes (Holubcova et al., 2015).

In case of meiosis II in *D. melanogaster* spermatocytes, the high efficiency of chromosome bi-orientation is even more surprising since my results unequivocally establish that sister kinetochores are still very closely associated in a side-by-side (SS) configuration on the same chromosome face rather than separated back-to-back (BB) with the chromosome in between. SS is predicted to cause far more initial erroneous syntelic and merotelic chromosome attachments to the spindle than BB (Hauf and Watanabe, 2004; Lampson and Grishchuk, 2017). Correction of initial attachment errors is predicted to require time.

To define features that might contribute to the high efficiency of chromosome bi-orientation in *D. melanogaster* spermatocytes, the dynamics of kinetochore and spindle assembly was analyzed. Moreover, to evaluate the role of mechanical tension in the bi-orientation process during meiosis I, centromeres were tracked in *mnm* mutant spermatocytes where univalents instead of bivalents with conjoined homologs are present. As discussed below, my observations are best explained by a model for bi-orientation in which initial end-on attachments occur rarely, in part because they are highly unstable in the absence of mechanical tension as resulting from proper amphitelic attachments to the spindle. However, the dependence of attachment stability on mechanical tension appears to decrease strongly with time, promoting the growth of strong KT-MT bundles during metaphase.

A timer governs the dynamics of progression through meiosis in *D. melanogaster* males

The preparations established here appear to preserve cyst integrity and viability better than previously published protocols for time lapse imaging of progression through meiosis with spermatocytes. Therefore, an analysis of temporal dynamics within a cyst over the complete meiotic process (meiosis I, interkinesis, meiosis II) was possible. Monitoring a ring canal marker (Septin2-GFP) in combination with His2Av-mRFP allowed an initial comparison of cell interconnectivity with the pattern, in which entry into meiosis I spreads across the cyst. The results demonstrate that meiosis I does not start invariably in one of the two cells that have the maximal number of four connected neighboring cells. In egg chambers of *D. melanogaster* females, the two germline cells with four ring canals have the highest meiotic potential. They assemble the most complete SCs. One of them, the oocyte, eventually completes meiosis, while the other along with the 14 additional germline cells in the cluster differentiates as a nurse cells rather than continuing the meiotic process (Lake and Hawley, 2012). Transport processes in combination with germline cell connectivity in egg chambers control important developomental decisions during oogenesis (Roth and Lynch, 2009). It remains also conceivable that spermatocyte connectivity determines Cdk1 regulator accumulation in a pattern that lowers meiosis initiation potential in cells with many ring canals, while the opposite is incompatible with the presented findings. Indeed, as male meiosis I was observed to start in cells with only one ring canal, this might be the rule. However, as only few cysts were analyzed and as 50% of the spermatocytes have only one ring canal, the data cannot exclude a random onset of meiosis I with the 16 cell cyst. While additional analyses are required to resolve the issue, my data strongly supports the speculation that positive feedback loops, as those activating Cdk1 during entry into mitosis, might spread the wave of entry into meiosis through ring canal connections. The entry wave was observed to spread largely along cell interconnections, although occasional activation of an additional wave origin in a distant spermatocyte appears to occur as well.

The particular pattern of entry into meiosis I that was observed within a cyst was repeated with only minor deviations during subsequent progression through meiosis. The transition from metaphase to anaphase I, entry into interkinesis and into meiosis II, as well as onset of anaphase II all occurred in a highly similar pattern. This finding strongly suggests that progression through male meiosis in *D. melanogaster* is primarily controlled by a timer mechanism. Cdk1 activation at entry into meiosis I for example might start a chain of reactions that dictates progression through meiosis.

Timing by autonomous oscillations in Cdk1 activity has been demonstrated most convincingly during progression through the early embryonic cleavage cycles in *Xenopus laevis*. During these mitotic cell cycles, surveillance pathways like the DNA damage/replication checkpoint and the spindle assembly checkpoint (SAC) are not functional. Thus problems during S or M phase cannot delay the Cdk1 oscillations which proceed with a pace that grants time windows for S and M phase that are sufficient for successful completion of these processes in unperturbed conditions.

In contrast, the SAC is functional during both meiotic divisions in *D. melanogaster* spermatocytes. In fact, my analyses demonstrate that the SAC is more robust during male meiosis than suggested so far (Buffin et al., 2007; Rebollo and Gonzalez, 2000). Nevertheless, SAC robustness in *D. melanogaster* male meiosis is modest in comparison to mammalian cells in culture. While exit from M phase was found to be delayed for up to 80 min by inhibition of microtubule assembly during meiosis I in *D. melanogaster* spermatocytes, the delay imposed by this condition can be as long as 24 hours in cultured human cells. Among different *D. melanogaster* cell types, SAC robustness varies considerably. Slippage out of a SAC arrest triggered by colcemid was reported to occur after average 5-7 hours in larval neuroblasts (Mirkovic et al., 2015) and cultured S2R+ cells, after >60 min in syncytial early embryos, after 30 min in cellularized embryos (Althoff, 2011). My findings indicate that SAC robustness is also different in meiosis I compared to meiosis II. The increase in SAC robustness during *C. elegans* embryogenesis has recently been ascribed to an accompanying decrease in cell size. In *D. melanogaster* male meiosis, cell size in meiosis II is also decreased compared to meiosis I (by 50%) but SAC robustness is actually lower rather than increased as expected based on the analyses during *C. elegans* development. In mouse oocytes, SAC-mediated delay during MI is far more extensive when it is triggered by univalents compared to prematurely separated sisters. Therefore, differences in kinetochore structure during MI and MII might explain why SAC robustness during *D. melanogaster* male meiosis I and II is distinct. In addition, rates of synthesis and degradation of certain SAC components might vary during progression through meiosis with consequences for SAC robustness.

While the SAC is clearly functional during *D. melanogaster* male meiosis, it is actually not required for normal meiotic chromosome segregation in otherwise unperturbed conditions. My findings demonstrate that chromosomes are not, or at most very rarely, missegregated when *mad2* null mutant spermatocytes progress through meiosis even though. Mad2 is an essential SAC component.

While chromosome segregation in the absence of Mad2 is largely normal during *D. melanogaster* male meiosis, the temporal dynamics of progression through the meiotic divisions is not normal. During both divisions, anaphase onset occurs prematurely in the *mad2* mutants. In principle, this premature anaphase onset might indicate that during normal meiosis the unattached kinetochores, which are necessarily present at the start of the meiotic divisions, activate the SAC transiently to the effect that the SAC delays anaphase onset for about 5-10 minutes beyond the time point where the autonomous timer mechanism gives permission for anaphase onset. Alternatively, as SAC components have also been proposed to be involved in controlling the speed of the autonomous timer in a manner that does not involve activation by unattached kinetochores (Meraldi et al., 2004a; Rahmani et al., 2009; Rodriguez-Bravo et al., 2014), it remains a possibility that the premature anaphase onset observed in *mad2* mutants meiosis reflects such a kinetochore status independent change in timer dynamics. While the precise mechanism is not yet clear, it is evident that the advancement of anaphase onset during the meiotic divisions in *mad2* mutants is not of an extent interfering with regular chromosome segregation. Even in the absence of *mad2* function, the timer sets anaphase onset to a time point where chromosomes are already properly bi-oriented in the large majority of spermatocytes. In other words, *mad2* loss of function does not advance the metaphase to anaphase transition so much that it occurs already before completion of prometaphase. The advancement only truncates metaphase (by about 50% of its normal length).

Chromosome bi-orientation during Drosophila male meiosis is highly efficient

SAC function is not needed in *D. melanogaster* male meiosis because chromosome bi-orientation succeeds rapidly. Tracking of kinetochores at high temporal and spatial resolution precisely revealed both the onset of their interactions with microtubules (as kinetochore jumps) as well as the final bi-orientation of the last chromosome. The corresponding interval (designated here as prometaphase B) is below 10 minutes during both MI and MII. Prometaphase B during MI in *D. melanogaster* spermatocytes is therefore about 50-100 fold faster than during MI in mouse and human oocytes (Holubcova et al., 2015; Kitajima et al., 2011; Webster and Schuh, 2017). Moreover, the turnover of kinetochore attachments (attachment of a kinetochore to the spindle followed by release) during meiosis I in mammalian oocytes is considerably higher compared to meiosis I in *D. melanogaster* spermatocytes. In these latter cells, the bipolar attachment of a bivalent with the spindle is almost never released after congression into the metaphase I plate (as indicated by chromosome position, stretch between the two kinetochores and angle between interkinetochore and spindle axis). In contrast, in human oocytes even correct attachments are not necessarily stable in metaphase I (Webster and Schuh, 2017).

How is the high efficiency of bi-orientation during *D. melanogaster* male meiosis achieved? Modeling of chromosome bi-orientation in mitosis has indicated that it can be achieved by a relatively simple mechanism in principle (Lampson and Grishchuk, 2017; Zaytsev and Grishchuk, 2015). All that is required for this most basic mechanism is a spatial arrangement of the two kinetochores making amphitelic attachments more probable than syntelic and merotelic attachments, in combination with occasional stochastic kinetochore attachment turnover. The optimal arrangement of the two kinetochores for this mechanism is back-to back (BB) with chromatin in between. The chromatin shields the kinetochores. Contact with microtubules at the front side of the kinetochore is possible, but not on the shielded back side. Once a stochastic search and capture process has established an initial microtubule connection between a kinetochore and a given spindle pole, the ensuing pull towards this pole will turn the front side of the unattached lagging kinetochore towards the opposite spindle pole, thereby favoring a subsequent correct bipolar attachment when microtubule from this opposite pole hit the unattached kinetochore. Occasional release of kinetochore attachments allows for correction of some rare initial attachment errors. After an erroneously attached chromosome is again released from the spindle, the geometrical attachment bias will favor a correct bipolar attachment during subsequent bi-orientation attempts. The efficiency of this bi-orientation mechanism depends strongly on the strength of the geometric bias.

Clearly, the kinetochore arrangement at the start of meiosis I and II in *D. melanogaster* spermatocytes is not favoring bipolar attachment geometrically. In MI the two kinetochores of a bivalent are far apart. The chromatin in between is readily deformed, as indicated by my time lapse imaging. Thus the two kinetochores are not necessarily presented with their fronts directed to opposite sides. Moreover, the HS organization revealed by EM (Goldstein, 1981) maximizes the probability of initial microtubule capture at the expense of shielding. In MII, the two sister kinetochores are closely associated in an SS arrangement. While a BB arrangement at the start of MII has been proposed earlier (Church, 1988), my results demonstrate unequivocally the presence of an SS arrangement at the start of MI that is converted into a BB arrangement as a consequence of bi-orientation. Rather than minimizing the probability of syntelic and merotelic attachments, the SS configuration at the start of MII is maximizing the probability of initial erroneous attachments and time consuming error correction. As neither BB geometry nor frequent and time-consuming error correction is characteristic for *D. melanogaster* male meiosis, the simplest model for chromosome bi-orientation is quite inadequate for these divisions.

However, modeling also confirms that regulation of the stability of kinetochore-spindle attachments can greatly improve the efficiency of error correction and chromosome bi-orientation overall (Lampson and Grishchuk, 2017; Zaytsev and Grishchuk, 2015). Thereby the trial and error mode of the most basic model is supplemented by Darwinian selection of correct attachments. Classic experiments have definitively established that mechanical tension can stabilize attachments (Nicklas and Koch, 1969). Accordingly, amphitelic attachments which result in forces pulling the two kinetochores of a bivalent to opposite poles are expected to generate mechanical tension stabilizing these correct attachments. In contrast, lack of comparable mechanical tension generated by incorrect attachments (syntelic and to a lesser degree also merotelic) is predicted to permit attachment turnover. The classic experiments involved chromosome micromanipulation during meiosis I in grasshopper spermatocytes. Micromanipulation of bivalents is feasible with *D. melanogaster* spermatocytes (Church et al., 1986) but even more demanding as even the largest chromosomes are smaller and meiosis I considerably faster than in grasshopper (about 1 hour versus 6 hours). Therefore to study the role of mechanical tension I performed kinetochore tracking in *mnm* mutants. *mnm* function is required for homolog conjunction during *D. melanogaster* male meiosis (Thomas et al., 2005).

My observations demonstrate that bivalents of normal appearance which are occasionally still present at NEBD I in *mnm* mutants are rapidly converted into univalents when microtubules start to interact with chromosomes. Compared to bivalents during normal meiosis I, the univalents oscillate for an extended period between spindle poles in *mnm* mutants, but they become stable eventually before exit from meiosis I. While chromosome position and inter sister kinetochore distance indicate that some of the univalents (class I) are stabilized as a result of sister kinetochore bi-orientation in *mnm* mutants, others maintain a stable position without any indications for sister kinetochore bi-orientation (class III). The observed extended period of extensive chromosome movements indicates that mechanical tension has a strong stabilizing effect on correct kinetochore-spindle attachments during normal meiosis. Moreover, the eventual stabilization of even class III univalents suggests that the stability of kinetochore-spindle attachments (including incorrect attachments) increases over time. The eventual stabilization presumably also results in SAC silencing and explains that the delay of meiosis I completion observed in *mnm* mutants is limited (10 minutes) and far lower than in the presence of colcemid.

Global stabilization of KT-MT attachments over time has also been described during mitosis in cultured mammalian cells (Kabeche and Compton, 2013), larval Drosophila neuroblasts (Mirkovic et al., 2015) and during meiosis I in mouse oocytes (Davydenko et al., 2013; Yoshida et al., 2015). Interestingly, the molecular basis of progressive global stabilization of attachments is distinct in somatic cells and mouse oocytes. While a decrease in Cdk1 activity causes progressive stabilization in somatic cells (Kabeche and Compton, 2013; Mirkovic et al., 2015), the opposite (a gradual increase in Cdk1 activity) is observed in oocytes (Davydenko et al., 2013). Further analyses will be required to clarify the mechanism operating during *D. melanogaster* male meiosis.

Based on my analyses, the following factors appear to be crucial for the remarkable efficiency of chromosome bi-orientation during *D. melanogaster* male meiosis.

1. Microtubule dynamics during spindle assembly causes a kinetochore independent gathering of chromosomes within the central region. This is the opposite of what happens in

mouse and human oocytes during meiosis I where central microtubule bundles displace the bivalents to the periphery into an equatorial prometaphase belt around the forming spindle with very broad acentrosomal poles (Holubcova et al., 2015; Kitajima et al., 2011). Efficient spindle pole focusing and bundling of inner nuclear microtubules is proposed to make a major contribution to the central chromosome gathering in particular during meiosis I in *D. melanogaster* spermatocytes. In addition, an axis of spindle formation perpendicular to the Rabl orientation of dyads is proposed to favor the efficiency of correct chromosome bi-orientation during meiosis II in secondary spermatocytes.

2. Initial poleward kinetochore jumps presumably mediated by lateral interactions between microtubules and kinetochore-bound dynein orient the inter kinetochore axis along the spindle axis. This generates a strong geometric bias favoring correct bipolar attachments over incorrect attachments (syntelic, merotelic).

3. End-on attachments develop rarely during the initial phase of prometaphase B. End-on attachments are highly unstable unless stabilized by mechanical tension resulting from correct bi-orientation. Correctly bi-oriented chromosomes therefore will accumulate over time.

4. The eventual global stabilization of attachments allows the development of strong KT-MT bundles on bi-oriented chromosomes for subsequent poleward segregation during anaphase.

As a result of these and perhaps additional features, erroneous attachments occur rarely and persist only very briefly when happening nevertheless during the meiotic divisions in *D. melanogaster* spermatocytes.

Sister kinetochore association is established by an elastic linkage during meiosis I

The meiosis I-specific sister kinetochore mono-orientation is crucial for regular segregation of homologs during meiosis I. The mechanisms that conjoin sister centromeres before meiosis I and enforce the assembly of a kinetochore structure, in which the two sister kinetochores cooperate in a single functional unit rather than individually, are still very poorly understood at the molecular level. The conversion that restores functional individuality of sister centromeres before meiosis II allowing sister kinetochore segregation during meiosis is equally important and poorly understood.

My time lapse imaging at high spatial and temporal resolution demonstrates that the conjunction of sister centromeres before meiosis I is not mediated by a rigid persistent molecular clamp. Such a clamp is not compatible with the occasional transient sister centromere breathing that was observed to occur during late G2, as well as during MI, interkinesis and early MII.

The monopolin complex is thought to function as a rigid clamp directly crosslinking the two sister kinetochores (Ye et al., 2016) but it is not excluded that the occasional transient release of one or the other sister kinetochore might occur. The meiosis-specific monopolin complex subunit appears to be specific to budding yeast and closely related species. Meikin/Moa1/Spo13 and meiosis-specific cohesin complexes are the factors implicated in sister centromere conjunction before meiosis I in fission yeast, plants and animals (Kim et al., 2015; Lee et al., 2002; Shonn et al., 2002; Yokobayashi and Watanabe, 2005). In *D. melanogaster*, a meikin homolog has not yet been identified. Moreover, the meiosis-specific cohesin complex appears to be unusual as it does not appear to include a Rec8-like α- kleisin. Instead, the protein products of the genes *ord*, *solo* and *sunn* appear to deliver the functions provided by Rec8 cohesin in other eukaryotes (Bickel et al., 1996; Goldstein, 1980; Gyuricza et al., 2016; Krishnan et al., 2014; Mason, 1976; Yan and McKee, 2013; Yan et al., 2010). These genes are required for sister centromere mono-orientation during meiosis I in both sexes.

It is not clear whether these proteins act directly within the Cid/Cenp-A containing centromere-specific chromatin. While the majority localizes to the pericentromeric region, it is not excluded that low but functional important amounts are present within the centromeric region. Occasional transient sister centromere breathing appears to be quite inconceivable if the sister centromeres are conjoined by multiple cohesin complexes throughout the centromere chromatin domain. In this case, breathing would require transient dissociation of all the cohesin complexes. On the other hand, if these complexes join the pericentromeric regions of sister chromatids, sister centromere breathing would be readily possible. However, as these complexes in the pericentromeric regions perdure until late metaphase II, they cannot be sufficient to enforce sister centromere conjunction. Otherwise, the sister centromeres would remain conjoined at the start of meiosis II. Therefore, they presumably cooperate with other yet unknown factors to enforce sister centromere conjoining before meiosis I.

Recent findings in *D. melanogaster* female meiosis have implicated the KMN component Spc105 in sister centromere conjoining (Radford et al., 2015). It might contribute to centromere localization of the postulated unknown factor. My results indicate that the Spc105 requirement for sister centromere conjoining during male meiosis is far more limited compared to female meiosis. While the spermatocyte-specific Spc105 knockdown resulted in a kinetochore null phenotype, sister centromeres remained largely conjoined in contrast to female meiosis (Radford et al., 2015). However, centromere breathing during male meiosis was observed to be increased clearly. It is conceivable that Spc105 contributes to protection of pericentromeric cohesin against the prophase cohesin release pathway. After Spc105 knockdown, decreased amount of pericentromeric cohesion might allow more pronounced breathing. My finding that Spc105 depletion in *mnm* or *snm* mutants did not result in more pronounced sister centromere disjoining before meiosis I demonstrates that the different significance of Spc105 for sister centromere joining in the two sexes does not reflect the function of the alternative homolog conjunction system in males. Interestingly, however, my time lapse imaging indicated that the alternative homolog conjunction complex does not just conjoin homologs but also sister chromatids at least in the arm regions. Apart from the pericentromeric Ord/Solo/Sunn meiotic cohesin there might not be any cohesin left after NEBD I within the arm region. Accordingly, the alternative homolog conjunction complex might be the only factor keeping sister chromatids joined within the arm regions.

The behavior of sister kinetochores during meiosis I in *mnm* mutants revealed by my time lapse imaging provides further confirmation that sister kinetochore are in a functionally distinct state at the start of meiosis I and II. While the sister kinetochores of univalents present in *mnm* mutants get bi-oriented occasionally during prometaphase I, this happens more slowly compared to their bi-orientation in dyads present during normal meiosis II. Moreover, the separation between sister kinetochores caused by bi-orientation during meiosis I in *mnm* mutants is less than what is observed in normal metaphase II.

My time-resolved analysis of the distance between bi-oriented sister kinetochores during meiosis I in *mnm* mutants suggests that elimination of sister centromere conjunction might occur downstream of APC/C activation. In some of the bi-oriented univalents in *mnm* mutant meiosis I, the distance between sister kinetochores was observed to increase around the time when APC/C is expected to become active. APC/C activation might cause sister centromere individualization indirectly via securin degradation and separase activation. However, earlier analyses have suggested that separase activity is not required for the individualization of sister centromeres (Blattner et al., 2016). APC/C activity might therefore target a factor other than securin to bring about sister centromere individualization during meiosis I. Moreover, since APC/C activity was not monitored directly during my time lapse imaging, the above suggestion remains speculative. It will yet have to be proven that the eventual increased separation of sister kinetochores in some of the bi-oriented univalents during meiosis I in *mnm* mutants occurs indeed downstream of APC/C activation. An alternative explanation for the increasing separation of sister kinetochore in some of the bi-oriented univalents present in *mnm* mutants is cohesion fatigue (Althoff et al., 2012; Daum et al., 2011). Cohesion fatigue occurs during prolonged metaphase when spindle forces keep pulling on kinetochores in combination with low level turnover of cohesin complexes.

The time-resolved analysis revealed a second phase of sister kinetochore separation in bi-oriented univalents during *mnm* mutant meiosis I. This second phase was observed during early telophase I. Therefore, the most likely explanation for the observed additional sister kinetochore separation during this second phase is chromosome decondensation during the final phase of spindle-mediated poleward pull. The separation of sister kinetochores during the second phase was often far greater than what is observed during normal metaphase II (up to threefold more). Moreover, this extensive separation was transient, followed by complete reversion. Presumably after termination of poleward pull on sister kinetochores by spindle disassembly, recoiling of the inner centromere chromatin brings sister kinetochores back together. Pericentromeric cohesion mediated by Ord/Solo/Sunn presumably prevents definitive separation of bi-oriented sister chromatids during *mnm* mutant meiosis I and assists in the reversal of the transient sister kinetochore separation. The complete reversal of the transient sister kinetochore separation observed in *mnm* mutant during exit from meiosis I and interkinesis indicates that sister kinetochores remain coupled by linkage that is highly elastic. This striking elasticity of sister kinetochore linkage before meiosis II is remarkably distinct from conclusions drawn from observations made during mitosis in mammalian cells where the linkage is quite plastic rather than fully elastic (Loncarek et al., 2007).

The elastic linkage between sister kinetochores revealed by time lapse imaging in *mnm* mutants keeps sister kinetochores in an SS arrangement until after the start of prometaphase B during normal meiosis II. Even with STED microscopy, no indications for an SS->BB conversion before prometaphase II was detected. This SS->BB conversion during meiosis II in *D. melanogaster* spermatocytes depends on the pulling forces resulting from bi-orientation. In the absence of microtubules or functional kinetochores, there is only a very limited and slow separation of sister kinetochores during meiosis II, presumably driven by the chromosome condensation process. The spindle dependence of the SS->BB conversion in *D. melanogaster* male meiosis II is in agreement with earlier analyses in grasshopper (Paliulis and Nicklas, 2005). But sister kinetochore arrangement during *D. melanogaster* male meiosis is remarkably distinct from that observed in human oocytes. In this case, sister kinetochores are spaced apart already at the start of meiosis I to an extent that is readily detectable by light microscopy. Moreover, with female age this spacing increases further, promoting erroneous chromosome attachments and hence aneuploidy (Patel et al., 2015; Webster and Schuh, 2017; Zielinska et al., 2015).

In conclusion, my time lapse imaging has clarified many but certainly not all aspects of chromosome segregation during *D. melanogaster* male meiosis. As demonstrated in this thesis, efficient time lapse imaging of progression through both meiotic divisions at high spatial and temporal resolution is now feasible in *D. melanogaster* spermatocytes. It can be combined readily with spermatocyte-specific knockdown (as shown for *Spc105*), mutant analyses (here with *mnm* mutants) and drug treatments (colcemid). Therefore, this experimental system can be expected to promote further progress and contribute to the clarification of the remaining mysteries required for the success of this fascinating process of meiosis.

Chapter 2

Exploration of experimental strategies for manipulation and monitoring of cohesin during *D. melanogaster* male meiosis

Introduction

Cohesin is a protein complex of crucial importance for chromatin organization during interphase, mitosis and meiosis (Haarhuis et al., 2014; Nasmyth, 2001, 2011; Uhlmann, 2016). The core complex is formed by three subunits: two SMC family proteins (SMC1 and SMC3) and an α-kleisin subunit. A number of additional proteins can associate with the core complex (SCC3/SA family proteins, Pds5, Wapl, Soronin). Its initial identification was based on its essential contribution to sister chromatid cohesions during G2 and early mitosis. During these stages, the sister chromatids are kept closely paired by the cohesin complex. By forming a ring like structure around sister chromatids cohesin appears to enforce a topological linkage between the sister chromatids.

While the molecular details of how the cohesin ring is assembled around sister chromatids is still intensely debated, it is clear that the α-kleisin subunit (Schleiffer et al., 2003) is important for maintenance of sister chromatid cohesion during progression through mitotic cell cycles until late metaphase. Just before anaphase onset, however, the α-kleisin subunit is proteolytically cleaved by the endoprotease separase. Separase cleavage eliminates residual sister chromatid cohesion and thereby allows segregation of sister chromatids to opposite spindle poles during anaphase.

As already indicated in the introduction of chapter 1, cohesin complexes are also of principal importance during meiosis. During canonical meiosis, they contribute early to synaptonemal complex formation and homologous recombination. During the final meiotic divisions, they are crucial for regular chromosome segregation. The bivalents present at the start of the meiotic divisions have up to three functionally distinct pools of cohesin bound at specific chromosomal locations. A centromeric pool has been proposed to keep sister centromeres paired so that sister kinetochores assemble a single function unit, allowing sister kinetochore mono-orientation during meiosis I. If indeed present, this centromeric pool would have to be removed before meiosis II, so that sister kinetochores can be bi-oriented during meiosis II. Similarly, the cohesin complexes within the chromosome arm regions need to be removed late in metaphase I so that chiasmata terminalization and homolog separation can proceed during anaphase I. Separase is known to cleave the α-kleisin subunit of the cohesin complexes present in the chromosome arm regions during late metaphase I. In contrast, the pericentromeric pool of cohesin must be protected against inactivation by separase during meiosis I. The pericentromeric pool keeps sister chromatids paired so that their sister kinetochores can be bi-oriented during meiosis II. However, separase-mediated inactivation of this pool occurs during late metaphase II, allowing sister chromatid segregation during meiosis II.

The regulated, chromosome region-specific inactivation of cohesin during meiosis I and II depends on the expression of Rec8, a meiosis-specific α-kleisin subunit (Watanabe and Kitajima, 2005). The α-kleisin subunit that is present during mitosis, Rad21/Scc1/Mcd1, is usually also expressed during meiosis, but it cannot be protected from cleavage during meiosis I. Rec8, however, is only cleaved by separase after phosphorylation. Shugoshin proteins recruit a phosphatase to the pericentromeric region which prevents Rec8 phosphorylation during meiosis I. During meiosis II, shugoshin is inactivated (Arguello-Miranda et al., 2017). Hence Rec8 is phosphorylated and cleaved by separase during meiosis II (Arguello-Miranda et al., 2017).

Rec8 has been conserved during evolution. It has been identified and functionally characterized in a wide range of species, including yeast, plants and mammals. Surprisingly, a true Rec8 ortholog has not been identified in *D. melanogaster*, while a Rad21 homolog (*verthandi* (*vtd*)/*rad21*) is clearly present in this species. In addition, the *c(2)M* gene codes for a highly diverged α-kleisin that might be derived from Rec8. *c(2)M* is specifically expressed during meiosis. However, its functional characterization has demonstrated that it does not provide the same functions as Rec8 in other species. While C(2)M protein is clearly required in female meiosis where it associates with the SC (synaptonemal complex) until prophase I, it is undetectable during the meiotic divisions (Heidmann et al., 2004). *c(2)M* is also expressed in testis, but mutant males are fertile and chromosome segregation appears unaffected. In principle, this might reflect functional redundancy with *Rad21* which is also expressed in testis. *Rad21* is also expressed during oogenesis. However, *Rad21* it is not required for normal chromosome segregation during the female meiotic divisions (Gyuricza et al., 2016; Urban et al., 2014). The role of *Rad21* during male meiosis has not yet been explored. Inhibition of *Rad21* function before male meiosis is technically challenging because *Rad21* is likely required during the gonial mitotic divisions that precede meiosis.

Based on their mutant phenotypes, several *D. melanogaster* genes appear to provide a *rec8*-like function during meiosis: *orientation disruptor* (*ord*), *sisters on the loose* (*solo*) and *sisters unbound* (*sunn*). Their sequences do not share similarities with Rec8. Expression of these genes occurs exclusively in the germline (Bickel et al., 1996; Khetani and Bickel, 2007; Krishnan et al., 2014; Webber et al., 2004). Mutations in these genes result in premature sister chromatid separation in meiosis in both sexes (Bickel et al., 2002; Krishnan et al., 2014; Miyazaki and Orr-Weaver, 1992; Yan and McKee, 2013; Yan et al., 2010). Their protein products are required for normal SMC1/3 localization during meiosis. A Solo-SMC1 interaction has been revealed by co-immunoprecipitation experiments (Yan and McKee, 2013). Therefore, Ord, Solo and Sunn most likely function in the context of a special meiosis-specific cohesin complex.

The peculiarities of *D. melanogaster* male meiosis might provide clear advantages for analyses concerning the existence, function and regulation of a putative centromere-specific cohesin pool. In Drosophilids, male meiosis is strikingly different from canonical meiosis. Formation of a synaptonemal complex (SC) and meiotic recombination does not occur in Drosophila male meiosis (Ault et al., 1982; Morgan, 1912). Therefore, the phenotypes resulting from cohesin inactivation are unlikely to result indirectly from problems during SC formation and meiotic recombination which is readily possible during canonical meiosis.

Instead of meiotic recombination in combination with sister chromatid cohesion in the distal arm regions, linkage of homologs before *D. melanogaster* male meiosis I is achieved with an alternative pairing system. Three genes (*snm*, *mnm*, *teflon*) are known to be specifically required for the function of this alternative homolog conjunction system (Thomas et al., 2005; Tomkiel et al., 2001). The biochemical function of the corresponding gene products is not yet understood. Recent research has provided evidence that separase is required for the inactivation of this alternate conjunction just before onset of anaphase I (Blattner et al., 2016). It is conceivable that the evolution of a cross-over independent alternative homolog conjunction system might have been accompanied by the elimination of a classical meiosis-specific Rec8 α-kleisin.

In summary, a number of interesting aspects of meiosis and *D. melanogaster* male meiosis in particular are not yet understood at the molecular level. It is still unclear whether a centromere-specific pool of cohesin generally mediates sister centromere mono-orientation during meiosis I in eukaryotes. Similarly, it is not known how pericentromeric cohesion is controlled in *D. melanogaster*. Is any of the putative special subunits (Ord, Solo, Sunn) inactivated by separase during meiosis II? It is also not known how separase eliminates homolog conjunction during *D. melanogaster* male meiosis I. Does it cleave Mnm, Snm or Teflon? Or do these proteins cooperate with an α-kleisin that is a separase target? Chapter 2 describes several approaches that were started in order to address these issues. On the one hand, strategies that might allow efficient and spermatocyte-specific elimination of Rad21 and C(2)M were explored. These included approaches based on RNAi, as well as approaches involving regulated protein degradation (DeGradFP and TEV, see below). Moreover, strategies allowing the monitoring of separase activity in time and space during meiosis were evaluated, as well as assays to assess whether various proteins (C(2)M, Ord, Solo) are separase substrates.

DeGradFP:

This strategy involves tissue- and stage-specific expression of a recombinant GFP-specific ubiquitin ligase (N-slmb-vhh-GFP4) in a background expressing a GFP fusion protein instead of the endogenous gene product (Caussinus et al., 2012). In the optimal case, the ubiquitin ligase will induce a rapid and complete degradation of the GFP fusion protein.

TEV mediated cleavage:

Instead of the DeGradFP system, tissue- and stage-specific expression of Tobacco Etch Virus protease (TEV) can also be used for targeted protein inactivation in an appropriate genetic background (Harder et al., 2008; Pauli et al., 2008). This system was shown to be very effective in experiments involving a Rad21 variant with TEV cleavage sites (Rad21^{TEV}). Inactivation before mitosis was shown to be fast and apparently complete (Pauli et al., 2008). Therefore, this system might be useful for analyses in spermatocytes.

Objectives

For further analysis of the role of cohesins and separase during meiosis, I addressed the following issues:

Characterization of transgenic lines for Rad21 and C(2)M depletion by RNAi

Characterization of cis-regulatory regions (*exu*^{m}, *exu*^{mf}, *ßTub85D*) that might allow spermatocytes-specific expression of various transgenes

Generation of additional transgenic lines for spermatocyte-specific DeGradFP

Characterization of spermatocyte-specific Rad21 inactivation by TEV

Generation and initial characterization of transgenes for assaying separase activity

Materials and methods

Oligonucleotides

AF50	ACATGGTCCTGCTGGAGTTC
CL174	AACTTTACTATCAAAATGGTGAGCAAGGGCGAGGAG
CL175	CTCCTCGCCCTTGCTCACCATTTTGATAGTAAAGTT
NT22	CTCTTGACCATGGGTTTAGG
OZH 30 (OZH-030)	ATATACGCGTTATCCGTACAGCCAGCTGTGGG
OZH24	CCTCCGGCAAGGGTCGAGTC
PVL46	ATATCAATTGAGATCTCTCATATGCCACGACACAG
RAS245	AAAGCTTGGGCTGCAGGTC
RAS252	CGGCATCTAGACACACCTAGCGGTGCACC
RAS253	ATGTTGCAATTGCTGTGCGTGGTGTTATCTCG
RAS42	CGAATTCATGGTGAGCAAGGGCGAG
RAS80	GGTCTAGATTACTTGTACAGCTCGTCCATG
RC36	CCCGAAGCTTATGGATCCATTTGTTGGCTG
SCH02 (SC002)	GACTGCGGCCGCTTAGCTGGAGACGGTGAC
SCH09	CCGAATTTTCTAGATTGCTTTTCGCAGATCATATAAGAAAATGGTTGCCGATGAATTCATGGTGAGCAAGGGCGAGGAG
SCH10	CCATGAATTCATCGGCAACCATTTTCTATTGAACTCCTTTTTCGTGTTGG
SCH11	GGACGGATCCGCAAGCAGAGGATGCCAAGAG
SCH12	GGTAGAATTCACGCATTTTGATAGTAAAGT
SCH13	GAGGCGACTGCCGATGAGGAG
SCH14	CGCCTCTAGACTGTCACTTTCGTAAGGCAAC
SCH15	ATCCGAATTCTTACTTGTACAGCTCGTCCA
SCH16	AATAAGATCTCCCATCGCGGCAGTTAGAAT
SCH17	GACTTCTAGAGTAGGCCTGCGACAGAATGAC
SCH18	CTAGCATCCTTGGAGCTCCTTCAGGAGGCGGTGCTACTGCTGGCGCTGGTGGAGCCGGTGGACCTGCGGGGTTAATTG

SCH19	CTAGCAATTAACCCCGCAGGTCCACCGGCTCCACCAGCGCCAGCAGTAGCACCGCCTCCTGAAGGAGCTCCAAGGATG
SCH20	GCGCTCTAGAGTGTCTAAGGGCGAAGAGCT
SCH21	GATGGCGGCCGCCTTGTACAGCTCGTCCATGCC
SCH22	GATGGCGGCCGCCATAACAATGAGAGAAGATTAC
SCH23	GACGGAATTCAGGTAGCTCATTTATTGATGA
SCH24	CATGGTCTGGGTGCCCTCG
SCH25	GTCTACTATGTGGACCACAG
SCH26	GTCCGAAAATGTGCCAATGAATG
SCH27	GTACCGAATTCGGCACGAGACAGTTTTAG
SCH28	GATCGGTACCGTTTGTACTTATGTTCAAAATAAATTATC
SCH29	AGCCCGTCACTTCATATCG
SCH30	CAACAATCTACATGAAGGC
SCH31	CCTCGAATTCGCGGCCGCCTCGCCGGTACCCACCATTTTGATAGTAAAGTT
SCH32	GGAACGGTACCATGATGAAAATGGAGACTGAC
SCH33	ACCATCTAGAGGCCGGTACCAAATTGCCGACCCCGGTC
SCH34	CTACGGTACCATCCTTGGAGCTCCTTCAGGA
SCH35	GGAAGGTACC ATGCCTAAGAAAAAGAGGAAG
SCH37	CAAGGCGGCCGCAATGTCTGACGACTGGGATGAT
SCH38	CATTGCGGCCGCGAGCAGCCCGAAAAATCTACC
SCH39	CAAGGCGGCCGCAATGTACGGAGAAACTACGCTA
SCH40	CATTGCGGCCGCTACGTTCTGCTGGACTTTGCC
SCH41	CAAGGCGGCCGCAATGAGCTTGAATTTATATG
SCH42	CATTGCGGCCGCCAGAGTCTCACTCAGCATAAG
SCH43	CGACCGCTAGCTCCAAAAGAGAAGTTTAGGC
SCH44	GCCAACCGGTATGCCACGACACAGCAGAGC
SCH45	GCTCTCTAGATGCTTTCCTGCTGCACGGTC
SCH46	CCGGTATGCCGTATCTAGAGC
SCH47	GGCCGCTCTAGATACGGCATA
SCH48	GCCATCAAATGGTTTTGGCG

SCH49	GCACTCGATCAATCTTCTG
SCH50	AGGCTTTGGTGAACCAAGC
SCH51	GTGGATGGATCAACATATGG
SCH52	CGACACCGTTGGCTCCATCA
SCH53	CCAGCTTGCTACAAAATGC
SCH54	ACATTCATTGGACGCCCATGC
SCH55	ACCATCGCGATCCATACCAG
SCH56	GTACTAAGTGACAATGGCG
SCH57	CGTCTTAAAGAAGTTTAAG
SCH58	GCAGATTGATCAATGTGAAGC
SCH59	CGCATTCAACATTCTTTGAGG
SCH59	CGCATTCAACATTCTTTGAGG
SCH60	CACCGGTGAGCGCATTGCGCC
SCH61	GAGCGCGAGCACTTGAGGC
SCH62	GTCAACGCGGCCAACGCCGG
SCH63	AGGAGAACATGCACATGAA

Plasmids

The regions of fragments inserted into widely used cloning vectors were all verified by sequencing.

1. pattB-5’UTR-exu^{m}-EGFP-3’UTR-exu

Primers Ras253 (forward for amplification of 5’ region, introduces a MunI site, but this site was not used for this cloning) and SCH10 (reverse primer, introduces a Kozak consensus sequence followed by an EcoRI site) were used for amplification of a fragment containing *exu*^{m} region from *pattB-5’UTR-exu*^{m}*-GAL4VP16-3’UTR* (Raychaudhuri, 2012). The PCR product was digested with PstI and EcoRI and inserted into the corresponding sites of *pattB-5’UTR-exu*^{mf}*-EGFP-3’UTR-exu* (see below). The protein encoded by this transgene construct is EGFP starting with MVADEF at the N-terminus (aa1-4 from Exu followed by aa5 and 6 introduced by the EcoRI site). The intron with the female specific promoter region is not present in this construct.

2. pattB-5’UTR-exu^{mf}-EGFP-3’UTR-exu

Primers SCH09 (introducing an XbaI site) and RC36 (introducing a NotI site) were used for amplification of the EGFP coding sequence from *pUAST-attB-MCS-EGFP*. The resulting PCR product was ligated into the corresponding sites of *pSLfa1180* resulting in *pSLfa1180-EGFP*. A NotI-SpeI fragment containing the *exu* 3’ region was isolated from *pattB-exu^{mf}-GAL4VP16topi* (Raychaudhuri, 2012) and inserted into this cloning intermediate resulting in *pSLfa1180-EGFP-exu3’*. From this cloning intermediate, the XbaI fragment containing the EGFP coding region and part of the 3’ *exu* region was used to replace the XbaI fragment containing GAL4VP16 coding region and part of exu 3’ in *pattB-exu^{mf}-GAL4VP16topi*. The EGFP variant encoded by this transgene construct has the same N-terminal sequence as described above for *pattB-5’UTR-exu^{m}-EGFP-3’UTR-exu.*

3. pattB-ßTub85DP-EGFP

Previously, *ßTub85D* cis regulatory sequences have been used to drive TEV and GAL4Δ expression with limited success (N. Taneja Raychaudhuri and C. F. Lehner, unpublished observations). To evaluate the functionality of the *ßTub85D* regulatory sequences used in the corresponding transgene constructs, the EGFP reporter construct pattB-*ßTub85DP*-EGFP was made for subsequent generation of transgenic lines and analysis of EGFP expression. However, slightly longer 5’ and 3’ regions were used. In the first cloning step, the 5’ region of *ßTub85D* was amplified using primers SCH11 (introduces BamH1) and SCH12 (introduces EcoRI) from w^1 genomic DNA and inserted into corresponding sites of pattB resulting in the cloning intermediate *pattB-5’ßTub85D*. Primers SCH13 (introduces EcoRI) and SCH14 (introduces XbaI) were used for amplification of the *ßTub85D* 3’ region from w^1 genomic DNA and inserted into *pattB-5’ßTub85D* resulting in *pattB-5’-3’-ßTub85D*. EGFP coding sequences were amplified with primers RAS42 and SCH15 from *pUAST-attB-mcs-EGFP* and inserted into *pattB-5’-3’-ßTub85D* to obtain a first version of *pattB-ßTub85DP-EGFP*. However, characterization of this version revealed a truncation resulting from the presence of a polymorphic EcoRI site in the w^1 genomic DNA. The truncation was corrected as follows. A fusion PCR was performed to generate an appropriate repair fragment. For this, PCR1 was done with SCH11 and CL175 using w^1 genomic DNA as template, and PCR2 with CL174 and SCH15 using *pUAST-attB-mcs-EGFP* as template. PCR1 and 2 were mixed and fused by PCR3 using OZH-30 and SCH15. After digestion of the PCR3 product with EcoRI, it was inserted into *pattB-5’part-3’ ßTub85D* to arrive at the final construct.

4. pattB-5’UTR-exu^{m}-TEV-3’UTR-exu

An EcoRI-NotI fragment with the sequences coding for TEV (with one SV40 large T nls and a V5 epitope tag at the N terminus and two additional SV40 large T nls at the C terminus) was isolated from *pUASp1-TEV* (Pauli et al. 2008) and used as an insert to replace the EcoRI-NotI fragment in *pattB-5’UTR-exu*^{m}*-EGFP-3’UTR-exu*. The resulting construct codes for nlsV5-TEV-2nls with a short extension at the N terminus.

5. pattB-5’UTR-exu^{mf}-TEV-3’UTR-exu

The EcoRI-NotI fragment with the sequences coding for TEV (see above) was also used to replace the EcoRI-NotI fragment in *pattB-5’UTR-exu*^{mf}*-EGFP-3’UTR-exu*. The resulting construct also expresses nlsV5-TEV-2nls with a short extension at the N terminus.

6. pattB-ßTub85D-vector

This vector can be used for the production of transgenic lines that express a given ORF of interest (contained within a KpnI-NotI fragment) under control of the testis-specific *ßTub85D cis*-regulatory region. Primers OZH30 and SCH31 were used for amplification of a PCR fragment from *pattB-ßTub85D-EGFP*. OZH30 is upstream of an EcoRI site. SCH31 introduces a KpnI site after the AUG and a second codon, followed by a NotI and an EcoRI site. After digestion with EcoRI, the resulting fragment was used to replace the EcoRI fragment within *pattB-ßTub85D-EGFP* to obtain the final plasmid.

7. pattB-ßTub85D-TEV

SCH35 and NT22 were used for amplification of a PCR fragment from *pUASp1-TEV* (Pauli et al., 2008). SCH35 introduces a KpnI site upstream of ATG and NT22 anneals downstream of a NotI site. The KpnI-NotI fragment was inserted into the corresponding sites of *pattB-ßTub85D-vector*. The construct codes for TEV (with one SV40 large T nls and a V5 epitope tag at N terminus and two additional SV40 large T nls at the C terminus) with four additional amino acids (MVGT) at the N terminus.

8. pattB-5’UTR-exu^{m}-NSlmb-3’UTR-exu

The sequences coding for NSlmb-vhh-GFP4 were amplified using OZH24 and SCH02 from *pUASp1-NSlmb-vhh-GFP4* (Urban et al., 2014). OZH24 is upstream of an EcoRI site and SCH02 introduces a NotI site. The PCR fragment was used to replace the EcoRI-NotI fragment (coding for EGFP) in *pattB-5’UTR-exu*^{m}*-EGFP-3’UTR-exu*. The resulting construct codes for NSlmb-vhh-GFP4 with a short extension at the N terminus (MVADEFK)

9. pattB-5’UTR-exu^{mf}-NSlmb-3’UTR-exu

The PCR fragment with the NSlmb-vhh-GFP4 coding sequence (see above) was also used to replace the EcoRI-NotI fragment in *pattB-5’UTR-exu*^{mf}*-EGFP-3’UTR-exu*.

10. pattB-ßTub85DP-NSlmb-vhh-GFP4

Primers SCH32 and SCH02 were used for amplification of a PCR fragment from *pUASp1-NSlmb-vhh-GFP4* (Urban et al., 2014). SCH32 introduces a KpnI site upstream of ATG and SCH02 a NotI site after stop. After digestion with KpnI and NotI, the resulting fragment was inserted into the corresponding sites of *pattB-ßTub85D-vector*. The resulting construct codes for NSlmb-vhh-GFP4 with a short extension at the N terminus (MVGT).

11. pCaSpeRmod-gSMC1P-Rad21^{TEV}

A construct for generating transgenic fly lines expressing Rad21 with TEV cleavage sites (3 TEV sites at position 271) under control of the *SMC1 cis*-regulatory region. Primers SCH27 (introducing an EcoRI site) and SCH28 (introducing a KpnI site) were used for amplification of the Rad21^{TEV} coding region from *Tub-Rad21(271-3TEV)-myc* (Pauli et al., 2008) and inserted into the corresponding sites of *pCaSpeRmod-gSMC1-Rad21-EGFP* (Chaurasia, 2012). The sequencing revealed the presence of a small deletion within the 10x-myc tag region and another at the start of the *Rad21* 3’UTR.

12. pUASp1-His2Av-happyLinker-TagRFPT-Rad21linker-EGFP (His2Av Sse biosensor)

His2Av-happy linker-TagRFPT was assembled in the *pslfa1180* vector backbone as follows: The His2Av coding region was amplified from cDNA (0-4 hr embryo cDNA library in pNB40) using primers SCH16/SCH17 and cloned into *pslfa1180* as a BglI-NotI fragment. The sequence coding for Tag-RFPT (PCR amplified with SCH20/SCH21 from a Tag-RFPT construct pCB87 (Shaner et al., 2008) was inserted into the resulting intermediate *pslfa1180-His2Av* using the XbaI-NotI sites. The ‘Happy linker’ sequence was introduced as a ds oligo (SCH18 annealed with SCH19) into the XbaI site. This resulted in the intermediate *pslfa1180-His2Av-happy linker-TagRFPT*. The Rad21 linker region and EGFP were amplified from *pCasPeRmod-Tub-Rad21-EGFP* (Urban et al., 2014) using primer pairs SCH22/SCH23 and Ras42/RaS80, respectively. The EGFP fragment was cloned into the *pUASp1* vector as a XbaI-EcoRI fragment, followed by insertion of the Rad21 linker region as a NotI-EcoRI fragment. Into the resulting intermediate *pUASp1-Rad21-linker-EGFP*, the *His2Av-happy linker-TagRFPT* region isolated as a BglII-NotI from *pslfa1180-His2Av-happy linker-TagRFPT* was inserted into the corresponding sites to arrive at the final construct *pUASp1-His2Av-happyLinker-TagRFPT-Rad21linker-EGFP*.

13. pMT-cid-happyLinker-TagRFPT-Rad21linker-EGFP (Cid Sse biosensor)

Primers PVL46 and SCH33 were used for amplification of the *cid* region from *pMT-Cid-fastFT-bla* (P. Lidsky and C.F. Lehner, unpublished). SCH33 introduces a KpnI site followed by an XbaI site before the stop codon at the C terminus of the *cid* coding region The EcoRI-XbaI PCR fragment was then ligated with the vector fragment to generate *pMT-cid-bla* (cloning intermediate). In this cloning intermediate, a KpnI and an XbaI site are present at the C terminus of *cid* while the C-terminal fastFT extension is no longer present. The subsequent steps that were originally planned did not work because a second KpnI site had been overlooked during planning. To by-pass the problem, a BamHI fragment containing the additional KpnI site was released by digesting *pMT-Cid-Bla* with BamHI followed by re-ligation. The deleted BamHI fragment contains the selection marker cassette (*copia* promoter-blasticidin resistance gene). The cloning intermediate resulting after deletion of the BamHI fragment was therefore called *pMT-Cid-wo-Copia-Bla*. In a final step, SCH34 and NT22 were used for amplification of the *happyLinker-TagRFPT-Rad21linker-EGFP* fragment from *pUASp1-His2Av-HappyLinker-TagRFPT-Rad21linker-EGFP* which was inserted into the KpnI-XbaI sites of *pMT-cid-wo-copia-bla*.

14. pMT-cid-happyLinker-TagRFPT-Rad21^{NC}linker-EGFP (Cid Sse^{NC} biosensor)

pUASp1-Rad21-linker-EGFP (cloning intermediate during production of His2Av Sse biosensor) was digested with EcoRI-NotI to release the wild type Rad21 linker region (with Sse cleavage sites). The mutant Rad21 linker region (NC, with mutations in Sse cleavage sites) was amplified with primer SCH22 (introducing NotI) and SCH23 (introducing EcoRI) from *pUASp1-FA-Rad21NC-myc* (obtained from S. Heidmann and E. Urban, University of Bayreuth) was inserted into the vector fragment, resulting in the cloning intermediate *pUASp1-Rad21NC-EGFP*. The XbaI-NotI fragment from this cloning intermediate was used to replace the corresponding fragment in *pMT-cid-happyLinker-TagRFPT-Rad21linker-EGFP* (=*pMT-cid-hali-TagRFPT-Rad21li-EGFP*) resulting in the final construct.

15. pMT-Cid-HappyLinker-TagRFPT-SOLO-EGFP-bla

The full coding region of *solo* was amplified from a cDNA clone (MIP03838, obtained from DGRC, Indiana University) using primers SCH37 and SCH38 which introduce NotI sites. After digestion with NotI, the PCR fragment was inserted into the NotI site of *pMT-Cid-HappyLinker-TagRFPT-(NotI)-EGFP-bla* (Blattner, 2016).

16. pMT-Cid-HappyLinker-TagRFPT-ORD-EGFP-bla

The full coding region of *ord* was amplified from a cDNA clone (AT13321, obtained from DGRC, Indiana University) using primers SCH39 and SCH40 which introduce NotI sites. After digestion with NotI, the PCR fragment was inserted into the NotI site of *pMT-Cid-HappyLinker-TagRFPT-(NotI)-EGFP-bla*.

17. pMT-Cid-HappyLinker-TagRFPT-C(2)M-EGFP-bla

The full coding region of *c(2)M* was amplified from cDNA clone (Mei910 14.1, (Heidmann et al., 2004) using primers SCH41 and SCH42 which introduce NotI sites. After digestion with NotI, the PCR fragment was inserted into the NotI site of *pMT-Cid-HappyLinker-TagRFPT-(NotI)-EGFP-bla*.

18. pCaSpeR4-gcid-cid-happyLinker-TagRFPT-Rad21linker-EGFP (cid-Cid-Sse biosensor)

cid 3'UTR was amplified from *pCaSpeR4-gCID-EGFP-CID (gCGC)* (Schuh et al., 2007) using primers SCH43 (introducing NheI at 5’ end) and Ras245 (distal from the XbaI site at the 3’ end of the *cid* 3’ UTR). The PCR fragment was digested with NheI and XbaI and inserted into the XbaI site of *pMT-cid-happyLinker-TagRFPT-Rad21linker-EGFP* giving rise to the cloning intermediate *pMT-cid-haLiTagRFP-Rad21-EGFP-3'cidUTR*. The MluI-XbaI fragment (with part of *cid* coding region C-terminal of MluI site followed by HappyLinker-TagRFPT-Rad21Linker-EGFP-cid3’-UTR) from this cloning intermediate was used to replace the corresponding MluI-XbaI fragment in *pCaSpeR4-gCID-EGFP-CID (gCGC)* to arrive at the final construct (abbreviated as *pCaSpeR4-gcid-cid-haLi-TagRFPT-Rad21Li-EGFP*)

19. pCaSpeR4-bam-cid-happyLinker-TagRFPT-Rad21linker-EGFP (bam-Cid-Sse biosensor)

First, a ds oligo (obtained by annealing SCH44 and SCH45, with an XbaI site in the middle) was used to replace the AgeI-NotI fragment (= NSlmb-vhh4GFP coding region) in *pCaSper4-bam-NSlmb-VhhGFP4,* resulting in cloning intermediate *pCaSper4-bam-AgeI*(XbaI)NotI**. Second, the N-terminal region of the *cid* coding region was amplified using primers SCH44 (introducing AgeI) and SCH45 (introducing XbaI) from *pCaSper4-gCID-EGFP-CID (gCGC)*. After digesting with AgeI and XbaI the fragment which includes an internal MluI site was inserted into the corresponding sites of *pCaSper4-bam-AgeI*(XbaI)NotI** giving rise to a second intermediate *pCaSper4-bam-Nterm-Cid*. Third, the MluI-XbaI fragment (coding for Cid region downstream of MluI followed by happyLinker-TagRFPT-Rad21linker-EGFP) was isolated from *pMT-Cid-Sse biosensor* and inserted into the corresponding sites of *pCaSper4-bam-Nterm-Cid* to arrive at the final construct.

20. pMT-TALE_1.686-Rad21SseBiosensor

The region coding for HappyLinker-TagRFPT-Rad21linker-EGFP was excised from *Cid-Sse biosensor* with Acc65I and XbaI and inserted into *pMT-TALE_1.686-BsiWI-bla* (Yuan et al., 2014), kindly provided by the P.H. O'Farrell, University of California San Francisco) after digesion with BsiWI and XbaI.

21. pMT-TALE_1.686-Rad21^{NC}SseBiosensor

The region coding for HappyLinker-TagRFPT-Rad21NClinker-EGFP was cut out from *Cid-Sse*^{NC} *biosensor* with Acc65I and XbaI and inserted into *pMT-TALE_1.686-BsiWI-bla* after digestion with BsiWI and XbaI.

22. pattB-exum-TALE_1.686-SseBiosensor

pattB-5'UTR-exum-EGFP-3'UTR-exu was digested with EcoRI (which cuts in front of EGFP coding sequence) and used as vector. Insert fragment (4700 bp, TALE_1.686 SseBiosensor lacking C-terminal EGFP coding sequence) was extracted as a EcoRI fragment from *pMT-TALE_1.686-Rad21SseBiosensor*. On sequencing the seemingly correct clone 48, a 300 bp piece from the Rad21 linker region (containing putative Sse cleavage site 2) was found to be missing (perhaps due to polymorphisms creating an extra EcoRI site or due to star activity). To correct this deletion, a fusion PCR was performed. For this, PCR1 amplified a 1100 bp fragment covering the missing 300 bp region and extending until the end of EGFP (primers SCH59/SCH15, template *pMT-TALE_1.686-Rad21SseBiosensor*). PCR2 amplified a 1300 bp fragment starting close to the end of the EGFP coding sequence and extending until the end of exu 3’ region (primers AF50/RAS252, template *pattB-5’UTR-exum-EGFP-3’UTR-exu*). PCR1 and 2 were fused in an additional PCR after mixing 1:1 and amplification in PCR3 using SCH59/RAS252. The final PCR3 product was digested using XhoI and XbaI and used to replace the corresponding region in clone 48. The resulting construct was found to have a 777 bp deletion removing the last part of the exu 3’ UTR. For restoration of this missing part *pattB-5’UTR-exum-EGFP-3’UTR-exu* was cut with BglII and XbaI and a 900 bp fragment was isolated und used to replace the BglII-XbaI fragment, thus arriving at the desired final construct.

Fly strains

Genotype	_Abbreviated name_	Reference/Source/ Comment
_w^1_	_w^1_	Lehner lab common stock
w*; P{w$^+$, ey-GAL4} (5/8)	_ey-GAL4_	(Hazelett et al., 1998)/ Lehner stock #444
w*; ; P{w$^+$, bamP-GAL4-VP16} (III)	_bam-GVP III_	(Chen and McKearin, 2003)
w*; ; P[w$^+$, nos-GAL4-VP16] III	_nos-GAL4_	(Van Doren et al., 1998)/Lehner stock #590
w*; P{matα4-GAL4-VP16}V2H	_mat-GAL4_	(Hacker and Perrimon, 1998)/Lehner stock #418
w*; P{w$^+$, gCid-EGFP-Cid} II.1	_Cid-EGFP (CGC)_	(Schuh et al., 2007)/Lehner stock #684
M(3)76A^1, kar^2, ry^1, Sb^1	_MKRS_	
TM6B, Tb, Antp^{Hu}	_TM6B_	
w*;; Rad21^{ex3}/TM3, Sb, P{w$^+$, Ubx-lacZ}.III	_Rad21^{ex3}/TM3, Sb_	(Pauli et al., 2008)/Lehner stock # NT132
w*; c(2)M^{EP2115}/CyO ; D^3/TM3,Sb	_c(2)M^{EP2115}/CyO ; D^3/TM3,Sb_	(Urban et al., 2014)/ Lehner stock #NT37

w*; P{GD24772} v13669/ CyO P[ry^{+}, ftz-LacZ]	UAS-GDvtd=Rad21^{RNAi} (II)	(Dietzl et al., 2007)/VDRC
y^{1} v^{1}; ; P{v^{+}, V20-rad21-CLb1}attP2 - Nr 4	UAS-V20vtd=Rad21^{shmiR1}	(Blattner, 2016)/Lehner stock #1453
y^{1} v^{1}; ; P{v^{+}, V20-rad21-CLb2}attP2 - Nr 18	UAS-V20vtd=Rad21^{shmiR2}	(Blattner, 2016)/Lehner stock #1454
y^{1} v^{1}; ; P{v^{+}, V20-c(2)M-CLb3}attP2 - Nr 1	UAS-V20c(2)M^{shmiR3}	(Blattner, 2016)/Lehner stock #1455
y^{1} v^{1}; ; P{v^{+}, V20-c(2)M-CLb4}attP40/CyO	UAS-V20c(2)M^{shmiR4}	This work/Lehner stock #1456
w*;; P{w[+mC]=UASP1^{FA}-Rad21^{NC}-9myc} III.11	UASp1 FA-Rad21^{NC}-9myc III.11	(Urban et al., 2014)/ S. Heidman, University of Bayreuth
w*;; P{w[+mC]=UASP1^{FA}-Rad21^{NC}-9myc} III.18/ TM3, Ser,	UASp1 FA-Rad21^{NC}-9myc III.18/ TM3, Ser	(Urban et al., 2014)/ S. Heidman, University of Bayreuth
w*; P{w[+mC]=UASP1^{FA}-Rad21^{NC}-9myc} II.1	UASp1 FA-Rad21^{NC}-9myc II.1	(Urban et al., 2014)/ S. Heidman, University of Bayreuth
w*; P{w[+mC]=UASP1^{FA}-Rad21^{NC}-9myc} II.5	UASp1 FA-Rad21^{NC}-9myc II.5	(Urban et al., 2014)/ S. Heidman, University of Bayreuth
w*; P{w^{+}, gSMC1P-Rad21(271-3TEV)-myc10} II.1 (7.1)	gSMC1-Rad21^{TEV} II.1	This work
w*;; P{ w^{+}, gSMC1-Rad21(271-3TEV)-myc10} III.1 (3.1)/ TM3, Sb P{w^{+}, Ubx-lacZ}	gSMC1-Rad21^{TEV} III.1/TM3,Sb	This work
w*;; P{gSMC1-Rad21(271-3TEV)-myc10} III.2 (4.2)/ TM6B, Tb, Antp^{Hu}	gSMC1-Rad21^{TEV} III.2/TM6B	This work
w*;; P{gSMC1-Rad21(271-3TEV)-myc10} III.3 (5.3)/ TM3, Sb P{w^{+}, Ubx-lacZ}	gSMC1-Rad21^{TEV} III.3/TM3,Sb	This work
w*;; P{gSMC1-Rad21(271-3TEV)-myc10} III.3 (5.3)	gSMC1-Rad21^{TEV} III.3	This work
w*; {w^{+}, ßTub85D-NSlmb-vhhGFP4 II.1}attP40	ßTub85D-DeGradFP II.1	This work

w*; {w^{+}, ßTub85D-NSlmb-vhhGFP4 II.4}attP40	ßTub85D-DeGradFP II.4	This work
w*; {w^{+}, exu^{m}-TEV II.1}attP40	exu^{m}-TEV II.1	This work
w*; {w^{+}, exu^{m}-TEV II.2}attP40	exu^{m}-TEV II.2	This work
w*; {w^{+}, exu^{mf}-TEV II.1}attP40	exu^{mf}-TEV II.1	This work
w*; {w^{+}, exu^{mf}-TEV II.2}attP40	exu^{mf}-TEV II.2	This work
w*; {w^{+}, ßTub85D-TEV II.2}attP40	ßTub85D-TEV II.2	This work
w*; {w^{+}, ßTub85D-TEV II.4}attP40	ßTub85D-TEV II.4	This work
w*; {w^{+}, exu^{mf}-NSlmb-vhhGFP4 II.1}attP40	exu^{mf}-deGradFP II.1	This work
w*; {w^{+}, exu^{m}-NSlmb-vhhGFP4 II.1}attP40	exu^{m}-deGradFP II.1	This work
w*; {w^{+}, exu^{m}-NSlmb-vhhGFP4 II.3}attP40	exu^{m}-deGradFP II.3	This work
w*; {w^{+}, exu^{m}-EGFP 4.1}attP40	exu^{m}-EGFP	This work
w*; {w^{+}, exu^{mf}-EGFP 3.1}attP40	exu^{mf}-EGFP	This work
w*; {w^{+}, ßTub85D-EGFP 4.1}attP40	ßTub85D-EGFP	This work
w*; P{w^{+}, cidP-Cid Sse sensor II.2}	cidP-Cid Sensor II.2	This work
w*; P{w^{+}, cidP-Cid Sse sensor II.4}	cidP-Cid Sensor II.4	This work
w*;; P{w^{+}, cidP-Cid Sse sensor III.1}	cidP-Cid Sensor III.1	This work
w*;; P{w^{+}, cidP-Cid Sse sensor III.2}	cidP-Cid Sensor III.2	This work
w*; P{w^{+}, bamP-Cid Sse sensor II.2}	bamP-Cid Sensor II.2	This work
w*; P{w^{+}, bamP-Cid Sse sensor II.3}	bamP-Cid Sensor II.3	This work
w*;; P{w^{+}, bamP-Cid Sse sensor III.1}	bamP-Cid Sensor III.1	This work
w*;; P{w^{+}, bam-Cid Sse sensor III.2}	bamP-Cid Sensor III.2	This work
w*; αTub84BP-Rad21$^{271\text{-}3TEV}$-myc10(#3), αTub84BP-Rad21$^{271\text{-}3TEV}$-myc10(#7)/ CyO {wg-LacZ}(floating); rad21^{ex3}	w*; αTub84BP-Rad21$^{271\text{-}3TEV}$-myc10(#3), αTub84BP-Rad21$^{271\text{-}3TEV}$-myc10(#7)/; rad21^{ex3}	(Pauli et al., 2008)/ Lehner stock #1086
w*; Rad21^{ex3}, P{w^{+}, αTub84BP-Rad21-GFP} III.2 (CyO, Dfd-EYFP andTM3,Ser floating)	Rad21^{ex3}, αTub84BP-Rad21-GFP III.2	Lehner stock #NT145
w*; Sp/CyO; Rad21^{ex3}, P{w^{+}, αTub84BP-Rad21-GFP}III.1/ TM3, Sb, P{w^{+}, Ubx-lacZ}	Sp/ CyO; Rad21^{ex3}, αTub84BP-Rad21-GFP III.1/ TM3,Sb	Lehner stock #NT144
w*; c(2)M^{EP2115}, gC(2)M-myc II.3/ CyO P[ry^{+}, ftz-LacZ] ; nos-Gal4	c(2)M^{EP2115}, gC(2)M-myc II.3/ CyO ; nos-Gal4	(Heidmann et al., 2004), Lehner stock #D28

w*; c(2)M^{EP2115}, gC(2)M-myc II.3/ CyO ; nos-Gal4/ TM6B, Tb, Antp^{Hu}	c(2)M^{EP2115}, gC(2)M-myc II.3/ CyO ; nos-Gal4/ TM6B	This work, re balanced Lehner stock #D28
w*; If/CyO ; UAS-V20vtd=Rad21^{shmiR2}/ TM6B, Tb, Antp^{Hu}	If/CyO; UAS-V20vtd=Rad21^{shmiR2}/TM6B	This work
w*; c(2)M^{EP2115}/ CyO; UAS-V20vtd=Rad21^{shmiR2}/ TM3, Sb, P{w^{+}, Ubx-lacZ}	c(2)M^{EP}/CyO; UAS-V20vtd=Rad21^{shmiR2}/ TM3, Sb	This work
w*; P{GD24772} v13669/ CyO P[ry^{+}, ftz-LacZ]; MKRS/TM6B, Tb, Antp^{Hu}	UAS-GDvtd=Rad21^{RNAi} (II)/CyO; MKRS/TM6B	This work
w*;; {w^{+mc},UASp-mRFP-p14-TEV} III	UASp-mRFP-p14-TEV III	Nadia Dubè (Damian Brunner lab)/ Lehner stock #NT14
w*; 2x Rad21^{TEV}, P{AP202,205}/CyO; rad21^{ex3}, P{w^{+},UASP1-TEV} III.3/TM3,Sb, P{w^{+},Ubx-lacZ}	2x Rad21^{TEV}, P{AP202,205}; rad21^{ex3}, UASP1-TEV III.3	Lehner stock #NT28
w*;; P{gSMC1P-Rad21$^{271-3TEV}$-myc10} III.2 (5.3), Rad21^{ex3} / TM6B, Tb, Antp^{Hu}	gSMC1P-Rad21^{TEV} III.2, Rad21^{ex3}/TM6B	This work
w*;; P{gSMC1P-Rad21$^{271-3TEV}$-myc10} III.3 (5.3), Rad21^{ex3} / TM3, Sb P{w^{+}, Ubx-lacZ}	gSMC1P-Rad21^{TEV} III.3, Rad21^{ex3}/TM3, Sb	This work
w*; If/ CyO; P{gSMC1P-Rad21$^{271-3TEV}$-myc10} III.3 (5.3), Rad21^{ex3} / TM6B, Tb, Antp^{Hu}	If/CyO; gSMC1P-Rad21^{TEV} III.3, Rad21^{ex3}/ TM6B	This work

Drosophila germline transformation

Transgenic lines were established by means of PhiC31-mediated (Groth et al., 2004) or P element-mediated germline-transformation (Rubin and Spradling, 1982). Some constructs were integrated by a commercial service (BestGene Inc.; Chino Hills, CA, USA). P element constructs were integrated into a w^{1118} strain by the commercial service and into w^1 in my injections. The pattB constructs were integrated either into the landing sites attP40 (chromosome 2) or attP2 (chromosome 3). For integration of P element constructs, I used the plasmid constructs described above in combination with the helper plasmid Δ2-3turbo (Rio, 1990). Injection of the plasmid mixtures into w^1 embryos was performed essentially as described (Herzig et al., 2002) with minor alterations. Instead of an oil-filled injection system, an air pressurized system (Eppendorf FemtoJet) was used. Moreover, Eppendorf Femtotips II were used as injection needles. The injection was performed with a M1 micromanipulator (Bachofer) which allowed for precise needle movements. Injected embryos were developed at 18°C. Shortly before hatching of the larvae they were transferred into a culture vial. Thereafter, culture vials were kept on 25°C. The transgene mapping protocol of Herzig (1999) was followed.

Testis and ovary fixation

Materials: forceps, needles and tungsten needles, scalpel, clear nail polish, poly-L-lysine coated slides, normal cover slips, liquid nitrogen, 100% ethanol (chilled to -20°C, or on dry ice) in a cylindrical glass slide container, FBS (fetal bovine serum), Testis Buffer: 183 mM KCl, 47 mM NaCl, 10 mM Tris-HCl (pH 6.8), Fixative: 4% Para formaldehyde (PFA), PBST (PBS + 0.1% Triton X-100), Permeabilizing buffer (0.01% Triton X-100 in Testis Buffer), Vectashield H-1000 (mounting medium, Vector Labratories, Inc.), Embryonenkleber (mounting medium: 70% glycerol, 50 mM Tris-HCl (pH 9.5), 10 mg/ml propyl gallate, 0.5 mg/ml p-phenylenediamine in 0.5x PBS).

Whole mount preparations

Flies were quickly anesthetized with CO_2 and transferred into a glass dish containing testis buffer. The dish with the flies was then kept on ice, which kept the flies anesthetized. One droplet of testis buffer was transferred to a slide. One fly was then transferred into this droplet and dissected under the binocular with forceps. Testes were isolated by cutting posterior to the seminal vesicle with a hypodermic needle (Terumo Neolus 27G, 0.4x20 mm). Testes were then separated from the accessory glands. 5-10 flies were dissected in a droplet and testes were then transferred to a droplet of 4% paraformaldehyde on a depression slide for fixation. After 10 min of fixation at room temperature, the fixative was carefully removed with a syringe under the binocular. For the fixation of ovaries, a similar protocol was used with a few alterations. Immunostaining of testes or ovaries was done as described (White-Cooper, 2003). All primary antibody incubations were done at 4°C overnight. Washing was done by rinsing once with PBST followed by three washes in PBST for 20 minutes each. A droplet of Hoechst staining solution (1 µg/mL Hoechst 33852 in PBST) was added for 10 min (protected from light). The staining solution was then removed with a syringe and testes were washed in a droplet of PBS. Testes were finally transferred into a droplet of mounting media (Vectashield H-1000 or Embryonenkleber) on a new slide and carefully (to avoid strong squashing of the testes) covered with a coverslip. After placing the stained ovaries in the mounting medium, the ovarioles were gently separated using needles to flatten out the tissue.

Squashed testis preparations

Testes were dissected from young adults (0-4 days old) in testis buffer. Testes were transferred in a drop of testis buffer on a poly-L-Lysine-treated slide and were cut carefully to spill the contents. A cover slip was placed gently to squash the testis. The preparation was frozen in liquid nitrogen until sizzling stopped. Thereafter the cover slip was popped off using a scalpel. The slide was marked around the sample region with a hydrophobic marker pen and placed in 100% EtOH at -20°C for 10 minutes. The slide was placed flat and 0.5-1 ml of 4% PFA solution was added; incubated for 10 min in a wet chamber. PFA was then removed by gently tipping the slide on paper towels vertically. Then they were kept in PBST in a glass slide container until all the slides were prepared and incubated 30 min or more, treating all the slides in the same manner. PBST was removed gently and 1 µg/ml Hoechst 33258 solution in PBST was added and incubated for 8 minutes. Washing was done with PBS twice for 10 min. Mounting was done in Embryonenkleber and edges were sealed with a clear nail polish.

Immunoblotting

Immunoblotting with total extracts of Drosophila embryos was done as previously described (Radermacher et al., 2014). For extracts prepared from testis without apical tips, whole testes were first dissected on ice. The apical tips were carefully severed using tungsten needles. Testes were immediately placed in SDS-PAGE sample buffer. For an estimation of relative concentrations of proteins detected by immunoblotting in extracts from different genotypes, samples containing known and increasing amounts of control testes (for example 3, 10 and 30) were resolved in parallel on the same gel as the experimental extracts.

Results

1. Functionality of C(2)M and Rad21 RNAi lines:

Several lines with transgenes allowing GAL4 dependent expression of shmiRs (Ni et al., 2011) targeting *c(2)M* or *Rad21* were available. The functionality of the *c(2)M* RNAi lines was tested by driving expression with *nos-GAL4*. This is expected to cause expression also in the female germline where *c(2)M* is required for synaptonemal complex formation and homologous recombination. The crosses were set up so that the flies with *nos-GAL4* and the *c(2)M* RNAi transgenes also contained a copy of *c(2)M-myc* transgene in the background. Immunostaining of ovaries with anti-myc indicated that C(2)M was depleted effectively. Compared to controls, C(2)M-myc levels were strongly reduced in the germarium (Fig. 1; n > 10 females). As expected, overall morphology of ovaries was not affected (data not shown), suggesting that there were no obvious off-target effects on genes required for normal ovary development and oogenesis. Potential off-target effects were also evaluated by using *ey-GAL4* for expression of the RNAi transgenes. *ey-GAL4* drives expression during eye development. Since *c(2)M* expression is meiosis-specific, eye abnormalities would indicate off target effects. However, such abnormalities were not observed (data not shown).

The *c(2)M* RNAi transgenes were also expressed using *bamP-GAL4*-VP16. This is expected to cause C(2)M depletion also in early spermatocytes. To assess the efficacy of depletion, crosses were again set up so that also a *c(2)M-myc* transgene was present, followed by immunostaining of whole mount testis preparations with anti-myc. I did not find any significant difference in the anti-myc signal intensities between controls without the *c(2)M* RNAi transgenes and those with these transgenes. However, as C(2)M expression levels in testis are low based on FlyBase, it remains a possibility that the observed anti-myc signals reflect exclusively non-specific staining. Although the *bamP-GAL4*-VP16 > *c(2)M* RNAi males were fertile, as expected based on the findings with *c(2)M* null mutants (Heidmann et al., 2004), their testes were not at all normal. DNA staining indicated large chromatin clumps of various shapes throughout the testis, scattered sperm heads, rows of nuclei apparently arrested during abnormal divisions were seen in more than 50% of the analyzed testes (data not shown). As such abnormalities were not reported to be present in *c(2)M* null males, it is conceivable that *bamP-GAL4*VP16 driven *c(2)M* RNAi during spermatogenesis causes off target effects. Additional analyses are therefore required to assess whether *c(2)M* knockdown by transgenic RNAi is feasible in testis. While the *c(2)M* mutant alleles can be used in principle instead of *c(2)M* depletion by RNAi, the latter would be attractive for *Rad21* and *c(2)M* double depletion which is genetically less complex than analyses with mutant alleles in combination with *Rad21* depletion.

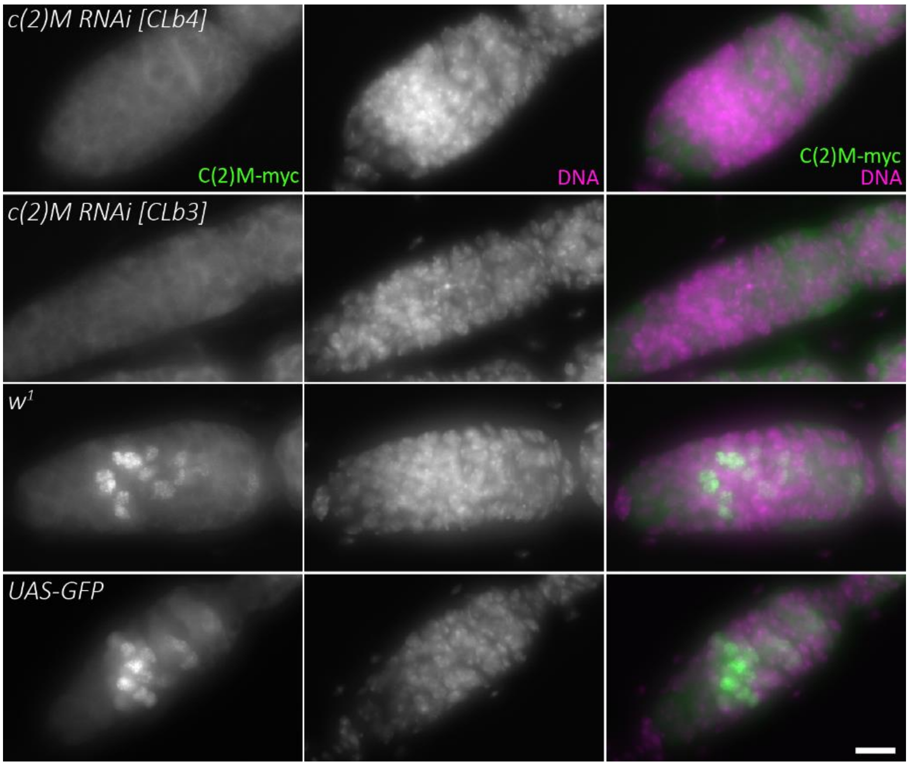

Fig 1: Functionality of C(2)M RNAi lines in females. *nos-GAL4* was used in combination with *UAS-shmiR* transgenes targeting *c(2)M*. Males of the indicated genotypes were crossed with *w*; gC(2)M-myc, C(2)M*^{EP}*/ CyO; nos-GAL4* virgins. Ovaries from F1 females (selected for absence of balancer chromosome) were fixed and stained with anti-myc and a DNA stain. Regions with the germarium are shown. Bottom row: For visualizing the pattern of expression driven by nos-GAL4, UAS-GFP was used as a positive control. Scale bar = 10 µm.

Analysis of the functionality of the *Rad21* RNAi lines was done in a similar manner. Gal4-dependent RNAi transgenes targeting *Rad21* were combined with the *bamP-GAL4VP16* transgene in a background with myc-tagged Rad21^{TEV} expressed under control of the *αTub84B* cis-regulatory region. Anti-myc staining revealed a clear reduction in signal intensity after *Rad21* knockdown (Fig. 2). No obvious morphological abnormalities were observed after Rad21 depletion. Moreover, these males were also fertile. This was true for all the tested RNAi transgenes. Additional analyses will be required to resolve whether *Rad21* function is indeed dispensable during spermatogenesis (perhaps as a consequence of functional redundancy with *c(2)M* or other genes like *ord*, *solo*, *sunn*) or whether the extent of depletion achieved in these experiments is not sufficiently complete to reveal potential *Rad21* requirements during spermatogenesis.

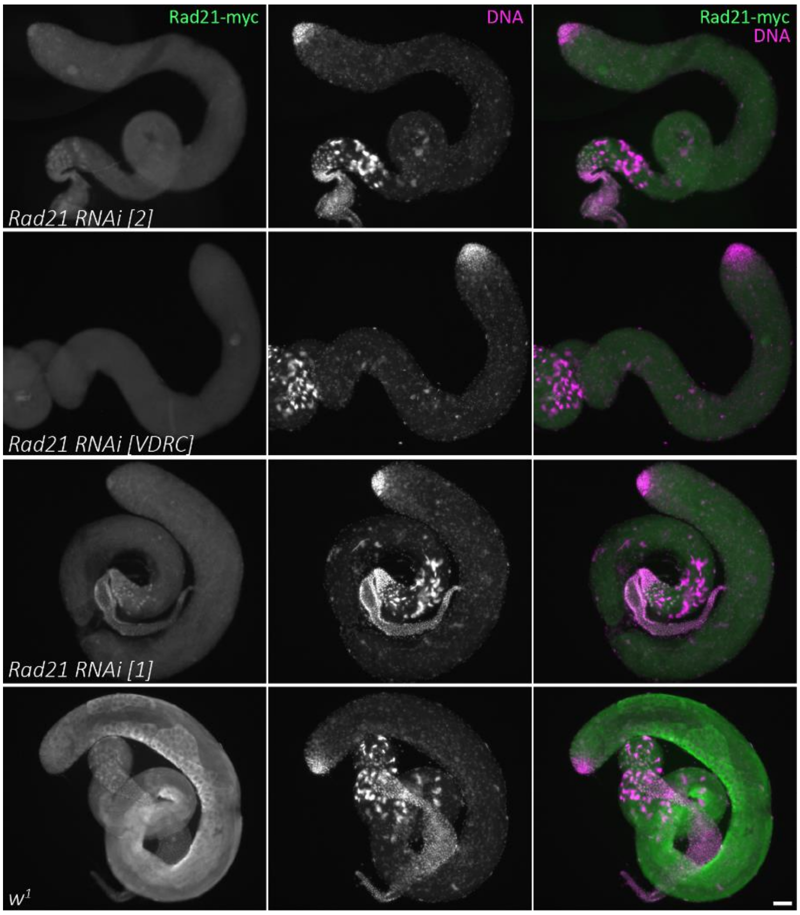

Fig 2: Functionality of Rad21 RNAi lines in males. *bam-GAL4VP16* was used in combination with *UAS-shmiR* transgenes targeting *Rad21*. Males of the indicated genotypes (Rad21 RNAi [2]: *UAS-V20vtd=Rad21*^{shmiR2}*),* (Rad21 RNAi [VDRC]: *UAS-GDvtd=Rad21*^{RNAi} *(II)*), *(*Rad21 RNAi [1]: *UAS-V20vtd=Rad21*^{shmiR1}), *w*^{1} were crossed with virgins of *w*; αTub84B-P-Rad21*^{TEV}*-myc; bam-GAL4VP16*. Whole mount testis preparations were stained with anti-myc and a DNA stain. Scale bar = 50 µm.

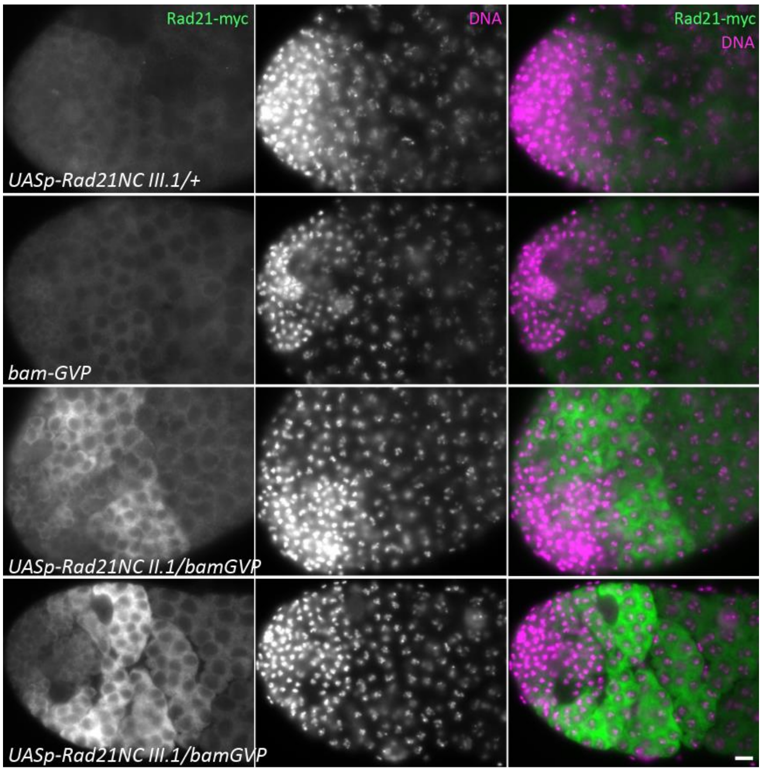

Fig 3: Expression pattern of non-cleavable Rad21 (Rad21NC) in males. *bam-GAL4VP16* (abbreviated as *bam-GVP*) was used for expression of the indicated *UASp-Rad21NC* transgene insertions. For control, testes from males having only *bam-GAL4VP16* or only a *UASp-Rad21NC* transgene insertion were analyzed as well. Anti-myc immunolabeling (Rad21-myc) was used to detect the expression of the *UASp-Rad21NC* transgene insertions which had a C terminal 10xmyc extension. Scale bar = 10 µm.

While Rad21 might not be required during spermatogenesis, it might still have to be cleaved by separase during progression through male meiosis. To explore whether Rad21 cleavage by separase is required for normal male meiosis, I analyzed the consequences of expression of a mutant Rad21 variant that cannot be cleaved by separase because of point mutations in the cleavage site (Urban et al., 2014). Cohesin complexes with non-cleavable Rad21 might result in anaphase bridges and mis-segregation of chromosomes during meiosis I and/or II. As the non-cleavable Rad21 variant had C-terminal myc-epitopes, its successful expression could readily be demonstrated (Fig. 3). However, no obvious meiotic defects resulted (n > 10 males). Similar observations were made in case of female meiosis (Urban et al., 2014). While expression in the female germline during oogenesis has no effect on meiosis, Rad21NC expression results in severe defects in chromosome segregation during the early mitotic divisions that follow just after completion of female meiosis. It appears likely, therefore, that Rad21 and also the non-cleavable variant are not assembled into cohesive structures before female and male meiosis. Future analyses will be required to confirm this proposal and clarify the mechanisms that prevent incorporation of non-cleavable Rad21 into cohesive structures specifically before meiosis.

Note that the predominantly cytoplasmic localization of Rad21-myc versions (as also apparent in Fig. 3) is also observed during mitotic division cycles in embryos that produce no endogenous Rad21. Since Rad21-myc restores Rad21 function in these embryos, it appears that some undetectable Rad21-myc is present on chromatin to provide sister chromatid cohesion during mitotic cycles in rescued embryos (Pauli et al., 2008).

2. Characterization of the *exu^m*, *exu^{mf}* and *ßTub85D* cis-regulatory regions

For analyses of meiotic consequences after target protein depletion by transgenic RNAi or induced target protein inactivation by DeGradFP or TEV, it is important that target depletion or degradation occur only at specific stages during spermatogenesis. Therefore, when using GAL4 driver transgenes in such experiments, it is crucial that they are expressed in an appropriate developmental pattern. (1) *GAL4* expression needs to start before meiosis. However, it should not start already during the preceding gonial mitotic division cycles. (2) Preferably, *GAL4* expression at the appropriate stages should occur at a high level. The GAL4 driver transgenes used so far for premeiotic expression in males are not optimal. For example, *bamP-GAL4VP16* expression starts a bit too early. It occurs already during the late gonial division cycles (Chen and McKearin, 2003). Moreover, its expression ceases relatively early during spermatocyte differentiation. Another driver, *topi-GAL4VP16* does not result in premature expression but its expression level, as gauged from GFP fluorescence when used in combination with UASt-GFP appears to be very weak (Raychaudhuri, 2012).

To explore cis-regulatory regions that might be more suitable for high level expression exclusively and ideally throughout spermatocyte maturation before meiosis, I generated transgenic lines with EGFP reporter transgenes. Three potentially suitable cis-regulatory regions (*exu^m, exu^{mf}, ßTub85D*) were used in these reporter transgenes to control the expression of EGFP. *exu^m* and *exu^{mf}* contain fragments from the upstream control region of the germline-specific *exu* gene. *exu^m* is predicted to cause expression exclusively in spermatocytes, while *exu^{mf}* is expected to drive expression also in the female germline in egg chambers during oogenesis. *ßTub85D* is a testis-specific ß-tubulin paralog.

The pattern of EGFP expression in the obtained transgenic lines was analyzed. In whole mount testes preparations (Fig 4), the expression driven by *exu^m* and *exu^{mf}* was found to start earlier during spermatocyte maturation than that driven by *ßTub85D.* Moreover, the latter was maintained for longer during spermatogenesis. Analyses with ovaries confirmed that *exu^{mf}* but not *exu^m* drives expression during oogenesis (data not shown).

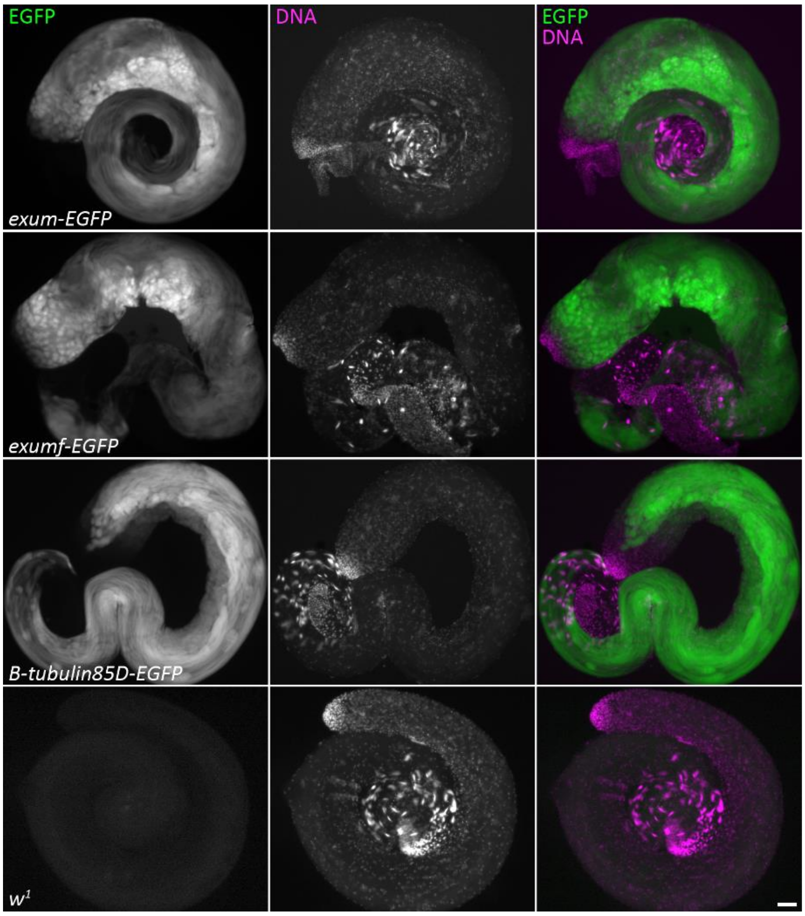

Fig 4: The pattern of expression during spermatogenesis directed by the cis-regulatory regions *exu*^{m}, *exu*^{mf} and *ßTub85D*. Whole mount testis preparations with transgenic lines of the indicated genotype are displayed. Testis were fixed and labeled with a DNA stain. GFP fluorescence is shown on the left column. Scale bar = 20 µm.

3. Generation of transgenic lines for efficient spermatocyte-specific DeGradFP

Initial experiments involving DeGradFP-mediated elimination of Rad21-EGFP specifically in spermatocytes in a background without endogenous Rad21 did not reveal phenotypic consequences (data not shown). This might be explained in three different ways. (1) Rad21 might not be required for male meiosis. (2) DeGradFP might not have caused Rad21 inactivation at all. However, earlier experiments have clearly demonstrated spermatocyte specific DeGradFP works in principle, at least in case of Cid-EGFP and separase-EGFP (Blattner et al., 2016; Raychaudhuri et al., 2012). (3) In case of Rad21, DeGradFP might work but inadequately. In these initial experiments, expression of *UASt-N-Slmb-vhh-GFP4* was driven with *topi-GAL4-VP16* and *bamP-GAL4VP16*, respectively. Based on the findings concerning pattern and level of the EGFP reporter transgene expression driven by the *exu*^{m}*, exu*^{mf} and *ßTub85D*, it appeared conceivable that transgenes driving expression of *N-Slmb-vhh-GFP4* directly under control of these regulatory regions might produce more efficient spermatocyte-specific DeGradFP. To facilitate future experiments involving TEV-mediated inactivation of target proteins, analogous TEV transgenic lines were generated in parallel.

For analysis of the functionality of the newly generated *exu*^{m}*-DeGradFP*, *exu*^{mf}*-DeGradFP* and *ßTub85D-DeGradFP* transgenes, these were crossed together with a Cid-EGFP transgene, followed by analysis of the Cid-EGFP expression pattern in testes. The results demonstrated that all the novel DeGradFP transgenes were functional as expected (Fig 5A).

In a subsequent step, *exu*^{m}*-DeGradFP* was used in combination with gSMC1-Rad21-EGFP to deplete Rad21 just before meiosis (in an otherwise Rad21^{+} or Rad21^{null} background). Although DeGradFP appeared to have a clear effect, as revealed by the absence of EGFP signals in spermatocyte nuclei (Fig 5B), progression through meiosis was not noticeably affected. Post-meiotic nuclei were of regular size. Moreover, males were fertile (data not shown).

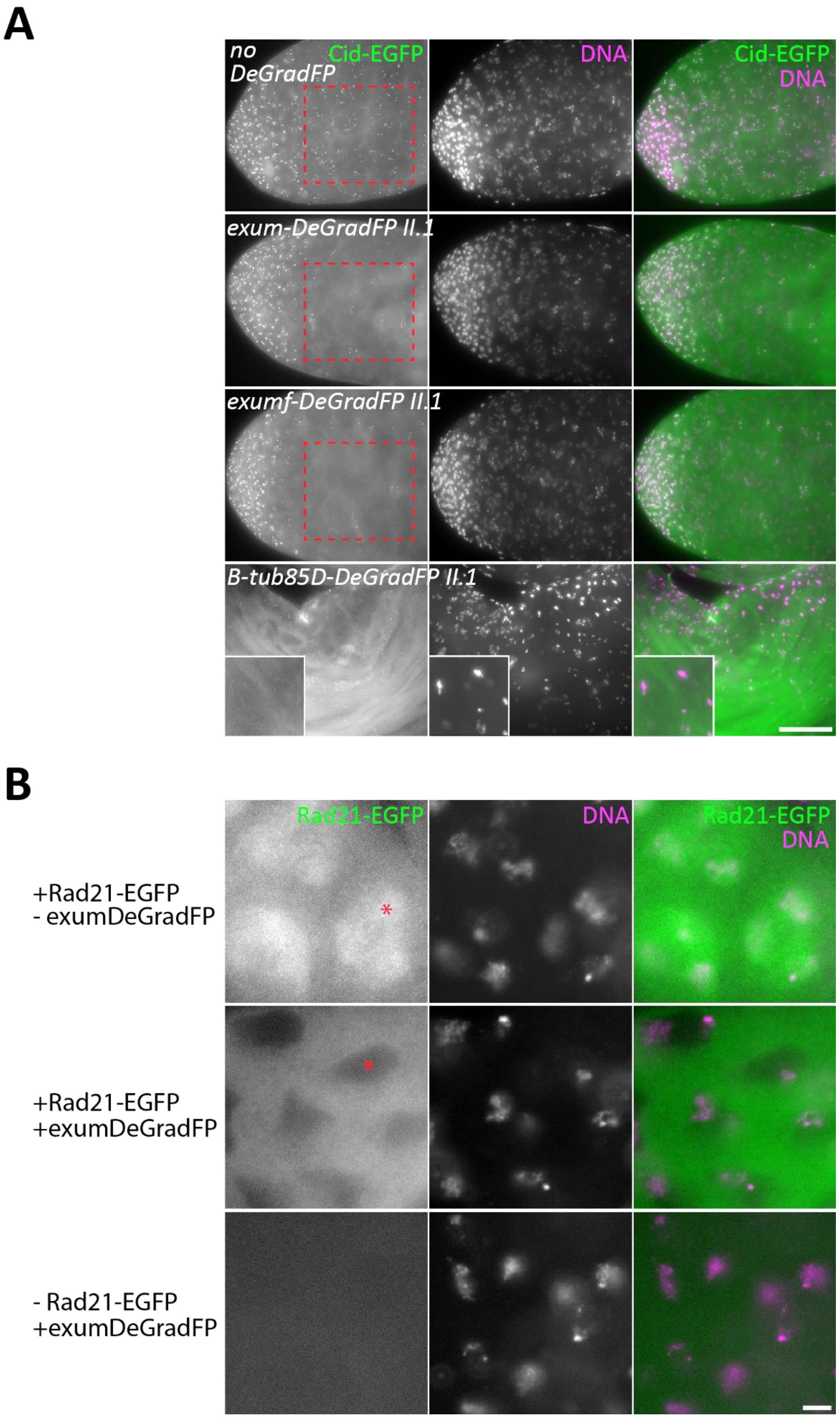
A
no DeGradFP
Cid-EGFP
DNA
Cid-EGFP
DNA
exum-DeGradFP II.1
exumf-DeGradFP II.1
B-tub85D-DeGradFP II.1
B
Rad21-EGFP
DNA
Rad21-EGFP
DNA
+Rad21-EGFP
- exumDeGradFP
*
+Rad21-EGFP
+exumDeGradFP
*
- Rad21-EGFP
+exumDeGradFP

Fig 5: Functionality of DeGradFP transgenes under control of the *exu*^{m}, *exu*^{mf} and *ßTub85D* cis regulatory regions. A. The indicated DeGradFP transgenes were crossed together with *Cid-EGFP*. Whole mount testis preparations were labeled with a DNA stain. Apical testis regions are displayed. The red dotted squares indicated regions where Cid-EGFP signals are depleted by the DeGradFP transgenes but not in the control. These DeGradFP transgenes are not expressed in the somatic cysts cells and therefore Cid-EGFP signals are present in these cells. The inset in the bottom row shows high magnification views of spermatocytes during meiotic divisions. No Cid-EGFP dots are observed in these meiotic stages, in contrast to controls (not shown; Raychaudhuri, 2012) Scale bar = 10 µm. **B.** Late primary spermatocytes expressing either or both exum-deGradFP and gSMC1-Rad21-EGFP are shown. All three conditions are in a rad21-null background. Red asterisk indicate the nuclear region which has Rad21-EGFP signal without DeGradFP (top row) and with DeGradFP (middle row). Scale bar = 5 µm.

4. Spermatocyte-specific elimination of *Rad21* function using TEV cleavage in combination with *gSMC1-Rad21*^{TEV}

Elimination of *Rad21* function using TEV in combination with a transgene expressing a TEV-cleavable Rad21-myc^{TEV} variant has been applied successfully in early embryos (Pauli et al., 2008). TEV mediated cleavage of Rad21-myc^{TEV} has also been attempted and assayed by immunobloting with whole testis samples (unpublished data, Nitika Taneja). In these experiments, UAS-TEV expression was driven with *bam-GAL4VP16*. The results of these experiments were inconsistent. Males with *bam-GAL4VP16* driven UAS-TEV expression in a background expressing exclusively Rad21-myc^{TEV} displayed a surprsingly variable fertility (either 100% or 0% in a poorly reproducible ratio). Moreover, significant Rad21-myc^{TEV} cleavage could not be detected on immunoblots. However, the immunoblotting experiments were not conclusive because of the following problem. Because *bam-GAL4VP16* is not expressed in the apical tip region of the testis, Rad21-myc^{TEV} will not be cut in this region. The presence of such uncut Rad21-myc^{TEV} in whole testis extracts precludes an accurate estimation of how much Rad21-myc^{TEV} might be cleaved in spermatocytes. Hence, I performed and repeated the immunoblot analyses using only the posterior testis part without the apical tip for extract preparation. In case of the control samples (*w*^{1} testis) the apical tips were not removed.

Unfortunately, the comparison of Rad21-myc^{TEV} samples without and with TEV expression did not reveal convincing differences (Fig 6A) indicating that the intended Rad21-myc^{TEV} elimination by TEV cleavage was not effective in testis.

Fig 6: Evaluation of TEV-mediated cleavage of Rad21^{TEV} in testis. A. Testis extracts were prepared from males with the indicated genotypes: +TEV (*2x αTub84Bp-Rad21-myc*^{TEV} *AP202, AP205*; *rad21*^{ex3}*, UASp1-TEV III.3/ rad21*^{ex3}*, bam-GAL4VP16*), –TEV (*2x αTub84Bp-Rad21-myc*^{TEV} *AP202, AP205*; *rad21*^{ex3}*/ rad21*^{ex3}*, bam-GAL4VP16*), w^{1} (*w*^{1}). The apical testes tips, where TEV is not yet expressed, were cut off before extract preparation (except in case of the *w*^{1} genotype). Immunoblots were probed using anti-myc to detect Rad21-myc^{TEV}. A dilution series prepared with the -TEV extract was loaded for quantitative comparison of the Rad21-myc^{TEV} bands detected by anti-myc. The expressed TEV variant has a V5-tag (Pauli et al. 2008) and was therefore detected using anti-V5 tag. **B.** Comparison of Rad21-myc^{TEV} protein levels resulting from transgenes under control of the cis regulatory region of either *αTub84B* or *SMC1* after immunoblotting of embryo extracts with anti-myc. A dilution series prepared with embryos expressing two copies of *αTub84Bp-Rad21-myc*^{TEV} served as a positive control for quantitative comparisons. Two independent lines *gSMC1-Rad21*^{TEV} *II.1 and gSMC1-Rad21*^{TEV} *III.3* were analyzed. *w*^{1} served as a negative control. *gSMC1-Rad21*^{TEV} clearly results in far lower expression when compared with *αTub84Bp-Rad21-myc*^{TEV}. AP202 and AP205 are two distinct insertions of the *αTub84Bp-Rad21-myc*^{TEV} transgene (Pauli et al., 2008).

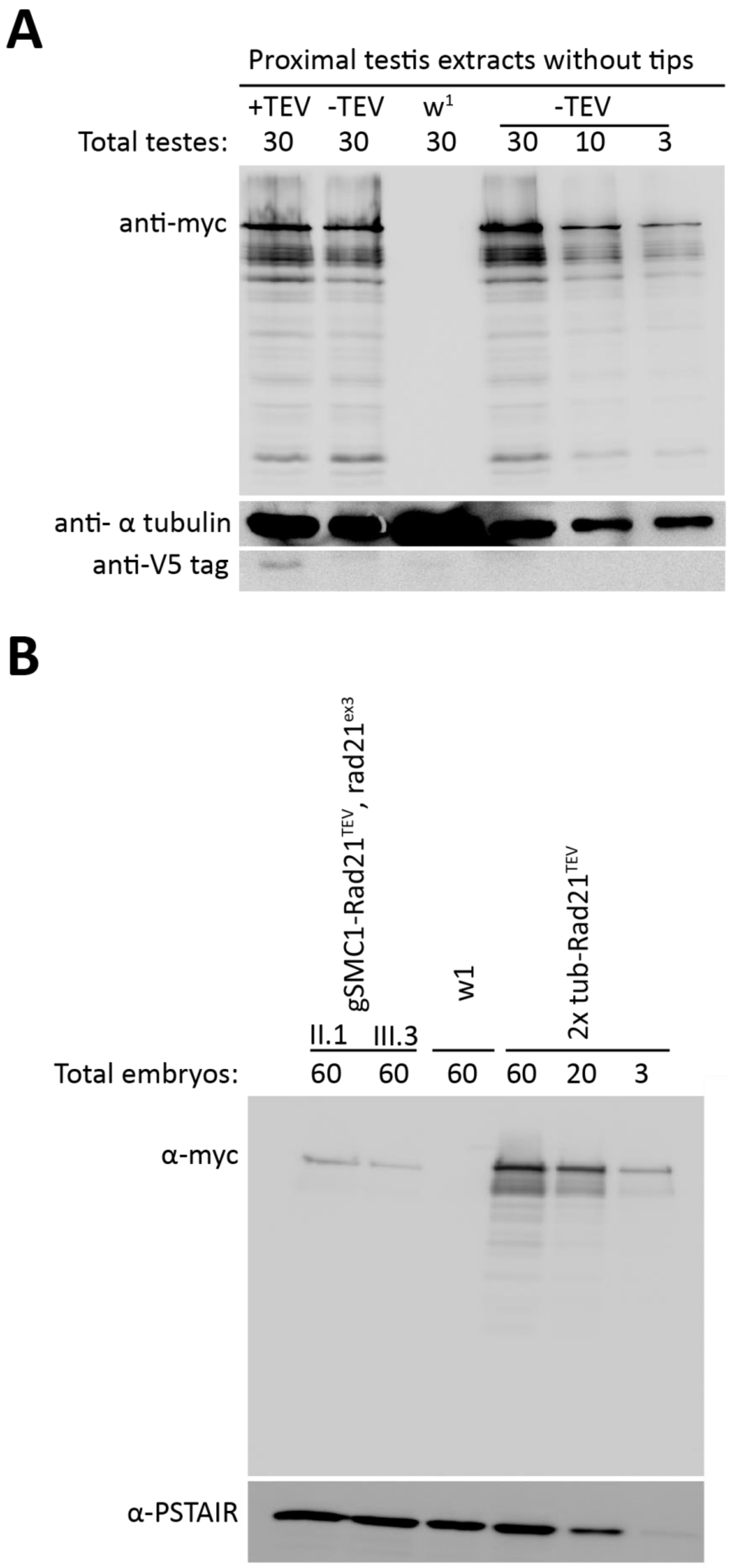
A
Proximal testis extracts without tips
+TEV
-TEV
w1
-TEV
Total testes: 30 30 30 30 10 3
anti-myc
anti- α tubulin
anti-V5 tag
B
gSMC1-Rad21TEV, rad21ex3
w1
2x tub-Rad21TEV
II.1
III.3
Total embryos: 60 60 60 60 20 3
α-myc
α-PSTAIR

The *Rad21-myc*^{TEV} transgene used in these experiments is under control of the *αTub84B* promoter which results in very strong expression in late spermatocytes. As the very high levels of Rad21-myc^{TEV} expressed in spermatocytes might prevent complete inactivation by TEV cleavage after spermatocyte-specific *UAS-TEV* expression driven by *bam-GAL4VP16*, I generated transgenic lines (*gSMC1-Rad21-myc*^{TEV}) where the cis-regulatory region of the *SMC1* gene drives expression of the TEV cleavable Rad21 variant, hopefully at lower levels in spermatocytes. As the *vtd/rad21* gene is within the pericentromeric heterochromatin, it is difficult to delineate and use its cis-regulatory sequences. As the *vtd/rad21* gene expresses a subunit that associates with SMC1, the cis-regulatory region of this latter euchromatic gene is predicted to drive expression at comparable levels and pattern as *vtd/rad21*.

After generation of transgenic *gSMC1-Rad21-myc*^{TEV} lines, I checked whether this transgene can complement a *vtd/rad21*-null mutation. I found that one copy of the transgene was insufficient to rescue the developmental lethality caused by *vtd/rad21*-null mutations. Recombination atttempts for the generation of chromosomes with double insertions of *gSMC1-Rad21-myc*^{TEV} were not successful.

Immunoblot experiments with embryo extracts confirmed expression of the *gSMC1-Rad21-myc*^{TEV} transgene (Fig 6B). As expected, this expression was considerably lower than that obtained with the *αTub84B-Rad21-myc*^{TEV} transgene (Fig 6B). These low expression levels might explain why one copy of *gSMC1-Rad21-myc*^{TEV} cannot rescue *vtd/Rad21*-null mutants in contrast to *αTub84B-Rad21-myc*^{TEV}*.* The latter transgene, however, is also not fully functional like the endogenous wild-type *vtd/Rad21*$^{+}$ gene, because normal fertility depends on the presence of two *αTub84B-Rad21-myc*^{TEV} copies in *vtd/Rad21* null mutants, while hemizygous *vtd/Rad21*$^{+}$*/Df* flies have normal fertility (Pauli et al., 2008).

5. In vivo assays for separase cleavage

Separase activity during meiosis is required for the regionally controlled step-wise cleavage of cohesin. In yeast, separase (Sse) is known to become active twice in meiosis, first before onset of anaphase I and later again before onset of anaphase II (Arguello-Miranda et al., 2017; Ishiguro et al., 2010; Katis et al., 2010). The temporal profile of separase activity has not been analyzed during *D. melanogaster* male meiosis. However, in principle this should be possible with the help of separase biosensors as successfully used during mitotic divisions in yeast and mammalian cells. (Agircan and Schiebel, 2014; Shindo et al., 2012; Yaakov et al., 2012). Moreover, with the help of modified biosensor constructs, it should also be possible to address whether proteins like C(2)M, Ord and Solo might be direct separase substrates.

The separase biosensor used successfully by Shindo et al. (2012) contains a Rad21 region including the separase cleavage sites flanked by a GFP and RFP on either end. In addition, the biosensor protein is fused on the RFP side to a domain that results in targeting to chromosomal regions. As a result of separase activition before the M/A transition, this chromosomal region suddenly loses green fluorescence when GFP diffuses away after cleavage and retains red fluorescence (Fig 7). Using this strategy, I have started to develop a biosensor that should allow separase activity monitoring during meiosis in spermatocytes.

Three generations of biosensor constructs were produced and evaluated. These generations included different domains for chromosomal targeting and different cis-regulatory regions for expression in flies. Moreover, in some constructs the linker region between the red and green fluorescent protein was not from Rad21 but from potential separase substrates (C(2)M, Ord and Solo).

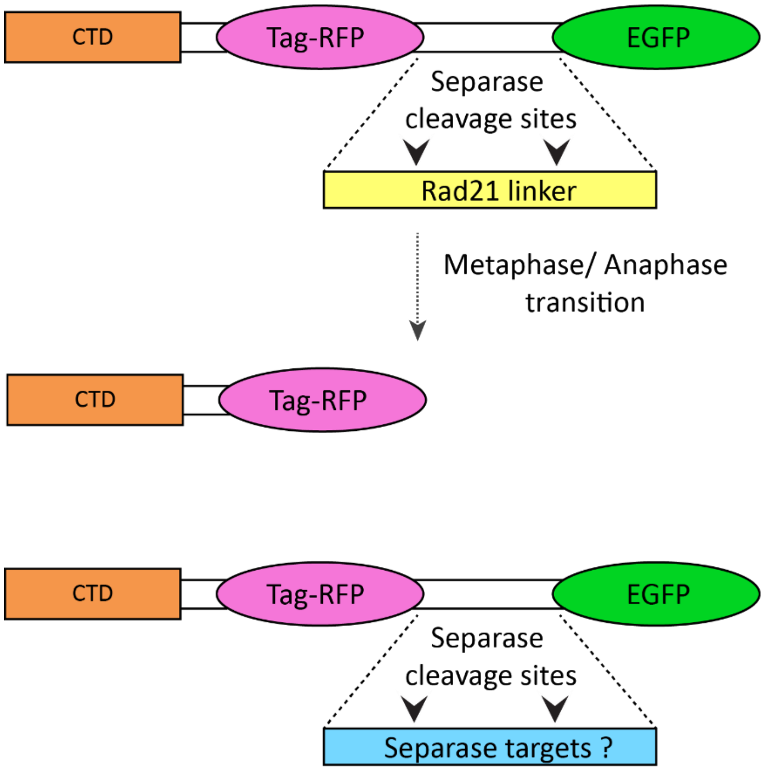

Fig 7: Principle of separase biosensors. A. Protease activity of endogenous separase can be assessed by change in fluorescence as GFP can diffuse away after cleavage by separase activity. B. by inserting regions from other proteins instead of the Rad21 linker regions, it can be assessed whether these proteins contain functional separase clevage sites. CTD= chromosome targeting domain. For details see text.

Generation 1:

1.1 His2Av Sse biosensor (pUASp1-His2Av-happyLinker-TagRFPT-Rad21linker-EGFP)

Initial attempts to develop a separase biosensor were highly analogous to the design of (Shindo et al., 2012). Transgenic lines expressing a *His2Av-happyLinker-TagRFPT-Rad21linker-EGFP* fusion protein from a UASp1 construct. In this construct, the chromatin targeting domain is histone H2Av (His2Av). This domain is linked via a short ‘happy linker’ sequence (Miyawaki et al., 2003) to the sensor part consisting of Tag-RFP-T followed by a Rad21 linker fragment and EGFP. The *D. melanogaster* Rad21 linker fragment includes two separase cleavage sites. Point mutations in these sites have been shown to cause phenotypes expected from resistance to separase cleavage (Urban et al., 2014). The Rad21 linker fragment does not contain the N- and C-terminal regions predicted to be required for binding to SMC3 and 1, respectively.

To evaluate the functionality of this biosensor, it was expressed in early embryos using the *mat-GAL4* driver. Unfortunately, the resulting high level of expression was associated with severe chromosome segregation defects. Moreover, a change from yellow to red fluorescence could not be observed during progression through these aberrant mitoses. Additional tests with other driver (with *bamP-GAL4VP16* in testis, *en-GAL4* in wing imaginal discs, and *Act5c-GAL4* after transient transfection in S2R+ cells) corroborated that this separase biosensor transgene could not be used. The resulting high expression levels might titrate away proteins like separase or other Rad21 partners from the endogenous cohesin, resulting in toxic effects.

Generation 2:

2.1 Cid Sse biosensor

Apart from histone H2B, Shindo et al. (2012) also used a domain that targets of the biosensor to the centromere. This version was actually shown to have superior properties. An analogous version exploiting Cid for centromere targeting was considered initially. However, initial preference was then given to His2Av because of the known dynamics of Cid loading (Lidsky et al., 2013; Schuh et al., 2007). Cid loading occurs during exit from mitosis. Newly loaded Cid might therefore partially abolish an efficient fluorescence change from yellow to red during exit from mitosis because of ongoing integration of new non-cleaved yellow Cid-biosensor. However, after the failure with the His2Av separase biosensor, Cid as chromatin targeting domain was evaluated nevertheless. Its functionality was first analysed after transient expression in S2R+ cells.

The expression of the Cid separase biosensor protein was under control of the metallothionein promoter. After co-transfection of S2R+ cells with the construct and pCoBlast, stable transformants were selected. Thereafter, Cid separase biosensor was induced for 48 hours with a concentration of $CuSO_4$ (500 µM) resulting in adequate levels of expression. Time lapse imaging was performed for 24 hours and the observed mitotic divisions were analyzed in detail. While nuclear signals were readily detected during interphase in many cells, localized centromeric signals could not be detected during interphase. However, in mitotic cells both GFP and RFP signals were found localized within the equatorial chromosome plate until metaphase. Interestingly, at the M/A transition, the EGFP signals dissipated away from the chromosomes for about 12 minutes until they reappeared in G1 (perhaps due to Cid loading). Therefore, the Cid separase biosensor is functional (Fig 8A). Imaging conditions were optimized for additional characterization.

2.2 Cid Sse biosensor control version

To confirm that the Cid separase biosensor indeed reports separase activity, I made a control construct. This construct was identical to the Cid separase biosensor construct except that the Rad21 linker region contained point mutations that destroy the two separase cleavage sites (R175A and R474A, numbers refer to aa positions in the wildtype *rad21* gene product). As a result, fluorescence change from yellow to red should not occur during progression through mitosis. As expected, this color change was no longer observed in experiments with this control constructs (Fig 8A).

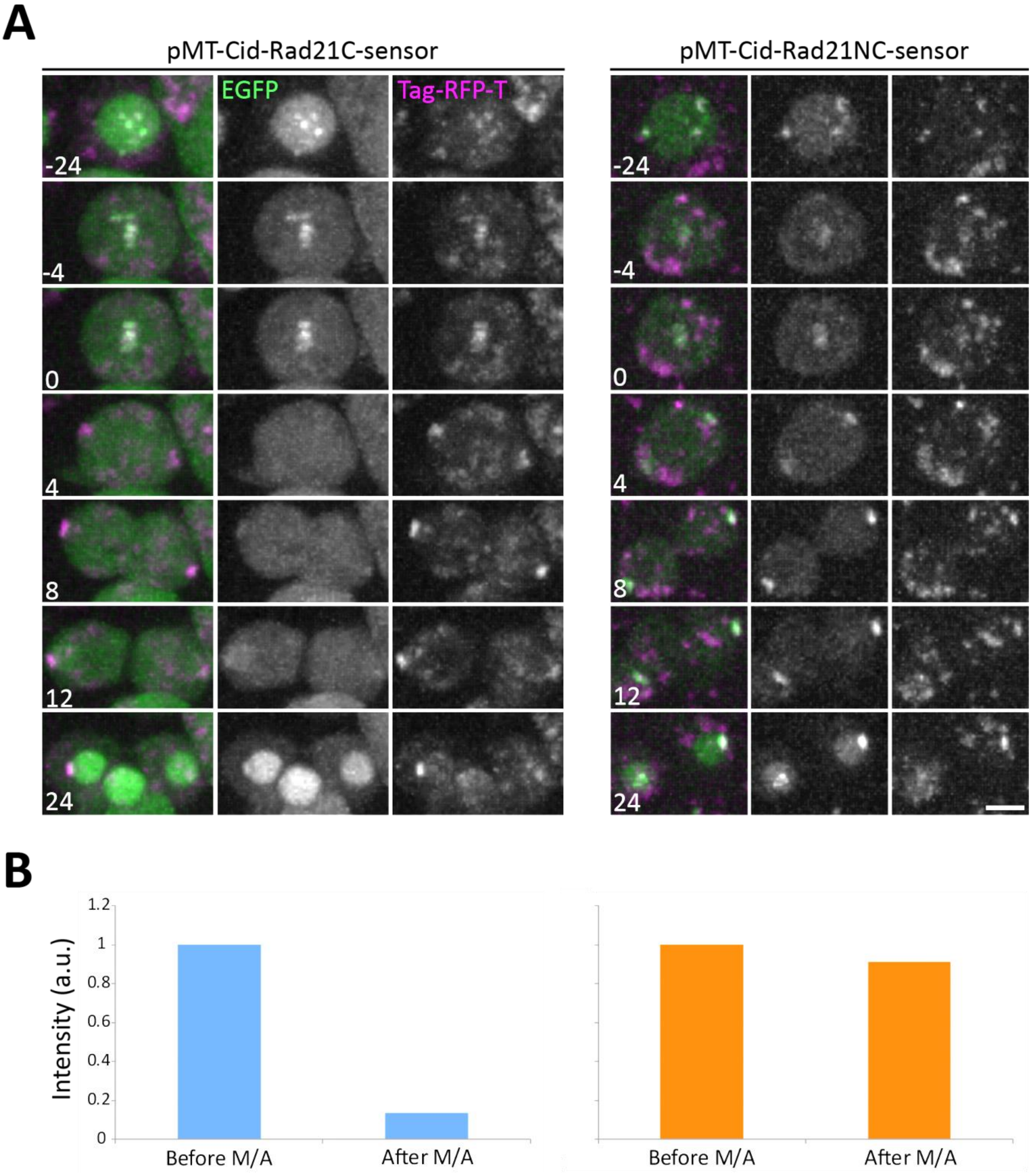

Fig 8: Cid Sse biosensor in S2R+ cells. A. Representative stills from experiments with the cleavable(C) and non cleavable (NC) Rad21 linker are shown. (Rad21C, n= 54; Rad21NC, n=32). Scale bar = 5 µm. **B.** Intensity quantification was done for the frame just before anaphase onset and two frames after anaphase onset clearly reveals massive drop in the ratio of GFP:RFP signals but only in case of the cleavable Rad21 linker. (Rad21C, n= 9; Rad21NC, n=10).

2.3 Cid Sse biosensor variants for evaluation of the presence of function Sse cleavage sites in proteins other than Rad21

To assess whether the proteins Ord, SOLO and C(2)M might contain functional Sse cleavage sites, I generated variants where the Rad21 linker region was replaced with the full length coding regions of these other proteins. These constructs were analyzed in experiments analogous to those performed with the Rad21 linker constructs. The expression of the new separase biosensor variants was found to be highly variable. Moreover, no specific intracellular localization on the centromeres was observed above the diffuse signals. Additional variants made with the coding regions of SNM, MNM and TEF did also not result in clear positive results. (Blattner, 2016).

2.4 Cid Sse biosensor variants for expression in testis

bam->Cid Sse biosensor

The Cid separase biosensor constructs used successfully for the demonstration that separase activity can be detected with the Rad21 linker region were not suitable for expression during meiosis in flies. Therefore, construct variants were generated followed by production of transgenic fly lines. In a first construct, *bam* cis-regulatory region was used. As expected, the transgene was expressed in early spermatocytes (Fig 9A). In late spermatocytes, however, the centromeric signals were no longer clearly above background in case of the green channel in part also because of increasing auto-fluorescence. As a result, these transgenes could not be used for analyses of separase activity during meiosis.

cid->Cid Sse biosensor

In an additional transgene construct, the *cid* cis-regulatory region was used. Centromere specific signals were again detectable in early spermatocytes. The centromeric Tag-RFP-T signals were already extremely weak compared to EGFP (Fig 9B). Unfortunately, in late spermatocytes (S5/S6) or meiotic stages it was no longer possible to detect centromeric signals above background.

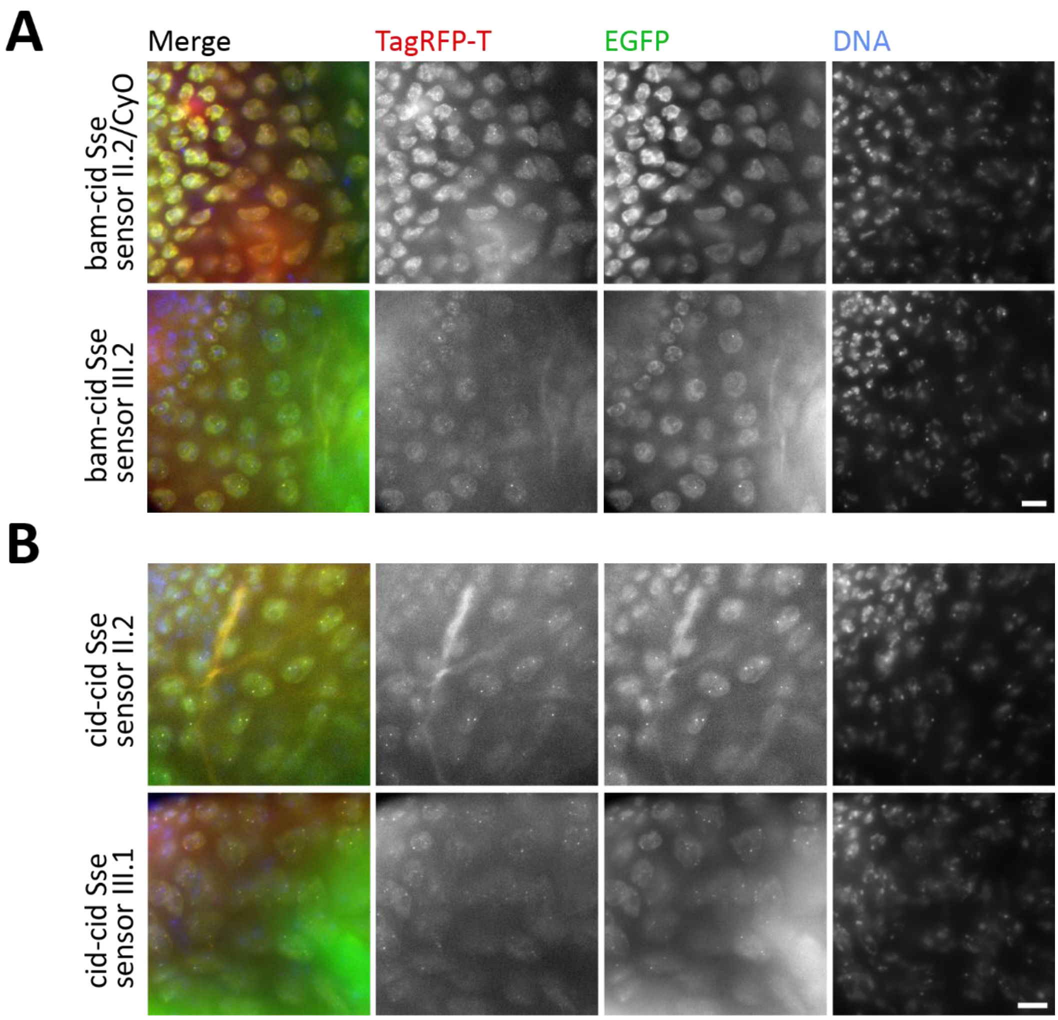

Fig 9: Expression of Cid Sse biosensor transgenes in testis. Representative stills of testis apical tip regions of whole mount preparations of indicated transgenic lines are shown. **A.** bam->Cid Sse biosensor. **B.** cid->Cid Sse biosensor. Scale bars = 10 µm.

Generation 3:

3.1 TALE-Sse biosensor

The third generation of separase biosensors was created using a TALE repeat for targeting specific pericentric DNA repeat sequences on autosomes (Yuan et al., 2014). Initial tests in S2R+ cells indicated that the TALE Sse biosensor was functional (Fig 10). However, similar as reported by Yuan et al (2014), the chromosomally localized signals were seen to drop substantially during mitosis. Minimal intensity was seen during metaphase. Apparently the TALE repeat domain is partially displaced from the chromosomes during M phase.

Nevertheless, the remaining signals were entirely sufficient to detect the indicative yellow to red color change during exit from mitosis.

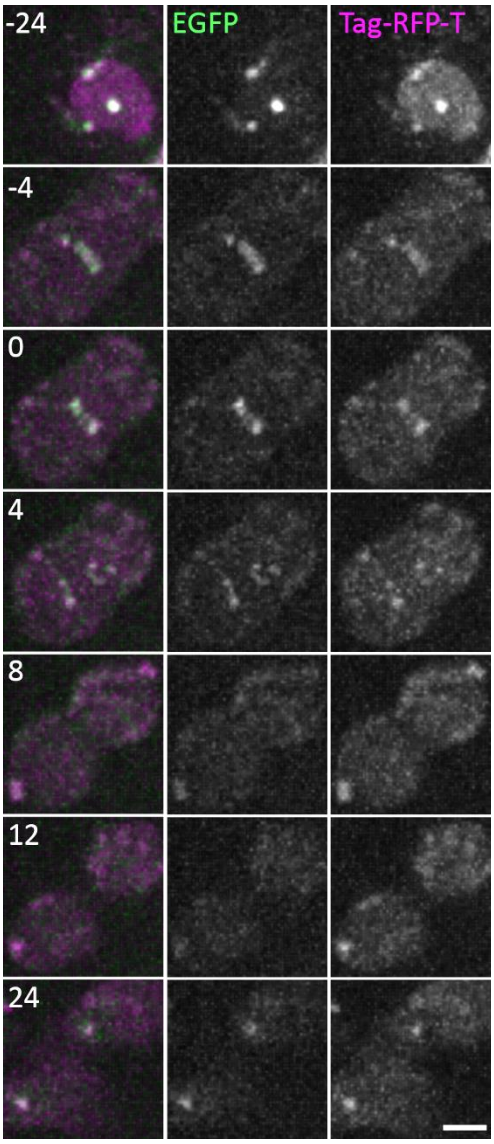

Fig 10: TALE Sse biosensor in S2R+ cells. Representative stills demonstrating the functionality of the TALE sensor. Scale bar= 5 µm.

Discussion

Males homozygous for *c(2)M* null mutations do not appear to suffer from any problems during spermatogenesis (Heidmann et al., 2004; Manheim and McKim, 2003) even though there seems to be low level expression of *c(2)M* in testes according to FlyAtlas (Chintapalli et al., 2007). In principle, the absence of a *c(2)M* mutant phenotype in testis might reflect functional redundancies. It is conceivable, *vtd/Rad21* and *c(2)M* might have partial functional overlap, as both code for α-kleisin family proteins. A comparison of the phenotypes caused by single mutations in *c(2)M* and *vtd/Rad21*, respectively, with those present in double mutants should therefore be of interest. Unfortunately, genetic elimination of *vtd/Rad21* function specifically in the male germline is not straightforward. *vtd/Rad21* is essential for development to the stages where spermatogenesis is underway. Moreover, the location of the *vtd/Rad21* gene in pericentromeric heterochromatin complicates clonal analyses. It precludes the application of the established efficient Flp/FRT-based approaches. As an alternative, Rad21 depletion by RNAi was considered. As double depletion by RNAi is technically simple in principle, C(2)M depletion by RNAi was considered as well. Unfortunately, this approach has not given conclusive evidence. Transgenic RNAi lines that appear to be functional could be identified in both cases. But expression in testis caused either no detectable abnormalities (in case of *vtd/Rad21*) or abnormalities that appear to reflect off target effects (in case of *c(2)M*). It remains to be excluded that the absence of abnormalities after expression of the *vtd/Rad21* RNAi transgene in testis is not explained by insufficient depletion. On the other hand, as *vtd/Rad21* function is no longer required in the female germline when oocytes progress through the meiotic divisions (Urban et al., 2014), this gene might not be required also during the male meiotic divisions. As in oogenesis, my results indicate that it is also impossible to induce defects during the male meiotic divisions by expression of a Rad21 variant that cannot be cleaved by separase.

Previous experiments in embryos have demonstrated that instead of RNAi an alternative approach involving TEV protease-mediated cleavage of a functional Rad21 variant with TEV cleavage sites can be used for rapid elimination of Rad21 function (Pauli et al., 2008). This approach was also applied in spermatocytes where it was observed to have surprisingly variable and hence puzzling effects on male fertility (N. Raychaudhuri, unpublished data). Yet another strategy that has been used successfully for spermatocyte-specific elimination of certain target proteins is the DeGradFP system (Caussinus et al., 2012). However, the initial attempts with this system did not result in promising results in case of Rad21.

To make future applications of RNAi, DeGradFP and TEV for protein elimination specifically in spermatocytes more convenient and more effective, I have successfully generated various transgenic lines using cis-regulatory regions from different genes (*exu*^{m}, *exu*^{mf}, *ßTub85D*, *SMC1*) for the control of expression. EGFP reporter transgenes controlled by *exu*^{m}, *exu*^{mf} and *ßTub85D* demonstrated that these regulatory regions drove expression in the desired patterns. These regulatory regions were therefore used for the production of transgenic lines expressing DeGradFP or TEV. The functionality of the DeGradFP transgenic lines could be demonstrated clearly in combination with Cid-EGFP. Similarly, experiments with gSMC1-Rad21-EGFP confirmed the functionality of the DeGradFP transgenes. By using the cis regulatory regions of SMC1, I was actually also successful in generating transgenes that express *Rad21* at a level lower than the previously generated *Rad21* transgenes under control of the *αTub84B* promoter (Pauli et al., 2008), as revealed by immunoblotting. These transgenic lines should be very useful for future analyses in testis not only in the context of the functional characterization of the α-kleisins (Rad21 and C(2)M) but also in case of other proteins of interest.

By adapting a strategy used successfully in cultured mammalian cells (Shindo et al., 2012), I have also been able to make substantial progress towards establishment of biosensors for the analysis of the spatial and temporal control of separase activity during the meiotic divisions. Cid as well as TALE repeats were shown to function sufficiently for chromosomal targeting of the separase biosensor proteins. Unfortunately, it has proven difficult so far to express the separase biosensor at a level that allows analyses during the meiotic divisions. This remains a challenge which however should be worth tackling as this strategy can also be used for an evaluation of potential additional separase substrates. Separase has been implicated in the removal of the alternative homolog conjunction system during meiosis I in *D. melanogaster* spermatocytes as well as in the removal of pericentromeric cohesion during meiosis II. Proteins like Mnm, Snm, Teflon, Ord, Sunn or Solo therefore might be cleaved by separase during meiosis. Further progress in analyses with separase biosensors during meiosis therefore would be of great interest.

References

Agircan, F.G., and Schiebel, E. (2014). Sensors at centrosomes reveal determinants of local separase activity. PLoS Genet *10*, e1004672.

Akiyoshi, B., Sarangapani, K.K., Powers, A.F., Nelson, C.R., Reichow, S.L., Arellano-Santoyo, H., Gonen, T., Ranish, J.A., Asbury, C.L., and Biggins, S. (2010). Tension directly stabilizes reconstituted kinetochore-microtubule attachments. Nature *468*, 576-579.

Althoff, F. (2011). Characterization of Drosophila Cyclin J and Mps1 (University of Zurich).

Althoff, F., Karess, R.E., and Lehner, C.F. (2012). Spindle checkpoint-independent inhibition of mitotic chromosome segregation by Drosophila Mps1. Mol Biol Cell *23*, 2275-2291.

Alushin, G., and Nogales, E. (2011). Visualizing kinetochore architecture. Curr Opin Struct Biol *21*, 661-669.

Anderson, L.K., Royer, S.M., Page, S.L., McKim, K.S., Lai, A., Lilly, M.A., and Hawley, R.S. (2005). Juxtaposition of C(2)M and the transverse filament protein C(3)G within the central region of Drosophila synaptonemal complex. Proc Natl Acad Sci U S A *102*, 4482-4487.

Arguello-Miranda, O., Zagoriy, I., Mengoli, V., Rojas, J., Jonak, K., Oz, T., Graf, P., and Zachariae, W. (2017). Casein Kinase 1 Coordinates Cohesin Cleavage, Gametogenesis, and Exit from M Phase in Meiosis II. Dev Cell *40*, 37-52.

Arya, G.H., Lodico, M.J., Ahmad, O.I., Amin, R., and Tomkiel, J.E. (2006). Molecular characterization of teflon, a gene required for meiotic autosome segregation in male Drosophila melanogaster. Genetics *174*, 125-134.

Asbury, C.L. (2017). Anaphase A: Disassembling Microtubules Move Chromosomes toward Spindle Poles. Biology (Basel) *6*.

Ault, J.G., Lin, H.P., and Church, K. (1982). Meiosis in Drosophila melanogaster. IV. The conjunctive mechanism of the XY bivalent. Chromosoma *86*, 309-317.

Basto, R., Scaerou, F., Mische, S., Wojcik, E., Lefebvre, C., Gomes, R., Hays, T., and Karess, R. (2004). In vivo dynamics of the rough deal checkpoint protein during Drosophila mitosis. Curr Biol *14*, 56-61.

Bennabi, I., Terret, M.E., and Verlhac, M.H. (2016). Meiotic spindle assembly and chromosome segregation in oocytes. J Cell Biol *215*, 611-619.

Bickel, S.E., Orr-Weaver, T.L., and Balicky, E.M. (2002). The sister-chromatid cohesion protein ORD is required for chiasma maintenance in Drosophila oocytes. Curr Biol *12*, 925-929.

Bickel, S.E., Wyman, D.W., Miyazaki, W.Y., Moore, D.P., and Orr-Weaver, T.L. (1996). Identification of ord, a Drosophila protein essential for sister-chromatid cohesion. EMBO J *15*, 1451-1459.

Biswas, U., Hempel, K., Llano, E., Pendas, A., and Jessberger, R. (2016). Distinct Roles of Meiosis-Specific Cohesin Complexes in Mammalian Spermatogenesis. PLoS Genet *12*, e1006389.

Blattner, A. (2016). Drosophila Meiosis: Separase, Kinetochores and Novel Regulators. In Mathematisch-naturwissenschaftlichen Fakultät (Universität Zürich).

Blattner, A.C., Aguilar-Rodriguez, J., Kranzlin, M., Wagner, A., and Lehner, C.F. (2017). Drosophila Nnf1 paralogs are partially redundant for somatic and germ line kinetochore function. Chromosoma *126*, 145-163.

Blattner, A.C., Chaurasia, S., McKee, B.D., and Lehner, C.F. (2016). Separase Is Required for Homolog and Sister Disjunction during Drosophila melanogaster Male Meiosis, but Not for Biorientation of Sister Centromeres. PLoS Genet *12*, e1005996.

Blower, M.D., Sullivan, B.A., and Karpen, G.H. (2002). Conserved organization of centromeric chromatin in flies and humans. Dev Cell *2*, 319-330.

Braun, R.E., Behringer, R.R., Peschon, J.J., Brinster, R.L., and Palmiter, R.D. (1989). Genetically haploid spermatids are phenotypically diploid. Nature *337*, 373-376.

Buffin, E., Emre, D., and Karess, R.E. (2007). Flies without a spindle checkpoint. Nat Cell Biol *9*, 565-572.

Buffin, E., Lefebvre, C., Huang, J., Gagou, M.E., and Karess, R.E. (2005). Recruitment of Mad2 to the kinetochore requires the Rod/Zw10 complex. Curr Biol *15*, 856-861.

Buonomo, S.B., Clyne, R.K., Fuchs, J., Loidl, J., Uhlmann, F., and Nasmyth, K. (2000). Disjunction of homologous chromosomes in meiosis I depends on proteolytic cleavage of the meiotic cohesin Rec8 by separin. Cell *103*, 387-398.

Cai, S., O'Connell, C.B., Khodjakov, A., and Walczak, C.E. (2009). Chromosome congression in the absence of kinetochore fibres. Nat Cell Biol *11*, 832-838.

Callan, H.G., and Jacobs, P.A. (1957). The meiotic process in mantis religiosa L. males. J Genet

Caussinus, E., Kanca, O., and Affolter, M. (2012). Fluorescent fusion protein knockout mediated by anti-GFP nanobody. Nat Struct Mol Biol *19*, 117-121.

Cenci, G., Bonaccorsi, S., Pisano, C., Verni, F., and Gatti, M. (1994). Chromatin and microtubule organization during premeiotic, meiotic and early postmeiotic stages of Drosophila- melanogaster spermatogenesis. J Cell Sci *107*, 3521-3534.

Chaurasia, S. (2012). The role of Drosophila Rad21 and Spc105 during male meiosis. Master thesis, Mathematisch-naturwissenschaftlichen Fakultät, Universität Zürich.

Cheeseman, I.M., and Desai, A. (2008). Molecular architecture of the kinetochore-microtubule interface. Nat Rev Mol Cell Biol *9*, 33-46.

Chelysheva, L., Diallo, S., Vezon, D., Gendrot, G., Vrielynck, N., Belcram, K., Rocques, N., Marquez-Lema, A., Bhatt, A.M., Horlow, C., *et al.* (2005). AtREC8 and AtSCC3 are essential to the monopolar orientation of the kinetochores during meiosis. J Cell Sci *118*, 4621-4632.

Chen, D., and McKearin, D.M. (2003). A discrete transcriptional silencer in the bam gene determines asymmetric division of the Drosophila germline stem cell. Development *130*, 1159-1170.

Chintapalli, V.R., Wang, J., and Dow, J.A. (2007). Using FlyAtlas to identify better Drosophila melanogaster models of human disease. Nat Genet *39*, 715-720.

Church, K., and Lin, H.P. (1982). Meiosis in Drosophila melanogaster. II. The prometaphase-I kinetochore microtubule bundle and kinetochore orientation in males. The Journal of cell biology *93*, 365-373.

Church, K., and Lin, H.P. (1985). Kinetochore microtubules and chromosome movement during prometaphase in Drosophila melanogaster spermatocytes studied in life and with the electron microscope. Chromosoma *92*, 273-282.

Church, K., Nicklas, R.B., and Lin, H.P. (1986). Micromanipulated bivalents can trigger mini-spindle formation in Drosophila melanogaster spermatocyte cytoplasm. J Cell Biol *103*, 2765-2773.

Church, k.a.L., H. P. (1988). Drosophila: a model for the study of aneuploidy. Aneuploidy *Part B*, pp. 227-255.

Colombie, N., Cullen, C.F., Brittle, A.L., Jang, J.K., Earnshaw, W.C., Carmena, M., McKim, K., and Ohkura, H. (2008). Dual roles of Incenp crucial to the assembly of the acentrosomal metaphase spindle in female meiosis. Development *135*, 3239-3246.

Corbett, K.D., Yip, C.K., Ee, L.S., Walz, T., Amon, A., and Harrison, S.C. (2010). The monopolin complex crosslinks kinetochore components to regulate chromosome-microtubule attachments. Cell *142*, 556-567.

Cox, D.N., Lu, B., Sun, T.Q., Williams, L.T., and Jan, Y.N. (2001). Drosophila par-1 is required for oocyte differentiation and microtubule organization. Curr Biol *11*, 75-87.

Cross, D.P., and Shellenbarger, D.L. (1979). The dynamics of Drosophila melanogaster spermatogenesis in in vitro cultures. J Embryol Exp Morphol *53*, 345-351.

Danzer, J.R., and Wallrath, L.L. (2004). Mechanisms of HP1-mediated gene silencing in Drosophila. Development *131*, 3571-3580.

Das, A., Shah, S.J., Fan, B., Paik, D., DiSanto, D.J., Hinman, A.M., Cesario, J.M., Battaglia, R.A., Demos, N., and McKim, K.S. (2016). Spindle Assembly and Chromosome Segregation Requires Central Spindle Proteins in Drosophila Oocytes. Genetics *202*, 61-75.

Daum, J.R., Potapova, T.A., Sivakumar, S., Daniel, J.J., Flynn, J.N., Rankin, S., and Gorbsky, G.J. (2011). Cohesion fatigue induces chromatid separation in cells delayed at metaphase. Curr Biol *21*, 1018-1024.

Davydenko, O., Schultz, R.M., and Lampson, M.A. (2013). Increased CDK1 activity determines the timing of kinetochore-microtubule attachments in meiosis I. J Cell Biol *202*, 221-229.

Di Fiore, B., and Pines, J. (2010). How cyclin A destruction escapes the spindle assembly checkpoint. J Cell Biol *190*, 501-509.

Dick, A.E., and Gerlich, D.W. (2013). Kinetic framework of spindle assembly checkpoint signalling. Nat Cell Biol *15*, 1370-1377.

Dietz, R. (1958). Multiple sex chromosomes in Ostracoda cypria, their evolution and division characteristics. Chromosoma *9*, 359-440.

Dietzl, G., Chen, D., Schnorrer, F., Su, K.C., Barinova, Y., Fellner, M., Gasser, B., Kinsey, K., Oppel, S., Scheiblauer, S*., et al.* (2007). A genome-wide transgenic RNAi library for conditional gene inactivation in Drosophila. Nature *448*, 151-156.

Dobbelaere, J., Josue, F., Suijkerbuijk, S., Baum, B., Tapon, N., and Raff, J. (2008). A genome-wide RNAi screen to dissect centriole duplication and centrosome maturation in Drosophila. PLoS Biol *6*, e224.

Dunleavy, E.M., Beier, N.L., Gorgescu, W., Tang, J., Costes, S.V., and Karpen, G.H. (2012). The cell cycle timing of centromeric chromatin assembly in Drosophila meiosis is distinct from mitosis yet requires CAL1 and CENP-C. PLoS Biol *10*, e1001460.

Endow, S.A., and Hallen, M.A. (2011). Anastral spindle assembly and gamma-tubulin in Drosophila oocytes. BMC Cell Biol *12*, 1.

Endow, S.A., and Komma, D.J. (1997). Spindle dynamics during meiosis in Drosophila oocytes. J Cell Biol *137*, 1321-1336.

Etemad, B., Kuijt, T.E., and Kops, G.J. (2015). Kinetochore-microtubule attachment is sufficient to satisfy the human spindle assembly checkpoint. Nat Commun *6*, 8987.

Fisher, D., Krasinska, L., Coudreuse, D., and Novak, B. (2012). Phosphorylation network dynamics in the control of cell cycle transitions. J Cell Sci *125*, 4703-4711.

Foley, E.A., and Kapoor, T.M. (2013). Microtubule attachment and spindle assembly checkpoint signalling at the kinetochore. Nat Rev Mol Cell Biol *14*, 25-37.

Fudenberg, G., Imakaev, M., Lu, C., Goloborodko, A., Abdennur, N., and Mirny, L.A. (2016). Formation of Chromosomal Domains by Loop Extrusion. Cell Rep *15*, 2038-2049.

Fuller, M.T., ed. (1993). Spermatogenesis (Cold Spring Harbor: Cold Spring Harbor Laboratory Press).

Galli, M., and Morgan, D.O. (2016). Cell Size Determines the Strength of the Spindle Assembly Checkpoint during Embryonic Development. Dev Cell *36*, 344-352.

Gao, S., Giansanti, M.G., Buttrick, G.J., Ramasubramanyan, S., Auton, A., Gatti, M., and Wakefield, J.G. (2008). Australin: a chromosomal passenger protein required specifically for Drosophila melanogaster male meiosis. J Cell Biol *180*, 521-535.

Gartner, S.M., Rathke, C., Renkawitz-Pohl, R., and Awe, S. (2014). Ex vivo culture of Drosophila pupal testis and single male germ-line cysts: dissection, imaging, and pharmacological treatment. J Vis Exp, 51868.

Gilliland, W.D., Hughes, S.E., Cotitta, J.L., Takeo, S., Xiang, Y., and Hawley, R.S. (2007). The Multiple Roles of Mps1 in Drosophila Female Meiosis. PLoS Genet *3*, e113.

Gluszek, A.A., Cullen, C.F., Li, W., Battaglia, R.A., Radford, S.J., Costa, M.F., McKim, K.S., Goshima, G., and Ohkura, H. (2015). The microtubule catastrophe promoter Sentin delays stable kinetochore-microtubule attachment in oocytes. J Cell Biol *211*, 1113-1120.

Goldstein, L.S. (1981). Kinetochore structure and its role in chromosome orientation during the first meiotic division in male D. melanogaster. Cell *25*, 591-602.

Goldstein, L.S.B. (1980). Mechanism of chromosome orientation revealed by two meiotic mutants in Drosophila melanogaster. Chromosoma *78*, 79-111.

Golubovskaya, I.N., Hamant, O., Timofejeva, L., Wang, C.J., Braun, D., Meeley, R., and Cande, W.Z. (2006). Alleles of afd1 dissect REC8 functions during meiotic prophase I. J Cell Sci *119*, 3306-3315.

Gorbsky, G.J. (2015). The spindle checkpoint and chromosome segregation in meiosis. FEBS J *282*, 2471-2487.

Greenbaum, M.P., Iwamori, T., Buchold, G.M., and Matzuk, M.M. (2011). Germ cell intercellular bridges. Cold Spring Harb Perspect Biol *3*, a005850.

Gregan, J., Riedel, C.G., Pidoux, A.L., Katou, Y., Rumpf, C., Schleiffer, A., Kearsey, S.E., Shirahige, K., Allshire, R.C., and Nasmyth, K. (2007). The kinetochore proteins Pcs1 and Mde4 and heterochromatin are required to prevent merotelic orientation. Curr Biol *17*, 1190-1200.

Groth, A.C., Fish, M., Nusse, R., and Calos, M.P. (2004). Construction of transgenic Drosophila by using the site-specific integrase from phage phiC31. Genetics *166*, 1775-1782.

Gruber, S. (2017). Shaping chromosomes by DNA capture and release: gating the SMC rings. Curr Opin Cell Biol *46*, 87-93.

Gyuricza, M.R., Manheimer, K.B., Apte, V., Krishnan, B., Joyce, E.F., McKee, B.D., and McKim, K.S. (2016). Dynamic and Stable Cohesins Regulate Synaptonemal Complex Assembly and Chromosome Segregation. Curr Biol *26*, 1688-1698.

Haarhuis, J.H., Elbatsh, A.M., and Rowland, B.D. (2014). Cohesin and its regulation: on the logic of X-shaped chromosomes. Dev Cell *31*, 7-18.

Hacker, U., and Perrimon, N. (1998). DRhoGEF2 encodes a member of the Dbl family of oncogenes and controls cell shape changes during gastrulation in Drosophila. Genes Dev *12*, 274-284.

Haering, C.H., Farcas, A.M., Arumugam, P., Metson, J., and Nasmyth, K. (2008). The cohesin ring concatenates sister DNA molecules. Nature *454*, 297-301.

Hallson, G., Syrzycka, M., Beck, S.A., Kennison, J.A., Dorsett, D., Page, S.L., Hunter, S.M., Keall, R., Warren, W.D., Brock, H.W*., et al.* (2008). The Drosophila cohesin subunit Rad21 is a trithorax group (trxG) protein. Proc Natl Acad Sci U S A *105*, 12405-12410.

Handke, B., Szabad, J., Lidsky, P.V., Hafen, E., and Lehner, C.F. (2014). Towards long term cultivation of Drosophila wing imaginal discs in vitro. PLoS One *9*, e107333.

Harder, B., Schomburg, A., Pflanz, R., Kustner, K., Gerlach, N., and Schuh, R. (2008). TEV protease-mediated cleavage in Drosophila as a tool to analyze protein functions in living organisms. Biotechniques *44*, 765-772.

Hardy, R.W., Tokuyasu, K.T., and Lindsley, D.L. (1981). Analysis of spermatogenesis in Drosophila melanogaster bearing deletions for Y-chromosome fertility genes. Chromosoma *83*, 593-617.

Hauf, S., and Watanabe, Y. (2004). Kinetochore orientation in mitosis and meiosis. Cell *119*, 317-327.

Hawley, R.S. (2002). Meiosis: how male flies do meiosis. Curr Biol *12*, R660-662.

Hayashi, A., Asakawa, H., Haraguchi, T., and Hiraoka, Y. (2006). Reconstruction of the kinetochore during meiosis in fission yeast Schizosaccharomyces pombe. Mol Biol Cell *17*, 5173-5184.

Hazelett, D.J., Bourouis, M., Walldorf, U., and Treisman, J.E. (1998). decapentaplegic and wingless are regulated by eyes absent and eyegone and interact to direct the pattern of retinal differentiation in the eye disc. Development *125*, 3741-3751.

Heeger, S., Leismann, O., Schittenhelm, R., Schraidt, O., Heidmann, S., and Lehner , C.F. (2005). Genetic inteactions of Separase regulatory subunits reveal the diverged Drosophila Cenp-C homolog. Genes Dev *19*, 2041-2053.

Heidmann, D., Horn, S., Heidmann, S., Schleiffer, A., Nasmyth, K., and Lehner, C.F. (2004). The Drosophila meiotic kleisin C(2)M functions before the meiotic divisions. Chromosoma *113*, 177-187.

Held, M., Schmitz, M.H., Fischer, B., Walter, T., Neumann, B., Olma, M.H., Peter, M., Ellenberg, J., and Gerlich, D.W. (2010). CellCognition: time-resolved phenotype annotation in high-throughput live cell imaging. Nat Methods *7*, 747-754.

Herzig, A., Lehner, C.F., and Heidmann, S. (2002). Proteolytic cleavage of the THR subunit during anaphase limits Drosophila separase function. Genes Dev *16*, 2443-2454.

Hime, G.R., Brill, J.A., and Fuller, M.T. (1996). Assembly of ring canals in the male germ line from structural components of the contractile ring. J Cell Sci *109*, 2779-2788.

Hirano, T., Kobayashi, R., and Hirano, M. (1997). Condensins, chromosome condensation protein complexes containing XCAP-C, XCAP-E and a Xenopus homolog of the Drosophila Barren protein. Cell *89*, 511-521.

Hirose, Y., Suzuki, R., Ohba, T., Hinohara, Y., Matsuhara, H., Yoshida, M., Itabashi, Y., Murakami, H., and Yamamoto, A. (2011). Chiasmata promote monopolar attachment of sister chromatids and their co-segregation toward the proper pole during meiosis I. PLoS Genet *7*, e1001329.

Hoffman, D.B., Pearson, C.G., Yen, T.J., Howell, B.J., and Salmon, E.D. (2001). Microtubule-dependent changes in assembly of microtubule motor proteins and mitotic spindle checkpoint proteins at PtK1 kinetochores. Mol Biol Cell *12*, 1995-2009.

Holubcova, Z., Blayney, M., Elder, K., and Schuh, M. (2015). Human oocytes. Error-prone chromosome-mediated spindle assembly favors chromosome segregation defects in human oocytes. Science *348*, 1143-1147.

Inoue, Y.H., Savoian, M.S., Suzuki, T., Mathe, E., Yamamoto, M.T., and Glover, D.M. (2004). Mutations in orbit/mast reveal that the central spindle is comprised of two microtubule populations, those that initiate cleavage and those that propagate furrow ingression. J Cell Biol *166*, 49-60.

Ishiguro, T., Tanaka, K., Sakuno, T., and Watanabe, Y. (2010). Shugoshin-PP2A counteracts casein-kinase-1-dependent cleavage of Rec8 by separase. Nat Cell Biol *12*, 500-506.

Kabeche, L., and Compton, D.A. (2013). Cyclin A regulates kinetochore microtubules to promote faithful chromosome segregation. Nature *502*, 110-113.

Karess, R. (2005). Rod-Zw10-Zwilch: a key player in the spindle checkpoint. Trends Cell Biol *15*, 386-392.

Katis, V.L., Lipp, J.J., Imre, R., Bogdanova, A., Okaz, E., Habermann, B., Mechtler, K., Nasmyth, K., and Zachariae, W. (2010). Rec8 phosphorylation by casein kinase 1 and Cdc7-Dbf4 kinase regulates cohesin cleavage by separase during meiosis. Dev Cell *18*, 397-409.

Khetani, R.S., and Bickel, S.E. (2007). Regulation of meiotic cohesion and chromosome core morphogenesis during pachytene in Drosophila oocytes. J Cell Sci *120*, 3123-3137.

Kim, J., Ishiguro, K., Nambu, A., Akiyoshi, B., Yokobayashi, S., Kagami, A., Ishiguro, T., Pendas, A.M., Takeda, N., Sakakibara, Y*., et al.* (2015). Meikin is a conserved regulator of meiosis-I-specific kinetochore function. Nature *517*, 466-471.

Kitajima, T.S., Kawashima, S.A., and Watanabe, Y. (2004). The conserved kinetochore protein shugoshin protects centromeric cohesion during meiosis. Nature *427*, 510-517.

Kitajima, T.S., Ohsugi, M., and Ellenberg, J. (2011). Complete kinetochore tracking reveals error-prone homologous chromosome biorientation in mammalian oocytes. Cell *146*, 568-581.

Kitajima, T.S., Sakuno, T., Ishiguro, K., Iemura, S., Natsume, T., Kawashima, S.A., and Watanabe, Y. (2006). Shugoshin collaborates with protein phosphatase 2A to protect cohesin. Nature *441*, 46-52.

Koh, D.S., and Hille, B. (1997). Modulation by neurotransmitters of catecholamine secretion from sympathetic ganglion neurons detected by amperometry. Proc Natl Acad Sci U S A *94*, 1506-1511.

Krishnan, B., Thomas, S.E., Yan, R., Yamada, H., Zhulin, I.B., and McKee, B.D. (2014). Sisters unbound is required for meiotic centromeric cohesion in Drosophila melanogaster. Genetics *198*, 947-965.

Kwenda, L., Collins, C.M., Dattoli, A.A., and Dunleavy, E.M. (2016). Nucleolar activity and CENP-C regulate CENP-A and CAL1 availability for centromere assembly in meiosis. Development *143*, 1400-1412.

Lake, C.M., and Hawley, R.S. (2012). The molecular control of meiotic chromosomal behavior: events in early meiotic prophase in Drosophila oocytes. Annu Rev Physiol *74*, 425-451.

Lampson, M.A., and Grishchuk, E.L. (2017). Mechanisms to Avoid and Correct Erroneous Kinetochore-Microtubule Attachments. Biology (Basel) *6*.

Lee, B., and Amon, A. (2001). Meiosis: how to create a specialized cell cycle. Curr Opin Cell Biol *13*, 770-777.

Lee, B.H., Amon, A., and Prinz, S. (2002). Spo13 regulates cohesin cleavage. Genes Dev *16*, 1672-1681.

Lee, J., Miyano, T., Dai, Y., Wooding, P., Yen, T.J., and Moor, R.M. (2000). Specific regulation of CENP-E and kinetochores during meiosis I/meiosis II transition in pig oocytes. Mol Reprod Dev *56*, 51-62.

Lei, L., and Spradling, A.C. (2016). Mouse oocytes differentiate through organelle enrichment from sister cyst germ cells. Science *352*, 95-99.

Li, X., and Nicklas, R.B. (1995). Mitotic forces control a cell-cycle checkpoint. Nature *373*, 630-632.

Li, X.T., and Nicklas, R.B. (1997). Tension-sensitive kinetochore phosphorylation and the chromosome distribution checkpoint in praying mantid spermatocytes. J Cell Sci *110*, 537-545.

Lidsky, P.V., Sprenger, F., and Lehner, C.F. (2013). Distinct modes of centromere protein dynamics during cell cycle progression in Drosophila S2R+ cells. J Cell Sci *126*, 4782-4793.

Lifschytz, E., and Meyer, G.F. (1977). Characterisation of male meiotic-sterile mutations in drosophila melanogaster. The genetic control of meiotic divisions and gametogenesis. Chromosoma *64*, 371-392.

Liu, D., Vader, G., Vromans, M.J., Lampson, M.A., and Lens, S.M. (2009). Sensing chromosome bi-orientation by spatial separation of aurora B kinase from kinetochore substrates. Science *323*, 1350-1353.

Liu, Y., Petrovic, A., Rombaut, P., Mosalaganti, S., Keller, J., Raunser, S., Herzog, F., and Musacchio, A. (2016). Insights from the reconstitution of the divergent outer kinetochore of Drosophila melanogaster. Open Biol *6*, 150236.

Loncarek, J., Kisurina-Evgenieva, O., Vinogradova, T., Hergert, P., La Terra, S., Kapoor, T.M., and Khodjakov, A. (2007). The centromere geometry essential for keeping mitosis error free is controlled by spindle forces. Nature *450*, 745-749.

Maciejowski, J., George, K.A., Terret, M.E., Zhang, C., Shokat, K.M., and Jallepalli, P.V. (2010). Mps1 directs the assembly of Cdc20 inhibitory complexes during interphase and mitosis to control M phase timing and spindle checkpoint signaling. J Cell Biol *190*, 89-100.

Magidson, V., Paul, R., Yang, N., Ault, J.G., O'Connell, C.B., Tikhonenko, I., McEwen, B.F., Mogilner, A., and Khodjakov, A. (2015). Adaptive changes in the kinetochore architecture facilitate proper spindle assembly. Nat Cell Biol *17*, 1134-1144.

Maiato, H., Gomes, A.M., Sousa, F., and Barisic, M. (2017). Mechanisms of Chromosome Congression during Mitosis. Biology (Basel) *6*.

Malone, C.D., Lehmann, R., and Teixeira, F.K. (2015). The cellular basis of hybrid dysgenesis and Stellate regulation in Drosophila. Curr Opin Genet Dev *34*, 88-94.

Manheim, E.A., and McKim, K.S. (2003). The Synaptonemal complex component C(2)M regulates meiotic crossing over in Drosophila. Curr Biol *13*, 276-285.

Marston, A.L. (2015). Shugoshins: tension-sensitive pericentromeric adaptors safeguarding chromosome segregation. Mol Cell Biol *35*, 634-648.

Mason, J.M. (1976). Orientation disruptor (ord): a recombination-defective and disjunction-defective meiotic mutant in Drosophila melanogaster. Genetics *84*, 545-572.

Mathe, E., Inoue, Y.H., Palframan, W., Brown, G., and Glover, D.M. (2003). Orbit/Mast, the CLASP orthologue of Drosophila, is required for asymmetric stem cell and cystocyte divisions and development of the polarised microtubule network that interconnects oocyte and nurse cells during oogenesis. Development *130*, 901-915.

McKee, B.D., Yan, R., and Tsai, J.H. (2012). Meiosis in male Drosophila. Spermatogenesis *2*, 167-184.

McKim, K.S., Jang, J.K., Theurkauf, W.E., and Hawley, R.S. (1993). Mechanical basis of meiotic metaphase arrest. Nature *362*, 364-367.

McKinley, K.L., and Cheeseman, I.M. (2016). The molecular basis for centromere identity and function. Nat Rev Mol Cell Biol *17*, 16-29.

Mehrotra, S., and McKim, K.S. (2006). Temporal analysis of meiotic DNA double-strand break formation and repair in Drosophila females. PLoS Genet *2*, e200.

Meraldi, P., Draviam, V.M., and Sorger, P.K. (2004a). Timing and checkpoints in the regulation of mitotic progression. Dev Cell *7*, 45-60.

Meraldi, P., Honda, R., and Nigg, E.A. (2004b). Aurora kinases link chromosome segregation and cell division to cancer susceptibility. Curr Opin Genet Dev *14*, 29-36.

Mirkovic, M., Hutter, L.H., Novak, B., and Oliveira, R.A. (2015). Premature Sister Chromatid Separation Is Poorly Detected by the Spindle Assembly Checkpoint as a Result of System-Level Feedback. Cell Rep *13*, 470-478.

Miyawaki, A., Sawano, A., and Kogure, T. (2003). Lighting up cells: labelling proteins with fluorophores. Nat Cell Biol *Suppl*, S1-7.

Miyazaki, W.Y., and Orr-Weaver, T.L. (1992). Sister-chromatid misbehavior in Drosophila ord mutants. Genetics *132*, 1047-1061.

Mochida, S., Rata, S., Hino, H., Nagai, T., and Novak, B. (2016). Two Bistable Switches Govern M Phase Entry. Curr Biol *26*, 3361-3367.

Morgan, T.H. (1912). Special Articles. Science *36*, 718-720.

Mosalaganti, S., Keller, J., Altenfeld, A., Winzker, M., Rombaut, P., Saur, M., Petrovic, A., Wehenkel, A., Wohlgemuth, S., Muller, F.*, et al.* (2017). Structure of the RZZ complex and molecular basis of its interaction with Spindly. J Cell Biol *216*, 961-981.

Musacchio, A. (2015). The Molecular Biology of Spindle Assembly Checkpoint Signaling Dynamics. Curr Biol *25*, R1002-1018.

Musacchio, A., and Desai, A. (2017). A Molecular View of Kinetochore Assembly and Function. Biology (Basel) *6*.

Musacchio, A., and Salmon, E.D. (2007). The spindle-assembly checkpoint in space and time. Nat Rev Mol Cell Biol *8*, 379-393.

Nasmyth, K. (2001). Disseminating the genome: joining, resolving, and separating sister chromatids during mitosis and meiosis. Annu Rev Genet *35*, 673-745.

Nasmyth, K. (2011). Cohesin: a catenase with separate entry and exit gates? Nat Cell Biol *13*, 1170-1177.

Nasmyth, K. (2015). A meiotic mystery: How sister kinetochores avoid being pulled in opposite directions during the first division. Bioessays *37*, 657-665.

Nasmyth, K., and Haering, C.H. (2005). The structure and function of SMC and kleisin complexes. Annu Rev Biochem *74*, 595-648.

Ni, J.Q., Zhou, R., Czech, B., Liu, L.P., Holderbaum, L., Yang-Zhou, D., Shim, H.S., Tao, R., Handler, D., Karpowicz, P.*, et al.* (2011). A genome-scale shRNA resource for transgenic RNAi in Drosophila. Nat Methods *8*, 405-407.

Nicklas, R.B. (1961). Recurrent pole-to-pole movements of the sex chromosome during prometaphase I in Melanoplus differentialis spermatocytes. Chromosoma *12*, 97-115.

Nicklas, R.B. (1965). Chromosome Velocity during Mitosis as a Function of Chromosome Size and Position. J Cell Biol *25*, SUPPL:119-135.

Nicklas, R.B. (1997). How cells get the right chromosomes. Science *275*, 632-637.

Nicklas, R.B., and Koch, C.A. (1969). Chromosome micromanipulation. 3. Spindle fiber tension and the reorientation of mal-oriented chromosomes. J Cell Biol *43*, 40-50.

Nicklas, R.B., and Ward, S.C. (1994). Elements of error-correction in mitosis - microtubule capture, release, and tension. J Cell Biol *126*, 1241-1253.

Nicklas, R.B., Ward, S.C., and Gorbsky, G.J. (1995). Kinetochore chemistry is sensitive to tension and may link mitotic forces to a cell-cycle checkpoint. J Cell Biol *130*, 929-939.

Novak, Z.A., Conduit, P.T., Wainman, A., and Raff, J.W. (2014). Asterless licenses daughter centrioles to duplicate for the first time in Drosophila embryos. Curr Biol *24*, 1276-1282.

O'Neill, R.S., and Clark, D.V. (2016). Partial Functional Diversification of Drosophila melanogaster Septin Genes Sep2 and Sep5. G3 (Bethesda) *6*, 1947-1957.

Ong, S., and Tan, C. (2010). Germline cyst formation and incomplete cytokinesis during Drosophila melanogaster oogenesis. Dev Biol *337*, 84-98.

Ottolini, C.S., Newnham, L.J., Capalbo, A., Natesan, S.A., Joshi, H.A., Cimadomo, D., Griffin, D.K., Sage, K., Summers, M.C., Thornhill, A.R*., et al.* (2015). Genome-wide maps of recombination and chromosome segregation in human oocytes and embryos show selection for maternal recombination rates. Nat Genet *47*, 727-735.

Paliulis, L.V., and Nicklas, R.B. (2005). Kinetochore rearrangement in meiosis II requires attachment to the spindle. Chromosoma *113*, 440-446.

Pandey, R., Heeger, S., and Lehner, C.F. (2007). Rapid effects of acute anoxia on spindle kinetochore interactions activate the mitotic spindle checkpoint. J Cell Sci *120*, 2807-2818.

Pandey, R., Heidmann, S., and Lehner, C.F. (2005). Epithelial re-organization and dynamics of progression through mitosis in Drosophila separase complex mutants. J Cell Sci *118*, 733-742.

Parra, M.T., Viera, A., Gomez, R., Page, J., Benavente, R., Santos, J.L., Rufas, J.S., and Suja, J.A. (2004). Involvement of the cohesin Rad21 and SCP3 in monopolar attachment of sister kinetochores during mouse meiosis I. J Cell Sci *117*, 1221-1234.

Patel, J., Tan, S.L., Hartshorne, G.M., and McAinsh, A.D. (2015). Unique geometry of sister kinetochores in human oocytes during meiosis I may explain maternal age-associated increases in chromosomal abnormalities. Biol Open *5*, 178-184.

Pauli, A., Althoff, F., Oliveira, R.A., Heidmann, S., Schuldiner, O., Lehner, C.F., Dickson, B.J., and Nasmyth, K. (2008). Cell-type-specific TEV protease cleavage reveals cohesin functions in Drosophila neurons. Dev Cell *14*, 239-251.

Pfender, S., Kuznetsov, V., Pasternak, M., Tischer, T., Santhanam, B., and Schuh, M. (2015). Live imaging RNAi screen reveals genes essential for meiosis in mammalian oocytes. Nature *524*, 239-242.

Pimenta-Marques, A., Bento, I., Lopes, C.A., Duarte, P., Jana, S.C., and Bettencourt-Dias, M. (2016). A mechanism for the elimination of the female gamete centrosome in Drosophila melanogaster. Science *353*, aaf4866.

Przewloka, M.R., and Glover, D.M. (2009). The kinetochore and the centromere: a working long distance relationship. Annu Rev Genet *43*, 439-465.

Przewloka, M.R., Venkei, Z., Bolanos-Garcia, V.M., Debski, J., Dadlez, M., and Glover, D.M. (2011). CENP-C is a structural platform for kinetochore assembly. Curr Biol *21*, 399-405.

Przewloka, M.R., Zhang, W., Costa, P., Archambault, V., D'Avino, P.P., Lilley, K.S., Laue, E.D., McAinsh, A.D., and Glover, D.M. (2007). Molecular analysis of core kinetochore composition and assembly in Drosophila melanogaster. PLoS ONE *2*, e478.

Radermacher, P.T., Myachina, F., Bosshardt, F., Pandey, R., Mariappa, D., Muller, H.A., and Lehner, C.F. (2014). O-GlcNAc reports ambient temperature and confers heat resistance on ectotherm development. Proc Natl Acad Sci U S A *111*, 5592-5597.

Radford, S.J., Hoang, T.L., Gluszek, A.A., Ohkura, H., and McKim, K.S. (2015). Lateral and End-On Kinetochore Attachments Are Coordinated to Achieve Bi-orientation in Drosophila Oocytes. PLoS Genet *11*, e1005605.

Radford, S.J., Jang, J.K., and McKim, K.S. (2012). The chromosomal passenger complex is required for meiotic acentrosomal spindle assembly and chromosome biorientation. Genetics *192*, 417-429.

Radford, S.J., Nguyen, A.L., Schindler, K., and McKim, K.S. (2017). The chromosomal basis of meiotic acentrosomal spindle assembly and function in oocytes. Chromosoma *126*, 351-364.

Rahmani, Z., Gagou, M.E., Lefebvre, C., Emre, D., and Karess, R.E. (2009). Separating the spindle, checkpoint, and timer functions of BubR1. J Cell Biol *187*, 597-605.

Raj, A., and Peskin, C.S. (2006). The influence of chromosome flexibility on chromosome transport during anaphase A. Proc Natl Acad Sci U S A *103*, 5349-5354.

Rankin, S. (2015). Complex elaboration: making sense of meiotic cohesin dynamics. FEBS J *282*, 2426-2443.

Raychaudhuri, N., Dubruille, R., Orsi, G.A., Bagheri, H.C., Loppin, B., and Lehner, C.F. (2012). Transgenerational propagation and quantitative maintenance of paternal centromeres depends on Cid/Cenp-A presence in Drosophila sperm. PLoS Biol *10*, e1001434.

Raychaudhuri, N.T. (2012). Epigenetic Control of Centromeric Cid/Cenp-A Levels During Spermatogenesis and Development (Universität Zürich).

Rebollo, E., and Gonzalez, C. (2000). Visualizing the spindle checkpoint in Drosophila spermatocytes. EMBO Rep *1*, 65-70.

Rebollo, E., Llamazares, S., Reina, J., and Gonzalez, C. (2004). Contribution of noncentrosomal microtubules to spindle assembly in Drosophila spermatocytes. PLoS Biol *2*, E8.

Richter, M.M., Poznanski, J., Zdziarska, A., Czarnocki-Cieciura, M., Lipinszki, Z., Dadlez, M., Glover, D.M., and Przewloka, M.R. (2016). Network of protein interactions within the Drosophila inner kinetochore. Open Biol *6*, 150238.

Rieder, C.L. (1982). The formation, structure, and composition of the mammalian kinetochore and kinetochore fiber. Int Rev Cytol *79*, 1-58.

Rieder, C.L., and Maiato, H. (2004). Stuck in division or passing through: what happens when cells cannot satisfy the spindle assembly checkpoint. Dev Cell *7*, 637-651.

Rieder, C.L., Schultz, A., Cole, R., and Sluder, G. (1994). Anaphase onset in vertebrate somatic cells is controlled by a checkpoint that monitors sister kinetochore attachment to the spindle. J Cell Biol *127*, 1301-1310.

Rio, D.C. (1990). Molecular mechanisms regulating Drosophila P element transposition. Annu Rev Genet *24*, 543-578.

Robb, J.A. (1969). Maintenance of imaginal discs of Drosophila melanogaster in chemically defined media. J Cell Biol *41*, 876-885.

Rodriguez-Bravo, V., Maciejowski, J., Corona, J., Buch, H.K., Collin, P., Kanemaki, M.T., Shah, J.V., and Jallepalli, P.V. (2014). Nuclear pores protect genome integrity by assembling a premitotic and Mad1-dependent anaphase inhibitor. Cell *156*, 1017-1031.

Rong, Y.S. (2008). Loss of the histone variant H2A.Z restores capping to checkpoint-defective telomeres in Drosophila. Genetics *180*, 1869-1875.

Roth, S., and Lynch, J.A. (2009). Symmetry breaking during Drosophila oogenesis. Cold Spring Harb Perspect Biol *1*, a001891.

Rubin, G.M., and Spradling, A.C. (1982). Genetic transformation of Drosophila with transposable element vectors. Science *218*, 348-353.

Sacristan, C., and Kops, G.J. (2015). Joined at the hip: kinetochores, microtubules, and spindle assembly checkpoint signaling. Trends Cell Biol *25*, 21-28.

Sakuno, T., Tada, K., and Watanabe, Y. (2009). Kinetochore geometry defined by cohesion within the centromere. Nature *458*, 852-858.

Salmon, E.D., and Tran, P. (2007). High-resolution video-enhanced differential interference contrast light microscopy. Methods Cell Biol *81*, 335-364.

Sambrook, J., Fritsch, E.F., and Maniatis, T. (1989). Molecular Cloning - A Laboratory Manual, 2 edn (Cold Spring Harbor Laboratory Press).

Sanborn, A.L., Rao, S.S., Huang, S.C., Durand, N.C., Huntley, M.H., Jewett, A.I., Bochkov, I.D., Chinnappan, D., Cutkosky, A., Li, J*., et al.* (2015). Chromatin extrusion explains key features of loop and domain formation in wild-type and engineered genomes. Proc Natl Acad Sci U S A *112*, E6456-6465.

Sarangapani, K.K., Duro, E., Deng, Y., Alves Fde, L., Ye, Q., Opoku, K.N., Ceto, S., Rappsilber, J., Corbett, K.D., Biggins, S*., et al.* (2014). Sister kinetochores are mechanically fused during meiosis I in yeast. Science *346*, 248-251.

Savoian, M.S. (2015). Using Photobleaching to Measure Spindle Microtubule Dynamics in Primary Cultures of Dividing Drosophila Meiotic Spermatocytes. J Biomol Tech *26*, 66-73.

Savoian, M.S., and Glover, D.M. (2014). Differing requirements for Augmin in male meiotic and mitotic spindle formation in Drosophila. Open Biol *4*, 140047.

Savoian, M.S., Goldberg, M.L., and Rieder, C.L. (2000). The rate of poleward chromosome motion is attenuated in Drosophila zw10 and rod mutants. Nat Cell Biol *2*, 948-952.

Scaerou, F., Aguilera, I., Saunders, R., Kane, N., Blottiere, L., and Karess, R. (1999). The rough deal protein is a new kinetochore component required for accurate chromosome segregation in Drosophila. J Cell Sci *112 (Pt 21)*, 3757-3768.

Schittenhelm, R.B., Althoff, F., Heidmann, S., and Lehner, C.F. (2010). Detrimental incorporation of excess Cenp-A/Cid and Cenp-C into Drosophila centromeres is prevented by limiting amounts of the bridging factor Cal1. J Cell Sci *123*, 3768-3779.

Schittenhelm, R.B., Chaleckis, R., and Lehner, C.F. (2009). Essential functional domains and intrakinetochore localization of Drosophila Spc105. EMBO J *28*, 2374-2386.

Schittenhelm, R.B., Heeger, S., Althoff, F., Walter, A., Heidmann, S., Mechtler, K., and Lehner, C.F. (2007). Spatial organization of a ubiquitous eukaryotic kinetochore protein network in Drosophila chromosomes. Chromosoma *116*, 385-402.

Schleiffer, A., Kaitna, S., Maurer-Stroh, S., Glotzer, M., Nasmyth, K., and Eisenhaber, F. (2003). Kleisins: a superfamily of bacterial and eukaryotic SMC protein partners. Mol Cell *11*, 571-575.

Schmidt, J.C., Arthanari, H., Boeszoermenyi, A., Dashkevich, N.M., Wilson-Kubalek, E.M., Monnier, N., Markus, M., Oberer, M., Milligan, R.A., Bathe, M.*, et al.* (2012). The kinetochore-bound Ska1 complex tracks depolymerizing microtubules and binds to curved protofilaments. Dev Cell *23*, 968-980.

Schuh, M., Lehner, C.F., and Heidmann, S. (2007). Incorporation of Drosophila CID/CENP-A and CENP-C into centromeres during early embryonic anaphase. Curr Biol *17*, 237-243.

Severson, A.F., and Meyer, B.J. (2014). Divergent kleisin subunits of cohesin specify mechanisms to tether and release meiotic chromosomes. Elife *3*, e03467.

Shaner, N.C., Lin, M.Z., McKeown, M.R., Steinbach, P.A., Hazelwood, K.L., Davidson, M.W., and Tsien, R.Y. (2008). Improving the photostability of bright monomeric orange and red fluorescent proteins. Nat Methods *5*, 545-551.

Shao, H., Li, R., Ma, C., Chen, E., and Liu, X.J. (2013). Xenopus oocyte meiosis lacks spindle assembly checkpoint control. J Cell Biol *201*, 191-200.

Shindo, N., Kumada, K., and Hirota, T. (2012). Separase Sensor Reveals Dual Roles for Separase Coordinating Cohesin Cleavage and Cdk1 Inhibition. Developmental Cell *23*, 112-123.

Shonn, M.A., McCarroll, R., and Murray, A.W. (2002). Spo13 protects meiotic cohesin at centromeres in meiosis I. Genes Dev *16*, 1659-1671.

Silverman-Gavrila, R.V., Hales, K.G., and Wilde, A. (2008). Anillin-mediated targeting of peanut to pseudocleavage furrows is regulated by the GTPase Ran. Mol Biol Cell *19*, 3735-3744.

Singleton, M.R. (2016). Getting to the heart of an unusual kinetochore. Open Biol *6*, 160040.

Skold, H.N., Komma, D.J., and Endow, S.A. (2005). Assembly pathway of the anastral Drosophila oocyte meiosis I spindle. J Cell Sci *118*, 1745-1755.

Suja, J.A., Antonio, C., Debec, A., and Rufas, J.S. (1999). Phosphorylated proteins are involved in sister-chromatid arm cohesion during meiosis I. J Cell Sci *112 (Pt 17)*, 2957-2969.

Suja, J.A., Antonio, C., and Rufas, J.S. (1992). Involvement of chromatid cohesiveness at the centromere and chromosome arms in meiotic chromosome segregation: a cytological approach. Chromosoma *101*, 493-501.

Tachibana-Konwalski, K., Godwin, J., Borsos, M., Rattani, A., Adams, D.J., and Nasmyth, K. (2013). Spindle assembly checkpoint of oocytes depends on a kinetochore structure determined by cohesin in meiosis I. Curr Biol *23*, 2534-2539.

Tanneti, N.S., Landy, K., Joyce, E.F., and McKim, K.S. (2011). A pathway for synapsis initiation during zygotene in Drosophila oocytes. Current biology : CB *21*, 1852-1857.

Tates, A.D. (1971). Cytodifferentiation during spermatogenesis in Drosophila melanogaster: An electron microscope study (Leiden, Netherlands, Rijksuniversiteit de Leiden).

Tauchman, E.C., Boehm, F.J., and DeLuca, J.G. (2015). Stable kinetochore-microtubule attachment is sufficient to silence the spindle assembly checkpoint in human cells. Nat Commun *6*, 10036.

Theurkauf, W.E., and Hawley, R.S. (1992). Meiotic spindle assembly in Drosophila females: behavior of nonexchange chromosomes and the effects of mutations in the nod kinesin-like protein. J Cell Biol *116*, 1167-1180.

Thomas, S.E., and McKee, B.D. (2007). Meiotic pairing and disjunction of mini-X chromosomes in drosophila is mediated by 240-bp rDNA repeats and the homolog conjunction proteins SNM and MNM. Genetics *177*, 785-799.

Thomas, S.E., Soltani-Bejnood, M., Roth, P., Dorn, R., Logsdon, J.M., Jr., and McKee, B.D. (2005). Identification of two proteins required for conjunction and regular segregation of achiasmate homologs in Drosophila male meiosis. Cell *123*, 555-568.

Tomkiel, J.E., Wakimoto, B.T., and Briscoe, A., Jr. (2001). The teflon gene is required for maintenance of autosomal homolog pairing at meiosis I in male Drosophila melanogaster. Genetics *157*, 273-281.

Touati, S.A., and Wassmann, K. (2016). How oocytes try to get it right: spindle checkpoint control in meiosis. Chromosoma *125*, 321-335.

Tsai, J.H., and McKee, B.D. (2011). Homologous pairing and the role of pairing centers in meiosis. J Cell Sci *124*, 1955-1963.

Tsuchiya, D., Gonzalez, C., and Lacefield, S. (2011). The spindle checkpoint protein Mad2 regulates APC/C activity during prometaphase and metaphase of meiosis I in Saccharomyces cerevisiae. Mol Biol Cell *22*, 2848-2861.

Tsurumi, C., Hoffmann, S., Geley, S., Graeser, R., and Polanski, Z. (2004). The spindle assembly checkpoint is not essential for CSF arrest of mouse oocytes. J Cell Biol *167*, 1037-1050.

Uhlmann, F. (2003). Chromosome cohesion and separation: from men and molecules. Curr Biol *13*, R104-114.

Uhlmann, F. (2016). SMC complexes: from DNA to chromosomes. Nat Rev Mol Cell Biol *17*, 399-412.

Urban, E., Nagarkar-Jaiswal, S., Lehner, C.F., and Heidmann, S.K. (2014). The cohesin subunit Rad21 is required for synaptonemal complex maintenance, but not sister chromatid cohesion, during Drosophila female meiosis. PLoS Genet *10*, e1004540.

van Daal, A., and Elgin, S.C. (1992). A histone variant, H2AvD, is essential in Drosophila melanogaster. Mol Biol Cell *3*, 593-602.

Van Doren, M., Williamson, A.L., and Lehmann, R. (1998). Regulation of zygotic gene expression in Drosophila primordial germ cells. Curr Biol *8*, 243-246.

Vazquez, J., Belmont, A.S., and Sedat, J.W. (2001). Multiple regimes of constrained chromosome motion are regulated in the interphase Drosophila nucleus. Curr Biol *11*, 1227-1239.

Vazquez, J., Belmont, A.S., and Sedat, J.W. (2002). The dynamics of homologous chromosome pairing during male Drosophila meiosis. Curr Biol *12*, 1473-1483.

Venkei, Z., Przewloka, M.R., and Glover, D.M. (2011). Drosophila Mis12 complex acts as a single functional unit essential for anaphase chromosome movement and a robust spindle assembly checkpoint. Genetics *187*, 131-140.

Venkei, Z., Przewloka, M.R., Ladak, Y., Albadri, S., Sossick, A., Juhasz, G., Novak, B., and Glover, D.M. (2012). Spatiotemporal dynamics of Spc105 regulates the assembly of the Drosophila kinetochore. Open Biol *2*, 110032.

Ventela, S., Toppari, J., and Parvinen, M. (2003). Intercellular organelle traffic through cytoplasmic bridges in early spermatids of the rat: mechanisms of haploid gene product sharing. Mol Biol Cell *14*, 2768-2780.

Warren, W.D., Steffensen, S., Lin, E., Coelho, P., Loupart, M., Cobbe, N., Lee, J.Y., McKay, M.J., Orr-Weaver, T., Heck, M.M., *et al.* (2000). The Drosophila RAD21 cohesin persists at the centromere region in mitosis. Curr Biol *10*, 1463-1466.

Watanabe, Y. (2005). Sister chromatid cohesion along arms and at centromeres. Trends Genet *21*, 405-412.

Watanabe, Y., and Kitajima, T.S. (2005). Shugoshin protects cohesin complexes at centromeres. Philos Trans R Soc Lond B Biol Sci *360*, 515-521, discussion 521.

Webber, H.A., Howard, L., and Bickel, S.E. (2004). The cohesion protein ORD is required for homologue bias during meiotic recombination. J Cell Biol *164*, 819-829.

Webster, A., and Schuh, M. (2017). Mechanisms of Aneuploidy in Human Eggs. Trends Cell Biol *27*, 55-68.

White-Cooper, H. (2003). Drosophila Cytogenetics Protocols. In Methods in Molecular Biology Spermatogenesis: Analysis of Meiosis and Morphogenesis.

Winey, M., Morgan, G.P., Straight, P.D., Giddings, T.H., Jr., and Mastronarde, D.N. (2005). Three-dimensional ultrastructure of Saccharomyces cerevisiae meiotic spindles. Mol Biol Cell *16*, 1178-1188.

Wolff, I.D., Tran, M.V., Mullen, T.J., Villeneuve, A.M., and Wignall, S.M. (2016). Assembly of Caenorhabditis elegans acentrosomal spindles occurs without evident microtubule-organizing centers and requires microtubule sorting by KLP-18/kinesin-12 and MESP-1. Mol Biol Cell *27*, 3122-3131.

Wurm, C.A., Neumann, D., Schmidt, R., Egner, A., and Jakobs, S. (2010). Sample preparation for STED microscopy. Methods Mol Biol *591*, 185-199.

Wynne, D.J., and Funabiki, H. (2015). Kinetochore function is controlled by a phospho-dependent coexpansion of inner and outer components. J Cell Biol *210*, 899-916.

Yaakov, G., Thorn, K., and Morgan, D.O. (2012). Separase biosensor reveals that cohesin cleavage timing depends on phosphatase PP2A(Cdc55) regulation. Dev Cell *23*, 124-136.

Yan, R., and McKee, B.D. (2013). The cohesion protein SOLO associates with SMC1 and is required for synapsis, recombination, homolog bias and cohesion and pairing of centromeres in Drosophila Meiosis. PLoS Genet *9*, e1003637.

Yan, R., Thomas, S.E., Tsai, J.H., Yamada, Y., and McKee, B.D. (2010). SOLO: a meiotic protein required for centromere cohesion, coorientation, and SMC1 localization in Drosophila melanogaster. J Cell Biol *188*, 335-349.

Ye, Q., Ur, S.N., Su, T.Y., and Corbett, K.D. (2016). Structure of the Saccharomyces cerevisiae Hrr25:Mam1 monopolin subcomplex reveals a novel kinase regulator. EMBO J *35*, 2139-2151.

Yokobayashi, S., and Watanabe, Y. (2005). The kinetochore protein Moa1 enables cohesion-mediated monopolar attachment at meiosis I. Cell *123*, 803-817.

Yoshida, S., Kaido, M., and Kitajima, T.S. (2015). Inherent Instability of Correct Kinetochore-Microtubule Attachments during Meiosis I in Oocytes. Dev Cell *33*, 589-602.

Yoshida, S., Sakakibara, Y., and Kitajima, T.S. (2016). Live Imaging of Intracellular Dynamics During Meiotic Maturation in Mouse Oocytes. Methods Mol Biol *1457*, 241-251.

Yuan, K., Shermoen, A.W., and O'Farrell, P.H. (2014). Illuminating DNA replication during Drosophila development using TALE-lights. Curr Biol *24*, R144-145.

Zaytsev, A.V., and Grishchuk, E.L. (2015). Basic mechanism for biorientation of mitotic chromosomes is provided by the kinetochore geometry and indiscriminate turnover of kinetochore microtubules. Mol Biol Cell *26*, 3985-3998.

Zhang, D., and Nicklas, R.B. (1999). Micromanipulation of chromosomes and spindles in insect spermatocytes. Methods Cell Biol *61*, 209-218.

Zhang, Z., and Pugh, B.F. (2011). Genomic organization of H2Av containing nucleosomes in Drosophila heterochromatin. PLoS One *6*, e20511.

Zielinska, A.P., Holubcova, Z., Blayney, M., Elder, K., and Schuh, M. (2015). Sister kinetochore splitting and precocious disintegration of bivalents could explain the maternal age effect. Elife *4*, e11389.

CURRICULUM VITAE

Personal Information

Surname: **CHAURASIA**

Name: **Soumya**

Date of birth: **18.12.1987**

Place of birth: **Bhopal (Madhya Pradesh)**

Nationality: **Indian**

Education

1995-2005	**Secondary education** Carmel Convent Sr. Sec. School, Central Board of Secondary Education (CBSE), B.H.E.L., Bhopal
2006-2010	**Bachelor of Technology** (B.Tech in Biotechnology) School of Bio science and technology, VIT University, Vellore, India
2011-2013	**Master of Science** (Cell and molecular biology) University of Zurich, Switzerland *Thesis title:* The role of Drosophila Rad21 and Spc105 during male meiosis
2013-Present	**PhD in Biology** MLS PhD program, Institute of molecular life sciences University of Zurich, Switzerland *Thesis title:* Dynamics of the meiotic division in Drosophila males

Publications

Blattner AC, **Chaurasia S**, McKee BD, Lehner CF. Separase Is Required for Homolog and Sister Disjunction during Drosophila melanogaster Male Meiosis, but Not for Biorientation of Sister Centromeres.
PLoS Genet. 2016 Apr 27;12(4).